



Developing methods to analyse intrusions

in the upper crust

by

Suraya Hilmi Hazim

(201072169)

Thesis submitted in accordance with the requirements of the University of Liverpool for the degree of Doctor of Philosophy.

28th August 2020.

Declaration

I declare that the work presented in this thesis is my own work as part of my PhD programme at the University of Liverpool. This thesis has been prepared in accordance with the requirements of the university's PGR Code of Practice. All outside work have been referenced accordingly. I confirm that the work that has been presented in this thesis has not been submitted for any other academic award.

Suraya Hilmi Hazim

School of Environmental Sciences
Faculty of Science and Engineering
University of Liverpool

August 2020

© Suraya Hilmi Hazim

The copyright of this thesis rests with the author. No quotation from it should be published without the author's prior written consent and information derived from it should be acknowledged accordingly

Abstract

The understanding of the physical and mechanical processes which drive volcanic eruptions are vital for better hazard mitigation in volcanic regions. As interest continues to grow in the study of Volcanic and Igneous Plumbing Systems (VIPS), it has become essential for researchers to examine, inform and improve methods that have been published, as well as to explore and come up with new methods that are both accessible and reproducible. This research presents a series of methods developed by the author to study intrusions in the field using field photographs as well as in a laboratory setting using analogue modelling.

Field photographs are effective tools which help researchers to capture observations in the field and disseminate information quickly as visual aids in presentations and publications. Other than being sources of good qualitative data, field photographs also capture a lot of quantitative information that can be extracted using digital image analysis methods. Chapter 2 of this thesis provides a step-by-step guide developed to extract quantitative data from field photographs using CorelDraw (pre-processing) and ImageJ (data collection). Also included are worked examples using photographs of the roof contacts found in Torres del Paine, Chile.

Chapters 3 and 4 explore the use of gelatine as an analogue material in laboratory modelling. Before the gelatine is used in experiments, the mechanical properties of the gelatine are rigorously tested using two methods in Chapter 3: firstly the indentation method and secondly by using a rotational rheometer. Both tests reveal that gelatine with the concentration of 1.0-3.5 wt.% at a constant temperature of 5-10°C behave in an elastic manner. Over time, the Young's modulus of gelatine reaches a plateau where it has achieved a stable internal arrangement which would stay the same unless acted upon by an external force. Gelatine is then used as an analogue material for host rock in the experiments presented in Chapter 4.

Chapter 4 presents a compilation results from select analogue experiments which simulate the formation of surface and subsurface deformation patterns induced by the propagation of magma-filled fractures in the Earth's crust. The models use dyed water as a magma analogue and solidified gelatine as an elastic crustal analogue. The gelatine is prepared in a square-based experimental tank measuring 40 x 40 x 30 cm³ using the preparation guidelines outlined in Chapter 3. Propagation of dykes in the Earth's crust is modelled by injecting fluid through the base of the tank into a single homogeneous layer of solidified gelatine, and the propagation of sills is modelled by injecting the fluid through the base of the tank into two superposed layers of solidified gelatine. Sills form when the top layer is more rigid than the bottom layer and exploit the weak interface between them. The experiments are monitored using digital cameras to record changes in the intrusion geometry over time and progressive deformation of the surface of the crustal analogue is recorded using an overhead laser scanner. Polarised light allows subsurface stress patterns to be observed as the intrusions grow. The evolving strain in the crustal analogue is quantified using digital image correlation (DIC).

The experimental results show that the propagation of dykes causes two topographic highs to form at the surface, flanking a linear region of topographic low directly above the dyke tip prior to an eruption. This deformation pattern is also evident during early stages of dyke growth where the dyke tip is consistently flanked by bow-tie shaped stress fields, which correlates well to the evolving strain where strain vectors are highly concentrated near the tip of the dyke. This prominent deformation pattern however is only clearly observed when the intrusion is closest to the surface of the gelatine (i.e. For dyke experiments, within the final 4 cm depth before eruption). Even then, the observed cumulative surface deformation is very small, with a maximum displacement of 1-2 millimetres. It is found that in experiments involving sills where the sill is

formed halfway down the experimental tank, the deformation on the surface is only expressed as regional uplift with no prominent topographic patterns forming on the surface of the gelatine. The evolving strain vectors continue to be concentrated at the tip of the dyke during the formation of the sill. As the sill propagates, the vectors become concentrated at the edge of the sill as well. This pattern is reflected in the bow-tie shaped stress field which remain concentrated at the tip of the dyke, while new colour fringes form and grow as the sill propagates away from the dyke.

Table of Contents

1	Introduction to Thesis.....	1
1.1	Background	1
1.1.1	Dyke and Sill Emplacement Models.....	7
1.1.2	Analogue Modelling of magma intrusions.....	8
1.2	Thesis Aims and Objectives.....	12
1.3	Thesis Structure	13
1.4	References	21
2	Quantitative Analysis of Field Images: The Torres del Paine Intrusive Complex (TPIC), Chile	30
2.1	Introduction to Chapter	30
2.2	Regional Geology: Torres del Paine Intrusive Complex (TPIC), Chile.....	30
2.2.1	Torres del Paine Intrusive Complex (TPIC), Chile.....	31
2.3	Description of Structures Associated with Magmatic Intrusions at Torres del Paine, Chile	37
2.3.1	Torres del Paine Intrusive Complex (TPIC), Chile.....	37
2.4	Method Development: ImageJ	41
2.4.1	ImageJ Sensitivity Analysis: Preparation of Test Images	42
2.4.2	Effect of Line Thickness.....	52

2.4.3	Effect of Line Angle	53
2.4.4	Effect of Two-Dimensional Shapes	56
2.4.5	Implications for Systematic Error.....	58
2.5	Field Image Analysis Workflow	58
2.5.1	Pre-processing Images: Pixel Value Mapping	58
2.5.3	Scaling Field Images for Image Analysis.....	63
2.5.4	Processing using ImageJ.....	65
2.5.5	Results: Torres del Paine Intrusive Complex, Chile.....	66
2.6	Discussion.....	70
2.6.1	Modelled Overpressures.....	70
2.6.2	Workflow Recommendation.....	71
2.7	Conclusion and Future Work	72
2.8	Chapter References.....	73
3	Characterisation of Gelatine as an Analogue Material for Modelling Magma Intrusion Growth in the Earth's Crust	76
3.1	Introduction	76
3.2	Methodology and Experimental Setup.....	78
3.2.1	Gelatine preparation.....	78
3.2.2	Classic scaling approach.....	80
3.2.3	Scaling of Gelatine.....	82
3.2.4	Indentation Experiment Setup.....	84
3.2.5	Rotational Rheometer Setup	87

3.2.6	Data Processing.....	89
3.3	Results.....	92
3.3.1	Indentation Experiment.....	92
3.3.2	Rotational Rheology Experiments.....	100
3.4	Discussion.....	106
3.5	Conclusion.....	108
3.6	Chapter References.....	108
3.7	MAGMA Lab Gelatine Preparation: Quick Guide.....	113
3.7.1	Notes:.....	113
4	Analogue Modelling of Surface Deformation Driven by Magma Movement at Depth	114
4.1	Introduction to Chapter	114
4.2	Background	114
4.3	Methodology and Experiment Setup.....	115
4.3.1	Gelatine Preparation and Scaling.....	115
4.3.2	Experimental Setup.....	117
4.3.3	Post-Processing Data.....	121
4.4	Results.....	124
4.4.1	Experimental Dyke Intrusions: Single Layer Experiments.....	125
4.4.2	Experimental Dyke Intrusions: Two-Layered Experiments	134
4.4.3	Experimental Sill Intrusions.....	141
4.5	Discussion.....	147

4.5.1	Modelling the host-rock as an elastic material.....	149
4.5.2	The effect of magma rheology on intrusion dynamics	152
4.5.3	The effect of stresses on magma intrusion.....	156
4.6	Conclusion.....	157
4.6.1	Propagation and Growth of Experimental Dykes	157
4.6.2	Propagation and Growth of Experimental Sills	158
4.7	Limitations and future work	159
4.8	Chapter References.....	160
4.9	Software Sources	166
5	Conclusions.....	167
5.1	Objectives Revisited.....	167
5.1.1	Chapter 2.....	167
5.1.2	Chapter 3.....	168
5.1.3	Chapter 4.....	169
5.2	Limitations.....	170
5.3	Future Work.....	171
6	Appendices	172
6.1	Publication (1): Challenging dyke ascent models using novel laboratory experiments: Implications for reinterpreting evidence of magma ascent and volcanism	
	172	
6.1.1	Contribution to Publication (1):	172

6.2	Publication (2): The impact of unloading stresses on post-caldera magma intrusions	173
6.2.1	Contribution to Publication (2):	173

List of Figures

Figure 1.1: Cartoon diagram showing different types of intrusions. Dykes (A, B), sills (C) and cone sheets (D) are examples of sheet intrusions which have a large length to thickness ratio. Laccoliths (E) and plutons (F) are examples of large igneous bodies which have a smaller length to thickness ratio. 2

Figure 1.2: Examples of dykes in the field: (A) An exposed cliff face in the Reykjanes Peninsula, Iceland, showing an arrested basaltic dyke (Gudmundsson and Loetveit, 2005). (B) A branched kimberlite dyke exposed in a vertical cliff face of Venetia Mine, South Africa. (C) Aerial photograph of the Ship Rock volcanic plug and dyke system (Townsend et al., 2015). (D) Small dyke cross-cutting composite dyke from Adamello, Italy. (from: Kavanagh, 2018) ... 3

Figure 1.3: (A) Basaltic dyke-fed sill, Breidavik volcano, NE Iceland (Photo: Elodie Saubin). (B) Exposed doleritic sills (white 's'), Traill Ø, East Greenland (Photo: Sverre Planke). (C) Panoramic image of Miocene andesitic sills (white 's'), Northern Neuquén Basin, Mendoza province, Argentina (Photo: Olivier Galland) (Senger et al., 2017). (From: Galland et al., 2018) 5

Figure 1.4: A) Schematic drawings illustrating distinct sill and flat-lying intrusion morphologies as defined from seismic data. (B) Characteristic seismic profile of Gleipne Sill Complex, Vøring Basin, mid-Norwegian margin, exhibiting several sill and flat-lying intrusion (strong reflectors) morphologies (Planke et al., 2005). (From: Galland et al., 2018) 5

Figure 1.5: Photograph showing up-domed layers of host rock on top of the Sandfell laccolith (Mattsson et al., 2018)..... 6

Figure 1.6: Changes in profile of Mt. St. Helens on the morning of May 18, 1980. Note the use of the term “cryptodome” to describe the intrusion in the first panel. (Lipman and Mullineaux, 1981) 6

Figure 1.7: Shows six different emplacement models used to describe the emplacement mechanism of magmatic intrusions (Spacapan et al., 2017)..... 8

Figure 1.8: Evolution of analogue experiments from (left to right) showing how imaging techniques have continued to improve over time allowing researchers to better model, record and analyse intrusions of different geometries in a laboratory setting. 10

Figure 2.1: Simplified geological map of the Torres del Paine Intrusive Complex (TPIC), modified after (Leuthold et al., 2012; Michel et al., 2008). The inset map shows the location of the TPIC in a regional context, approximately 51°S of the Andean Cordillera in Southern Patagonia (Müntener et al., 2018). “External intrusions” in this geological map refer to the calc-alkaline gabbro intrusions that are not co-genetic with the TPIC (Leuthold et al., 2013; Michael, 1991). 32

Figure 2.2: Cross section of the Torres del Paine Intrusive Complex and Paine Mafic Complex from west to east (Profile A-B on the map in Figure 2.1), with a diagram explaining the emplacement of the intrusions in stages by under-accretion (Stages 1 and 2) and over-accretion (Stage 3 and 4). The times presented in this figure are based on field and chronological data. Figure modified from Leuthold et al. (2014, 2013, 2012). 34

Figure 2.3: The three different types of dykes as categorised by Müntener et al. (2018). (A) Type 1: Dykes related to the emplacement of the granitic sheet terminating into fractures. Seen here are “horse tail” shaped dykes. (B) Type 2: Basaltic dykes found by the feeder zone, and (C) Type 3: Bimodal dyke with clear mafic borders and a felsic core. 36

Figure 2.4: A terrain map of Torres del Paine with locality and landmark pins. (Google Earth) 37

Figure 2.5: Emplacement parallel or sub-parallel to the layers of the host rock. (A) Close up of Cerro Nido de Condor and (B) East of Cuernos del Paine. Dashed lines are used in this figure to emphasize the host rock bedding. 38

Figure 2.6: Emplacement into host rock perpendicular to the intrusive body. The host rock is traced to show stopped blocks of host rock. Dashed lines are once again used to emphasise the host rock bedding. Arrows are pointing at stopped blocks which have broken off the intruded host. 39

Figure 2.7: Complex contacts between the intrusion and the host rock. (A) Multiple dykes radiating from a terminated granite sheet into the host rock. (B) Intrusive breccia formed by granite emplacement where angular host-rock fragments are surrounded by granite..... 40

Figure 2.8: Distinct colour changes between the granitic units make it easy to distinguish the individual granite sheets.....	41
Figure 2.9: The screen capture shows where to find the Color Palette Manager from the Window tab on CorelDraw. This can be used to manage existing colour palettes or to create new ones.	44
Figure 2.10: Options available for use in the Color Palette Manager. Options 1 and 5 are used in this guide to create custom colour palettes from scratch.	44
Figure 2.11: The Palette Editor menu allows users to add colours manually to any palette.	45
Figure 2.12: The Select Color menu allows users to choose the colour model and hue. The example shows the selection of a very light gray (254) on the Greyscale colour model.	45
Figure 2.13: The CorelDraw greyscale palette containing 256 shades of grey can be accessed as shown above in the Palette Libraries which is found in the Color Palette Manager.	46
Figure 2.14: Drop down menu on CorelDraw to select the “nib” size of the digital pen. The default options include but are not limited to Hairline, 1 px, 2 px, 3 px, 4 px, 5 px, 8 px, 10 px, 16 px, 20 px and 25 px as shown above. (N.B. This menu is only available when Pixel is selected as the default unit. Should the unit be different, access Object Properties to change the unit.)	47
Figure 2.15: Three sets of images used to test the sensitivity of ImageJ by area calculations. Set (A) shows lines of equal length (1000 pixels) with different widths. Set (B) shows lines of equal length (1000 pixels) and width (20 pixels) with different angles. Set (C) shows different shapes with a predefined area of 1000000 px ² . Note that all images presented are independent of scale.	50
Figure 2.16: Comparison between the calculated area (by user) and the measured area (ImageJ). The values returned by ImageJ are 1000 px ² smaller on lines created using an odd-numbered “nib”.	52
Figure 2.17: Close-up of each line at 1200% magnification. The active pixels used in the area calculation. The bands in grey represent inactive pixels, prominent on lines drawn with odd-numbered digital “nib”.	53
Figure 2.18: Comparison of pixel error (%) of the area produced user-defined thresholds and the area calculated using ImageJ. The lower negative values (closer to positive) indicate an	

overestimation of the calculated area. The higher negative values (away from positive)	
indicate an underestimation of the calculated area.....	55
Figure 2.19: Close up of line edges magnified at 1600% on ImageJ. The red region represents the region of active pixels used for analysis. The grey boxes of different shades at the edges represent inactive pixels which are excluded from the calculation of area.....	56
Figure 2.20: Cerro Nido de Condor before and after pre-processing using CorelDraw.....	61
Figure 2.21: Field photograph of Cuernos del Paine here there are differences in the depth of the photograph (darkest shade is closest to the foreground and light shade is furthest away from the foreground.) This complexity needs to be taken into account for image analysis using ImageJ.....	62
Figure 2.22: Steps 1-4 of scaling images by using known points on a field photograph and the Path tool on Google Earth Pro.....	64
Figure 2.23: How the photograph is scaled on ImageJ using the length obtained from the Path tool on Google Earth Pro. The yellow line shows a straight line drawn onto the photograph between Points 1 and 7 from the original photograph, which gives the distance in pixels.....	65
Figure 3.1: (i) Schematic diagram showing the indentation method to measure the Young's Modulus of gelatine from the deflection of the surface of the gelatine by a load of known mass and dimensions (modified after Kavanagh et al., 2013) where E is the Young's Modulus (Pa), ML is the mass of the load (kg), g is the gravitational acceleration (9.81 ms^{-1}), ν is the Poisson's ratio for gelatine (0.5), DL is the diameter of the load (m), DC is the diameter of the container (m) and w is the displacement caused by the load (m) which is calculated. To calculate w , the measurements needed are x_0 (ii) which is the initial measurement to the surface of the gelatine (m) and (iii) the displacement caused, measured with the load on top, x_1 (m) as well as the thickness of the load, β (m).....	85
Figure 3.2: Illustration showing the volume and height of gelatine in each experimental tank measuring 0.2 m in diameter and 0.2 m in height. The height of the gelatine solid in each tank is as follows: (i) 2L, $h = 7.0 \text{ cm}$, (ii) 3L, $h = 10.5 \text{ cm}$, (iii) 4L, $h = 14.0 \text{ cm}$	86
Figure 3.3: Schematic diagram of the rheometer setup. The zoom bubble shows two geometries used in these experiments: (i) The P35 Ti L 35 mm parallel plate head geometry with a fixed	

gap of 0.5 mm between the head and the sample plate and (ii) the P60/1° Ti L 60 mm cone plate head geometry which tapers at 1° from its circular base with a gap of 0.052 mm. The sample is loaded on the sample plate which is static and the head geometry is lowered down onto the sample plate. The sample then fills the gap between the head geometry and the sample plate. 88

Figure 3.4: The evolution of Young’s modulus values for 4-litres of 2.0 wt.% gelatine at 5°C over time as measured using loads (i) MO1, (ii) MO2, (iii) MO3 and (iv) MO4. The relationship between the Young’s modulus values over time in this plot is best expressed using the exponential line of best fit $E = E^\infty(1 - e^{-t\tau})$. Note that the trendlines are unweighted. The growing error bars illustrate the growing uncertainties in E over time associated with the different experimental loads applied to the surface of the gelatine solid. 94

Figure 3.5: The evolution of Young’s modulus values over time for 4-litres of 2.0 wt.% gelatine at 5°C (Experiment 9). The Young’s modulus values were calculated using deflection measurements collected using loads MO1, MO2, MO3 and MO4 (See Table 3.1 for load properties). The relationship between the Young’s modulus values over time in this plot is best expressed using the exponential line of best fit $E = E^\infty(1 - e^{-t\tau})$ where $E^\infty = 4579.55$ Pa and $\tau = 15$ hours. The line is weighted using the weighting dataset (WT) which takes into account $WLOAD$ and $W\Delta E/E$ (Refer Tables 3.2 and 3.3) 96

Figure 3.6: The evolution of Young’s modulus values in 2.0 wt.% gelatine at 5°C in Experiments 7, 8 and 9 using three different volumes of gelatine: i) 2 litres ($E^\infty = 4537.17$ Pa, $\tau = 9$ hours), ii) 3 litres, ($E^\infty = 4570.96$ Pa, $\tau = 12$ hours) and iii) 4 litres, ($E^\infty = 4668.74$ Pa, $\tau = 15$ hours) measured using the same experimental load (MO3). 97

Figure 3.7: The evolution of Young’s modulus values measured using experimental load MO3 across four different concentrations of gelatine: 1.5 wt.% (Experiment 6), 2.0 wt.% (Experiment 9), 2.5 wt.% (Kavanagh et al., 2013), 3.0 wt.% (Experiment 15) and 3.5 wt.% gelatine (Experiment 18) at a fixed volume of 4 litres. Higher E values are recorded in experiments with a higher concentration of gelatine. The trendlines are weighted using weighting dataset WT and the equation for line of best fit is $E = E^\infty(1 - e^{-t\tau})$. Error bars have been omitted for clarity. 99

Figure 3.8: Young’s modulus plateau values (E^∞ , Pa) plotted against concentration of gelatine (wt.%) for experiments with volumes of 4 litres and a temperature of 5°C. The plot shows strong positive linear correlation with an R^2 value of 0.98, where E^∞ increases with increasing concentration. 100

Figure 3.9: G' (shear storage modulus) and G'' (shear loss modulus) plotted against time (seconds) for gelatine at 5°C with concentrations: i) 1.0 wt.%, ii) 1.5 wt.%, iii) 2.0 wt.%, iv) 2.5 wt.%, v) 3.0 wt.% and vi) 3.5 wt.%. (Note the logged y-axis) 103

Figure 3.10: G' (shear storage modulus) and G'' (shear loss modulus) plotted against time (seconds) for gelatine at 10°C with concentrations: i) 1.0 wt.%, ii) 1.5 wt.%, iii) 2.0 wt.%, iv) 2.5 wt.%, v) 3.0 wt.% and vi) 3.5 wt.%. (Note the logged y-axis) 104

Figure 3.11: Rheometer amplitude sweep test results showing Stress vs. Strain of gelatine samples with different concentration (colours) and temperature (5°C = circles, 10°C = triangles). 106

Figure 4.1: Experimental setup to record changes in surface topography using the Micro-Epsilon laser scanner, an overhead laser scanner that records the changes in surface elevation (x-y plane). The laser scanner is paired with software ScanCONTROL which acquires data from the laser transect. The growing intrusion is monitored by cameras HD-1 (x-z plane), HD-2 (y-z plane) and HD-3 (x-y plane). Camera HD-1 films the evolution of internal stresses through a pair of polarising sheets attached to the outside of the tank. Camera HD-2 records the changes in intrusion geometry. Camera HD-3 records changes on the surface of the experiment. 118

Figure 4.2: Experimental setup for Tracer Particles. The gelatine is seeded with fluorescent particles and is illuminated by a laser sheet fired from a New Wave Solo-PIV III Laser positioned at the side of the tank. The laser sheet is positioned to intercept the central injection port. The displacement of particles during the experiment is recorded on two CCD cameras. 119

Figure 4.3: Calibration plate used to calibrate the camera for Digital Image Correlation (DIC) on Dantec Dynamic Studio. The calibration plate consists of evenly-spaced black dots (3 mm diameter, 10 mm spacing) on a white background. The dot in the centre is 4 mm in size with

the smaller dots (2 mm) acting as axis markers to the top and bottom and left and right of the dot in the centre. 123

Figure 4.4: The three key stages of experimental dyke growth as illustrated by: (a) Changes in intrusion geometry (height and width) and (b) Changes in vertical growth rate over time. . 128

Figure 4.5: Photographs of Experiment SD-07 taken at three different time steps: (i) 60 seconds, (ii) 240 seconds and (iii) 480 seconds. The photographs are captured in the following orientations: (a) y-z plane, (b) x-z plane and (c) x-z plane. The photographs in row (c) are greyscale photographs of the photographs in row (b) where the bow-tie shape is more pronounced. The position and orientation of the laser transect is visible at the top of the frame in all coloured photographs..... 130

Figure 4.6: Progressive change in surface topography 120 seconds prior to eruption in Experiments SD-07 and SD-09. Figure (a) highlights the patterns produced by the dyke in Experiment SD-07: Two regions of topographic high flanking a region of topographic low. Figure (b) illustrates the surface deformation patterns resulting from the inclined propagation path of the dyke in Experiment SD-09. There is a single prominent region of topographic high expressed next to a region of topographic low. 132

Figure 4.7: The results are presented as a series of vector maps which highlight the following key observations: 1) The vector arrows highlight the direction and magnitude of host material displacement and 2) The coloured contours show the intensity of strain as viewed through cross-sectional planes exx (horizontal displacement), ezz (vertical displacement) and exz (shear displacement). Regions in red represent the local positive, where fluorescent particles are moving closer together and regions in blue represent the local negative, where the fluorescent particles are moving further away from one another..... 134

Figure 4.8: Three key stages of dyke growth in a two-layered experiment (Experiment SD-13): (a) Changes in intrusion geometry and (b) Changes in vertical growth rate over time. The position of the interface separating the top and bottom layer is marked on the figure. The experimental dyke comes into contact with the stiffer upper layer approximately 450 seconds into the experiment..... 136

Figure 4.9: Annotated photographs of Experiment SD-13 and Experiment SD-14 taken at four different time steps: (i) 60 seconds, (ii) 240 seconds and (iii) 360 seconds and (iv) 470 seconds. The photographs were captured in the following orientations: (a) and (c) y-z plane, (b) and (d) x-z plane. The position of the gelatine interface is marked at the top of each frame. Note: The scale bar for Experiment SD-13 = 5 cm. The scale bar for Experiment SD-14 = 8 cm. 137

Figure 4.10: The progressive change in surface topography as a dyke propagates through layered elastic media: (a) Experiment SD-13 and (b) Experiment SD-14. The profiles show two elevated regions on each side of the dyke tip. Note the inclination of the propagation path in both experiments: (a) approximately 5° and (b) approximately 15°. Note that the dykes are dipping in the opposite direction to the experiment photographs in Figure 4.9 due to camera being positioned on the opposite side of the experimental tank. 139

Figure 4.11: The evolution of strain in the host material (gelatine) during dyke propagation in layered elastic media (Experiment PLT-5) as seen through three planes: (i) exx : Strain along the horizontal axis, (ii) ezz : Strain along the vertical axis and (ii) exz : Shear strain in the x-z plane. The images are arranged to show four key stages of dyke propagation: (a) Inception of the experimental dyke, (b) Propagation and growth of the experimental dyke where the dyke meets the interface and stalls, (c) Pre-eruption ascent towards the surface and (d) Eruption at the surface. 141

Figure 4.12: Photographs of (a) Experiment SD-16 and (b) Experiment SD-17 taken at three different time steps: (i) 60 seconds, (ii) 135 seconds, (iii)(a) 300 seconds and (iii)(b) 260 seconds respectively. Figure (iv) shows the top-down view (x-y plane) of each experiment to show the angle of rotation of experimental dyke. 143

Figure 4.13: The plots above show the progressive change in surface topography for Experiments SD-16 and SD-17. The vertical scale has been removed to exaggerate the changes observed between each time stamp. The cumulative surface displacement for Experiment SD-16 is 2.25 mm. The cumulative surface displacement for Experiment SD-17 is 2.5 mm. 145

Figure 4.14: The evolution of strain in the host material (gelatine) during dyke and sill formation as observed through three planes: (i) exx : Strain along the horizontal axis, (ii) ezz : Strain along the vertical axis and (ii) exz : Shear strain in the x-z plane. The images are arranged to show

four key stages of sill inception and propagation: (a) Inception of the experimental dyke, (b) Propagation and growth of the experimental dyke where the dyke meets the interface and stalls, (c) Diversion of the propagating dyke along the interface (sill formation) and (d) Sill propagation. 147

Figure 4.15: The flow curves of different fluid rheologies based on the relationship between shear stress and strain rate (Kavanagh et al., 2018) 153

List of Tables

Table 1.1: The following table lists analogue experiments in chronological order, adding onto the compilation of experiments by Galland et al. (2018) and Kavanagh et al. (2018). The table lists the type of intrusion, the processes studied, the underlying conceptual framework, the host and magma analogue, the imaging technique, details on the experiments and their respective experimental setups (Constrained vs. Unconstrained), and the reference paper(s) from which the information was obtained.	14
Table 2.1: Summary of dimensions of each test shape created using CorelDraw. All shapes have a calculated area of 1000000 px². <i>Lx</i> represents the length measured along the x-axis and <i>Ly</i> represents the length measured along the y-axis.	49
Table 2.2: General formulae to calculate the area of the test shapes used.	51
Table 2.3: Effect of line angle on the area calculated using ImageJ. Table showing the measured pixel areas of a line of known dimensions (Length: 1000 pixels, Outline width: 20 px) when rotated at different angles and using two different pixel value assignments: (1) A user-defined pixel value which assigns the pixel value to 0, and (2) ImageJ's default threshold settings, which applies different ranges of pixel values depending on the angle of the line. The maximum of the range is noted in this table as Max. Threshold. The measurements obtained from the line at 0o are used as a reference set. <i>Lx</i> and <i>Ly</i> are the line length of the x and y-axis respectively.....	54
Table 2.4: The area and perimeter of the test shapes (1) Square, (2) Vertical rectangle, (3) Horizontal rectangle, (4) Vertical ellipse, (5) Circle and (6) Horizontal ellipse.	57
Table 2.5: Example of how the components of the photograph are assigned different pixel values using the Greyscale colour chart.	60
Table 2.6: Magma overpressure calculations for select intrusions of the TPIC, using the aspect ratio from length and thickness values measured using ImageJ	68
Table 2.7: Magma overpressure calculations for select intrusions of the TPIC using values an predefined aspect ratio of 1:1000	69

Table 3.1: Properties of the loads used in the Young's Modulus experiments. DL is the diameter of the experimental load (m), β is the thickness of the experimental load (m) and ML is the mass of the experimental load (kg).....	85
Table 3.2: Qualitative weighting protocol based on the uncertainties produced by each load. The lightest load is given a weighting value of 1 (MO2) and the heaviest load is given a weighting value of 4 (MO3).....	91
Table 3.3: Quantitative weighting protocol based on the calculated values of $\Delta E/E$ (%). 1 represents the lowest weighting and 5 represents the highest weighting.	91
Table 3.4: Summary of the experimental conditions. C_{gel} is the concentration of gelatine used in wt.%, V_{gel} is the volume of gelatine used in litres. T_{mix} denotes the temperature of the mixture when the hot gelatine concentrate is diluted with cold water. T_0 is the temperature of the mixture as it is placed in the refrigerator and the clock is started (t_0). The temperature of the refrigerator (TR) is kept constant at 5oC throughout the experiment and all experimental tanks have a diameter of 20 cm (DC).....	93
Table 3.5: Experimental conditions for the rotational rheometer experiments. C_{gel} is the concentration of the gelatine used (wt.%), T is the fixed temperature ($^{\circ}C$) at which the gelatine is set to cool down to and t (s) is the total length of time in which the oscillation time sweep is conducted before the amplitude sweep begins.	102
Table 4.1: Experimental parameters of laboratory experiments. The experiment reference tags are in the column "Experiment." Other notations and units: Concentration of gelatine " C_{gel} " (wt.%) , height " H " (cm), mixture temperature " T_{mix} " ($^{\circ}C$), temperature of the gelatine solid at the beginning of the experiment " T_{exp} " ($^{\circ}C$), Young's modulus values " E " (Pa), volumetric flux of the injected fluid " Q " (m^3/s). Imaging technique: "PL" = Polarised Light, "SD" = Surface Deformation, "TP" = Tracer Particles.	126
Table 4.2: Continuation of Table 4.1 with the same notations and units. For experiments in two-layered media, the Subscript (1) is used to describe the bottom layer in the experimental tank and Subscript (2) is used to describe the top layer in the experimental tank.	127

List of Notations and Abbreviations

Notations and units

L_x	Length along x-axis (px)
L_y	Length along y-axis (px)
r	Radius (px)
a, b	Coefficients used to calculate area of an ellipse (px)
A_U	User-defined area (px ²)
A_D	ImageJ calculated area (px ²)
ΔA_U	Difference in area with reference to control line (User-defined)
ΔA_D	Difference in area with reference to control line (ImageJ calculated)
ΔA	Percentage difference of calculated area (%)
ΔP	Percentage difference of calculated area (%)
C_{gel}	Concentration of gelatine (wt.%)
M_w	Mass of water (g)
M_g	Mass of gelatine powder (g)
M_t	Total mass of water and gelatine powder (g)
T_{mix}	Temperature of gelatine mixture after dilution (°C)
E	Young's modulus (Pa)
M_L	Mass of experimental load (kg)
g	Gravitational acceleration = 9.81 ms ⁻¹
ν	Poisson's ratio of gelatine = 0.5
D_L	Diameter of experimental load (m)
w	Displacement caused by experimental load (m)
x_1	Displacement of gelatine measured with the experimental load on the surface (m)

x_0	Initial measurement taken without experimental load (m)
β	Thickness of experimental load (m)
D_C	Diameter of container (m)
V_{gel}	Volume of gelatine (litres)
t_0	Starting time when gelatine is left to cool (s)
T_0	Starting temperature recorded at t_0 (°C)
G'	Storage modulus (Pa)
G''	Loss modulus (Pa)
W_L	Weighting factor – Load
$W_{\Delta E/E}$	Weighting factor – Calculated $\Delta E/E$
W_T	Weighting factor – Total (Load + Calculated $\Delta E/E$)
T_R	Temperature of refrigerator (°C)
E_∞	Young's modulus plateau value (Pa)
τ	Empirical value derived from Equation 3.7 (hours)
$0.99E_\infty$	Effective Young's modulus plateau value (Pa)
$t_{0.99E_\infty}$	Curing time to reach material stability
Q	Volumetric flux (m^3/s)
h	Height of gelatine solid (m)
e_{xx}	Incremental strain along the horizontal axis
e_{zz}	Incremental strain along the vertical axis
e_{xz}	Incremental shear strain in the x-z plane
v_y	Dyke vertical velocity (cm/s)
v_x	Sill horizontal velocity (cm/s)
t	Time (s)

Abbreviations

px	Pixels
TPIC	Torres del Paine Intrusive Complex
PMC	Paine Mafic Complex
MSF	Motzfeldt SØ Formation
DIC	Digital Image Correlation
TP	Tracer Particles
PMMA	Poly(methyl methacrylate)
CCD	Charged Coupled Device
fps	Frames per second
LOESS	Locally Weighted Scatterplot Smoothing
VIPS	Volcanic and Igneous Plumbing Systems
dpi	Dots per inch
LEFM	Linear Elastic Fracture Mechanics
VI	Viscous Indentation/ Viscous Indenter
HEC	Hydroxyethyl Cellulose

Acknowledgements

First and foremost, I would like to thank to my funding bodies, The Malaysian Ministry of Education and The National University of Malaysia (UKM), for providing with this opportunity for me to pursue my PhD abroad. On this journey, I have made new friends, learned new things and found a place to call my home away from home.

Special thanks goes out to my supervisory team: Janine Kavanagh, Catherine Annen, Alan Boyle and David Dennis. Thank you all for your support throughout my PhD journey. I am truly grateful that I have all of you to help guide me through the most stressful and confusing years in my academic life. Thank you for the pick-me-ups when I felt lost (and when I needed, some tough love). Thank you to my examiners, Steffi Burchardt and Dan Faulkner for taking the time to read my thesis cover to cover. Thank you for making the examination and discussion session an enjoyable, memorable one.

Next, I would like to thank my lab family – the MAGMA Lab. Tea, cake, fur-babies and more cake... I mean, who could ask for more in a lab group? Thank you for giving me meetings for me to look forward to and for ideas that helped shape my PhD project into what it has become. Thank you to all members, past and present, but especially: Simon Martin, Ayleen Gaete, Alec Burns and Astrid Donadio.

Speaking of labs, my lab work has seen its fair share of trials and tribulations (Read: The Great Deionised Water Shortage of 2016/17™) and I wouldn't have been able to carry out my lab work without the help of these amazing people: John Kavanagh, Carmel Pinnington, Joshua Hicks, Sandra Collins and Sabine Hiltcher. Thanks is also due to Paula Houghton who has always been a friendly face in the Finance office to help with all my PhD spending. Not forgetting Karen Li and Jan Wilson, who helped with my (many) purchase orders.

This PhD journey has been a roller coaster of emotions and I wouldn't have made it through with my sanity in tact if it wasn't for my girlfriends. (Well, that, and University Counselling Services.) Shout-out to these lovely ladies (in no particular order): Caroline Harkin, Louise Hawkins, Tsvetomila Mateeva, Nik Nur Izzati, Sarah Khalida and Dayang Norabrizah. Thank you for filling my PhD days with joy and silliness (and lots of food!). From Just Dance to the

Great British Bake Off, here's to many more years of memes, gifs, shopping, travelling, café hunting and noms together.

To my family back home in warm sunny Malaysia, thank you for being there for me since day one. Thank you, Mama, for inspiring me to pursue Geology. I wish I inherited your Geophysics genes, because boy there is more math in Geology than I expected! Thank you, Bak, for sending me photos of Meemo and all the other cats after her who have called your home their home. Thank you, Abah, for the words of support yelled with gusto in the background when I'm on the phone to Mama to vent about my PhD. (I'm sorry you never got to read this thesis in its entirety. May your soul rest in peace.) Thank you to my little sisters Ana, Jaja and Shihah for the moral support in the form of texts, calls and funny videos. Maarten Verlinde, you are technically part of the family too, so I'd like to thank you for always reminding me of how cool my research is whenever I feel like I've failed as a scientist.

Last but certainly not least, my little family here in Liverpool: Elliot Wood and Murphy. Murphy, woof woof woof woof (You are the best-est boy!) My dearest Elliot, I can't imagine what this PhD journey would've been like without the unconditional love and support you have given me over the years. Thank you for being the best, most patient field assistant I've ever had. Thanks for letting me choose the music in our office (even if it was One Direction for the gazillionth time). Thanks for all the top quality banter we've had over cheeky Nando's. Most of all, thank you for believing in me. x

1 Introduction to Thesis

1.1 Background

Volcanic plumbing systems are made up of a complex network of magmatic intrusions with different geometries that reflect the different emplacement mechanisms driving their formation (Galland et al., 2015). These emplacement mechanisms are dictated by factors such as magma rheology, host rock deformation mode and ambient stress field (Burchardt, 2018a). The different types of magmatic intrusions (Figure 1.1) can be divided into two main groups based on their aspect ratio (length: thickness). Dykes, sills and cone sheets are examples of sheet intrusions which have a large length to thickness ratio (Burchardt et al., 2018; Galland et al., 2018; Kavanagh, 2018). Laccoliths and plutons are large, massive intrusive bodies with a smaller length to thickness ratio (Cruden et al., 2018).

Dykes are sheet intrusions which cut across bedding planes in a discordant manner. Due to their vertical to subvertical nature, dykes are often said to have two 'extended walls'. Dykes commonly form pathways for magma to travel from the source at depth, through the lithosphere to the shallow crust and potentially the surface. Dykes help to transport magma into deep magma reservoirs (e.g. magma chambers or sills), and as the magmatic system evolves new dykes can act as conduits which transport this magma upwards into a volcanic edifice and onto the Earth's surface to create a volcanic eruption (Burchardt, 2018b). However, only approximately 10% of all dykes propagate to the surface and erupt (Crisp, 1984), which means that the large majority of dykes remain unerupted under the Earth's surface. Dykes which erupt to the surface are referred to as feeder dykes and dykes that remain unerupted under the Earth's surface are referred to as non-feeder dykes (Geshi et al., 2010; Kavanagh, 2018). Figure 1.2 shows a few examples of dykes in the field.

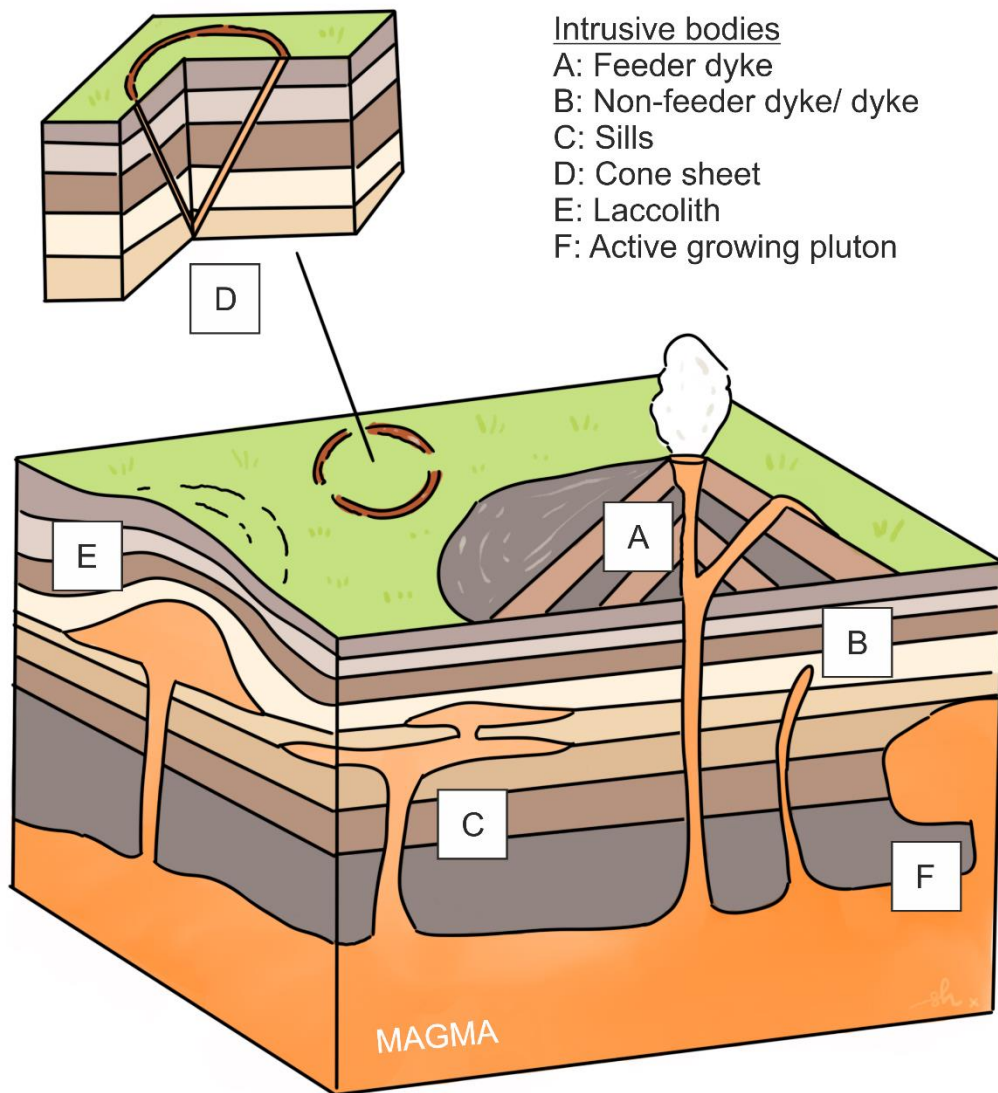


Figure 1.1: Cartoon diagram showing different types of intrusions. Dykes (A, B), sills (C) and cone sheets (D) are examples of sheet intrusions which have a large length to thickness ratio. Laccoliths (E) and plutons (F) are examples of large igneous bodies which have a smaller length to thickness ratio.

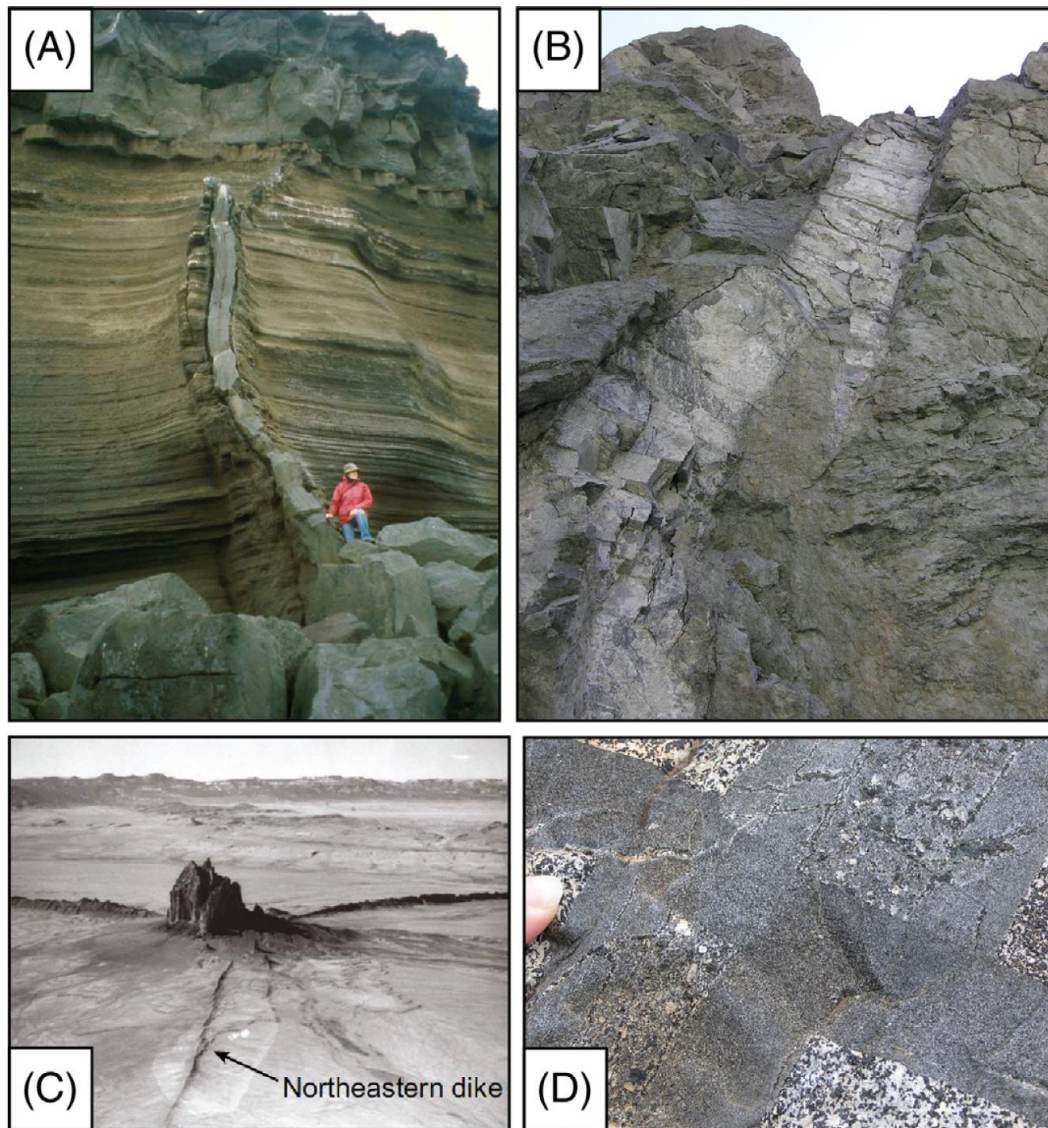


Figure 1.2: Examples of dykes in the field: (A) An exposed cliff face in the Reykjanes Peninsula, Iceland, showing an arrested basaltic dyke (Gudmundsson and Loetveit, 2005). (B) A branched kimberlite dyke exposed in a vertical cliff face of Venetia Mine, South Africa. (C) Aerial photograph of the Ship Rock volcanic plug and dyke system (Townsend et al., 2015). (D) Small dyke cross-cutting composite dyke from Adamello, Italy. (from: Kavanagh, 2018)

Sills are sheet intrusions which form horizontally or sub-horizontally, concordant to bedding planes. However, locally discordant behaviour can be commonly found in sills, such as 'saucer-shaped' geometries or sill 'transgressions'. For example, saucer-shaped sills are the resulting geometry of an initially flat central sill with inclined sheets at the edges; the 3D geometry of sills have been imaged in the shallow sub-surface through seismic reflection surveys (Magee et al., 2019; Magee and Jackson, 2020) whereas field exposures often produce only a 2D section (Kjøll et al., 2019). Figure 1.3 shows how sills are observed in the field and Figure 1.4 shows an example of sills in seismic sections. While sills function as a pathway for magma transport, they also play a larger role in magma storage as large magmatic bodies such as laccoliths and plutons (Annen, 2009; Menand, 2008) can grow from the stacking of sheet intrusions and subsequent inflation (Burchardt, 2018b).

Laccoliths on the other hand, have a flat-floor but a domed upper surface; the host rock strata surrounding the dome is often arched parallel to the curve of the domed top (Gilbert, 1877). An example of laccolith exposed in the field are the Sandfell Laccolith in Iceland (Mattsson et al., 2018). Laccoliths that form close to the surface are also referred to as cryptodomes; examples would be the Mt. St. Helens cryptodome in 1980 (Lipman and Mullineaux, 1981) and intrusions associated with the rhyolite eruption at Puyehue-Cordon Caulle in 2011 (Magnall et al., 2019, 2017). The examples described are presented in Figure 1.4, showing a field photograph of the Sandfell Laccolith with the arched host rock above it and a cross-section and Figure 1.5 showing a cross-section of Mt. St. Helens

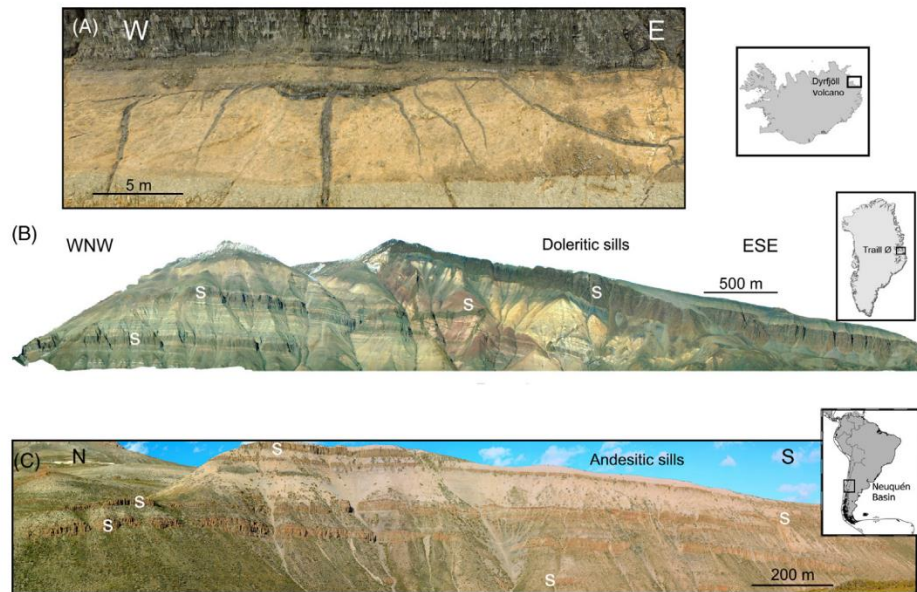


Figure 1.3: (A) Basaltic dyke-fed sill, Breidavik volcano, NE Iceland (Photo: Elodie Saubin). (B) Exposed doleritic sills (white 's'), Traill Ø, East Greenland (Photo: Sverre Planke). (C) Panoramic image of Miocene andesitic sills (white 's'), Northern Neuquén Basin, Mendoza province, Argentina (Photo: Olivier Galland) (Senger et al., 2017). (From: Galland et al., 2018)

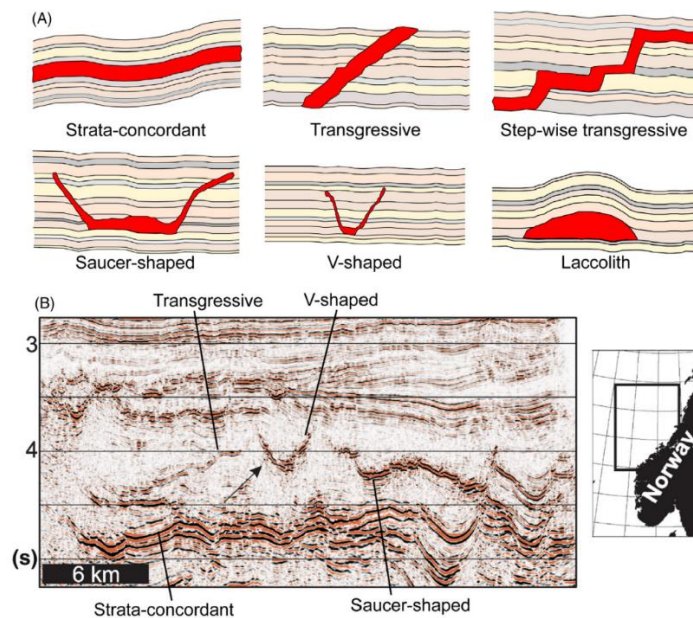


Figure 1.4: A) Schematic drawings illustrating distinct sill and flat-lying intrusion morphologies as defined from seismic data. (B) Characteristic seismic profile of Gleipne Sill Complex, Vøring Basin, mid-Norwegian margin, exhibiting several sill and flat-lying intrusion (strong reflectors) morphologies (Planke et al., 2005). (From: Galland et al., 2018)

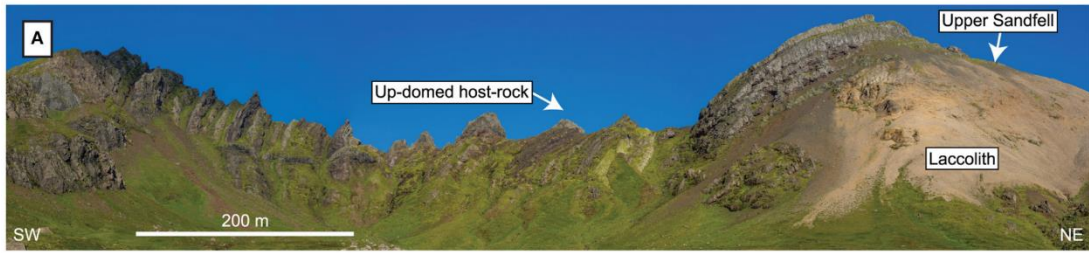


Figure 1.5: Photograph showing up-domed layers of host rock on top of the Sandfell laccolith (Mattsson et al., 2018)

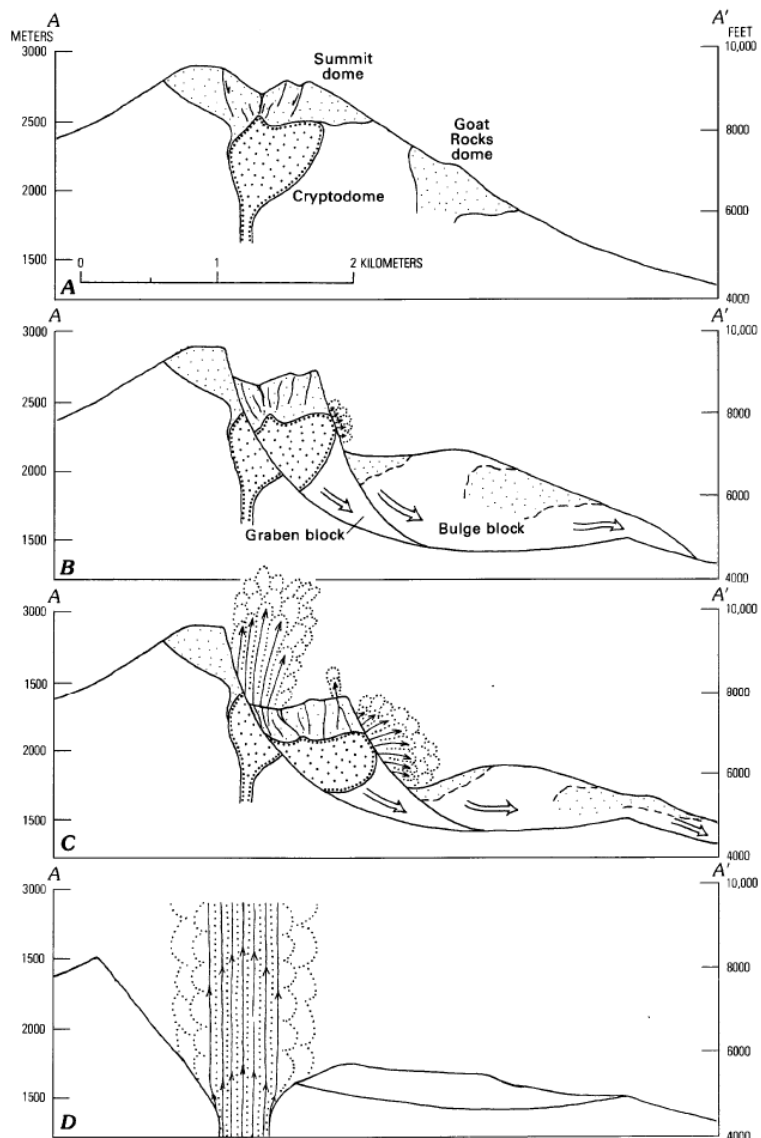


Figure 1.6: Changes in profile of Mt. St. Helens on the morning of May 18, 1980. Note the use of the term “cryptodome” to describe the intrusion in the first panel. (Lipman and Mullineaux, 1981)

1.1.1 Dyke and Sill Emplacement Models

Two contrasting emplacement models have been developed to describe the emplacement of dykes and sills: the Linear Elastic Fracture Mechanics (LEFM) model (also known as the Hydraulic Fracture model) and the Viscous Indenter model. These models arise because the geometry of intrusions reflect the different emplacement mechanisms driving their formation, such as magma rheology, host rock deformation mode, magmatic flux, ambient stress field and magmatic overpressure (Rubin, 1995).

The LEFM model infers an elastic crust and that intrusions are defined as magma-filled hydrofractures driven dominantly by magmatic overpressure (Timoshenko and Goodier, 1951). The fracture opens up as a Mode I fracture, and the opening mechanism is entirely tensile. The fracturing and opening at the tip region, in a movement similar to unzipping, introduces a space in which magma then fills and the intrusion as a whole then propagates (Lister and Kerr, 1991). The intrusion will continue to propagate in the direction in which the fracture has formed unless the intrusion comes into contact with a stiffer layer resulting in arrest (Gudmundsson, 2011) or diversion into an alternative pathway due to a change in stress field (Roberts, 1970). LEFM model intrusions typically have a tip terminating in a pointy geometry and the fluid-filled fracture has an elliptical cross section.

The Viscous Indenter model infers ductile deformation of the Earth's crust. This model implies that instead of the crust fracturing (Mode I) to accommodate the intruding magma, the crust deforms plastically to accommodate the intruding magma (Galland, 2012). This type of emplacement is more common in sedimentary environments where the rocks are less consolidated and have a bulk-behaviour that is plastic rather than elastic. This type of emplacement mode is also commonly associated with high viscosity magmas and the inflation of magmatic reservoirs such as laccoliths (Mattsson et al., 2018).

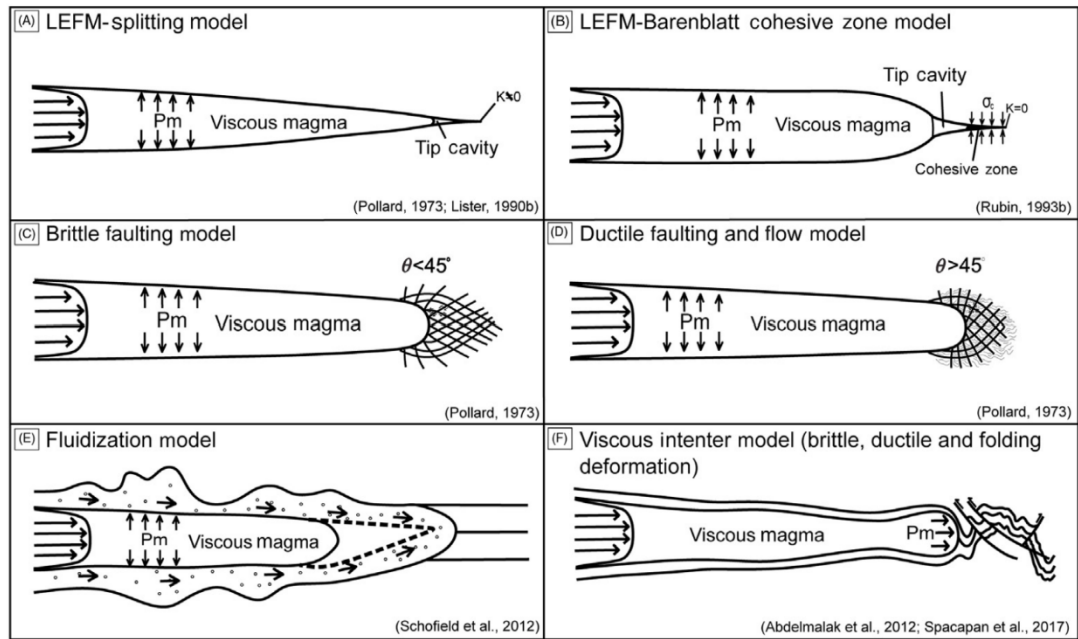


Figure 1.7: Six different emplacement models used to describe the emplacement mechanism of magmatic intrusions (Spacapan et al., 2017)

1.1.2 Analogue Modelling of magma intrusions

Analogue modelling (as the models employ an “analogue” for the systems being studied), also referred to sometimes as ‘Laboratory modelling’, is a method to study geological processes on smaller, more manageable lengths than their natural counterpart. This method is also useful to model processes that are difficult and/or impossible to observe in real time. The emplacement of magma in the Earth’s crust is challenging both in terms of the length scale and timescales involved, and the fact that the intrusion process cannot be directly observed; therefore analogue modelling has proved to be an important methodology to study geometrics, kinematics and dynamics of magma intrusion (Kavanagh et al., 2018b). Volcanic plumbing systems are complex, intricate systems to model as a whole, comprising multiple interacting components, and therefore models developed to study volcanic plumbing systems often consider one part of the system rather than the system as a whole (Galland et al., 2015; Kavanagh et al., 2018b).

Table 1.1 (attached at the end of this chapter for ease of reading and reference) provides a comprehensive list of examples of analogue experiments developed to study intrusions in a laboratory setting. The selection of analogue materials for modelling volcanic plumbing systems are made depending on the underlying conceptual framework on which the models are to be developed (either the Linear Elastic Fracture Mechanics model or the Viscous Indenter model). The host rock and magma analogue materials are then assigned based on the assumption of the host rock deformation mode and magma rheology, and the specific intrusion type and style being considered (such as dykes, sills and other intrusion types). The experiments are listed in chronological order, showing how analogue experiments have been carried out in the past and how these experimental setups continue to evolve and improve over time. One of the earliest examples of the use of analogue modelling in intrusion studies is the hydraulic fracturing in gelatine experiment carried out by Hubbert and Willis (1957). Many early experiments focused on the geometry of the intrusions formed under different experimental conditions, then progressed to developing methods to quantify deformation observed within the host material, and ultimately the relationship between intrusion geometry and deformation expressed at the surface. The most recent experiment methodologies pay special attention to improving experimental setups to making them more efficient, solving problems faced in previous research work such as the inability to see through granular material when conducting experiments. Figure 1.8 shows the evolution of analogue studies over time in a graphical panel which puts together images of select analogue modelling experiments.

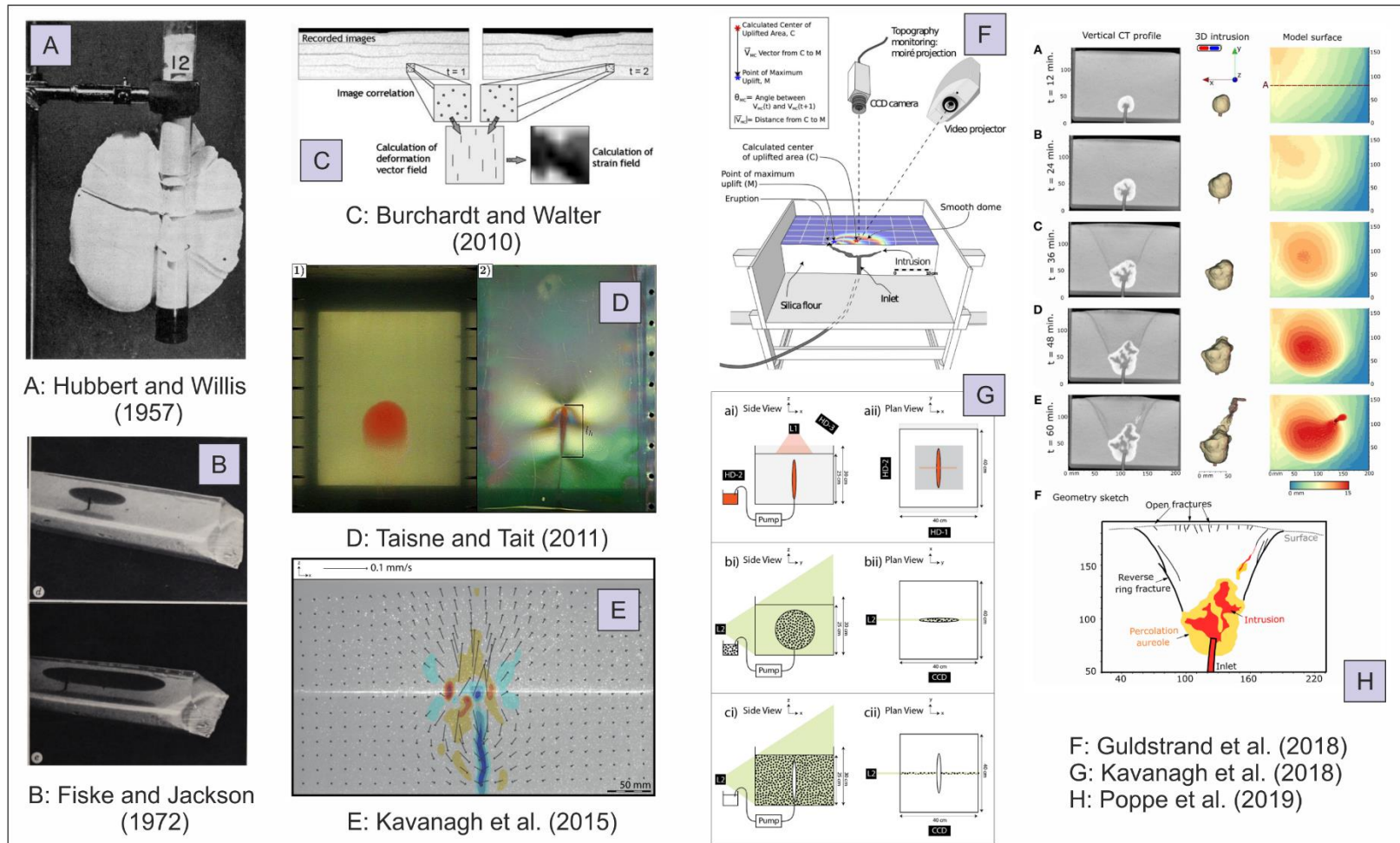


Figure 1.8: Evolution of analogue experiments from (left to right) showing how imaging techniques have continued to improve over time allowing researchers to better model, record and analyse intrusions of different geometries in a laboratory setting.

Gelatine is an appealing choice for host rock analogue that explores the LEFM model of magma intrusion due to its elastic and transparent nature (Di Giuseppe et al., 2009; Kavanagh et al., 2013). The transparency of gelatine allows for researchers to observe the growth of modelled intrusions in real time, which is highly beneficial when studying the mechanisms of magma emplacement and intrusion geometry. Gelatine is most favourable as a material in modelling an elastically behaving crust, where the material deforms in a tensile manner (Mode I) but less favourable for modelling more brittle-ductile crustal behaviour. Other examples of gelatine analogue experiments include Takada (1990), Rivalta et al. (2005), McLeod and Tait (1999) and Kavanagh et al. (2018).

Granular materials such as sand and flour are used as host rock analogues in analogue experiments which explore the 'viscous indenter' model and assume that the host deforms in shear failure (Mode II: Brittle-ductile deformation). The strength of the granular material differs from one material to the other and needs to be taken into consideration when selecting materials for scaling purposes. Quartz sand is an example of a material which has low cohesion and therefore low strength. Materials with a finer grain on the other hand such as gypsum powder, flour and corn starch have stronger cohesion when packed. Example granular material experiments to explore intrusion processes include: Donnadiou and Merle (1998), Galland (2012), Gulstrand et al. (2017, 2018) and Poppe et al. (2019).

Finally, the magma analogue is chosen based on the desired magmatic rheology. Water, silicone oil and vegetable are suitable for modelling low viscosity magmas and are commonly used in modelling sheet intrusions such as mafic dykes and sills (Table 1.1). Honey, golden syrup and silicon putty are suitable for modelling high viscosity magma and are commonly used to model sills, laccoliths and cryptodomes (Table 1.1).

1.2 Thesis Aims and Objectives

The main aim and overarching theme of this thesis is to develop robust and reproducible methods to study intrusions in the upper crust. The methods developed in this thesis are designed with field applications and laboratory modelling experiments in mind.

The following are the specific objectives of this thesis:

- 1) To develop a method to quantify field observations using field photographs. The development of this method will cover the process step-by-step from the acquisition of photographs in the field to how photographs are processed for image analysis. The methodology will then be tested on real photographs taken in the field. Successful development of this method would be particularly useful for field campaigns carried out in difficult to access or inaccessible field areas.
- 2) To introduce rigorous testing methods to characterise gelatine as an analogue material, with focus on laboratory modelling of shallow intrusions. This methodology will cover two approaches, one using manual indentation and the other using a rotational rheometer. The outcome of this investigation would be of benefit to the intrusion modelling community to establish a benchmark for experiments using gelatine. Having two approaches to characterise gelatine will make the material characterisation process more accessible to more researchers.
- 3) To demonstrate how laboratory modelling using gelatine as an analogue material can be used to study surface and subsurface deformation and how the results from these experiments relate to examples in nature, which can be beneficial for volcano monitoring programmes and hazard mitigation in volcanic regions.

1.3 Thesis Structure

Each chapter in this thesis will begin with a brief introduction to the chapter followed by the methodology employed to carry out the study. This is followed by a detailed presentation of results and key findings. The discussion section will elaborate on how these studies tie into the bigger picture (in comparison to previous literature and what contribution to knowledge base is made). Finally, each chapter will wrap up with a conclusion, summarising the key findings of that chapter.

Chapter 2 will expand on the structures related to the emplacement of intrusions in the field, using field photographs from the Torres del Paine Intrusive Complex (TPIC) in Chile. The chapter will then delve into the steps taken to develop an image analysis workflow which uses the software ImageJ to quantify observations from these field photographs.

Chapter 3 will provide insight into how the indentation method and rotational rheometry are both robust and reproducible methods that can be used to characterise gelatine as an analogue material for modelling magma intrusion growth in the Earth's crust.

Chapter 4 will elaborate on how gelatine is used as a crustal analogue to model surface and subsurface deformation in the laboratory. This chapter will demonstrate how to employ different observational techniques to get the most out of a simple experimental setup by using gelatine as the host material. Parts of this chapter and the methodology presented have been published and will be included as part of the Appendices.

Lastly, Chapter 5 will summarise all the key findings from each chapter, circling back to the specific objectives of this thesis. This chapter will conclude with notes on the limitations of the approaches presented in the thesis as well as recommendations for future work.

Table 1.1: The following table lists analogue experiments in chronological order, adding onto the compilation of experiments by Galland et al. (2018) and Kavanagh et al. (2018). The table lists the type of intrusion, the processes studied, the underlying conceptual framework, the host and magma analogue, the imaging technique, details on the experiments and their respective experimental setups (Constrained vs. Unconstrained), and the reference paper(s) from which the information was obtained.

Intrusion	Process(es) studied	Conceptual framework	Host Analogue	Magma Analogue	Imaging Technique	Experiment setup type and details	Reference(s)
Dyke, sill, saucer-shape intrusion	Hydraulic fracturing in different stress fields	LEFM	Gelatine	Mud	Artificial light, camera	<i>Constrained.</i> 2-gallon polyethylene bottle with its top cut off and glass tubing inserted	(Hubbert and Willis, 1957)
Dyke, sill	Propagation and ascent of intermediate dykes and sills (internal pressure driven)	LEFM	Gelatine	Water	Artificial light, camera	<i>Unconstrained.</i> Triangular metal mould: 60 cm (l) x 10 cm (h), gelatine was un moulded and placed on a rigid base plate	(Fiske and Jackson, 1972)
Sill, laccolith	Sill and laccolith emplacement	LEFM	Gelatine	Grease	No information available	<i>Constrained.</i> Plexiglass container with glass tube	(Pollard and Johnson, 1973)
Dyke, sill, laccolith	Dyke, sill and laccolith emplacement under volcanic cone	LEFM	Gelatine	Water-gelatine solution	Artificial light, camera	<i>Constrained.</i> Glass tank: 100 cm (l) x 100 cm (w) x 30 cm (h)	(Hyndman and Alt, 1987)
Dyke	Ascent of low viscosity dykes (buoyancy driven)	LEFM	Gelatine	Air	Artificial light, camera	<i>Constrained.</i> Acrylic tanks: 30 cm (l) x 30 cm (w) x 50 cm (h) and 20 cm (l) x 20 cm (w) x 20 cm (h)	(Takada, 1990)
Dyke, sill	Propagation of ascent of intermediate dykes and sills (internal pressure driven)	LEFM	Gelatine	Water	Artificial light, camera	<i>Constrained.</i> Acrylic tanks: 30 cm (l) x 30 cm (w) x 50 cm (h) and 20 cm (l) x 20 cm (w) x 20 cm (h)	(Takada, 1990)

Intrusion	Process(es) studied	Conceptual framework	Host Analogue	Magma Analogue	Imaging Technique	Experiment setup type and details	Reference(s)
Dyke	Dyke propagation along level of neutral buoyancy	LEFM	Agar-sugar gel	Water-glycerol solution	Artificial light, camera	<i>Constrained.</i> Perspex tank: 60 cm (l) x 21 cm (w) x 50 cm (h)	(Lister and Kerr, 1991)
Sill, stock-like intrusions	Inflating intra-edifice stock-like intrusions (cryptodomes), driven by external overpressures. Deflating sill or stock-like magma chambers	Viscous Indentation	Sand-flour mix	Silicone putty	No information available	<i>Unconstrained.</i> Brittle cone: 6-15 cm (h), Perspex box (2D cross section): 20 cm (l) x 2.5 cm (w) x 15 cm (h)	(Donnadiou and Merle, 1998)
Dyke, sill	Propagation and ascent of intermediate dykes and sills (internal pressure driven)	LEFM	Gelatine	Water	Artificial light, camera	<i>Constrained.</i> Cylindrical Perspex tank: 29 cm (d) x 40 cm (h)	(McLeod and Tait, 1999)
Dyke	Dyke propagation and nucleation	LEFM	Gelatine	Silicone oils	Artificial light, camera	<i>Constrained.</i> Cylindrical Perspex tank: 29 cm (d) x 40 cm (h)	(McLeod and Tait, 1999)
Dyke	Dyke nucleation from model magma reservoir	LEFM	Gelatine	Water-Natrosol solution	Artificial light, camera	<i>Constrained.</i> Cylindrical Perspex tank: 29 cm (d) x 40 cm (h)	(McLeod and Tait, 1999)
Dyke	Dyke propagation and nucleation, and composite dyke emplacement	LEFM	Gelatine	Water-Glycerine	Artificial light, camera	<i>Constrained.</i> Acrylic tank: 40 cm (l) x 20 cm (w) x 20 cm (h)	(Takada, 1999)
Dyke	Ascent of low viscosity dykes (buoyancy driven)	LEFM	Gelatine	Air	Artificial light, polarised light, camera	<i>Constrained.</i> Plexiglass tank: 30 cm (l) x 11 cm (w) x 22 cm (h)	(Muller et al., 2001)
Sill-like, laccolith	Deflating sill-like or laccolithic intrusions	Viscous Indentation	Sand or sand with silicone layers	Balloon	Artificial light, camera	<i>Constrained.</i> Glass tank: Approximately 100 cm ³	(Walter and Troll, 2001)

Intrusion	Process(es) studied	Conceptual framework	Host Analogue	Magma Analogue	Imaging Technique	Experiment setup type and details	Reference(s)
Dyke, sill	Propagation of ascent of intermediate dykes and sills	LEFM	Gelatine	Water	Artificial light, digital camera	<i>Constrained.</i> Plexiglass tank: 30 cm (l) x 30 cm (w) x 50 cm (h)	(Menand and Tait, 2002, 2001)
Dyke	Interaction between ascending dykes	LEFM	Gelatine	Hexane	Artificial light, digital camera	<i>Constrained.</i> Experimental tank: 30 cm (l) x 11 cm (w) x 22 cm (h), Top conical mould: 25 cm wide base, 110-degree flare at the apex	(Ito and Martel, 2002)
Dyke	Dyke propagation and nucleation	LEFM	Gelatine	Silicone oils	Artificial light, digital camera	<i>Constrained.</i> Perspex tank: 58.5 cm (l) x 26.0 cm (w) x 35.0 cm (h)	(Watanabe et al., 2002)
Dyke, sill	Propagation of ascent of intermediate dykes and sills (internal pressure driven)	LEFM	Gelatine	Water	Artificial light, digital camera	<i>Unconstrained.</i> Gelatine (mould radius: 5-40 cm, height: 5-20 cm) placed directly on PVC plate drilled with holes	(Walter and Troll, 2003)
Dyke	Ascent of low viscosity dykes (buoyancy driven)	LEFM	Gelatine	Air	Artificial light, digital camera	<i>Constrained.</i> Acrylic rectangular container: 40 cm (l) x 30 cm (w) x 50 cm (h) and acrylic cylindrical container: 26 cm (d) x 50 cm (h)	(Rivalta et al., 2005)
Dyke, sill	Propagation and ascent of intermediate dykes and sills (internal pressure driven)	LEFM	Gelatine	Water	Artificial light, digital camera	<i>Constrained.</i> Perspex tank: 40 cm (l) x 40 cm (w) x 30 cm (h)	(Kavanagh et al., 2006)
Dyke	Ascent of low viscosity dykes (buoyancy driven)	LEFM	Gelatine	Air	Artificial light, digital camera	<i>Constrained.</i> Acrylic cylindrical container: 26 cm (d) x 50 cm (h), and an acrylic cuboid container: 40 cm (l), 30 cm (w) and 50 cm (h)	(Rivalta and Dahm, 2006)

Intrusion	Process(es) studied	Conceptual framework	Host Analogue	Magma Analogue	Imaging Technique	Experiment setup type and details	Reference(s)
Dyke, sill, saucer-shape intrusions	Propagation and inflation of dykes, sills and saucer-shaped intrusions driven by internal pressure	Viscous Indentation	Ignimbrite powder	Golden syrup	Artificial light, digital camera	<i>Constrained.</i> Wooden box: 40 cm (l) x 40 cm (w) x 40 cm (h)	(Mathieu et al., 2008)
Dyke	Caldera collapse and dyke propagation	Viscous Indentation	Sand-plaster mix	Golden syrup	Artificial light, digital camera	<i>Constrained.</i> Wooden box: 40 cm (l) x 40 cm (w) x 20 cm (h)	(Kervyn et al., 2009)
Dyke	Caldera collapse and dyke propagation	LEFM	Gelatine	Water/Air	Artificial light, digital camera	<i>Constrained.</i> Plexiglass tank: 20 cm (w) x 20 cm (h)	(Kervyn et al., 2009)
Dyke, sill, saucer-shape intrusions	Propagation and inflation of dykes, sills and saucer-shaped intrusions driven by internal pressure	Viscous Indentation	Ignimbrite powder	Golden syrup	Artificial light, digital camera, excavated intrusion (after)	<i>Constrained.</i> Wooden box: 40 cm (l) x 40 cm (w) x 40 cm (h)	(Mathieu et al., 2008)
Dyke	Propagation and arrest of buoyancy-driven dyke	LEFM	Gelatine	Water-Sugar solution	Artificial light, polarised light, digital camera	<i>Constrained.</i> Plexiglass tank: 30 cm (l) x 30 cm (w) x 50 cm (h)	(Taisne and Tait, 2009)
Sill-like, stock-like intrusions	Deflating stock-like or sill-like intrusions	Viscous Indentation	Sand or sand with silicone layers	Rigid piston	Artificial light, CCD camera	<i>Constrained.</i> Sand and silicone layers of varying heights placed between two parallel glass panes (100 cm long) 10 cm apart on a rigid basal plate	(Burchardt and Walter, 2010)
Dyke, sill	Dyke and sill propagation in the presence of pore fluid overpressure	Viscous Indentation	Diatomite powder	RTV silicone	Excavated intrusion	<i>Constrained.</i> Hardwood wooden box: 40 cm (l) x 40 cm (w) x 50 cm (h)	(Gressier et al., 2010)
Dyke	Cooling effects on dyke propagation	LEFM	Gelatine	Molten wax	Artificial light, polarised light, digital camera	<i>Constrained.</i> Plexiglass tank: 30 cm (l) x 30 cm (w) x 50 cm (h)	(Taisne and Tait, 2011)

Intrusion	Process(es) studied	Conceptual framework	Host Analogue	Magma Analogue	Imaging Technique	Experiment setup type and details	Reference(s)
Dyke, sill	Propagation and ascent of intermediate dykes and sills (internal pressure driven)	LEFM	Gelatine	Water	Artificial light, digital camera	<i>Constrained.</i> Plexiglass tank: 30 cm (w) x 30 cm (l) x 50 cm (h)	(Taisne et al., 2011)
Dyke, sill, saucer-shape intrusions	Propagation and inflation of dykes, sills and saucer-shaped intrusions driven by internal pressure	Viscous Indentation	Silica powder	Vegetable oil	Projector, CCD camera and excavated intrusion (after)	<i>Constrained.</i> 2006: 60 cm (l) x 40 cm (w) x 20 cm (h); 2012: Square wooden box: 40 cm wide, variable thickness	(Galland, 2012)
Dyke	Propagation and inflation of dykes driven by internal pressure	Viscous Indentation	Silica powder	Golden syrup	Artificial light, digital camera	<i>Constrained.</i> Hele-Shaw cell: 50 cm (l) x 2.5 cm (w) x 35 cm (h)	(Abdelmalak et al., 2012)
Dyke	Caldera collapse and dyke propagation	Viscous Indentation	Sand-plaster mix	Golden syrup	Artificial light, digital camera	<i>Unconstrained.</i> Sand-plaster mix (varying heights) placed on top of a flat rigid base with a hole drilled	(Delcamp et al., 2012)
Sill	Deflating sill-like intrusions	Viscous Indentation	Sand and gypsum	"Creamed" honey	Artificial light, digital camera	<i>Unconstrained.</i> Sand/Gypsum pack (about 40 cm wide and 4-10 cm high) on top of a table	(Holohan et al., 2013)
Dyke	Ascent of low viscosity dykes (buoyancy driven)	LEFM	Gelatine	Air	Artificial light, digital camera	<i>Constrained.</i> Perspex tank: 40 cm (l) x 40 cm (w) x 30 cm (h)	(Le Corvec et al., 2013)
Dyke	Dyke formation and geometry in volcanic rifting systems	LEFM	Gelatine	Water	Artificial light, digital camera	<i>Unconstrained.</i> Gelatine placed directly on a flat plastic board (30 x 40 cm) with a series of holes at a regular spacing of 2 cm	(Tibaldi et al., 2014)

Intrusion	Process(es) studied	Conceptual framework	Host Analogue	Magma Analogue	Imaging Technique	Experiment setup type and details	Reference(s)
Dyke, sill	Propagation and ascent of intermediate dykes and sills (internal pressure driven)	LEFM	Gelatine	Water	Fluorescent particles, CCD camera	<i>Constrained.</i> Perspex tank: 40 cm (l) x 40 cm (w) x 30 cm (h)	(Kavanagh et al., 2015)
Dyke, sill	Cooling effects on dyke and sill emplacement	LEFM	Gelatine	Vegetable oil	Artificial light, digital camera	<i>Constrained.</i> Acrylic tank: 40.0 cm (l) x 39.8 cm (w) x 28.9 cm (h)	(Daniels and Menand, 2015)
Dyke	Martian dyke-induced deformation	Viscous Indentation	Sand	Paraffin wax	Artificial light, digital camera, cross section of model, excavated intrusion (after)	<i>Unconstrained.</i> Wooden box: 6-10 cm layers of unconstrained sand (edges)	(Wyrick et al., 2015)
Dyke	Deformation induced by progressive dyke intrusions	Both	Sand	Iron plates	Artificial light, digital camera, laser scanner	<i>Constrained.</i> Glass box: 25 cm (l) x 45 cm (w) x 15 cm (h)	(Trippanera et al., 2015)
Dyke, sill	Cooling effects on dyke and sill emplacement	LEFM	Gelatine	Vegetable oil	Artificial light, digital camera	<i>Constrained.</i> Experimental tank: 40 cm (l) x 40 cm (w) x 40 cm (h)	(Chanceaux and Menand, 2016, 2014)
Dyke, cone sheet	Surface deformation induced by ascending intrusions	Viscous Indentation	Fine grain silica powder	Vegetable oil	Projector, CCD camera and excavated intrusion (after)	<i>Constrained.</i> 40 cm wide square box	(Guldstrand et al., 2018, 2017)
Dyke	Propagation of dykes	LEFM	Gelatine	Water	Artificial light, polarised light, digital camera, fluorescent particles, CCD camera	<i>Constrained.</i> Perspex tank: 40 cm (l) x 40 cm (w) x 30 cm (h)	(Kavanagh et al., 2018a)

Intrusion	Process(es) studied	Conceptual framework	Host Analogue	Magma Analogue	Imaging Technique	Experiment setup type and details	Reference(s)
Dyke	Impact of crustal inhomogeneities and topographic loads on the direction and extent of dyke propagation/ arrest	LEFM	Gelatine	Water	Artificial light, digital camera	<i>Constrained.</i> Plexiglass box: 33 cm (l) x 58 cm (w) x 38.5 cm (h)	(Urbani et al., 2018)
Dyke (circumferential), cone sheet	Impact of unloading on post-caldera magma intrusions	LEFM	Gelatine	Water	Artificial light, polarised light, digital camera, fluorescent particles, CCD camera	<i>Constrained.</i> Perspex tank: 40 cm (l) x 40 cm (w) x 30 cm (h)	(Gaete et al., 2019)
Dyke	Effect of magmatic reservoir pressure on the propagation of dikes that approach from below	LEFM	Gelatine	Oil	Polarised light, digital camera	<i>Constrained.</i> Experimental tanks: 40 cm (l) x 40 cm (w) x 30 cm (h) and 50 cm (l, w, h)	(Pansino et al., 2019)
Dyke, cryptodome, cone sheet, inclined sheet	Deformation induced by magmatic intrusions with different intrusion geometries	Viscous Indentation	Silica sand - gypsum powder mix	Golden syrup	X-Ray Computed Tomography (CT)	<i>Constrained.</i> Plexiglass tank: 20 cm (l) x 20 cm (w) x 16 cm (h)	(Poppe et al., 2019)
Dyke, sill	Dyke and sill propagation	LEFM	Gelatine	Water	Artificial light, digital camera	<i>Constrained.</i> Perspex tank: 40.5 cm (l) x 29 cm (w) x 40 cm (h)	(Sili et al., 2019)

1.4 References

- Abdelmalak, M.M., Mourgues, R., Galland, O., Bureau, D., 2012. Fracture mode analysis and related surface deformation during dyke intrusion: Results from 2D experimental modelling. *Earth Planet. Sci. Lett.* 359–360, 93–105.
- Annen, C., 2009. From plutons to magma chambers: Thermal constraints on the accumulation of eruptible silicic magma in the upper crust. *Earth Planet. Sci. Lett.* 284, 409–416.
- Burchardt, S., 2018a. Volcanic and igneous plumbing systems: Understanding magma transport, storage, and evolution in the earth's crust, *Volcanic and Igneous Plumbing Systems: Understanding Magma Transport, Storage, and Evolution in the Earth's Crust.* Elsevier.
- Burchardt, S., 2018b. Chapter 1 - Introduction to Volcanic and Igneous Plumbing Systems—Developing a Discipline and Common Concepts. In: Burchardt, S.B.T.-V. and I.P.S. (Ed.), . Elsevier, pp. 1–12.
- Burchardt, S., Walter, T.R., 2010. Propagation, linkage, and interaction of caldera ring-faults: Comparison between analogue experiments and caldera collapse at Miyakejima, Japan, in 2000. *Bull. Volcanol.* 72, 297–308.
- Burchardt, S., Walter, T.R., Tuffen, H., 2018. Growth of a volcanic edifice through plumbing system processes-volcanic rift zones, magmatic sheet-intrusion swarms and long-lived conduits. In: *Volcanic and Igneous Plumbing Systems: Understanding Magma Transport, Storage, and Evolution in the Earth's Crust.* Elsevier, pp. 89–112.
- Chanceaux, L., Menand, T., 2014. Solidification effects on sill formation: An experimental approach. *Earth Planet. Sci. Lett.* 403, 79–88.

- Chanceaux, L., Menand, T., 2016. The effects of solidification on sill propagation dynamics and morphology. *Earth Planet. Sci. Lett.* 442, 39–50.
- Crisp, J.A., 1984. Rates of magma emplacement and volcanic output. *J. Volcanol. Geotherm. Res.* 20, 177–211.
- Cruden, A.R., McCaffrey, K.J.W., Bungler, A.P., 2018. Geometric Scaling of Tabular Igneous Intrusions: Implications for Emplacement Laccolith emplacement and Growth Laccolith growth. In: *Advances in Volcanology*. Springer, pp. 11–38.
- Daniels, K.A., Menand, T., 2015. An experimental investigation of dyke injection under regional extensional stress. *J. Geophys. Res. Solid Earth* 120, 2014–2035.
- Delcamp, A., Troll, V.R., van Wyk de Vries, B., Carracedo, J.C., Petronis, M.S., Pérez-Torrado, F.J., Deegan, F.M., 2012. Dykes and structures of the NE rift of Tenerife, Canary Islands: A record of stabilisation and destabilisation of ocean island rift zones. *Bull. Volcanol.* 74, 963–980.
- Di Giuseppe, E., Funicello, F., Corbi, F., Ranalli, G., Mojoli, G., 2009. Gelatins as rock analogs: A systematic study of their rheological and physical properties. *Tectonophysics* 473, 391–403.
- Donnadieu, F., Merle, O., 1998. Experiments on the indentation process during cryptodome intrusions: new insights into Mount St. Helens deformation. *Geology* 26, 79–82.
- Fiske, R.S., Jackson, E.D., 1972. Orientation and Growth of Hawaiian Volcanic Rifts: The Effect of Regional Structure and Gravitational Stresses. *Proc. R. Soc. A Math. Phys. Eng. Sci.* 329, 299–326.
- Gaete, A., Kavanagh, J.L., Rivalta, E., Hilmi Hazim, S., Walter, T.R., Dennis, D.J.C., 2019. The

impact of unloading stresses on post-caldera magma intrusions. *Earth Planet. Sci. Lett.* 508, 109–121.

Galland, O., 2012. Experimental modelling of ground deformation associated with shallow magma intrusions. *Earth Planet. Sci. Lett.* 317–318, 145–156.

Galland, O., Bertelsen, H.S., Eide, C.H., Guldstrand, F., Haug, T., Leanza, H.A., Mair, K., Palma, O., Planke, S., Rabbel, O., Rogers, B., Schmiedel, T., Souche, A., Spacapan, J.B., 2018. Storage and transport of magma in the layered crust-formation of sills and related flat-lying intrusions. In: *Volcanic and Igneous Plumbing Systems: Understanding Magma Transport, Storage, and Evolution in the Earth's Crust*. Elsevier, pp. 113–138.

Galland, O., Holohan, E., van Wyk de Vries, B., Burchardt, S., 2015. Laboratory Modelling of Volcano Plumbing Systems: A Review. In: *Advances in Volcanology*. Springer Berlin Heidelberg, pp. 1–68.

Geshi, N., Kusumoto, S., Gudmundsson, A., 2010. Geometric difference between non-feeder and feeder dikes. *Geology* 38, 195–198.

Gilbert, G.K., 1877. *Geology of the Henry Mountains, Monograph*. Washington, D.C.

Gressier, J.B., Mourgues, R., Bodet, L., Matthieu, J.Y., Galland, O., Cobbold, P., 2010. Control of pore fluid pressure on depth of emplacement of magmatic sills: An experimental approach. *Tectonophysics* 489, 1–13.

Gudmundsson, A., 2011. Deflection of dykes into sills at discontinuities and magma-chamber formation. *Tectonophysics* 500, 50–64.

Guldstrand, F., Burchardt, S., Hallot, E., Galland, O., 2017. Dynamics of Surface Deformation Induced by Dikes and Cone Sheets in a Cohesive Coulomb Brittle Crust. *J. Geophys. Res.*

Solid Earth 122, 8511–8524.

Guldstrand, F., Galland, O., Hallot, E., Burchardt, S., 2018. Experimental Constraints on Forecasting the Location of Volcanic Eruptions from Pre-eruptive Surface Deformation. *Front. Earth Sci.* 6, 7.

Holohan, E.P., Walter, T.R., Schöpfer, M.P.J., Walsh, J.J., Van Wyk De Vries, B., Troll, V.R., 2013. Origins of oblique-slip faulting during caldera subsidence. *J. Geophys. Res. Solid Earth* 118, 1778–1794.

Hubbert, M., Willis, D., 1957. Mechanics of hydraulic fracturing: AIME Petroleum Transactions.

Hyndman, D.W., Alt, D., 1987. Radial Dikes, Laccoliths, and Gelatin Models. *J. Geol.*

Ito, G., Martel, S.J., 2002. Focusing of magma in the upper mantle through dike interaction. *J. Geophys. Res. Solid Earth* 107, ECV 6-1-ECV 6-17.

Kavanagh, J.L., 2018. Mechanisms of Magma Transport in the Upper Crust—Dyking. In: *Volcanic and Igneous Plumbing Systems*. Elsevier, pp. 55–88.

Kavanagh, J.L., Boutelier, D., Cruden, A.R., 2015. The mechanics of sill inception, propagation and growth: Experimental evidence for rapid reduction in magmatic overpressure. *Earth Planet. Sci. Lett.* 421, 117–128.

Kavanagh, J.L., Burns, A.J., Hilmi Hazim, S., Wood, E.P., Martin, S.A., Hignett, S., Dennis, D.J.C., 2018a. Challenging dyke ascent models using novel laboratory experiments: Implications for reinterpreting evidence of magma ascent and volcanism. *J. Volcanol. Geotherm. Res.* 354, 87–101.

Kavanagh, J.L., Engwell, S., Martin, S.A., 2018b. A review of analogue and numerical

modelling in volcanology. *Solid Earth Discuss.* 95194, 1–80.

Kavanagh, J.L., Menand, T., Daniels, K.A., 2013. Gelatine as a crustal analogue: Determining elastic properties for modelling magmatic intrusions. *Tectonophysics* 582, 101–111.

Kavanagh, J.L., Menand, T., J. Sparks, R.S., Sparks, R.S.J., 2006. An Experimental Investigation of Sill Formation and Propagation in Layered Elastic Media. *Earth Planet. Sci. Lett.* 245, 799–813.

Kervyn, M., Ernst, G.G.J., van Wyk de Vries, B., Mathieu, L., Jacobs, P., 2009. Volcano load control on dyke propagation and vent distribution: Insights from analogue modeling. *J. Geophys. Res.* 114.

Kjøll, H.J., Galland, O., Labrousse, L., Andersen, T.B., 2019. Emplacement mechanisms of a dyke swarm across the brittle-ductile transition and the geodynamic implications for magma-rich margins. *Earth Planet. Sci. Lett.* 518, 223–235.

Le Corvec, N., Menand, T., Lindsay, J., 2013. Interaction of ascending magma with pre-existing crustal fractures in monogenetic basaltic volcanism: An experimental approach. *J. Geophys. Res. Solid Earth* 118, 968–984.

Lipman, P.W., Mullineaux, D.R., 1981. The 1980 eruptions of Mount St. Helens, Washington, Professional Paper.

Lister, J.R., Kerr, R.C., 1991. Fluid-mechanical models of crack propagation and their application to magma transport in dykes. *J. Geophys. Res.* 96, 10049–10077.

Magee, C., Jackson, C.A.-L., 2020. Seismic reflection data reveal the 3D structure of the newly discovered Exmouth Dyke Swarm, offshore NW Australia. *Solid Earth* 11, 579–606.

Magee, C., Muirhead, J., Schofield, N., Walker, R.J., Galland, O., Holford, S., Spacapan, J.,

- Jackson, C.A.-L., McCarthy, W., 2019. Structural signatures of igneous sheet intrusion propagation. *J. Struct. Geol.* 125, 148–154.
- Magnall, N., James, M.R., Tuffen, H., Vye-Brown, C., 2017. Emplacing a cooling-limited rhyolite lava flow: Similarities with basaltic lava flows. *Front. Earth Sci.* 5, 44.
- Magnall, N., James, M.R., Tuffen, H., Vye-Brown, C., Ian Schipper, C., Castro, J.M., Davies, A.G., 2019. The origin and evolution of breakouts in a cooling-limited rhyolite lava flow. *Bull. Geol. Soc. Am.* 131, 137–154.
- Mathieu, L., van Wyk de Vries, B., Holohan, E.P., Troll, V.R., 2008. Dykes, cups, saucers and sills: Analogue experiments on magma intrusion into brittle rocks. *Earth Planet. Sci. Lett.* 271, 1–13.
- Mattsson, T., Burchardt, S., Almqvist, B.S.G.G., Ronchin, E., 2018. Syn-Emplacement Fracturing in the Sandfell Laccolith, Eastern Iceland—Implications for Rhyolite Intrusion Growth and Volcanic Hazards. *Front. Earth Sci.* 6, 5.
- McLeod, P., Tait, S.R., 1999. The growth of dykes from magma chambers. *J. Volcanol. Geotherm. Res.* 92, 231–246.
- Menand, T., 2008. The mechanics and dynamics of sills in layered elastic rocks and their implications for the growth of laccoliths and other igneous complexes. *Earth Planet. Sci. Lett.* 267, 93–99.
- Menand, T., Tait, S.R., 2001. A phenomenological model for precursor volcanic eruptions. *Nature* 411, 678–680.
- Menand, T., Tait, S.R., 2002. The propagation of a buoyant liquid-filled fissure from a source under constant pressure: An experimental approach. *J. Geophys. Res. Solid Earth* 107,

2306.

Muller, J.R., Ito, G., Martel, S.J., 2001. Effects of volcano loading on dike propagation in an elastic half-space. *J. Geophys. Res. Solid Earth* 106, 11101–11113.

Pansino, S., Emadzadeh, A., Taisne, B., 2019. Dike Channelization and Solidification: Time Scale Controls on the Geometry and Placement of Magma Migration Pathways. *J. Geophys. Res. Solid Earth* 124, 9580–9599.

Pollard, D.D., Johnson, A.M., 1973. Mechanics of growth of some laccolithic intrusions in the Henry mountains, Utah, II. Bending and failure of overburden layers and sill formation. *Tectonophysics* 18, 311–354.

Poppe, S., Holohan, E.P., Galland, O., Buls, N., Van Gompel, G., Keelson, B., Tournigand, P.Y., Brancart, J., Hollis, D., Nila, A., Kervyn, M., 2019. An inside perspective on magma intrusion: Quantifying 3d displacement and strain in laboratory experiments by dynamic X-ray computed tomography. *Front. Earth Sci.* 7, 62.

Rivalta, E., Böttlinger, M., Dahm, T., Bottinger, M., 2005. Buoyancy-driven fracture ascent: Experiments in layered gelatine. *J. Volcanol. Geotherm. Res.* 144, 273–285.

Rivalta, E., Dahm, T., 2006. Acceleration of buoyancy-driven fractures and magmatic dikes beneath the free surface. *Geophys. J. Int.* 166, 1424–1439.

Roberts, J.L., 1970. The intrusion of magma into brittle rocks, *Journal of. ed, Mechanism of Igneous Intrusion*. Liverpool Letterpress Limited, Liverpool.

Rubin, A.M., 1995. Propagation of magma-filled cracks. *Annu. Rev. Earth Planet. Sci.* 23, 287–336.

Sili, G., Urbani, S., Acocella, V., 2019. What Controls Sill Formation: An Overview From

Analogue Models. *J. Geophys. Res. Solid Earth* 124, 8205–8222.

Spacapan, J.B., Galland, O., Leanza, H.A., Planke, S., 2017. Igneous sill and finger emplacement mechanism in shale-dominated formations: a field study at Cuesta del Chihuido, Neuquén Basin, Argentina. *J. Geol. Soc. London*. 174, 422–433.

Taisne, B., Tait, S.R., 2009. Eruption versus intrusion? arrest of propagation of constant volume, buoyant, liquid-filled cracks in an elastic, brittle host. *J. Geophys. Res. Solid Earth* 114, B06202.

Taisne, B., Tait, S.R., 2011. Effect of solidification on a propagating dike. *J. Geophys. Res. Solid Earth* 116, B01206.

Taisne, B., Tait, S.R., Jaupart, C., 2011. Conditions for the arrest of a vertical propagating dyke. *Bull. Volcanol.* 73, 191–204.

Takada, A., 1990. Experimental study on propagation of liquid-filled crack in gelatin: shape and velocity in hydrostatic stress condition. *J. Geophys. Res.* 95, 8471–8481.

Takada, A., 1999. Variations in magma supply and magma partitioning: The role of tectonic settings. *J. Volcanol. Geotherm. Res.* 93, 93–110.

Tibaldi, A., Bonali, F.L., Corazzato, C., 2014. The diverging volcanic rift system. *Tectonophysics* 611, 94–113.

Timoshenko, S., Goodier, J.N., 1951. *Theory of Elasticity*, by S. Timoshenko and J.N. Goodier, ... 2nd Edition, *Journal of Elasticity*.

Trippanera, D., Ruch, J., Acocella, V., Rivalta, E., 2015. Experiments of dike-induced deformation: Insights on the long-term evolution of divergent plate boundaries. *J. Geophys. Res. Solid Earth* 120, 6913–6942.

- Urbani, S., Acocella, V., Rivalta, E., 2018. What Drives the Lateral Versus Vertical Propagation of Dikes? Insights From Analogue Models. *J. Geophys. Res. Solid Earth* 123, 3680–3697.
- Walter, T.R., Troll, V.R., 2001. Formation of caldera periphery faults: An experimental study. *Bull. Volcanol.* 63, 191–203.
- Walter, T.R., Troll, V.R., 2003. Experiments on rift zone evolution in unstable volcanic edifices. *J. Volcanol. Geotherm. Res.* 127, 107–120.
- Watanabe, T., Masuyama, T., Nagaoka, K., Tahara, T., 2002. Analog experiments on magma-filled cracks: Competition between external stresses and internal pressure. *Earth, Planets Sp.* 54, 1247–1261.
- Wyrick, D.Y., Morris, A.P., Todt, M.K., Watson-Morris, M.J., 2015. Physical analogue modelling of Martian dyke-induced deformation. *Geol. Soc. Spec. Publ.* 401, 395–403.

2 Quantitative Analysis of Field Images: The Torres del Paine Intrusive Complex (TPIC), Chile

2.1 Introduction to Chapter

This chapter delves into the processes involved in developing an image analysis method which aims to help extract quantitative data from field photographs informed by geological observations made in the field. First, a brief introduction to the regional geology of the Torres del Paine Intrusive Complex (TPIC) in Chile is presented. The introduction to the geology is followed by the author's descriptions of structures observed in the field accompanied by annotated photographs illustrating those structures. Next, the readers are introduced to image analysis software ImageJ and the series of tests devised and carried out to determine the sensitivity of ImageJ as an image analysis tool. The results from these sensitivity tests are used to inform the development of a step-by-step method to (1) pre-process field photographs using graphics editor CorelDraw and (2) process the images to collect quantitative data using ImageJ. The results from the worked example are presented in this chapter. The chapter concludes with a discussion of the suitability of the parameters used in the models and recommendations for future modelling works. All photographs of the TPIC were taken on the author's field campaign to Torres del Paine in 2016.

2.2 Regional Geology: Torres del Paine Intrusive Complex (TPIC), Chile

The glacier-carved landscape of Torres del Paine makes it an excellent field area for field image analysis. The exceptionally exposed landscape features a clear view of the zone contacts where the uppermost part of the intrusion is in contact with the host rock and the floor contacts where the bottom of the intrusion is in contact with the host rock. This makes the exposure at Torres del Paine especially unique because the geometry of the solidified

intrusion can be viewed in three dimensions, which provides researchers with the opportunity to study the relationship between the intrusive body and the host rock.

2.2.1 Torres del Paine Intrusive Complex (TPIC), Chile

The Torres del Paine Intrusive Complex (TPIC) is a Miocene aged intrusive complex covering an area of approximately 80 km² of the Patagonian Andes (Leuthold et al., 2014). The TPIC consists of a succession of granitic sills (Michel et al., 2008) which are underplated by a mafic sill complex (Leuthold et al., 2013, 2012). The magma bodies intruded into early mid-Cretaceous flysch formations (Wilson, 1991): the Punta Barossa Formation, consisting of thick bedded sandstones with intercalated shale, and the Cerro Toro Formation, consisting of shale intercalated with marl and lenses of sand and conglomerate (Altenberger et al., 2003). A simplified geological map of Torres del Paine is presented in Figure 2.1.

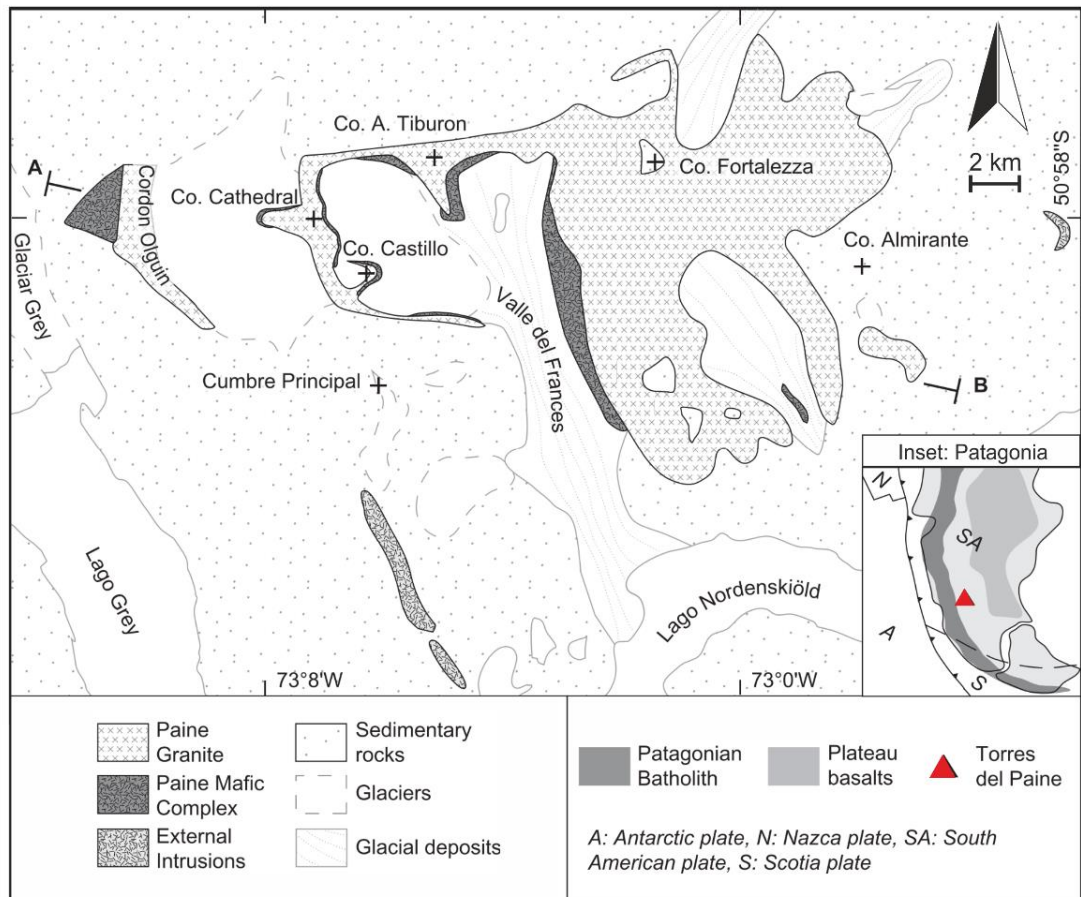


Figure 2.1: Simplified geological map of the Torres del Paine Intrusive Complex (TPIC), modified after (Leuthold et al., 2012; Michel et al., 2008). The inset map shows the location of the TPIC in a regional context, approximately 51°S of the Andean Cordillera in Southern Patagonia (Müntener et al., 2018). “External intrusions” in this geological map refer to the calc-alkaline gabbro intrusions that are not co-genetic with the TPIC (Leuthold et al., 2013; Michael, 1991).

The TPIC is characteristically compositionally bimodal, consisting of multiple pulses of mafic and felsic magma (Leuthold et al., 2012; Müntener et al., 2018). The eastern part of the TPIC consists of a sill complex with sub-horizontal contacts between sills (Leuthold et al., 2014). The western part of the TPIC consists of sub-vertical structures which are discordant to the folded country rocks (Leuthold et al., 2012). These sub-vertical structures are mafic in composition and have been identified as dykes which represent the feeder zone of the complex (Leuthold et al., 2013; Michel et al., 2008). Together with the underplated basal

mafic units, these igneous bodies comprise the Paine Mafic Complex (PMC) (Leuthold et al., 2013). A cross-section through the TPIC (W-E) is presented in Figure 2.2.

The chronology of emplacement of the TPIC can be divided into four stages: two stages of under-accretion where the new intrusion underplates the existing intrusions and two stages of over-accretion where the new intrusions build on top the existing intrusions (Leuthold et al., 2012). During Stages 1 and 2, Granite I (1') is underplated by Granite II (2) and Granite III (3). During Stage 3, a Hornblende-Gabbro intrusion (labelled 4) forms beneath Granites I, II and III. During Stage 4, over-accretion of the mafic unit takes place where the mafic intrusions (labelled 5, 6 and 6') build up on top of the Hornblende-Gabbro intrusion, but beneath the granitic intrusions. The study by Leuthold et al. (2012) concludes that the TPIC as a whole was constructed in 162 ± 11 ka (from 12.593 ± 0.009 Ma to 12.431 ± 0.006 Ma) with a total volume of approximately 88 km^3 , representing an average construction rate of 0.0005 km^3 per year. During Stages 1 and 2, this value is then estimated to be 0.0008 km^3 per year when the weighted mean age of the oldest and youngest units as well as the total exposed volume (also labelled in Figure 2.2) are considered. During the emplacement of the mafic units (Stages 3 and 4), the rate of construction decreased to 0.0002 km^3 per year. This is reflected in the size of the mafic units in comparison to the granitic units which were emplaced at a higher construction rate. However, it should be noted that compared to other plutons and large igneous bodies, these are considered to be small growth rates (Leuthold et al., 2012).

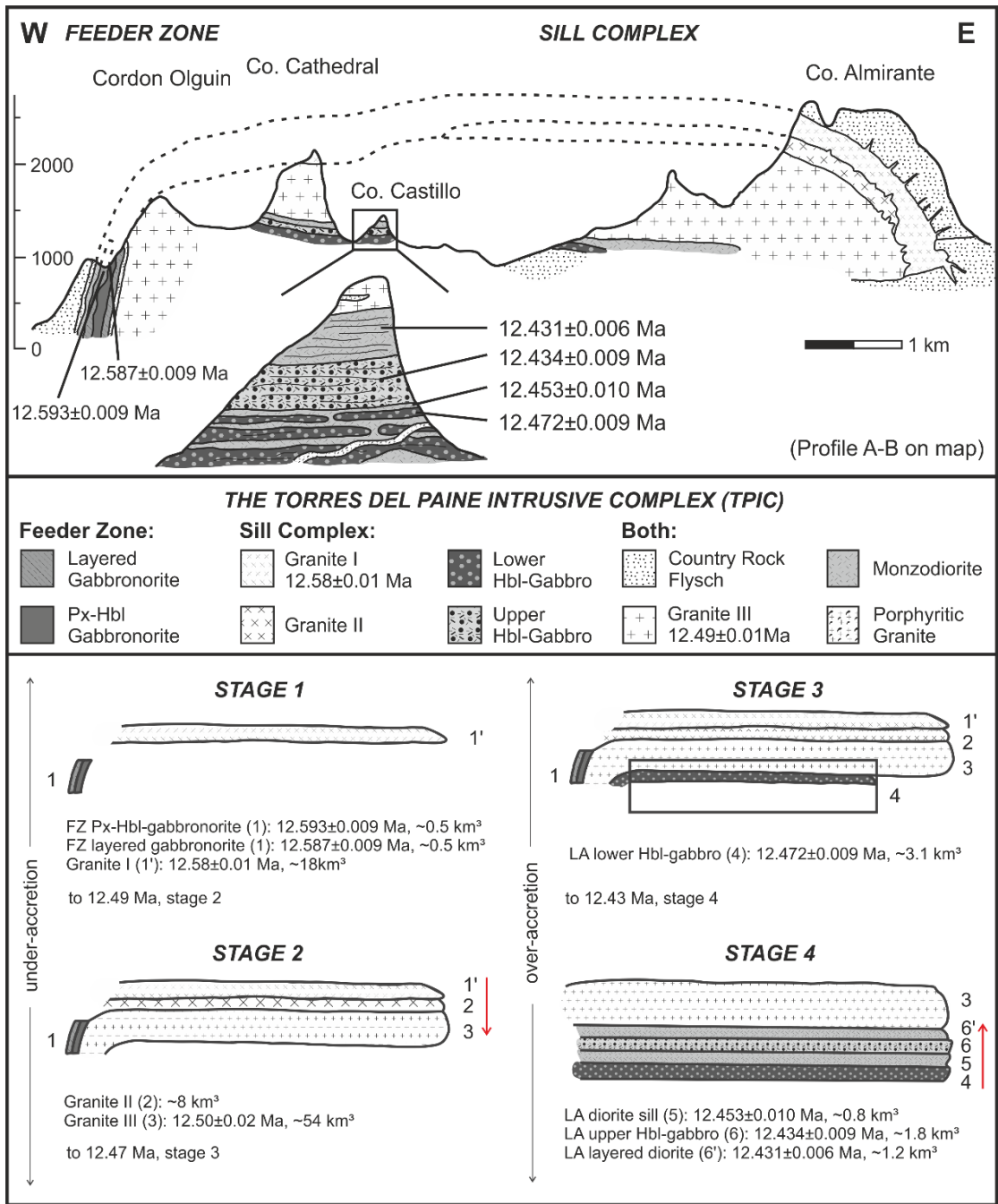


Figure 2.2: Cross section of the Torres del Paine Intrusive Complex and Paine Mafic Complex from west to east (Profile A-B on the map in Figure 2.1), with a diagram explaining the emplacement of the intrusions in stages by under-accretion (Stages 1 and 2) and over-accretion (Stage 3 and 4). The times presented in this figure are based on field and chronological data. Figure modified from Leuthold et al. (2014, 2013, 2012).

The TPIC has three distinguishable types of dykes which are characterised based on their composition and size (Müntener et al., 2018). The first type (Type 1) consists of dykes related to the emplacement of the granitic sheets. These felsic dykes are tens to hundreds of metres long and tens of metres wide. These dykes pinch to millimetre or centimetre scale along the tips of the dykes before terminating in a series of fractures. Some of these dykes resemble the tails of horses and are named horse-tail dykes. The second type of dyke (Type 2) commonly found in Torres del Paine are the metre-scaled basaltic and andesitic dykes with chilled margins. These mafic dykes are subvertical and are mostly found near the feeder zone (Leuthold et al., 2013) although not exclusively, with some found to crosscut the Paine granite. The third type of dyke (Type 3) are the bimodal dykes measuring several meters wide and a few kilometres long. Type 3 dykes can be found intruded in granite or intruded in the host rock, recognisable from its dark basaltic to andesitic outer border and its lighter-coloured granitic to granophyric core. The contacts between the mafic and felsic parts of these dykes can be wavy or sharp, but the outer borders and the inner cores can easily be distinguished with the naked eye. Examples of each type of dyke as observed during the field campaign to Torres del Paine is presented in Figure 2.3. Figure 2.3 (A) shows an example of Type 1, where the dyke terminates into a series of fractures and forms “horse-tail dykes”. This locality is found in Valle del Frances (see map: Figure 2.5) next to the Aleta de Tiburon. Figure 2.3 (B) shows an example of Type 2, where there is a mafic dyke which has crosscut the Paine granite near the feeder zone, which is also located in Valle del Frances. Lastly, Figure 2.3 (C) shows a clear example of a bimodal dyke (Type 3) where the intrusion consists of dark mafic borders with a felsic core. This can be observed at the Cerro Nido de Condor located north-east of the national park.

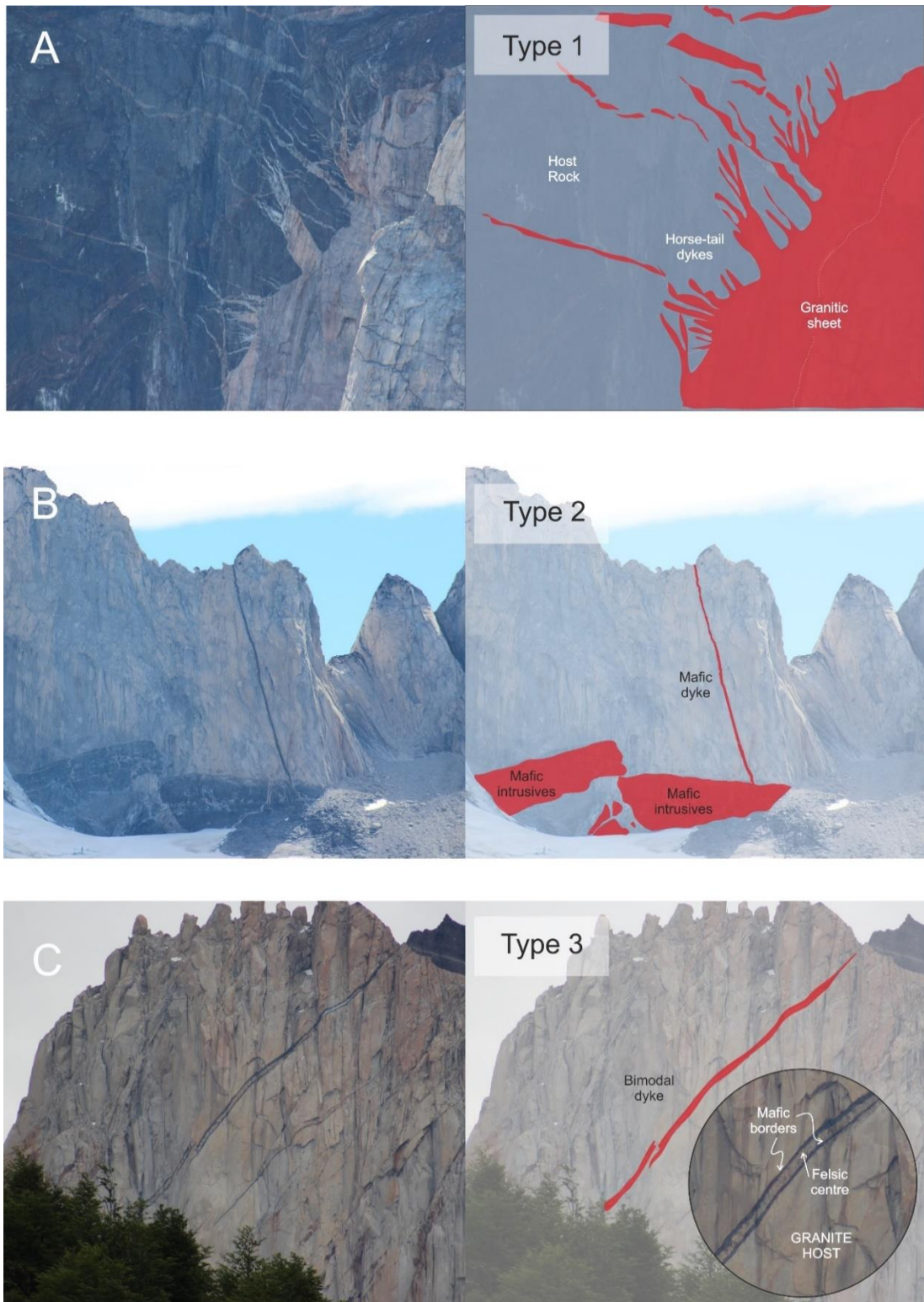


Figure 2.3: The three different types of dykes as categorised by Müntener et al. (2018). (A) Type 1: Dykes related to the emplacement of the granitic sheet terminating into fractures. Seen here are “horse tail” shaped dykes. (B) Type 2: Basaltic dykes found by the feeder zone, and (C) Type 3: Bimodal dyke with clear mafic borders and a felsic core.

2.3 Description of Structures Associated with Magmatic Intrusions at Torres del Paine, Chile

2.3.1 Torres del Paine Intrusive Complex (TPIC), Chile

The previous sections have described the types of intrusions present in Torres del Paine as published in literature. The following descriptions in this section are based on observations made during the field campaign to Torres del Paine in 2016. The map below shows the localities visited as well as some landmarks referred to within this thesis.

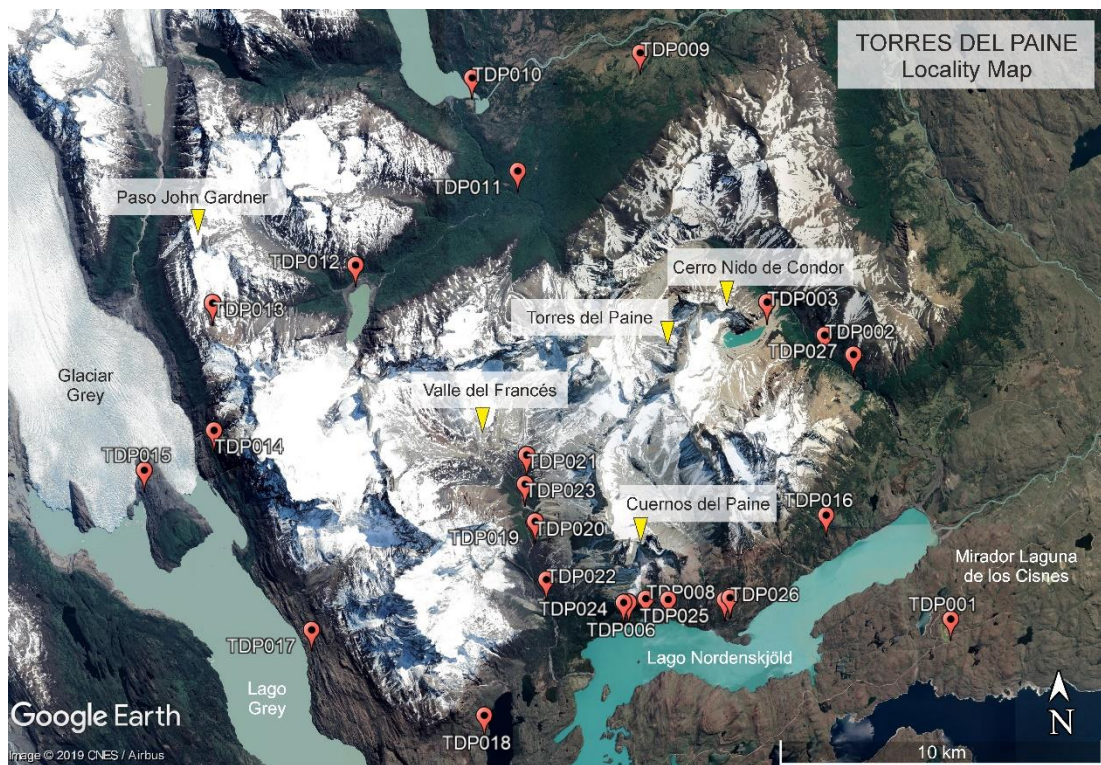


Figure 2.4: A terrain map of Torres del Paine with locality and landmark pins. (Google Earth)

2.3.1.1 Contacts between intrusion and host rock

The contact between the intrusion and the host rocks are observed to be sharp, and the sheets are parallel or sub-parallel to the bedding of the host rock, which forms the roof of the intrusion. The best locality to observe this type of contact is the Cerro Nido de Condor

(Figure 2.5) which lies to the east of the Torres del Paine (or the Paine Towers, which gives the national park its name). This exposure can be seen clearly from the El Chileno campsite (TDP-027). The intrusion was emplaced parallel to host rock bedding, with small apophyses of granite which cut across the host rock layers. The presence of granitic apophyses which cut across the folds are evidence that the magma emplacement episode happened after the host rock folding and was not the cause of the folding. Another locality to observe roof zone contacts (sub-parallel to layering) is to the east of Cuernos del Paine, which forms the centrepiece of the national park. Figure 2.5 (B) is photographed from TDP-001.

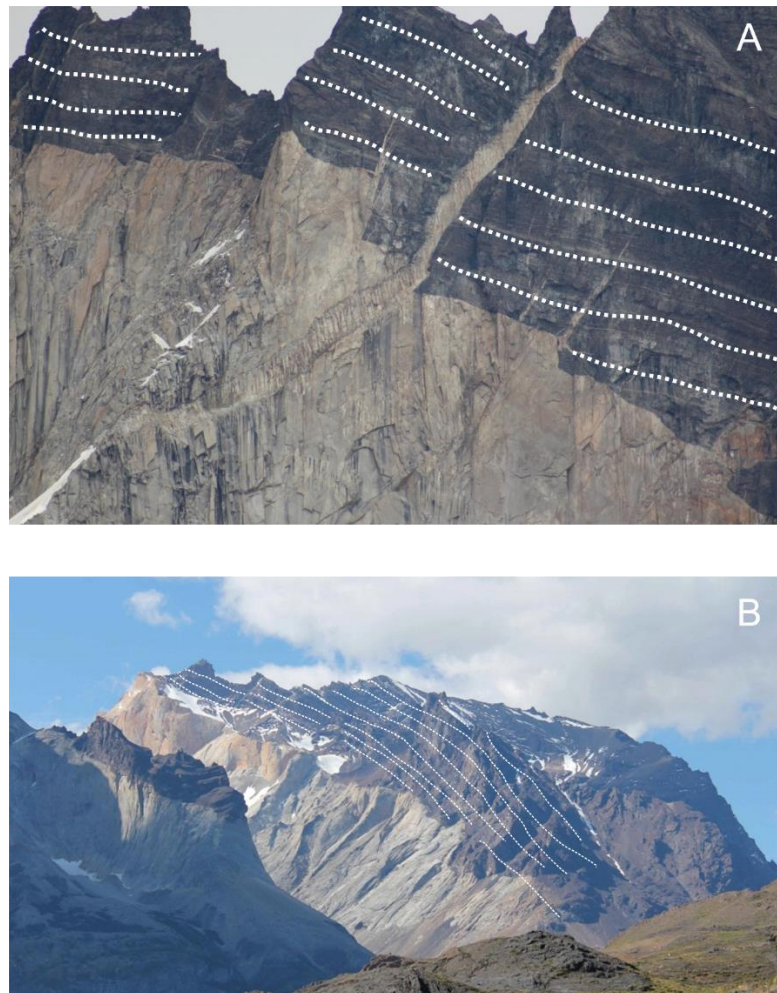


Figure 2.5: Emplacement parallel or sub-parallel to the layers of the host rock. (A) Close up of Cerro Nido de Condor and (B) East of Cuernos del Paine. Dashed lines are used in this figure to emphasize the host rock bedding.

In contrast to the intrusions that are emplaced parallel or sub-parallel to the layering of the host rock, there are also sharp contacts between intrusions and host rock with layering perpendicular to the intrusive body. These contacts are more commonly observed in the western part of the TPIC, for example the Cuernos del Paine is emplaced discordant to the layering of the host rock (Figure 2.6). There are a few stoped blocks observed at this locality. Some blocks are partially unhinged but still attached to the host rock, and others are completely broken off from the host rock.

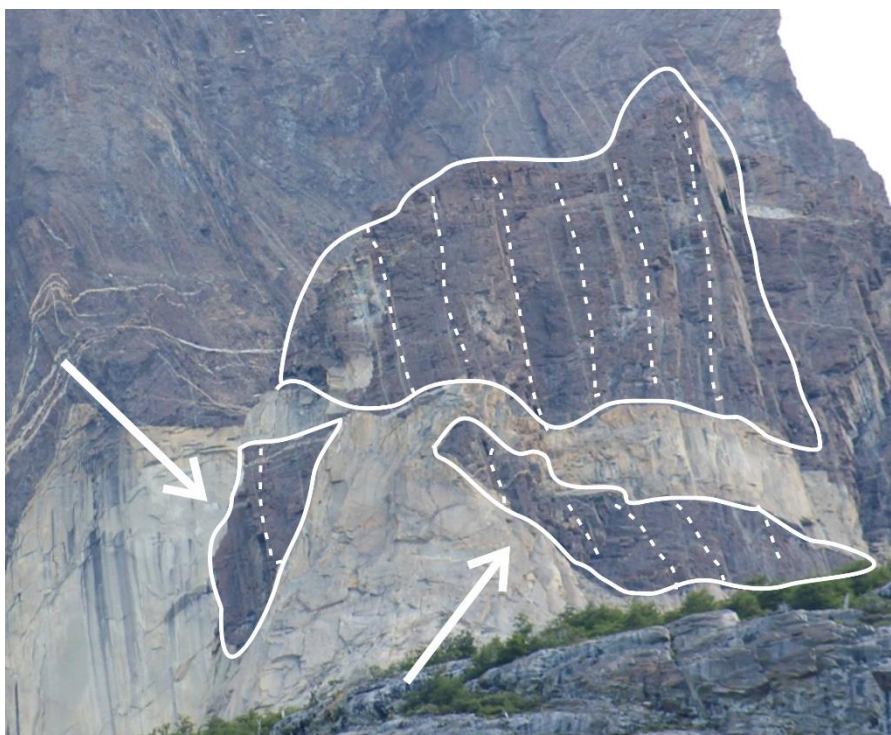


Figure 2.6: Emplacement into host rock perpendicular to the intrusive body. The host rock is traced to show stoped blocks of host rock. Dashed lines are once again used to emphasise the host rock bedding. Arrows are pointing at stoped blocks which have broken off the intruded host.

Contacts between the intrusion and the host rock are more complex in Valle del Frances where the granite sheet terminates into smaller dykes which radiate into the host rock as presented in Figure 2.7 (A). A prominent region of intrusive breccia is also observed to the

west of Aleta de Tiburon (the Shark Fin) showing brecciated host rock as a result of granite emplacement, presented in Figure 2.7 (B).

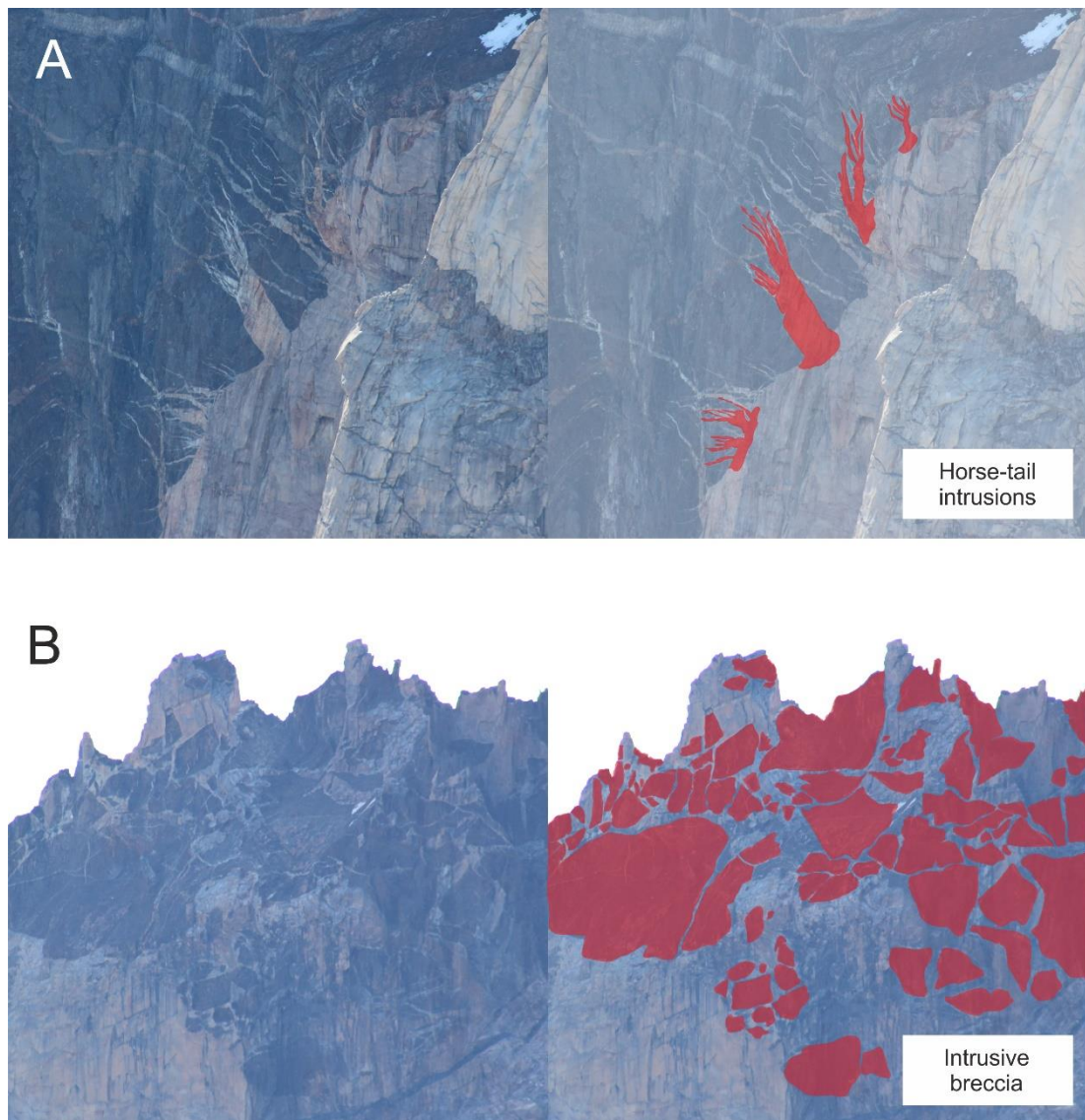


Figure 2.7: Complex contacts between the intrusion and the host rock. (A) Multiple dykes radiating from a terminated granite sheet into the host rock. (B) Intrusive breccia formed by granite emplacement where angular host-rock fragments are surrounded by granite.

2.3.1.2 Contacts between intrusive sheets

The contact between the intrusive sheets, both mafic and felsic, can easily be traced to distinguish the individual intrusive sheets. While the evidence of emplacement of multiple

sheets is abundant in Torres del Paine National Park, the best locality to observe the contacts between intrusive sheets is in Valle Frances. This locality is in the centre of the TPIC with the PMC to the west of the valley and the Paine Granite to the east of the valley. An excellent example of these intra-plutonic contacts as seen in the Paine Granite are presented below in Figure 2.8.



Figure 2.8: Distinct colour changes between the granitic units make it easy to distinguish the individual granite sheets.

2.4 Method Development: ImageJ

Geoscientists have used ImageJ for a variety of research projects including, but not limited to, statistical analysis of sediment texture and structure at a micro scale (Lewis et al., 2010) and determination of depositional events within shell deposits (Sanger, 2015). ImageJ has also been vigorously tested against the image analysis software Blob3D to study the reproducibility of counting vesicles present in volcanic rocks on two separate software programs, where both programs produced similar results when the manually set thresholds were similar (Baker et al., 2011). While the images used in the studies mentioned above are of micro and small-scale structures, ImageJ is also capable of macro scale analysis. Spatial calibration is available using this software to provide real world measurements in units defined by the user, be it in nanometres or kilometres. Field photographs of rock exposure

showcase a number of different geological features such as folds, faults, dykes and sills as shown in Sections 2.2 and Section 2.3. These features not only provide evidence for the chronological order in which these rock formations were created, but also the physical conditions in which those rocks were formed (i.e. depth of intrusion, temperature, surrounding stress, etc.). Analysing these features quantitatively will help contribute towards a better understanding of the processes involved in the propagation and growth of large igneous bodies within the Earth's crust.

2.4.1 ImageJ Sensitivity Analysis: Preparation of Test Images

In this section a systematic method is developed to test the sensitivity of ImageJ so that this can be used to analyse field images. This section will showcase the capabilities and limitations of ImageJ and makes recommendations on how to make the most of ImageJ as an analytical tool. The sensitivity analysis focuses on the effect of line thickness, line angle rotations and transformation of two-dimensional shapes on the area calculated by ImageJ. Area is used as a benchmark in this analysis as it is possible to quantify the errors of the values produced by ImageJ by comparing the areas calculated by ImageJ to the areas calculated using mathematical formulae. Area is also chosen as a benchmark taking into consideration one of the potential applications of ImageJ, where the area of intrusive rock exposure can be used to infer the volume and geometry of the original intrusive bodies.

Test images were first created using the drawing tools available on digital graphics editor CorelDraw and were subsequently filled in with a colour corresponding to the assigned pixel value for that particular component. For the purpose of this analysis, the 8-bit greyscale image format has been selected for the straightforwardness in its range of colours where the colour scale is composed of a single range of pixels of 0 to 255; 0 corresponding to pure black, 255 corresponding to pure white and the values in between representing the different shades of grey.

There are two methods to set and save the colour palette on CorelDraw. The first method is to create a custom colour palette which saves the colours used for analysis on a separate palette to the default colour palette on CorelDraw. This can be done using the Colour Palette Manager which is accessible under the following tabs: Windows > Dockers. First, click on the “Creates a new empty colour palette” button (Figure 2.9). This will prompt the user to create a new empty colour palette. After giving the new palette a file name and saving the new palette, select the new colour palette and click on the “Opens the palette editor” button (Figure 2.10). This step brings up the “Palette editor” dialogue box (Figure 2.11) which allows the user to add multiple colours to the empty colour palette using the following steps: 1) Click on “Add Colour”, 2) Click on “Select Colour” (Figure 2.12). Select Greyscale from the drop-down menu for Model and enter the desired values in the box for Level Component (The box next to “L”) and 3) Click on “OK” to save. Once all colours are added to the palette, click “OK” to exit the “Palette editor”. These colours are now saved as a new colour palette and can be easily accessed to be used for the preparation of multiple images across different files. This method is useful for preparing images with only a few discrete components to analyse, allowing the user to quickly access specific colours for specific components. The second method is to use the existing Greyscale colour palette on CorelDraw named “256 Shades of Grey” which is accessible from the Colour Palette Editor under the tab labelled “Palette Libraries” (Figure 2.13). This pre-existing palette gives the user access to all 256 colours available within the Greyscale spectrum without having to manually add colours to a new palette. This method is particularly useful when preparing an image with many discrete components for analysis, allowing the user to have more colours at their disposal to differentiate the different components present within the image. It is important that the colour palette is established ahead of the image preparation stage to ensure a consistent colour profile is used throughout the process.

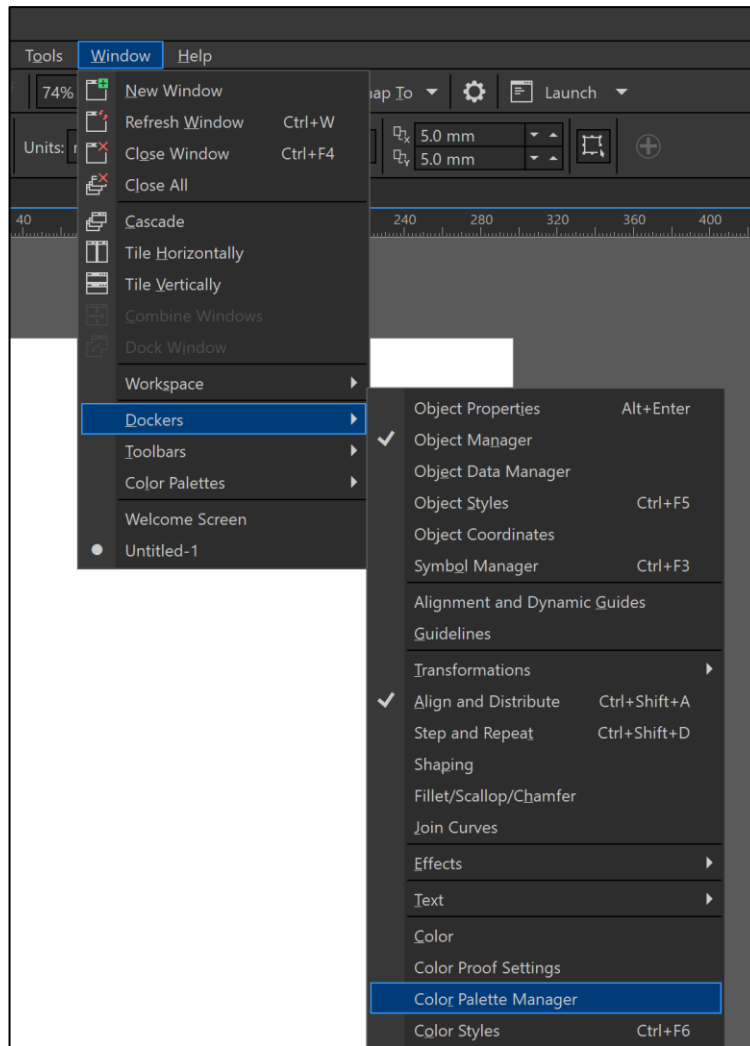


Figure 2.9: The screen capture shows where to find the Color Palette Manager from the Window tab on CorelDraw. This can be used to manage existing colour palettes or to create new ones.

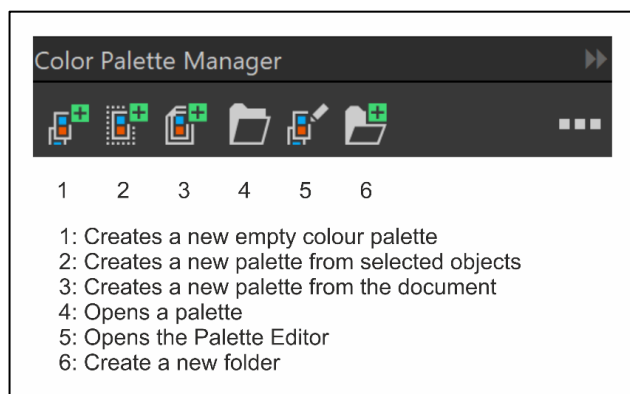


Figure 2.10: Options available for use in the Color Palette Manager. Options 1 and 5 are used in this guide to create custom colour palettes from scratch.

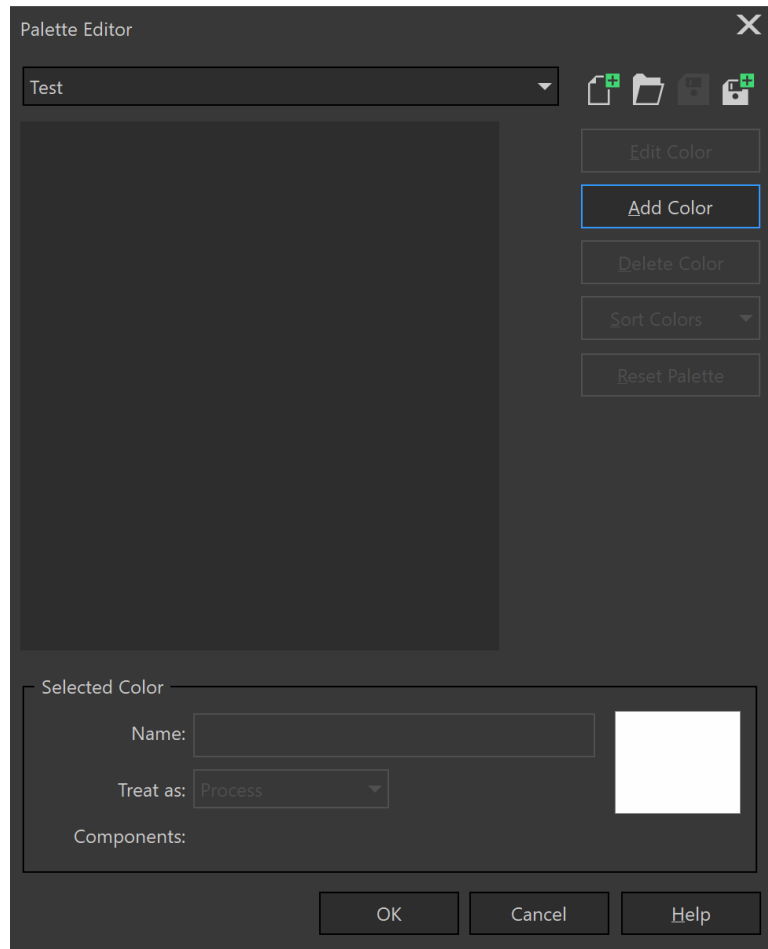


Figure 2.11: The Palette Editor menu allows users to add colours manually to any palette.

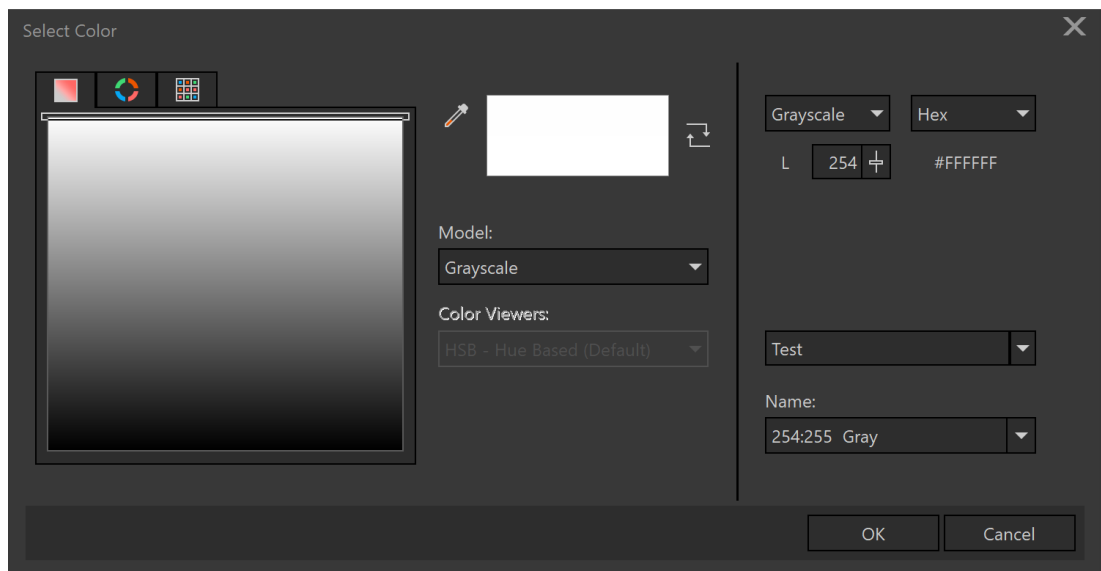


Figure 2.12: The Select Color menu allows users to choose the colour model and hue. The example shows the selection of a very light gray (254) on the Greyscale colour model.

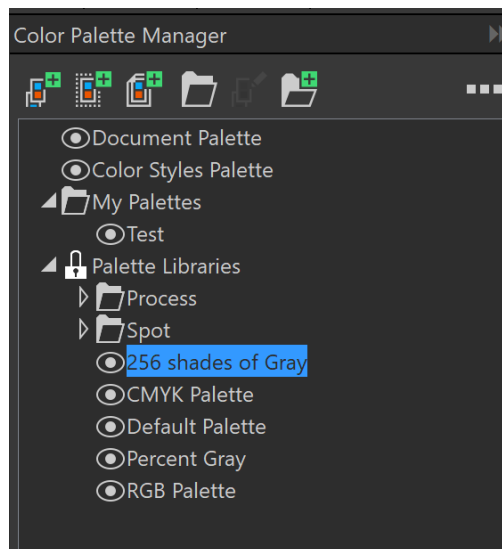


Figure 2.13: The CorelDraw greyscale palette containing 256 shades of grey can be accessed as shown above in the Palette Libraries which is found in the Color Palette Manager.

Once the colour palette has been set and saved, then the creation of test images for analysis can begin. First, the outline of the test shape is created using the pen tool with a known width and then the shape is filled to create an opaque shape. Both the outline and the fill colour are set to a pixel value of 0 (pure black). This designation of pixel values will allow ImageJ to perform discrete analysis using the Threshold function. Note that this particular step will be important later on when preparing field images for analysis as the images are made up of more than one component for analysis. The test images are then saved and exported as 8-bit greyscale Portable Network Graphics (.png) files. The anti-aliasing was left turned on as this was the default settings on CorelDraw and was kept on throughout the preparation stage for consistency. Aliasing happens when objects comprising of smooth continuous curves are rasterised using pixels which gives the objects a sharp jagged appearance. Therefore, anti-aliasing is a technique employed in computer graphics to help smooth out jagged edges in images rendered using pixels.

Most digital graphics editors allow users to choose the size of their on-screen digital pen. Figure 2.14 shows where this option is present on the CorelDraw user interface. The values

shown in the drop down menu show the size of the “nib” of the digital pen. For example, a 2 px digital pen will create a point that is 2 pixels wide, a 3 px digital pen will create a point that is 3 pixels wide and so on. Using this digital pen to draw a straight line introduces a component of length. Together, width (px) and length (px) can be used to calculate the area of the line produced in pixel-squared units (px²). For consistency, the length of all the lines are set to 1000 pixels. The following widths are considered for evaluation in this section: Hairline, 1 px, 2 px, 3 px, 4 px, 5 px, 6 px, 7 px, 8 px, 9 px and 10 px. These horizontal lines (Figure 2.15 (A)) are used to test the effect of line thickness on the area calculated by ImageJ. The upper and lower threshold values are both manually set to 0 for analysis.

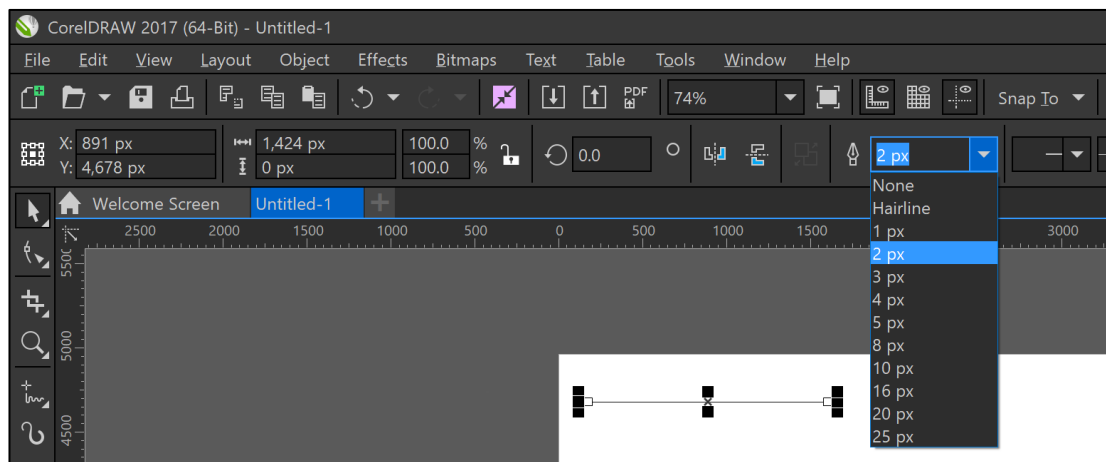


Figure 2.14: Drop down menu on CorelDraw to select the “nib” size of the digital pen. The default options include but are not limited to Hairline, 1 px, 2 px, 3 px, 4 px, 5 px, 8 px, 10 px, 16 px, 20 px and 25 px as shown above. (N.B. This menu is only available when Pixel is selected as the default unit. Should the unit be different, access Object Properties to change the unit.)

Next, a horizontal line 20 pixels wide and 1000 pixels long is created with the starting angle marked as 0°. This horizontal line is then rotated at 15° intervals to create rotated lines representing the angles between 0 and 180°. These images are tested using two threshold settings: 1) User-defined threshold settings, where the upper and lower threshold values are manually set to 0 for analysis and 2) ImageJ’s default threshold settings, which automatically

takes into account darker shades of grey in addition to pixels with the value 0 (pure black). This set of lines (Figure 2.17 (B)) is used to test the effect of line angles on the area calculated by ImageJ.

Lastly, the sensitivity test is expanded to include select geometrical shapes of equal area (by manual calculation) to test the accuracy of calculated areas by ImageJ. The following shapes (Figure 2.17 (C)) with a predefined area of 1000000 px^2 are considered for evaluation: 1) A square, 2) a horizontal rectangle, 3) a vertical rectangle, 4) a circle, 5) a horizontal ellipse and 6) a vertical ellipse. Table 2.1 summarises the dimensions used to create each shape to achieve a calculated area of 1000000 px^2 . The dimensions in the table refer to the length as measured in the x and y-axes respectively (L_x and L_y). The formulae used to manually calculate the area and perimeter of each shape are presented in Table 2.2. For calculations involving circles and ellipses, the following values are used: Radius, $r = 564$, $a = 282$ and $b = 1128$. (N.B. These numbers have been rounded from the values 564.19, 282.095 and 1128.38 as the calculations in ImageJ are carried out on pixels carrying full pixel values, any pixels with partial pixel values are omitted in the process of pixel value mapping.)

Table 2.1: Summary of dimensions of each test shape created using CorelDraw. All shapes have a calculated area of 1000000 px². L_x represents the length measured along the x-axis and L_y represents the length measured along the y-axis.

Shape	L_x	L_y	Area (px ²)	Perimeter(px)
Square	1000	1000	1000000	4000
Rectangle (Horizontal)	2000	500	1000000	5000
Rectangle (Vertical)	500	2000	1000000	5000
Circle	1128	1128	1000131	3545
Ellipse (Horizontal)	2257	564	1000131	4840
Ellipse (Vertical)	564	2257	1000131	4840

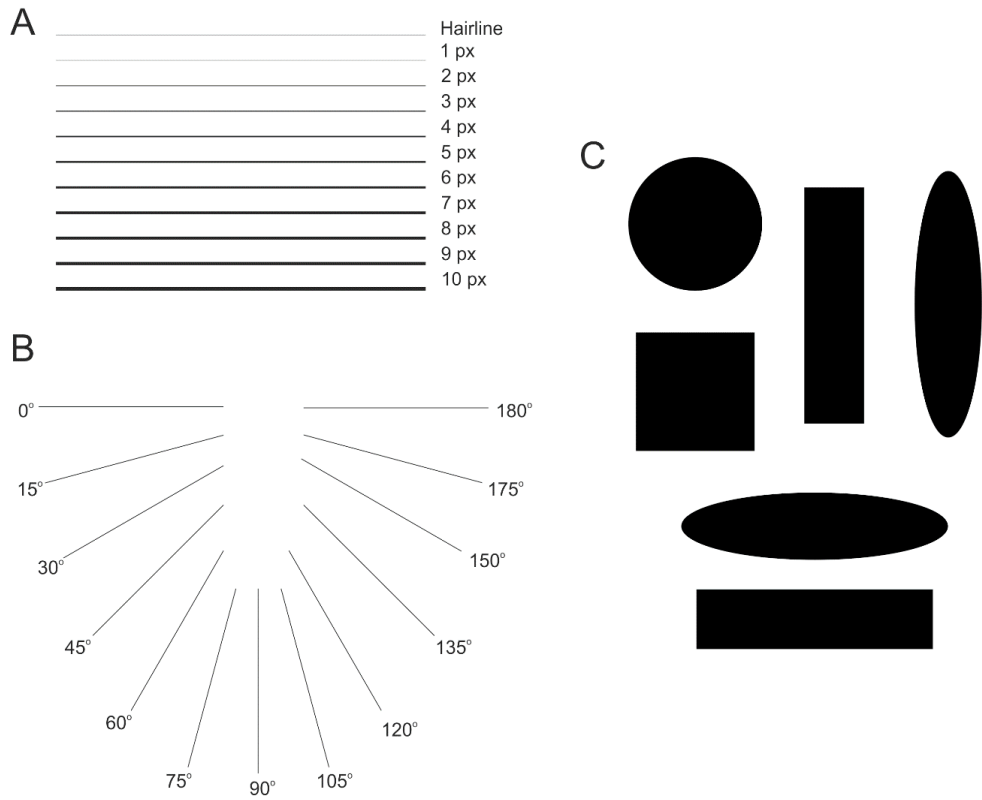
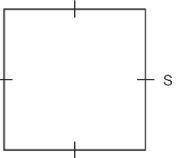
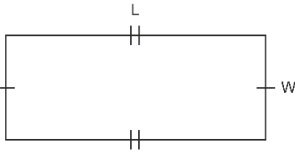
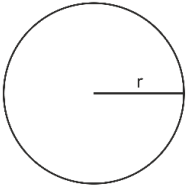
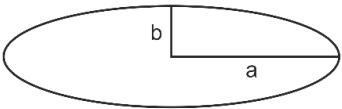


Figure 2.15: Three sets of images used to test the sensitivity of ImageJ by area calculations. Set (A) shows lines of equal length (1000 pixels) with different widths. Set (B) shows lines of equal length (1000 pixels) and width (20 pixels) with different angles. Set (C) shows different shapes with a predefined area of 1000000 px². Note that all images presented are independent of scale.

Table 2.2: General formulae to calculate the area of the test shapes used.

Shape	Area	Perimeter/ Circumference
<p style="text-align: center;">Square (4 equal sides, S)</p> 	$S \times S$	$4S$
<p style="text-align: center;">Rectangle (Length, L and Width, W)</p> 	$L \times W$	$2L + 2W$
<p style="text-align: center;">Circle (Radius, r)</p> 	πr^2	$2\pi r$
<p style="text-align: center;">Ellipse</p> 	πab	The perimeter has been calculated by using mathematical approximation

2.4.2 Effect of Line Thickness

The manually calculated area (using the formula of width times length) shows that the area of the line grows linearly with increasing line width (Figure 2.16). However, the area calculated by ImageJ (blue bars) shows that there is a notable underestimate of calculated area on lines created using odd-numbered widths. The area of the lines drawn with 3 px, 5 px, 7 px and 9 px digital pens are 1000 px² smaller than its actual size. Zooming in on the lines at 1200% on the ImageJ user interface (Figure 2.17) reveals the presence of inactive pixels (shown in grey) on the top and bottom of the band of active pixels (highlighted in red). The presence of inactive pixels means that there are fewer active pixels used in the area calculation by ImageJ, hence the calculated area would be smaller than its actual size. If the threshold is left undefined by the user, ImageJ will automatically include these inactive pixels in its area calculation.

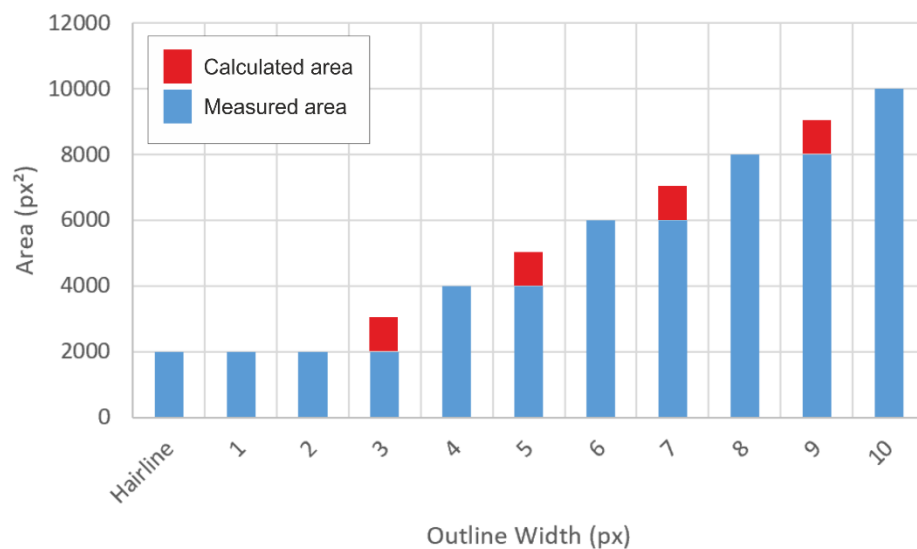


Figure 2.16: Comparison between the calculated area (by user) and the measured area (ImageJ). The values returned by ImageJ are 1000 px² smaller on lines created using an odd-numbered “nib”.

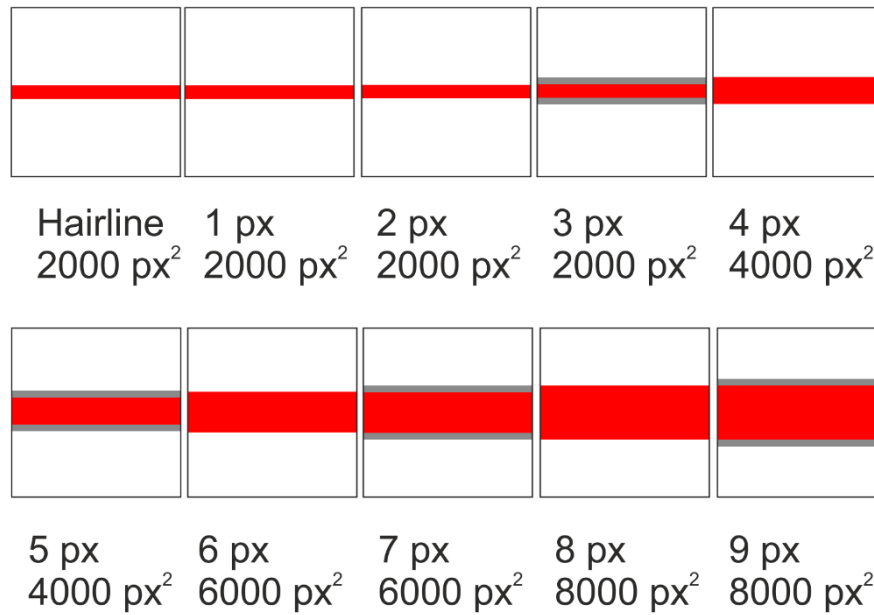


Figure 2.17: Close-up of each line at 1200% magnification. The active pixels used in the area calculation. The bands in grey represent inactive pixels, prominent on lines drawn with odd-numbered digital “nib”.

2.4.3 Effect of Line Angle

For the second set of tests, each line in Figure 2.15(B) undergoes two sets of analysis in ImageJ: 1) Area calculation using the user-defined single pixel value for analysis, and 2) Area calculation using ImageJ’s default selection of a range of pixel values for analysis. The area calculated for each line is reported in Table 2.3 as A_U (User-defined) and A_D (Default), with the differences in area compared to the control line (0° , where A_U and $A_D = 20000 \text{ px}^2$) denoted as ΔA_U and ΔA_D . The pixel error percentage (%), which provides an indicator of the percentage of inactive pixels present during analysis is calculated using Equation 2.1.

$$\frac{\Delta A_n}{A_n} \times 100 = \text{Pixel error percentage (\%)} \quad [2.1]$$

Table 2.3: Effect of line angle on the area calculated using ImageJ. Table showing the measured pixel areas of a line of known dimensions (Length: 1000 pixels, Outline width: 20 px) when rotated at different angles and using two different pixel value assignments: (1) A user-defined pixel value which assigns the pixel value to 0, and (2) ImageJ's default threshold settings, which applies different ranges of pixel values depending on the angle of the line. The maximum of the range is noted in this table as Max. Threshold. The measurements obtained from the line at 0o are used as a reference set. Lx and Ly are the line length of the x and y-axis respectively.

Angle (°)	Lx (px)	Ly (px)	User-defined Pixel Value			ImageJ Default Threshold					
			A _D (px ²)	ΔA _D	Pixel error (%)	A _U (px ²)	ΔA _U	Pixel error (%)	Max. Threshold	Δ Threshold	Threshold Increase (%)
0	1000	0	20000	0	0.00	20000	0	0.00	128	0	0.00
15	966	259	20280	-238	-1.17	18822	-238	-1.26	161	33	20.50
30	866	500	20183	-335	-1.66	18684	-335	-1.79	156	28	17.95
45	707	707	20518	0	0.00	19076	0	0.00	174	46	26.44
60	500	866	20198	-320	-1.58	18694	-320	-1.71	156	28	17.95
75	259	966	20258	-260	-1.28	18810	-260	-1.38	161	33	20.50
90	0	1000	20000	-518	-2.59	19960	-518	-2.60	132	4	3.03
105	259	966	20258	-260	-1.28	18810	-260	-1.38	161	33	20.50
120	500	866	20198	-320	-1.58	18694	-320	-1.71	156	28	17.95
135	707	707	20518	0	0.00	19076	0	0.00	174	46	26.44
150	866	500	20182	-336	-1.66	18684	-336	-1.80	156	28	17.95
165	966	259	20280	-238	-1.17	18822	-238	-1.26	161	33	20.50
180	1000	0	20000	-518	-2.59	20000	-518	-2.59	128	0	0.00

The pixel error percentage (%) is plotted against the angle of rotation of each test image in Figure 2.18 which compares the combined effects of the angle of rotation and the mode of analysis on the percentage of pixel errors.

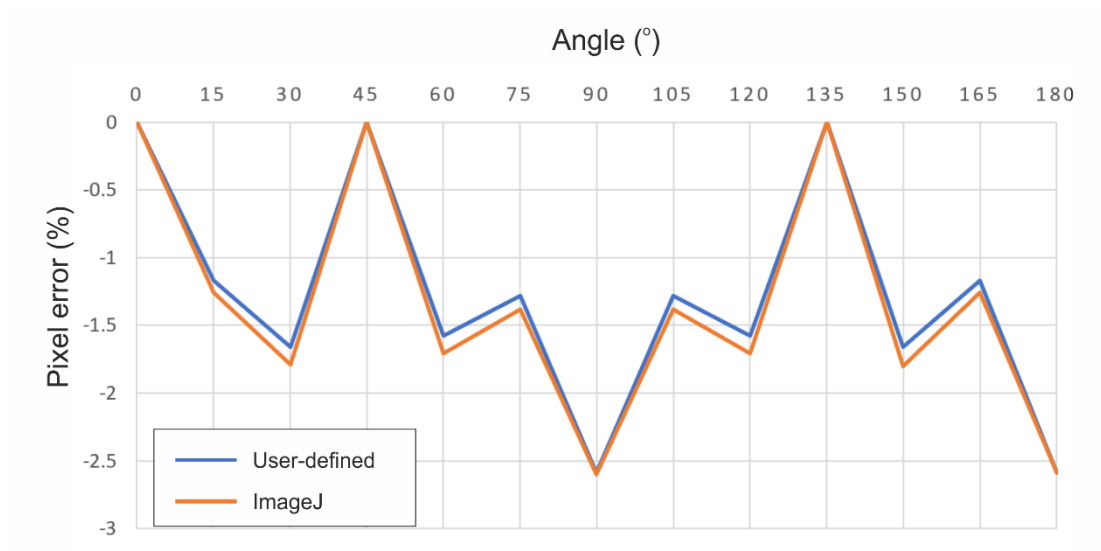


Figure 2.18: Comparison of pixel error (%) of the area produced user-defined thresholds and the area calculated using ImageJ. The lower negative values (closer to positive) indicate an overestimation of the calculated area. The higher negative values (away from positive) indicate an underestimation of the calculated area.

The results from this test show how the selection of pixel values for analysis plays an important role on the calculations made using ImageJ. ImageJ's default selection of pixels encompasses a larger range of pixel values which means that more active pixels are present for analysis. Selecting the pixel value for analysis limits the number of active pixels for analysis exclusively to the pixels carrying the value defined by the user. Using a single defined pixel value however results in an underestimation of area and perimeter of a given shape, as less active pixels are highlighted on the software. For example, when the pixel value is set to 0 for analysis on a 45° line, it can be observed that there is a border of grey pixels forming along the outline of the line drawn. However, using ImageJ's default threshold settings, the software picks up all pixels on the 45° line as active pixels, operating on a larger range of pixel

values between 0 (pure black) and 174 (light grey). The close-up images (magnified at 1600% on ImageJ) for the line rotated at 45° and other lines are presented in Figure 2.19. The pixels in red represent the active pixels used in the analysis.

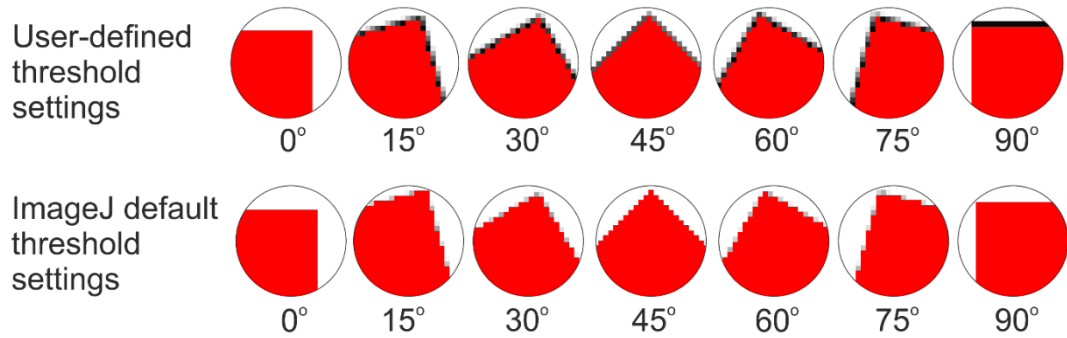


Figure 2.19: Close up of line edges magnified at 1600% on ImageJ. The red region represents the region of active pixels used for analysis. The grey boxes of different shades at the edges represent inactive pixels which are excluded from the calculation of area.

2.4.4 Effect of Two-Dimensional Shapes

The third set of tests explore the effects of different shapes (Figure 2.15(C)) on the area and perimeter calculated by ImageJ using discrete threshold value assignment (setting the threshold value to 0). The values calculated for both area and perimeter, both manually using formulae (Table 2.2) and using ImageJ, are presented in Table 2.4 for comparison.

The results show that for different shapes, there is not much difference between the area manually calculated using the dimensions of the shape and the formulae in Table 2.2 and the area measured by ImageJ. The percentage of error for the calculated area falls below 0.5%. However, note that there is a greater percentage of error with circular shapes (Shapes 4, 5 and 6 in Table 2.4) for the calculation of the shape perimeter with approximately 5% error.

Table 2.4: The area and perimeter of the test shapes (1) Square, (2) Vertical rectangle, (3) Horizontal rectangle, (4) Vertical ellipse, (5) Circle and (6) Horizontal ellipse.

Shape	Shape	Lx	Ly	Area		ΔA (%)	Perimeter		ΔP (%)
				Calculated	ImageJ		Calculated	ImageJ	
1	Square	1000	1000	1000000	1003002	0.30	4000.00	4003.66	0.091
2	Rectangle (Vertical)	500	2000	1000000	1002501	0.25	5000.00	5001.66	0.033
3	Rectangle (Horizontal)	2000	500	1000000	1002501	0.25	5000.00	5001.66	0.033
4	Ellipse (Vertical)	564	2257	1000131	1002902	0.28	4839.86	5064.31	4.638
5	Circle	1128	1128	1000131	1001084	0.10	3545.37	3739.73	5.482
6	Ellipse (Horizontal)	2257	564	1000131	1003284	0.32	4839.86	5065.73	4.667

2.4.5 Implications for Systematic Error

The results from the ImageJ sensitivity analysis tests present a few options to reduce errors and maximise the accuracy of the data obtained from ImageJ:

- Use a small nib size (Hairline to 3 px) and minimise the use of sub-horizontal lines. Perfectly horizontal and perfectly vertical lines produce the least amount of errors as no new pixels are introduced.
- Lines that are sub-horizontal should be avoided as the most pixels are introduced to the line in this orientation. Sub-vertical lines are fine to use and have less pixels introduced compared to the sub-horizontal line.
- If the perimeter of the shape is of interest, keep the shapes as angular as possible as rounded shapes produce greater errors. On the other hand, it is noted that curvature does not have a significant impact on the calculated area.
- Turn off anti-aliasing during image preparation. The anti-aliasing function introduces pixels made with lighter shades of grey to smooth out the line on screen during rotation or the creation of curved line.







2.5 Field Image Analysis Workflow

2.5.1 Pre-processing Images: Pixel Value Mapping

The objective of pre-processing the field images is to allow ImageJ to correctly identify the lithological components present in the image for discrete analysis. This process of categorical discrimination can be done using ImageJ's built-in threshold slider which allows the user to select a range of pixel values to be actively used for analysis. The threshold slider can only be used on greyscale images which include (but are not limited to) the following formats: RGB (Red-Green-Blue) stack, HSB (Hue-Saturation-Brightness) stack and 8-bit greyscale. For

consistency, all field images analysed have been manually formatted to comply with the 8-bit greyscale format as the test images have been formatted in Section 2.4. The individual components which make up the image (i.e. the different lithologies) are carefully traced using a digital stylus and filled with the colours corresponding to the assigned pixel values (see Table 2.5) to ensure that ImageJ correctly discriminates between the individual components for discrete analysis. Higher resolution images have a higher pixel density, which means that a lot of information can be captured even when zoomed-in. For example, the photograph of Torres del Paine used in Figure 2.20 has a vertical and horizontal resolution of 4272 pixels by 2838 pixels with 72 dpi (dots per inch). A scale bar of known pixel length and pixel value is added to image for calibration purposes. Lastly, the azimuth directions to the left and right of the image is added on (also assigned its own pixel value) as a directional reference in which the image was originally captured. Figure 2.20 shows an example of an image which has undergone all the pre-processing steps mentioned above and is ready for analysis using ImageJ. While this process may be tedious, it is definitely more beneficial to manually trace out the components of the image as this enables the software to correctly identify the discrete components present within the image. The process of tracing high resolution images are quite forgiving as there are more pixels to work with in the photograph. Using Figure 2.20 as an example again, once scaled (jump to Section 2.5.3) the photograph has a resolution of approximately 0.21 metres per pixel. This relative to the size of the actual outcrop which measures about 1 km across means that there is wiggle room for error while preparing the photographs for analysis.

Table 2.5: Example of how the components of the photograph are assigned different pixel values using the Greyscale colour chart.

Greyscale Colour	Pixel Value	Rock Type/ Image Component
	0	Host Rock (Sedimentary)
	20	Scale Bar and Azimuth
	60	Felsic Intrusion (Granite II)
	80	Mafic Intrusion
	100	Red Intrusion
	120	Main Granitic Body (Granite I)

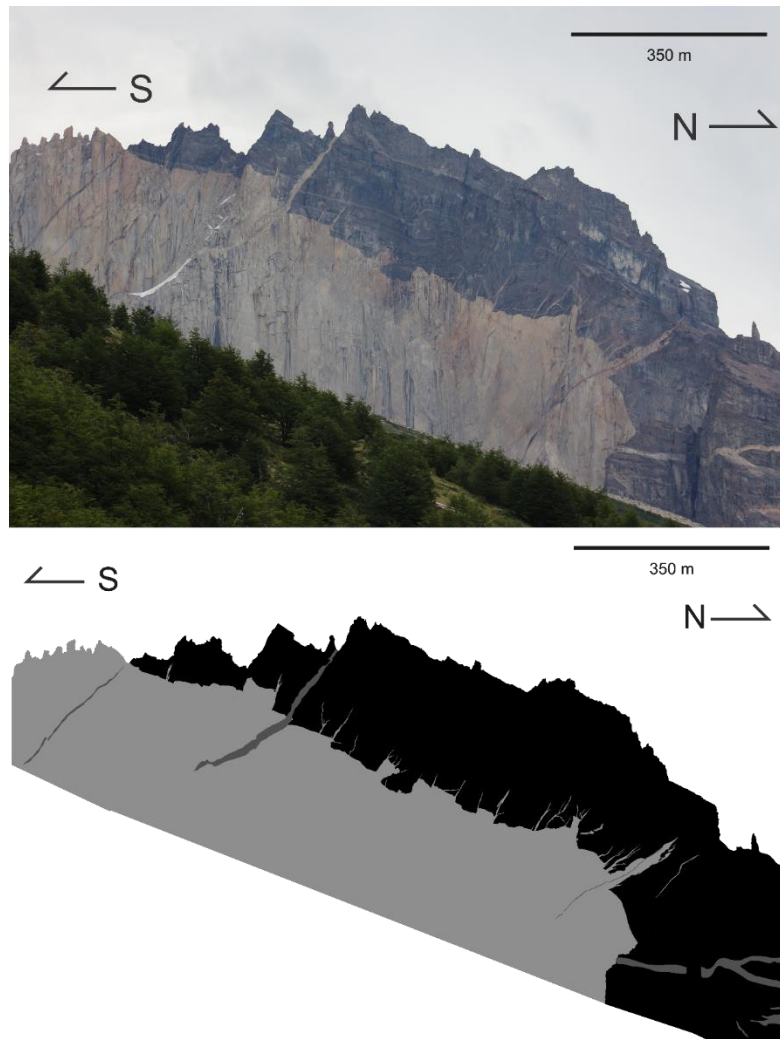


Figure 2.20: Cerro Nido de Condor before and after pre-processing using CorelDraw.

It is important to note that not all images will consist of an outcrop plane of the same orientation and the same depth of field within an image. In the event of irregular surfaces or differences in the depth of field (exposure being closer or further away from the photographer), the image will have to first be segmented into individual segments which share the same orientation and distance away from the camera (similar two-dimensional surfaces). Figure 2.21 shows an example of a more complex image where there are rock exposures both in the foreground and the background of the image. These segments will then be assigned individual scale bars to account for the differences in depth of field between the different segments.

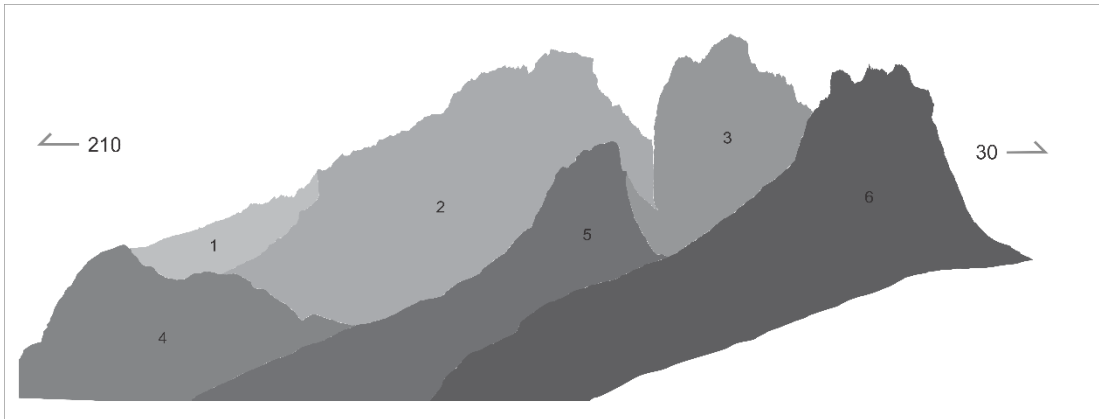
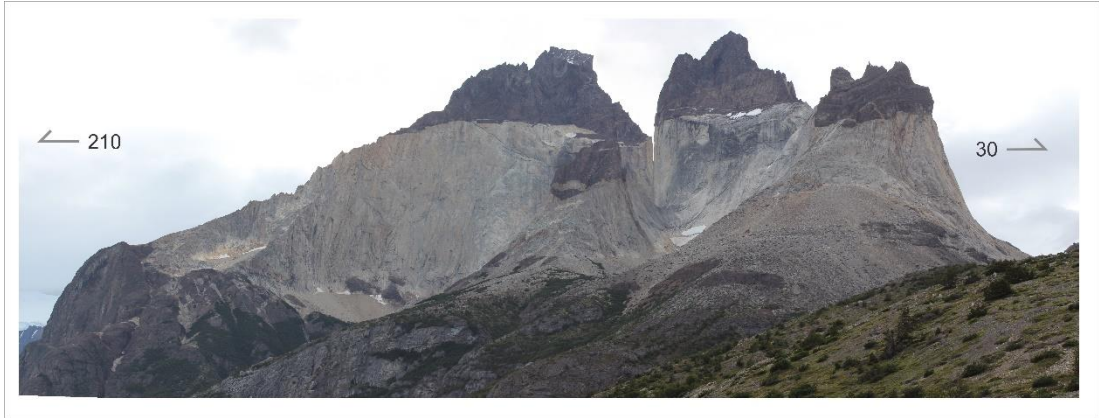


Figure 2.21: Field photograph of Cuernos del Paine here there are differences in the depth of the photograph (darkest shade is closest to the foreground and light shade is furthest away from the foreground.) This complexity needs to be taken into account for image analysis using ImageJ.

2.5.3 Scaling Field Images for Image Analysis

Proper scaling allows for accurate quantitative analysis to be carried out using the visual data (e.g. video footage and photographs). Ground control points are commonly used to establish the scale and orientation in field photogrammetry. Ground control points are clearly visible physical markers of known coordinates which are deployed in the field before acquiring visual data (Westoby et al., 2012). However, ground control points could be difficult to place in remote field areas. The scale of the structures within a field photograph however can still be obtained without ground control points using triangulation. This is done by identifying distinctive features on the outcrop such as displaced bedding, dyke tips and intrusive contacts that can be easily recognised in both field photographs and satellite imagery. These features are then marked as points on the field photograph and are numbered for reference. Next, using Google Earth Pro, the following points are added as Placemarks on the satellite view of the field area: 1) The position of the photographer, using GPS coordinates taken in the field and 2) The position of the features identified and numbered in the field photograph. After establishing the position of these markers, two lines connecting the position of the photographer to the two “ends” of the ends of the photograph are made using the “Path” tool. Lastly, a third “Path” line is drawn where the two lines are at an equal distance from the photographer, creating a triangle. The steps so far are presented in Figure 2.22. Next, the distance measured along this final “Path” is the horizontal distance across the photograph and will be used as the “Known distance” when establishing the global scale in ImageJ. The “Distance in pixels” is obtained from the length of the line drawn across the field photograph using ImageJ. Figure 2.23 captures the rest of the steps mentioned in this paragraph.

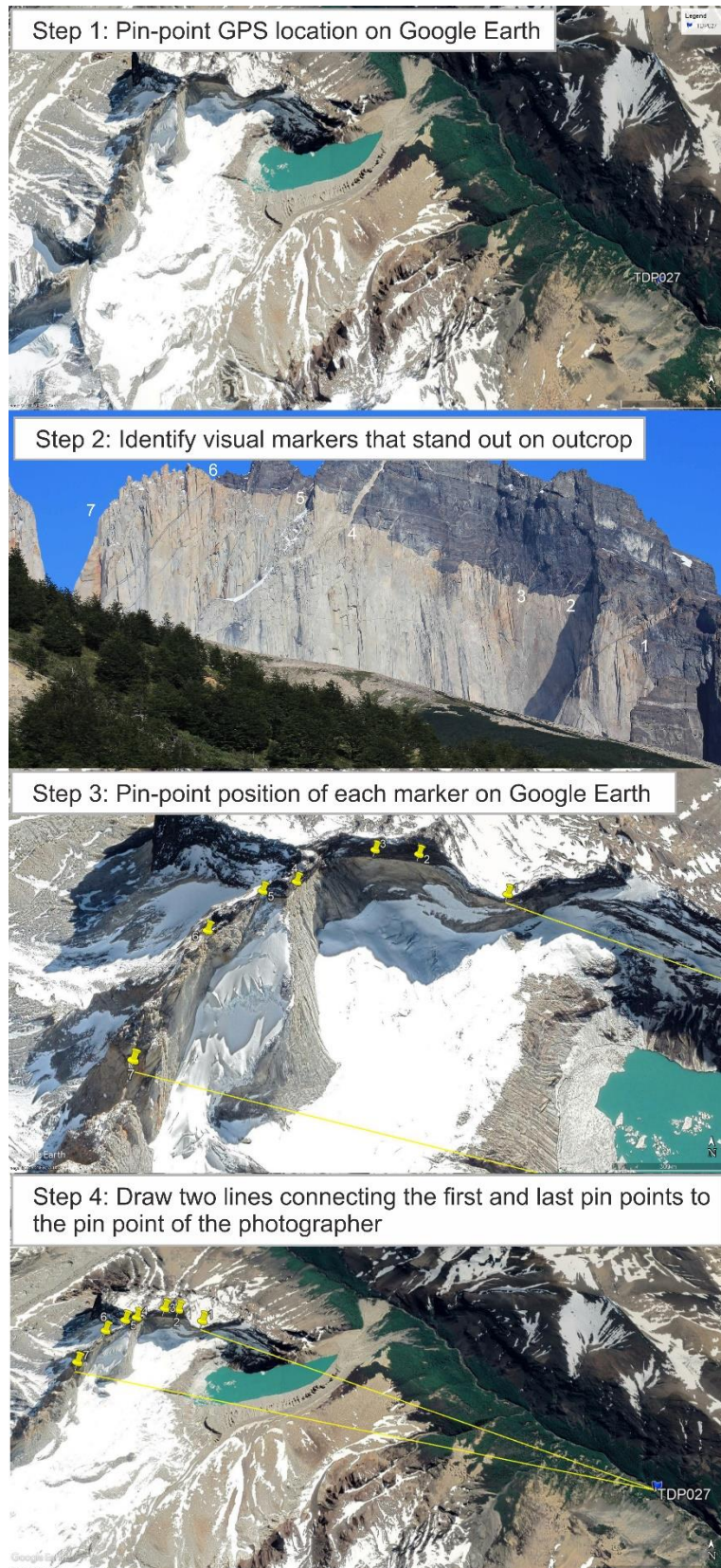


Figure 2.22: Steps 1-4 of scaling images by using known points on a field photograph and the Path tool on Google Earth Pro.

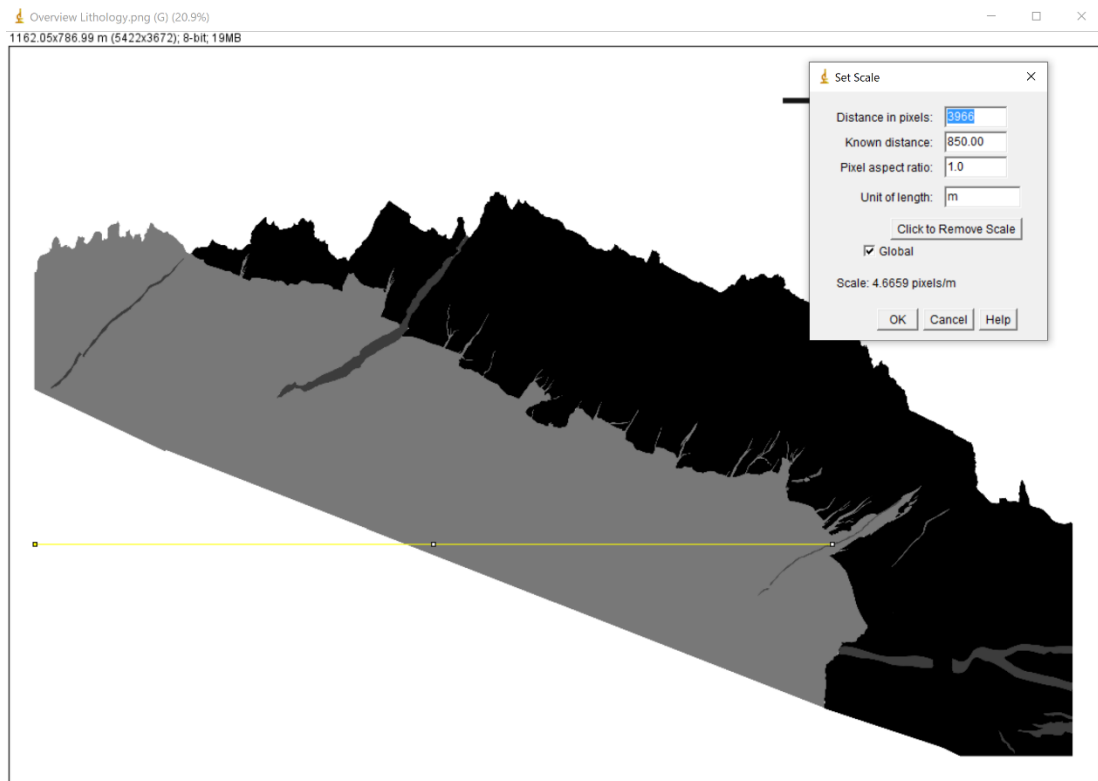


Figure 2.23: How the photograph is scaled on ImageJ using the length obtained from the Path tool on Google Earth Pro. The yellow line shows a straight line drawn onto the photograph between Points 1 and 7 from the original photograph, which gives the distance in pixels.

2.5.4 Processing using ImageJ

The next step after preparing the photographs in an 8-bit greyscale format and establishing the horizontal scale across the photograph is to extract quantitative data from the photograph using ImageJ. For the following worked examples, the photographs have been processed using ImageJ to provide geometrical data in the form of intrusion lengths and thicknesses to calculate magma overpressure.

The length of each intrusion in the photograph is obtained by using the “Analyse Particles” function on ImageJ, which can be found under the “Analyse” tab. To use this function, the user must first set the colour threshold for analysis as demonstrated in Section 2.4. The estimated length of the intrusion is found under the column “Major” which marks the length

of the major axis of the ellipse of best fit around the actively highlighted intrusions. The thickness of each intrusion in the photograph is measured using two methods: 1) Using the “Straight” function (depicted as a line icon on the toolbar) where straight lines are drawn perpendicular to the intrusion length to measure the thickness of the intrusion along the length of the intrusion. The average thickness of each intrusion is then used in overpressure calculations as done by Kavanagh and Sparks (2011) on dykes in Helam Mine, 2) Using the maximum thickness of the ellipse, or the length of the minor axis of the ellipse of best fit around the highlighted intrusion which can be found under the “Minor” column after processing the image using the “Analyse Particles” function. This method of thickness estimation was used in the calculations of overpressure of non-feeder dykes in the Miyakejima volcano by Kusumoto et al. (2013). The results are presented in Tables 2.6 and 2.7 of this thesis.

2.5.5 Results: Torres del Paine Intrusive Complex, Chile

The intrusions of interest in the photograph of Torres del Paine shows a granitic intrusion which has intruded in the Paine granite. Therefore, the constants for granite as used as follows:

From Zhu (2012):

- Young’s Modulus, E (Pa) = 10-70 GPa,
- $\nu = 0.1-0.3$

From Li et al. (1999):

- Young’s Modulus (from Dynamic triaxial compressive tests), $E = 51.63-88.33$ GPa
- $\nu = 0.173-0.336$

The results below are presented in Tables 2.6 and 2.7, where the values presented in Table 2.6 are calculated using aspect ratio derived from the length and thickness measured on ImageJ (TDP-001a and TDP-002a). The following lists compile the ranges of P_0 values calculated:

Aspect ratio using length and thickness from ImageJ (TDP-001a and TDP-002a):

- 10 GPa, $\nu = 0.1 - 0.3$, $P_0 = 70 - 100$ MPa

- 30 GPa, $\nu = 0.1 - 0.3$, $P_0 = 340 - 510$ MPa

- 70 GPa, $\nu = 0.1 - 0.3$, $P_0 = 480 - 720$ MPa

Aspect ratio of 1:1000 (TDP-001b and TDP-002b):

- 10 GPa, $\nu = 0.1 - 0.3$, $P_0 = 5$ MPa

- 30 GPa, $\nu = 0.1 - 0.3$, $P_0 = 25$ MPa

- 70 GPa, $\nu = 0.1 - 0.3$, $P_0 = 35$ MPa

Table 2.6: Magma overpressure calculations for select intrusions of the TPIC, using the aspect ratio from length and thickness values measured using ImageJ

Intrusion	E (GPa)	ν	Half-length (a)	Half- thickness (b)	Aspect ratio (a/b)	P_0 (MPa)
TDP-001a	10	0.1	204.83	4.19	49	102.17
TDP-002a			87.96	1.21	73	68.79
TDP-001a		0.2	204.83	4.19	49	102.32
TDP-002a			87.96	1.21	73	68.89
TDP-001a		0.3	204.83	4.19	49	102.99
TDP-002a			87.96	1.21	73	69.34
TDP-001a	50	0.1	204.83	4.19	49	510.84
TDP-002a			87.96	1.21	73	343.93
TDP-001a		0.2	204.83	4.19	49	511.61
TDP-002a			87.96	1.21	73	344.44
TDP-001a		0.3	204.83	4.19	49	514.96
TDP-002a			87.96	1.21	73	346.70
TDP-001a	70	0.1	204.83	4.19	49	715.17
TDP-002a			87.96	1.21	73	481.50
TDP-001a		0.2	204.83	4.19	49	716.25
TDP-002a			87.96	1.21	73	482.22
TDP-001a		0.3	204.83	4.19	49	720.94
TDP-002a			87.96	1.21	73	485.38

Table 2.7: Magma overpressure calculations for select intrusions of the TPIC using values an predefined aspect ratio of 1:1000

Intrusion	E (GPa)	ν	Half-length (a)	Half- thickness (b)	Aspect ratio (a/b)	P_0 (MPa)
TDP-001b	10	0.1	4185.00	4.19	1000	5.00
TDP-002b			1210.00	1.21	1000	5.00
TDP-001b		0.2	4185.00	4.19	1000	5.01
TDP-002b			1210.00	1.21	1000	5.01
TDP-001b		0.3	4185.00	4.19	1000	5.04
TDP-002b			1210.00	1.21	1000	5.04
TDP-001b	50	0.1	4185.00	4.19	1000	25.00
TDP-002b			1210.00	1.21	1000	25.00
TDP-001b		0.2	4185.00	4.19	1000	25.04
TDP-002b			1210.00	1.21	1000	25.04
TDP-001b		0.3	4185.00	4.19	1000	25.20
TDP-002b			1210.00	1.21	1000	25.20
TDP-001b	70	0.1	4185.00	4.19	1000	35.00
TDP-002b			1210.00	1.21	1000	35.00
TDP-001b		0.2	4185.00	4.19	1000	35.06
TDP-002b			1210.00	1.21	1000	35.06
TDP-001b		0.3	4185.00	4.19	1000	35.29
TDP-002b			1210.00	1.21	1000	35.29

2.6 Discussion

2.6.1 Modelled Overpressures

It is important to note that the output produced is only as good as the numbers that have been plugged in. There are three components to the equation. The first is geometric, which is the length and thickness of the intrusions which are measured from Image J. The second is dynamic, which is the Young's modulus of the host material which is obtained from literature. These values are most likely to be obtained by uniaxial or triaxial compression experiments which may not be representative of the deformation of the rocks in nature. The samples used in the lab are cold and pristine, while in a natural system as the rocks are being intruded at depth, the rocks are hot and damaged and therefore easier to deform. The third component of the equation is the Poisson's ratio, which is also obtained from published literature. The Poisson's ratio represents the compressibility of a material, where a material would be more compressible if brittle and damaged. As a reference point for comparing the values calculated, here are some published P_0 values for known intrusions:

- Kavanagh and Sparks, 2011: 4-70 MPa (Kimberlites)
- Geshi et al., 2012: 7-12 MPa (Miyakejima, non-feeder dykes, basaltic?)
- Daniels et al., 2012
 - 37-1990 MPa (Rum dykes – Olivine basalt, tholeiitic),
 - 4-40 MPa (Swartruggens dykes – Kimberlites)
- Poland et al., 2008: 4.6-148.3 MPa (Summer Coon – Silicic)
- Pollard and Muller, 1976
 - 0.35-4.8 MPa (Walsen – Silicic)
 - 3.6-50 MPa (Theatre Canyon – Silicic)

2.6.2 Workflow Recommendation

2.6.2.1 Capturing photographs for image analysis

The following list presents some recommendations on how to best capture photographs and record data in the field for visual analysis. The list is arranged in order of completeness, where having the “Basic” components are sufficient to carry out image analysis using the methodology presented in this chapter. The rule of thumb is that more information is better.

- **Basic/Good:** GPS coordinates of where photos were taken, direction in which photograph was taken, field notes (stand-out features on outcrop) and clear satellite imagery of field area. Medium to high-resolution photographs are fine to use, provided that the standout features on the outcrop can be traced and picked out from the photograph
- **Better:** Camera with geotagging function, high-resolution photographs for accurate positioning and tracing, clear satellite imagery, Comprehensive EXIF data from camera: Zoom level, altitude, GPS, time taken, etc. Having detailed field notes recording this information and having detailed field sketches help to better inform the image analysis software when the images are being processed for analysis
- **Best:** All of the above, with ground control points and high resolution satellite imagery of the field area

2.6.2.2 Image processing using ImageJ

The following list presents some recommendations on how best to process images using image analysis software, ImageJ:

- **Input:** It is important to note that while ImageJ is a useful tool for image analysis, it only works as well as the input received. Therefore, it is important to isolate the

individual components of the photograph as carefully as possible, especially with images with a lower resolution. High resolution photographs provide more wiggle room when tracing due to its high pixel density.

- Make use of ImageJ's Threshold function: Establish a colour palette and the colours for individual components in the image. This makes it easy for ImageJ to pick out the individual components and easy for users to visually pick out the individual components from the photograph.
- Measuring: There are multiple ways to measure the same thing. Identify which way works best (factoring in run-time, etc.) For example: Length and thickness of an intrusion can be measured manually using the line tool, but can also be estimated using the Major and Minor ellipse axes.

2.7 Conclusion and Future Work

ImageJ is an incredibly useful tool for image analysis and can be used for a wide range of analyses, but the output depends highly on the input (tracing accuracy, choice of parameters, etc.) The methodology presented in this chapter can be used as a base for researchers to carry out image analysis on their own field photographs to extract data relevant to their studies. For example, the models presented in this chapter only take into consideration the geometric parameters of the intrusions (length and thickness), the Young's modulus of the and the Poisson's ratio. This is not entirely representative of the natural system and therefore future models should also take into consideration the fluid dynamics of the intruding magma.

2.8 Chapter References

- Altenberger, U., Oberhänsli, R., Putlitz, B., Wemmer, K., 2003. Tectonic controls and Cenozoic magmatism at the Torres del Paine, southern Andes (Chile, 51 degrees 10'S). *Rev. geológica Chile* 30, 65–81.
- Baker, D.R., Polacci, M., LaRue, A., 2011. A study on the reproducibility of counting vesicles in volcanic rocks. *Geosphere* 7, 70–78.
- Daniels, K.A., Kavanagh, J.L., Menand, T., Sparks, R.S.J., 2012. The shapes of dikes: Evidence for the influence of cooling and inelastic deformation. *Bull. Geol. Soc. Am.* 124, 1102–1112.
- Geshi, N., Kusumoto, S., Gudmundsson, A., 2012. Effects of mechanical layering of host rocks on dike growth and arrest. *J. Volcanol. Geotherm. Res.* 223–224, 74–82.
- Kavanagh, J.L., Sparks, R.S.J., 2011. Insights of dyke emplacement mechanics from detailed 3D dyke thickness datasets. *J. Geol. Soc. London.* 168, 965–978.
- Kusumoto, S., Geshi, N., Gudmundsson, A., 2013. Aspect ratios and magma overpressures of non-feeder dikes observed in the Miyake-jima volcano (Japan), and fracture toughness of its upper part. *Geophys. Res. Lett.* 40, 1065–1068.
- Leuthold, J., Muntener, O., Baumgartner, L.P., Putlitz, B., 2014. Petrological Constraints on the Recycling of Mafic Crystal Mushes and Intrusion of Braided Sills in the Torres del Paine Mafic Complex (Patagonia). *J. Petrol.* 55, 917–949.
- Leuthold, J., Muntener, O., Baumgartner, L.P., Putlitz, B., Chiaradia, M., 2013. A detailed geochemical study of a shallow arc-related laccolith; the Torres del Paine mafic complex (Patagonia). *J. Petrol.* 54, 273–303.

- Leuthold, J., Müntener, O., Baumgartner, L.P., Putlitz, B., Ovtcharova, M., Schaltegger, U., 2012. Time resolved construction of a bimodal laccolith (Torres del Paine, Patagonia). *Earth Planet. Sci. Lett.* 85–92.
- Lewis, T., Francus, P., Bradley, R.S., Kanamaru, K., 2010. An automated system for the statistical analysis of sediment texture and structure at the micro scale. *Comput. Geosci.* 36, 1374–1383.
- Li, H.B., Zhao, J., Li, T.J., 1999. Triaxial compression tests on a granite at different strain rates and confining pressures. *Int. J. Rock Mech. Min. Sci.* 36, 1057–1063.
- Michel, J., Baumgartner, L., Putlitz, B., Schaltegger, U., Ovtcharova, M., 2008. Incremental growth of the Patagonian Torres del Paine laccolith over 90 k.y. *Geology* 36, 459–462.
- Müntener, O., Ewing, T., Baumgartner, L.P., Manzini, M., Roux, T., Pellaud, P., Allemann, L., 2018. Source and fractionation controls on subduction-related plutons and dike swarms in southern Patagonia (Torres del Paine area) and the low Nb/Ta of upper crustal igneous rocks. *Contrib. to Mineral. Petrol.* 173, 38.
- Poland, M.P., Moats, W.P., Fink, J.H., 2008. A model for radial dike emplacement in composite cones based on observations from Summer Coon volcano, Colorado, USA. *Bull. Volcanol.* 70, 861–875.
- Pollard, D.D., Muller, O.H., 1976. The effect of gradients in regional stress and magma pressure on the form of sheet intrusions in cross section. *J. Geophys. Res.* 81, 975–984.
- Sanger, M.C., 2015. Determining depositional events within shell deposits using computer vision and photogrammetry. *J. Archaeol. Sci.* 53, 482–491.
- Westoby, M.J., Brasington, J., Glasser, N.F., Hambrey, M.J., Reynolds, J.M., 2012. “Structure-

from-Motion” photogrammetry: A low-cost, effective tool for geoscience applications.
Geomorphology 179, 300–314.

Wilson, T.J., 1991. Transition from back-arc to foreland basin development in the southernmost Andes: stratigraphic record from the Ultima Esperanza District, Chile.
Geol. Soc. Am. Bull.

Zhu, T.Y., 2012. Some Useful Numbers on the Engineering Properties of Materials (Geologic or Otherwise). GEOL 615. Stanford University, Stanford, California.

3 Characterisation of Gelatine as an Analogue Material for Modelling Magma Intrusion Growth in the Earth's Crust

3.1 Introduction

Analogue modelling is a very useful technique in Earth Sciences, where the processes studied can occur at a wide range of scales and across time periods of a few seconds to thousands or millions of years (Galland et al., 2015; J. L. Kavanagh et al., 2017; Kavanagh et al., 2013). Some processes also occur at depth and are obscured from direct observations, for example magma intrusion (Burchardt, 2018a; Kavanagh et al., 2017). Selection of appropriate analogue materials is of fundamental importance in analogue modelling (Galland et al., 2013; Kavanagh et al., 2017). Ideally, the material should be scaled geometrically, kinematically and dynamically (Hubbert, 1937). However, one common challenge to using analogue models is that there are limitations and simplifications that need to be made to model the complex behaviours of the Earth processes (Burchardt, 2018b).

Gelatine is a common term used to describe biopolymers which are naturally occurring long chain polymers of both plant (agar, carrageenan) and animal (porcine, bovine) origin (Di Giuseppe et al., 2009; van Otterloo and Cruden, 2016). Gelatine polymers have branches of hydrogen in their structure which can form bonds with water molecules making gelatine a hydrocolloid, a substance which forms a gel in the presence of water (Schrieber and Gareis, 2007). Gelatine polymers are flexible long chains that can assume a complex 3D structure upon solidification (Djabourov et al., 1988a). When gelatine is heated up in the presence of water (i.e. in a hot gelatine mixture) the long chains are broken (Djabourov et al., 1988b). When the gelatine mixture is cooled down, the gelatine polymers re-tangle to form a three-dimensional matrix (Ross-Murphy, 1992) changing the state from liquid gelatine to solid gelatine (Djabourov et al., 1993; Fairclough and Norman, 2003). Solid gelatine, which is in its

“gel state”, is characterised to behave elastically (van Otterloo and Cruden, 2016), which makes it a suitable analogue material to model geological processes in the Earth’s crust such as the simulation of shallow magmatic intrusions. A number of intrusive processes have been modelled using gelatine over the years, including but not limited to: the formation and evolution of dykes (e.g. Jackson and Pollard, 1988; Taisne and Tait, 2011; Takada, 1999), the formation of laccoliths (e.g. Hyndman and Alt, 1987; Jackson and Pollard, 1988), and the formation and propagation of sills (e.g. Kavanagh et al., 2006; Menand, 2008). The uses of gelatine however are not limited to modelling elastic regimes as gelatine exhibits a more complex material behaviour, showing a visco-elasto-brittle type rheology in its “gel state” and a viscous rheology in its liquid or “sol state” (Di Giuseppe et al., 2009). This range of rheological properties indicate that gelatine is a viscoelastic material. Viscoelastic materials such as gelatine display a delayed, time-dependent response when stress is applied or removed (Di Giuseppe et al., 2009; Kavanagh et al., 2013; van Otterloo and Cruden, 2016). Using a viscoelastic material such as gelatine in analogue modelling means a single analogue material can be utilised to model various processes of the Earth just by altering the mechanical properties to be more viscous or more elastic as needed. Another property which makes gelatine a favoured analogue material is that gelatine is photo-elastic (Kavanagh et al., 2018; Taisne and Tait, 2011), which means that internal stresses of deformed gelatine can easily be visualized with the aid of a few polarizing sheets of polarising film (similar to the polarising filters used in optical microscopes). Gelatine is also transparent which is useful in experiments which require real time observations, such as experiments studying the dynamics of magmatic intrusions in the Earth’s crust (Fiske and Jackson, 1972; Kavanagh et al., 2013; McLeod and Tait, 1999). Analogue models using gelatine are very easy to prepare and when properly scaled, can be tailored to suit various experimental needs (Merle, 2015).

Previous studies exploring the properties of gelatine have characterised gelatine for the following concentrations using various rheometric techniques (e.g. oscillation sweep,

amplitude sweep and temperature sweep): 1.0 wt.% - 4.0 wt.% gelatine (Di Giuseppe et al., 2009) and 1.0 wt.% - 10.0 wt.% (van Otterloo and Cruden, 2016). Kavanagh et al. (2013) have characterised gelatine by introducing different loads of known mass and dimensions onto the free surface of the gelatine solid (indentation method) for concentrations ranging between 2.0 wt.% and 30.0 wt.% gelatine. This chapter will elaborate on the characteristics of gelatine within the lower concentration range (1.0 wt.% to 3.5 wt.% gelatine) using both methods, the indentation method and rheometry, which will be used to inform analogue models of magma intrusion growth in Chapter 4. The characteristics of gelatine presented in this chapter will be beneficial to members of the Volcanic and Igneous Plumbing systems (VIPS) community by comparing results between different laboratories for benchmarking purposes to encourage reproducibility of experimental models.

3.2 Methodology and Experimental Setup

The following sub-sections will expand on the methods used to prepare the gelatine samples by first elaborating on the generic preparation method, followed by a detailed description of the different experimental setups used to measure the physical properties of gelatine (i.e. the indentation method and rheometry using a rotational rheometer).

3.2.1 Gelatine preparation

The gelatine mixture is prepared according to the methodology outlined by Kavanagh et al. (2013) using pig-skin gelatine powder supplied by Gelita UK (260 bloom, 10 mesh). The specific amount of gelatine powder used for different concentrations of gelatine (C_{gel}) can be calculated using Equation 3.2 (simplified from Equation 3.1) where M_w is the mass of water (g), M_g is the mass of gelatine powder (g) and M_t is the total mass of water and gelatine powder used (g). The experiments in this chapter will use gelatine with C_{gel} ranging between 1.0 wt.% and 3.5 wt.% gelatine.

$$C_{gel} (M_w + M_g) = M_g \quad [3.1]$$

$$C_{gel} (M_t) = M_g \quad [3.2]$$

The specific amount of water needed to dilute the gelatine to the desired concentration is calculated using Equation 3.3:

$$M_w = (100 - C_{gel})(M_t) \quad [3.3]$$

A hot concentrated mixture of gelatine powder and water is prepared by dissolving gelatine powder in half of the total mass of water at a temperature of approximately 80°C. Deionised water is used to inhibit the growth of bacteria in the gelatine (Kavanagh et al., 2013) which is crucial to ensure the longevity of the gelatine over the timescale of one week. The use of deionised water also ensures the reproducibility of this experiment, as there will be no impact from local water composition on the gelatine's properties (Djabourov et al., 1988b). The gelatine mixture is then stirred thoroughly to achieve a smooth consistency with no visible lumps. The mixture is left aside to cool and is covered to prevent dehydration. Once the mixture has cooled down to approximately 40°C, the hot mixture is then diluted with the remaining amount of deionised water, which has been chilled to 5°C, to achieve a mixing temperature (T_{mix}) of approximately 22.5°C. This temperature is ideal for transferring the gelatine mixture from the preparation containers into the individual experimental containers, as it is cool enough to handle comfortably and is close to the onset of gelling which begins at approximately 20°C such that gelling commences shortly after being placed into the experimental container (Kavanagh et al., 2017). The gelatine mixture is poured carefully into the experiment container to avoid creating bubbles on the surface of the gelatine. Any bubbles formed on the surface during this process are carefully removed using a metal spoon. A thin layer of vegetable oil is then added to the surface of the gelatine using a spoon, as this prevent a tough skin from forming on the surface of the gelatine which would otherwise form

due to dehydration. Lastly, the experimental containers are covered with plastic wrapping to prevent any agitation by the cooling fans in the refrigerator which could affect the homogeneity of the mixture. The time taken between pouring the mixture into the experimental containers to placing the containers in the refrigerator is kept short to keep the temperature as low as possible and as close to the onset of gelling as possible, and the mixture temperature once in the containers is measured. The gelatine is allowed to evolve at a constant temperature of 5°C over the course of one week (maximum), with a total timespan of no less than 140 hours (Kavanagh et al., 2013).

3.2.2 Classic scaling approach

The classic scaling approach by Hubbert (1937) covers three levels of scalability: geometric, kinematic and dynamic scaling. The scaling process makes use of a scale factor (often denoted with an asterisk after the parameter name, e.g. h^* or t^*) which is derived from the ratio between parameters present in the model to the parameters in nature. The model ratios are defined by the following fundamental units: Length [L], Time [T] and Mass [M] which are expressed as dimensionless numbers (Merle, 2015). The first level, geometric scaling, provides a comparison of size between the model and the natural system using the fundamental unit of Length [L]. A modelled object which is a replica of an existing object to size (upsized or downsized) is geometrically scaled. Examples of objects that are geometrically scaled are architectural models of buildings and miniature car models. While these models capture the exact shape and scaled size of their true-sized counterparts, the models do not capture the strength of the materials used to create them (Reber et al., 2020). The scaling factor for these models can be expressed using Equation 3.4 (Merle, 2015), where the ratio between the height of the model, h_m and the height of the natural object, h_n gives the scaling factor of h^* .

$$h^* = \frac{h_m}{h_n} \quad [3.4]$$

The next level of scaling is kinematic scaling, where a model is said to be kinematically similar to nature when it remains geometrically similar to nature during deformation. Kinematics focuses only on the movement of an object without regarding the forces that cause the object to move. Therefore this movement can be defined using fundamental units Length [L] and Time [T]. If properly scaled, the time taken to complete movement between the model and natural system are expected to be similar over the course of the experiment. This kinematic scaling can be expressed as scale factor t^* (Equation 3.5), the ratio between the time taken to complete the movement, t_m and the time taken to complete the movement in nature, t_n (Merle, 2015).

$$t^* = \frac{t_m}{t_n} \quad [3.5]$$

The third and most advanced level of scaling is dynamic scaling, where the driving forces in the model and the natural system are dynamically similar (Merle, 2015; Reber et al., 2020). For example, if the natural system is affected by forces of gravity F_{ng} and inertia F_{ni} , then the modelled system should also be affected by forces of gravity F_{mg} and inertia F_{mi} as shown in Equation 3.6.

$$F^* = \frac{F_{mg}}{F_{ng}} = \frac{F_{mi}}{F_{ni}} \quad [3.6]$$

Force (Unit: kg m s⁻²) can be defined using the three fundamental units Length [L], Time [T] and Mass [M] as [MLT⁻²]. Mass plays an especially important role in calculations of force and therefore must also be scaled appropriately using scale factor m^* (Equation 3.7) which is the ratio of mass between the model, m_m and the natural system, m_n (Merle, 2015).

$$m^* = \frac{m_m}{m_n} \quad [3.7]$$

Different models require the use of different scale factors which are more specific to the experiment being carried out. This can be done by defining the desired parameter using their

fundamental units (e.g. Force = $[MLT^{-2}]$, Density = $[ML^{-3}]$, etc.). It is important to note that the scaling guide presented in this section is hierarchal, whereby for an experiment to be dynamically scaled, it must first be both geometrically and kinematically scaled to nature (Reber et al., 2020).

3.2.3 Scaling of Gelatine

The previous section has highlighted the different levels of scaling using the classic scaling approach using the three fundamental scaling factors of length, time and mass. For an experiment to be properly scaled to its natural counterpart according to this approach, it would require the definition of all three of these scaling factors. (Hubbert, 1937; Merle, 2015; Reber et al., 2020). As mentioned in the introduction to this chapter, the geological processes studied can occur at a wide range of scales and across time periods of a few seconds to thousands or millions of years (Galland et al., 2015; J. L. Kavanagh et al., 2017; Kavanagh et al., 2013) with some processes also occurring at depth and are obscured from direct observations, for example magma intrusion (Burchardt, 2018a; Kavanagh et al., 2017). The process of scaling therefore allows for geological processes to be modelled and studied in the laboratory within the working time of the researcher (Galland et al., 2015). The scaling of gelatine to model the growth of intrusions in the Earth's crust has been previously investigated by Kavanagh et al. (2013) and has been used as the key reference for other laboratory experiments which use gelatine as the host rock analogue.

The approach by Kavanagh et al. (2013) defines a series of scale factors built on the assumption that the length scale of the fracture is defined by its buoyancy length (L_b). This length refers to the length of the fracture at which the buoyancy forces balance the resistive forces of the fracture as expressed in Equation 3.8 (Taisne and Jaupart, 2009) where K_c is the fracture toughness and $\Delta\rho$ is the difference in density between the injected fluid and its host material.

$$L_b = \left(\frac{K_c}{\Delta\rho}\right)^{2/3} \quad [3.8]$$

Using this equation, Kavanagh et al. (2013) defined four scale factors: Length (L^*), Time (T^*), Velocity (U^*) and Stress (E^*). The four scale factors are defined individually below, where the subscript m refers to model, subscript n refers to the natural system, ρ_{solid} is the density of the host material and ψ is the thickness of the intrusion:

$$L^* = \frac{L_m}{L_n} = \left(\frac{K_c^*}{\Delta\rho^*}\right)^{2/3} \quad [3.9]$$

$$T^* = \frac{T_m}{T_n} = \rho_{solid}^{*\frac{1}{2}} K_c^{*\frac{1}{3}} (\Delta\rho)^{-\frac{5}{6}} \quad [3.10]$$

$$U^* = \frac{U_m}{U_n} = (\Delta\rho^*)^{\frac{1}{6}} K_c^{*\frac{1}{3}} \rho_{solid}^{*\frac{1}{2}} \quad [3.11]$$

$$E^* = \frac{E_m}{E_n} = \Delta\rho^* L_b^* \left(\frac{L_b}{\psi}\right)^* \quad [3.12]$$

The experiments conducted by Kavanagh et al. (2013) show that for experiments with a concentration between 2.0-5.0 wt.% carried out at a temperature of 5-10°C will have the scale factors defined as follows:

- $L^* = 2 \times 10^{-3}$, where 1 m of the experimental dyke is equivalent to 500 m in a natural system
- $T^* = 9 \times 10^{-2}$, where 1 second of the experiment is equivalent to 11 seconds in a natural system
- $U^* = 2 \times 10^{-2}$, where 0.001 m/s in the experiment is equivalent to 0.05 m/s in a natural system
- $E^* = 2 \times 10^{-6}$ to 2×10^{-5} , where the Young's modulus spans between 2000-3000 Pa in the experiments which corresponds to natural rocks with Young's modulus of 0.1-1.5 GPa

All of the values above which are geologically reasonable show how the experiment has been successfully scaled geometrically (L^* , which carries the fundamental unit [L]) kinematically (U^* , relating fundamental units [L] and [T]) and dynamically (E^* , using all three fundamental units [L], [T] and [M]). The representative experiments discussed in Chapter 4 are prepared using the methodology outlined by Kavanagh et al. (2013) with a similar range in concentration and temperatures. Therefore the scaling factors presented here are relevant and applicable to those experiments as well.

3.2.4 Indentation Experiment Setup

To measure the evolving Young's modulus of the gelatine solid, the indentation method (described by Kavanagh et al., 2013) is used. Experimental loads of known mass and dimensions (refer Table 3.1) are sequentially placed onto the surface of the gelatine, and the indentation that they cause is used to calculate the Young's modulus of the gelatine solid (Timoshenko and Goodier, 1970):

$$E = \frac{M_L g (1 - \nu^2)}{D_L w} \quad [3.13]$$

Where E is the Young's modulus (Pa), M_L is the mass of the experimental load (kg), g is the gravitational acceleration (9.81 ms^{-1}), ν is the Poisson's ratio for gelatine (0.5 (Crisp, 1952; Righetti et al., 2004; van Otterloo and Cruden, 2016)), D_L is the diameter of the load (m) and w is the displacement caused by the experimental load (m), calculated using Equation 3.14:

$$w = (x_1 + \beta) - x_0 \quad [3.14]$$

x_1 is the displacement of the gelatine measured with the experimental load placed on top of the surface, β is the thickness of the experimental load and x_0 is the initial measurement taken to the surface of the gelatine without the experimental load. A schematic diagram showing how the deflection is measured for this set of calculations is shown in Figure 3.1.

Table 3.1: Properties of the loads used in the Young's Modulus experiments. D_L is the diameter of the experimental load (m), β is the thickness of the experimental load (m) and M_L is the mass of the experimental load (kg)

Load	Material	Diameter, D_L (mm)	Thickness, β (mm)	Mass, M_L (kg)
MO1	Aluminium	25.11	12.29	0.0164
MO2	Aluminium	25.11	9.27	0.0124
MO3	Brass	25.02	12.05	0.0501
MO4	Brass	25.02	10.07	0.0418

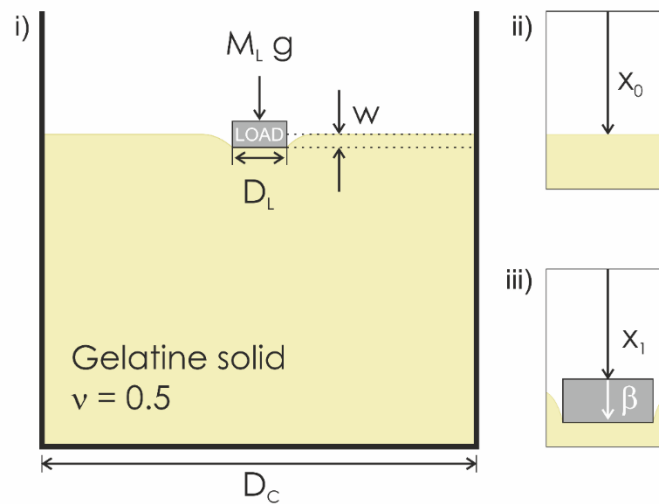


Figure 3.1: (i) Schematic diagram showing the indentation method to measure the Young's Modulus of gelatine from the deflection of the surface of the gelatine by a load of known mass and dimensions (modified after Kavanagh et al., 2013) where E is the Young's Modulus (Pa), M_L is the mass of the load (kg), g is the gravitational acceleration (9.81 ms^{-1}), ν is the Poisson's ratio for gelatine (0.5), D_L is the diameter of the load (m), D_C is the diameter of the container (m) and w is the displacement caused by

the load (w) which is calculated. To calculate w , the measurements needed are x_0 (ii) which is the initial measurement to the surface of the gelatine (m) and (iii) the displacement caused, measured with the load on top, x_1 (m) as well as the thickness of the load, β (m).

The gelatine solid is prepared as described in Section 3.2.1 and portioned into three experimental tanks of equal size (0.2 m in diameter, D_C and 0.2 m in height) as shown in Figure 3.2. These are then filled with volumes (V_{gel}) of 2 litres (7.0 cm height), 3 litres (10.5 cm height) and 4 litres (14.0 cm height) of gelatine. The temperature reading taken immediately after the mixture is diluted with cold deionised water is denoted as T_{mix} . The starting time at which the gelatine is left to cool in the refrigerator is recorded as t_0 and the temperature of the gelatine at the starting time is recorded as T_0 .

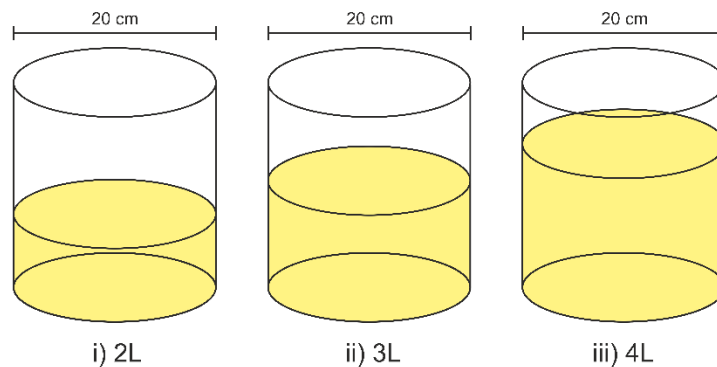


Figure 3.2: Illustration showing the volume and height of gelatine in each experimental tank measuring 0.2 m in diameter and 0.2 m in height. The height of the gelatine solid in each tank is as follows: (i) 2L, $h = 7.0$ cm, (ii) 3L, $h = 10.5$ cm, (iii) 4L, $h = 14.0$ cm.

Measurements of the Young's modulus commences once the gelatine has gelled and is able to support the experimental loads on its free surface (Young's modulus approximately 1000 Pa). Before taking the initial reading, the thin layer of oil protecting the surface is carefully removed. Most of the oil can be easily removed by using a metal spoon. However, it is recommended to use tear-resistant paper towels (2 or 3-ply) in addition to the use of the metal spoon to remove any excess oil on the surface. This additional step ensures that there

is complete contact between the surface of the gelatine and the experimental load placed on top of it.

Each container is taken out of the refrigerator for no longer than 10 minutes at a time to ensure that the temperature at which the measurements are taken is at a constant $5^{\circ}\text{C} \pm 1^{\circ}\text{C}$, which allows for the study of the evolution of gelatine over time with a constant base temperature. Three consecutive measurements of surface deflection are taken for each experimental load placed on the surface of the gelatine. The average of these three measurements are used to calculate the Young's modulus value.

These readings are taken every one to two hours (when possible) for up to a minimum of 150 hours (over 6 days).

3.2.5 Rotational Rheometer Setup

The rheological properties of a gelatine can be defined by its storage and loss moduli, denoted G' and G'' respectively (Mezger, 2009). An increase in both G' and G'' values over time illustrate the continuous evolution within the gelatine structure. When a stable structural arrangement is met within the gelatine, the G' and G'' values plateau, with the onset of the plateau marked as the curing time (Di Giuseppe et al., 2009). Gelatine mixtures of different concentrations achieve stability at different times. These properties can be measured using a rotational rheometer.

The Haake Mars III rotational rheometer (Thermo Fisher) was used to test the gelatine's properties in two phases: 1) An oscillation time sweep, which collects data on the evolution of mechanical properties of gelatine over a set amount of time under constant shear stress of 1 Pa, followed by 2) an amplitude sweep, which observes the change in mechanical properties under increasing rotational shear stress (0.01-10000 Pa). Both phases of the experiments were carried out in succession on the same sample by implementing the use a

35 mm parallel plate head geometry with a fixed gap between the head and the sample plate of 0.5 mm (Figure 3.3 (i)). Samples with a low concentration of gelatine (1.0 wt.% and 1.5 wt.% gelatine) were analysed using a 60 mm cone plate head geometry, which tapers at 1° from its circular base, as the increased surface area of contact is more sensitive for low viscosity fluids. When lowered, the tip of the cone head geometry approaches the centre of the sample plate as shown in Figure 3.3 (ii) with a gap of 0.052 mm. The Haake Mars III Rheometer is operated by the software 'RheoWin Job Manager' and 'RheoWin Data Manager' is used to display the measurement data for quantitative analysis.

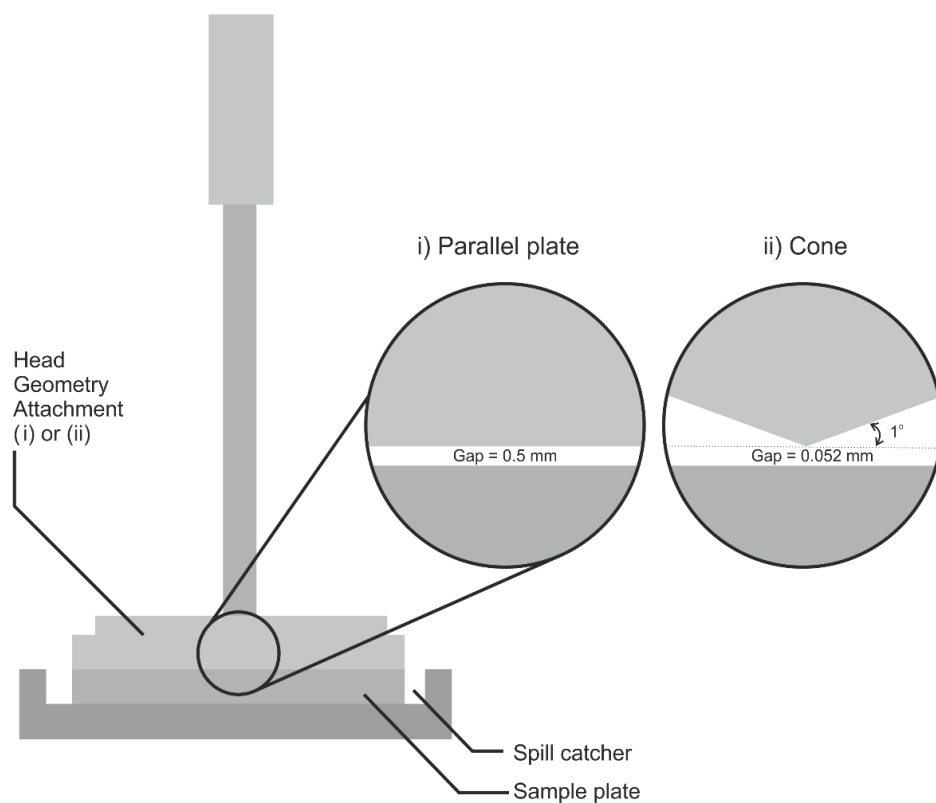


Figure 3.3: Schematic diagram of the rheometer setup. The zoom bubble shows two geometries used in these experiments: (i) The P35 Ti L 35 mm parallel plate head geometry with a fixed gap of 0.5 mm between the head and the sample plate and (ii) the P60/ 1° Ti L 60 mm cone plate head geometry which tapers at 1° from its circular base with a gap of 0.052 mm. The sample is loaded on the sample plate which is static and the head geometry is lowered down onto the sample plate. The sample then fills the gap between the head geometry and the sample plate.

3.2.6 Data Processing

Identifying the sources of uncertainty and quantifying all errors associated is an important step before carrying out any form of data analysis. For these experiments, it is especially important to identify the uncertainties and their sources early on as hundreds of individual readings are collected for each experiment. Two steps were taken to process the data before modelling the experimental results: 1) Quantifying the propagation of errors to show how the errors evolve over time (Section 3.2.4.1) and 2) Weighting the data to emphasize the effects of different loads on the modelled experimental results (Section 3.2.4.2).

3.2.6.1 Propagation of Errors

The differences in the mass of the load, the diameter of the load and the deflection caused by the load, collectively contribute to the compound uncertainty associated with the Young's modulus value measured (see Equation 3.13). The relative errors associated with the calculation of Young's modulus values, E can be expressed using Equation 3.15 below:

$$\frac{\Delta E}{E} = \frac{\Delta M_L}{M_L} + \frac{\Delta D_L}{D_L} + \frac{\Delta w}{w} \quad [3.15]$$

Where Δ is the absolute error associated with each parameter and the uncertainties related to w are influenced by the readings for x_0 , x_1 and β (Equation 3.14). All measurements of x_0 and x_1 are made three times in succession and the average value is used in the calculations in each experimental setup using Equation 3.13.

3.2.6.2 Weighting Data

Previous studies have shown how different experimental loads create different amounts of surface deflection, as heavier loads deflect the surface of the gelatine solid more than their lighter counterparts (Kavanagh et al., 2013). This must be considered when analysing the data as a whole as the error associated with the measurement of the deflection is the same

for each load, but the relative error is greater for light loads. For the relative uncertainties associated with each Young's modulus measurement to be accounted for during analysis, the data has been weighted. The weighting criteria are qualitatively based on load weight (Table 3.2) and quantitatively based on the relative error $\Delta E/E$ (Table 3.3). The lightest load (MO2) is given the lowest weighting value of 1 and the heaviest load (MO3) is given the highest weighting value of 4. A cumulative weighting (W_T) summing the qualitative and quantitative weightings is then created, and subsequently used to create trendlines through E data with a weighted fit.

Table 3.2: Qualitative weighting protocol based on the uncertainties produced by each load. The lightest load is given a weighting value of 1 (MO2) and the heaviest load is given a weighting value of 4 (MO3).

LOAD	W_L
MO1	2
MO2	1
MO3	4
MO4	3

Table 3.3: Quantitative weighting protocol based on the calculated values of $\Delta E/E$ (%). 1 represents the lowest weighting and 5 represents the highest weighting.

$\Delta E/E$ (%)	$W_{\Delta E/E}$
<5	5
5-10	4
10-20	3
20-50	2
>50	1

3.3 Results

3.3.1 Indentation Experiment

18 experiments have been carried out in total (see Table 3.4) with varying gelatine concentrations and volumes. In the following sub-sections, the results from example experiments which best illustrate the correlation between the concentration of the gelation solid (C_{gel}), the volume of gelatine in each experimental container (V_{gel}) and the calculated Young's modulus value (E) over time, are described.

3.3.1.1 Effect of Time

Figure 3.4 shows the evolution of Young's modulus values for 4-litres of 2.0 wt.% gelatine (Experiment 9) at 5°C over time as measured using different loads of known masses and dimensions (see Table 3.1). The error bars show the growing uncertainties of E with time, where the error bars are smaller at the beginning of the experiment and bigger as it approaches the end of the experiment. There is also a visual correlation observed between the size of the error bars and the experimental loads used. Comparing the error bars produced by loads MO2 (the lightest load) and MO3 (the heaviest load), it is observed that the error bars are larger in experiments using the load MO2 than the ones using load MO3. This is because the Young's modulus values calculated rely on the amount of deflection created by the load. At the end of each experiment when the gelatine solid is "stiffer", loads MO1 and MO2 are simply too light to create a significant amount of deflection to provide the appropriate readings for Young's modulus calculations. Loads MO3 and MO4 however are still able to deflect the surface of gelatine, which allows for better measurements to be taken, which provides more accurate calculated Young's modulus values.

Table 3.4: Summary of the experimental conditions. C_{gel} is the concentration of gelatine used in wt.%, V_{gel} is the volume of gelatine used in litres. T_{mix} denotes the temperature of the mixture when the hot gelatine concentrate is diluted with cold water. T_0 is the temperature of the mixture as it is placed in the refrigerator and the clock is started (t_0). The temperature of the refrigerator (T_R) is kept constant at 5°C throughout the experiment and all experimental tanks have a diameter of 20 cm (D_C)

Experiment	C_{gel} (wt.%)	V_{gel} (L)	T_{mix} (°C)	T_0 (°C)	T_R (°C)	D_C (m)
1	1.0	2	23.0	22.5	5	0.2
2	1.0	3	23.0	22.5	5	0.2
3	1.0	4	23.0	22.5	5	0.2
4	1.5	2	22.5	22.0	5	0.2
5	1.5	3	22.5	22.0	5	0.2
6	1.5	4	22.5	22.0	5	0.2
7	2.0	2	22.0	21.0	5	0.2
8	2.0	3	22.0	21.0	5	0.2
9	2.0	4	22.0	21.0	5	0.2
10	2.5	2	23.0	22.0	5	0.2
11	2.5	3	23.0	22.0	5	0.2
12	2.5	4	23.0	22.0	5	0.2
13	3.0	2	23.0	21.5	5	0.2
14	3.0	3	23.0	21.5	5	0.2
15	3.0	4	23.0	21.5	5	0.2
16	3.5	2	22.0	21.0	5	0.2
17	3.5	3	22.0	21.0	5	0.2
18	3.5	4	22.0	21.0	5	0.2

Experiment 9: 2.0 wt.% Gelatine, 4 Litres

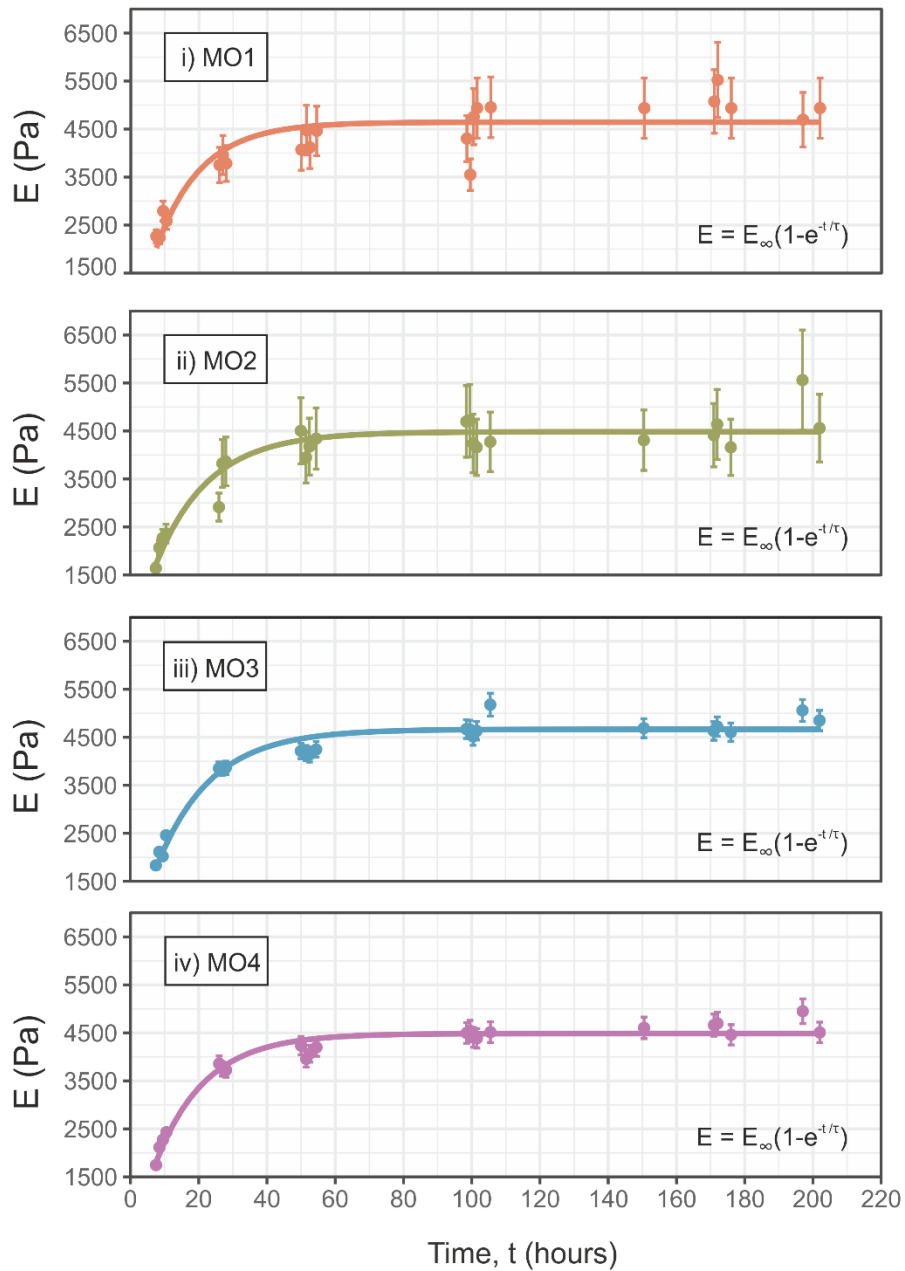


Figure 3.4: The evolution of Young's modulus values for 4-litres of 2.0 wt.% gelatine at 5°C over time as measured using loads (i) MO1, (ii) MO2, (iii) MO3 and (iv) MO4. The relationship between the Young's modulus values over time in this plot is best expressed using the exponential line of best fit $E = E_{\infty}(1 - e^{-t/\tau})$. Note that the trendlines are unweighted. The growing error bars illustrate the growing uncertainties in E over time associated with the different experimental loads applied to the surface of the gelatine solid.

Figure 3.5 shows the evolution of Young's modulus values over time for 4 litres of 2.0 wt.% gelatine at 5°C (Experiment 9). The first measurement was taken 5 hours into the experiment when the surface was able to support an experimental load. The Young's modulus value at this point is calculated to be approximately 1500 Pa. The plot illustrates how the Young's modulus values increase rapidly within the first 20 hours (approximately) before reaching a maximum plateau value where the Young's modulus is considered to be approximately constant and will no longer evolve with time, unless the experimental conditions are changed. This relationship between Young's modulus values and time can be expressed mathematically as shown in Equation 3.16:

$$E = E_{\infty} \left(1 - e^{-\frac{t}{\tau}}\right) \quad [3.16]$$

E is the calculated Young's modulus value (y-axis) and t is the time in hours (x-axis). E_{∞} (the Young's modulus plateau value, Pa) and τ (hours) are empirical values derived from the plotted line of best fit, which takes into account the weighting factor (W_T) discussed above. The values for E_{∞} and τ derived from the trendline in Figure 3.5 are 4579.55 Pa and 15 hours respectively. It is observed that E reaches the "effective plateau" of 4533.75 Pa ($0.99E_{\infty}$) at approximately 50 hours ($t_{0.99E_{\infty}}$).

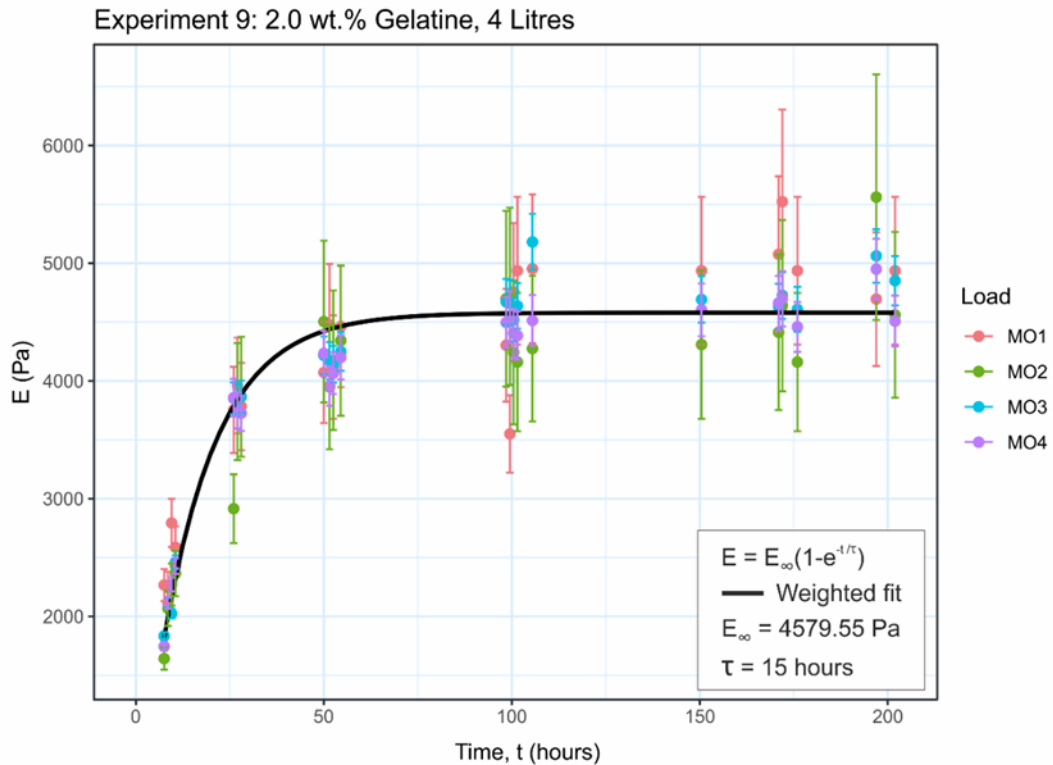


Figure 3.5: The evolution of Young's modulus values over time for 4-litres of 2.0 wt.% gelatine at 5°C (Experiment 9). The Young's modulus values were calculated using deflection measurements collected using loads MO1, MO2, MO3 and MO4 (See Table 3.1 for load properties). The relationship between the Young's modulus values over time in this plot is best expressed using the exponential line of best fit $E = E_{\infty}(1 - e^{-\frac{t}{\tau}})$ where $E_{\infty} = 4579.55$ Pa and $\tau = 15$ hours. The line is weighted using the weighting dataset (W_T) which takes into account W_{LOAD} and $W_{\Delta E/E}$ (Refer Tables 3.2 and 3.3)

3.3.1.2 Effect of Volume

Figure 3.6 shows the evolution of Young's modulus values of 2.0 wt.% gelatine at 5°C in experiments using three different volumes of gelatine: i) 2 litres (Experiment 7), ii) 3 litres (Experiment 8) and iii) 4 litres (Experiment 9), all measured using the same experimental load (MO3). The E_{∞} values for each plot derived from the line of best fit shows that there is not much difference in the evolution of Young's modulus values, despite the difference in volume between experiments, as the fitted E_{∞} values ranged by only approximately 100 Pa (at

4537.17 Pa, 4570.96 Pa and 4668.74 Pa, respectively). There is a notable difference between the τ values which are recorded at 9, 12 and 15 hours. These values correspond to the shape of the slope of each graph where Figure 3.6(i) has a tighter slope compared to Figure 3.6(iii). The “effective plateau” value ($0.99E_{\infty}$) on each graph (4491.79 Pa, 4525.25 Pa and 4622.05 Pa, respectively) reveals that it takes approximately 50 hours ($t_{0.99E_{\infty}}$) of curing time to reach material stability independent of V_{gel} . This shows that gelatine prepared using the same C_{gel} (2.0 wt.%) left to set at similar temperature ($T_0 = 5^{\circ}\text{C}$) evolve to reach a similar E_{∞} value and achieves “effective plateau” value ($0.99E_{\infty}$) at approximately the same time ($t_{0.99E_{\infty}} \approx 50$ hours), further emphasizing that volume does not have a significant impact on the evolution of Young’s modulus values.

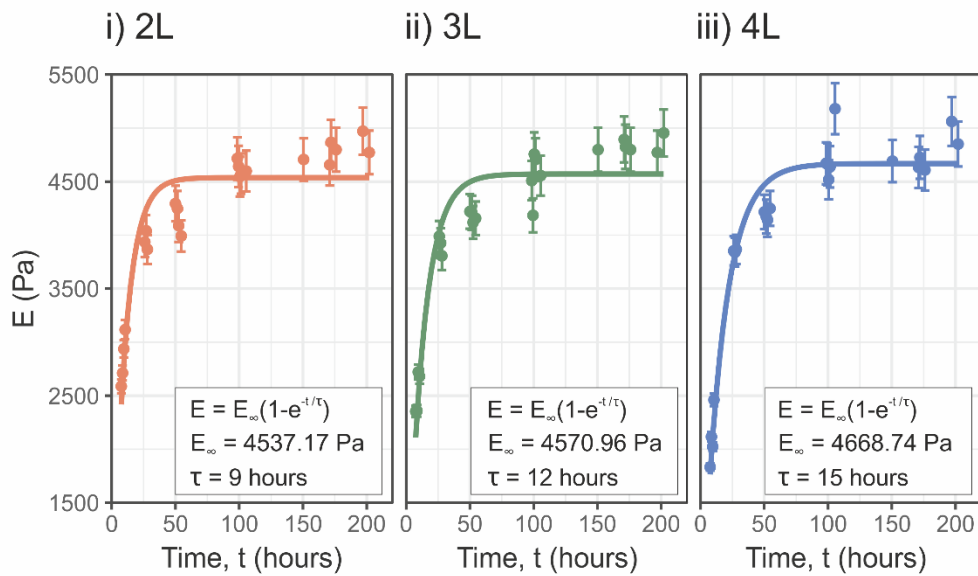


Figure 3.6: The evolution of Young’s modulus values in 2.0 wt.% gelatine at 5°C in Experiments 7, 8 and 9 using three different volumes of gelatine: i) 2 litres ($E_{\infty} = 4537.17$ Pa, $\tau = 9$ hours), ii) 3 litres, ($E_{\infty} = 4570.96$ Pa, $\tau = 12$ hours) and iii) 4 litres, ($E_{\infty} = 4668.74$ Pa, $\tau = 15$ hours) measured using the same experimental load (MO3).

3.3.1.3 Effect of Concentration

Figure 3.7 shows the evolution of Young's modulus values measured using experimental load MO3 across five different concentrations of gelatine: 1.5 wt.% (Experiment 6), 2.0 wt.% (Experiment 9), 2.5 wt.%, 3.0 wt.% (Experiment 15) and 3.5 wt.% (Experiment 18) gelatine at a fixed volume of 4 litres. The values for 2.5 wt.% gelatine are plotted using published data provided by Kavanagh et al. (2013) and is labelled accordingly. The plot illustrates a strong correlation between the Young's modulus plateau value (E_{∞}) and the concentration of gelatine used in the experiments. Experiments using a low concentration of gelatine, e.g. 1.5 wt.%, produce lower Young's modulus plateau values (approximately 2500 Pa). Experiments with a higher concentration of gelatine, e.g. 3.5 wt.%, produce higher Young's modulus plateau values (approximately 13,000 Pa).

The individual E_{∞} values of 4 litres of gelatine cured at 5°C can also be plotted against the different concentrations of gelatine to further support this correlation as shown in Figure 3.8. The plot shows a strong positive linear correlation ($R^2=0.9489$) between the concentration of gelatine used and their corresponding Young's modulus plateau values, showing that experiments with a higher concentration of gelatine reach a higher Young's modulus plateau value.

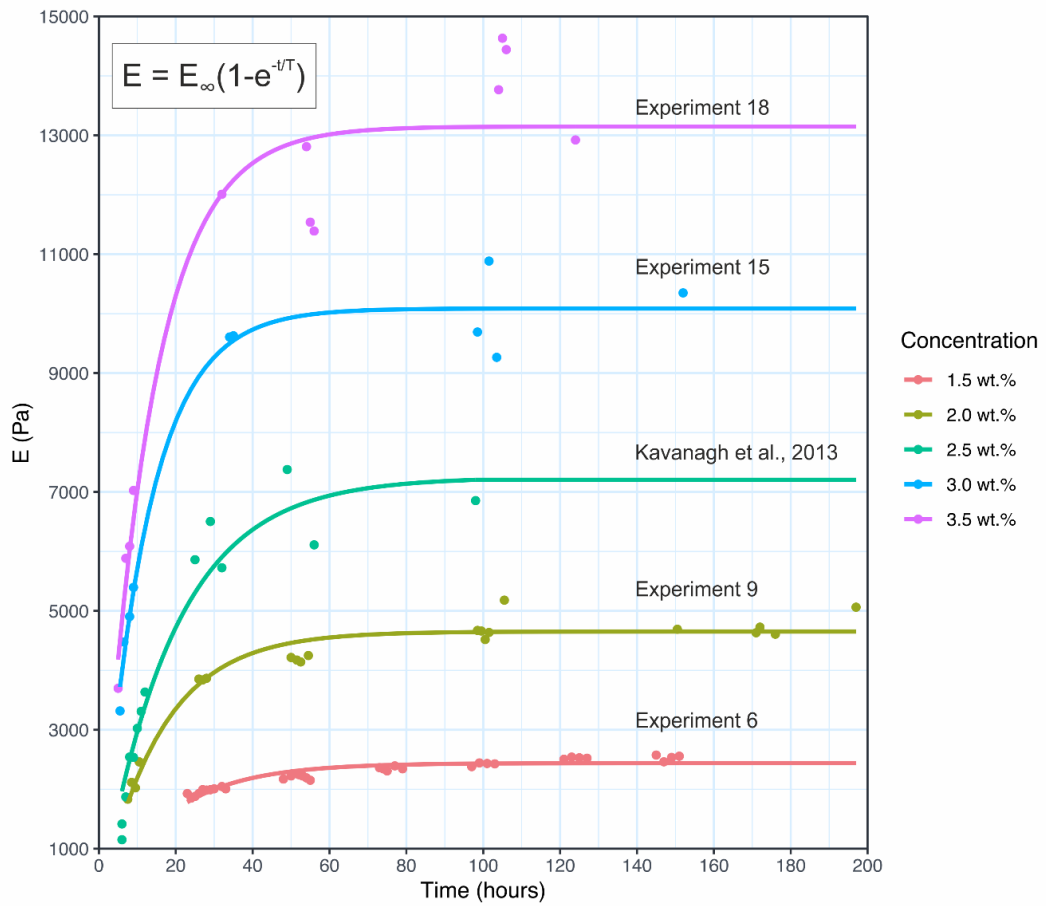


Figure 3.7: The evolution of Young's modulus values measured using experimental load MO3 across four different concentrations of gelatine: 1.5 wt.% (Experiment 6), 2.0 wt.% (Experiment 9), 2.5 wt.% (Kavanagh et al., 2013), 3.0 wt.% (Experiment 15) and 3.5 wt.% gelatine (Experiment 18) at a fixed volume of 4 litres. Higher E values are recorded in experiments with a higher concentration of gelatine. The trendlines are weighted using weighting dataset W_T and the equation for line of best fit is $E = E_{\infty}(1 - e^{-\frac{t}{T}})$. Error bars have been omitted for clarity.

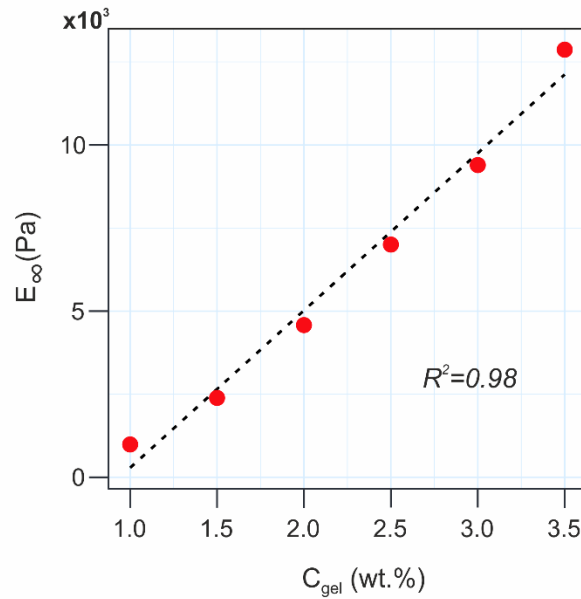


Figure 3.8: Young's modulus plateau values (E_{∞} , Pa) plotted against concentration of gelatine (wt.%) for experiments with volumes of 4 litres and a temperature of 5°C. The plot shows strong positive linear correlation with an R^2 value of 0.98, where E_{∞} increases with increasing concentration.

3.3.2 Rotational Rheology Experiments

16 experiments were carried out to study the mechanical properties of gelatine using the Haake Mars III rheometer (see Table 3.5 for experimental parameters). The following results will elaborate on 1) the stability of gelatine over time and 2) its elastic behaviour, both at two temperatures: 5°C and 10°C.

3.3.2.1 Gelatine Stabilisation Time: Oscillation Sweep Results

Figure 3.9 shows an example of the evolution of shear storage modulus, G' and shear loss modulus, G'' of a 2.5 wt.% gelatine sample for a duration of 10800 seconds (3 hours) at 5°C in an oscillation sweep experiment. The onset of the curing where a plateau of G' values forms on the plot is at approximately 3700 seconds (just over an hour) with a maximum G' value of under 10^3 Pa. These results match quite closely to the time recorded by Kavanagh

et al., 2013 for a similar setup (2.5 wt.% gelatine, 5°C) where material stability is achieved at approximately 3600 seconds into the experiment, where G' is approximately 10^3 Pa.

Figure 3.10 shows the evolution of G' and G'' (Pa) against time for all concentrations at 5°C in oscillation sweep tests. The results show that lower gelatine concentration mixtures take longer to achieve a stable structural arrangement. For example, the experiment with 1.0 wt.% gelatine (Figure 3.10 (i)) has a G' curve that appears to still be increasing at the end of the experiment (10800 seconds). However, by this time the experiment with 3.5 wt.% gelatine shows a more prominent plateau and the onset of stability is observed at approximately 3000 seconds.

Table 3.5: Experimental conditions for the rotational rheometer experiments. C_{gel} is the concentration of the gelatine used (wt.%), T is the fixed temperature ($^{\circ}\text{C}$) at which the gelatine is set to cool down to and t (s) is the total length of time in which the oscillation time sweep is conducted before the amplitude sweep begins.

Experiment	T ($^{\circ}\text{C}$)	C_{gel} (wt.%)	t (s)	Head Geometry
RP05-1A	5	1.0	10800	Parallel plate, P35 Ti L
RC05-1A	5	1.0	10800	Large cone, P60/1 $^{\circ}$ Ti L
RP05-1B	5	1.5	10800	Parallel plate, P35 Ti L
RC05-1B	5	1.5	10800	Large cone, P60/1 $^{\circ}$ Ti L
RP05-2A	5	2.0	10800	Parallel plate, P35 Ti L
RP05-2B	5	2.5	10800	Parallel plate, P35 Ti L
RP05-3A	5	3.0	10800	Parallel plate, P35 Ti L
RP05-3B	5	3.5	10800	Parallel plate, P35 Ti L
RP10-1A	10	1.0	10800	Parallel plate, P35 Ti L
RC10-1A	10	1.0	10800	Large cone, P60/1 $^{\circ}$ Ti L
RP10-1B	10	1.5	10800	Parallel plate, P35 Ti L
RC10-1B	10	1.5	10800	Large cone, P60/1 $^{\circ}$ Ti L
RP10-2A	10	2.0	10800	Parallel plate, P35 Ti L
RP10-2B	10	2.5	10800	Parallel plate, P35 Ti L
RP10-3A	10	3.0	10800	Parallel plate, P35 Ti L
RP10-3B	10	3.5	10800	Parallel plate, P35 Ti L

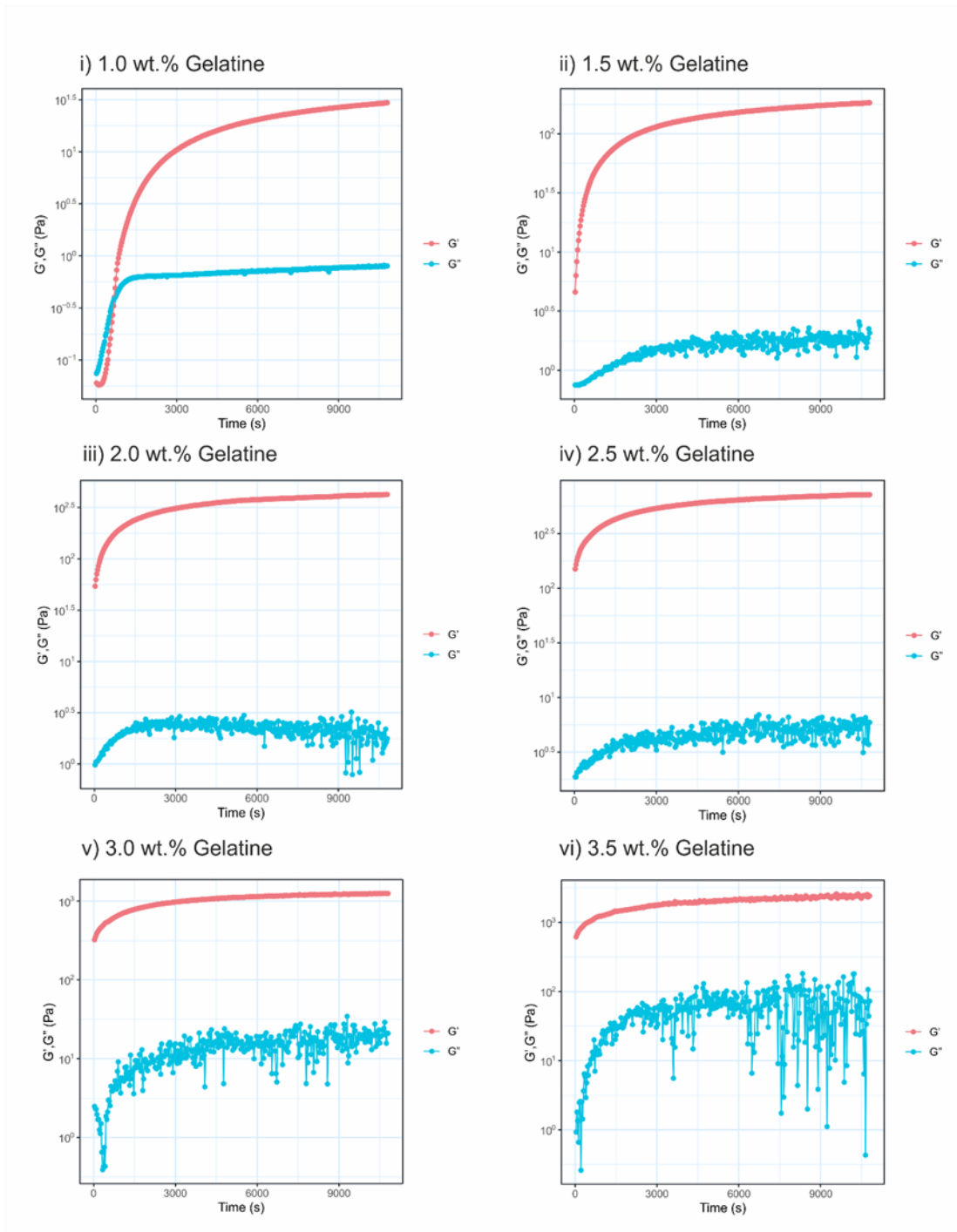


Figure 3.9: G' (shear storage modulus) and G'' (shear loss modulus) plotted against time (seconds) for gelatine at 5°C with concentrations: i) 1.0 wt.%, ii) 1.5 wt.%, iii) 2.0 wt.%, iv) 2.5 wt.%, v) 3.0 wt.% and vi) 3.5 wt.%. (Note the logged y-axis)

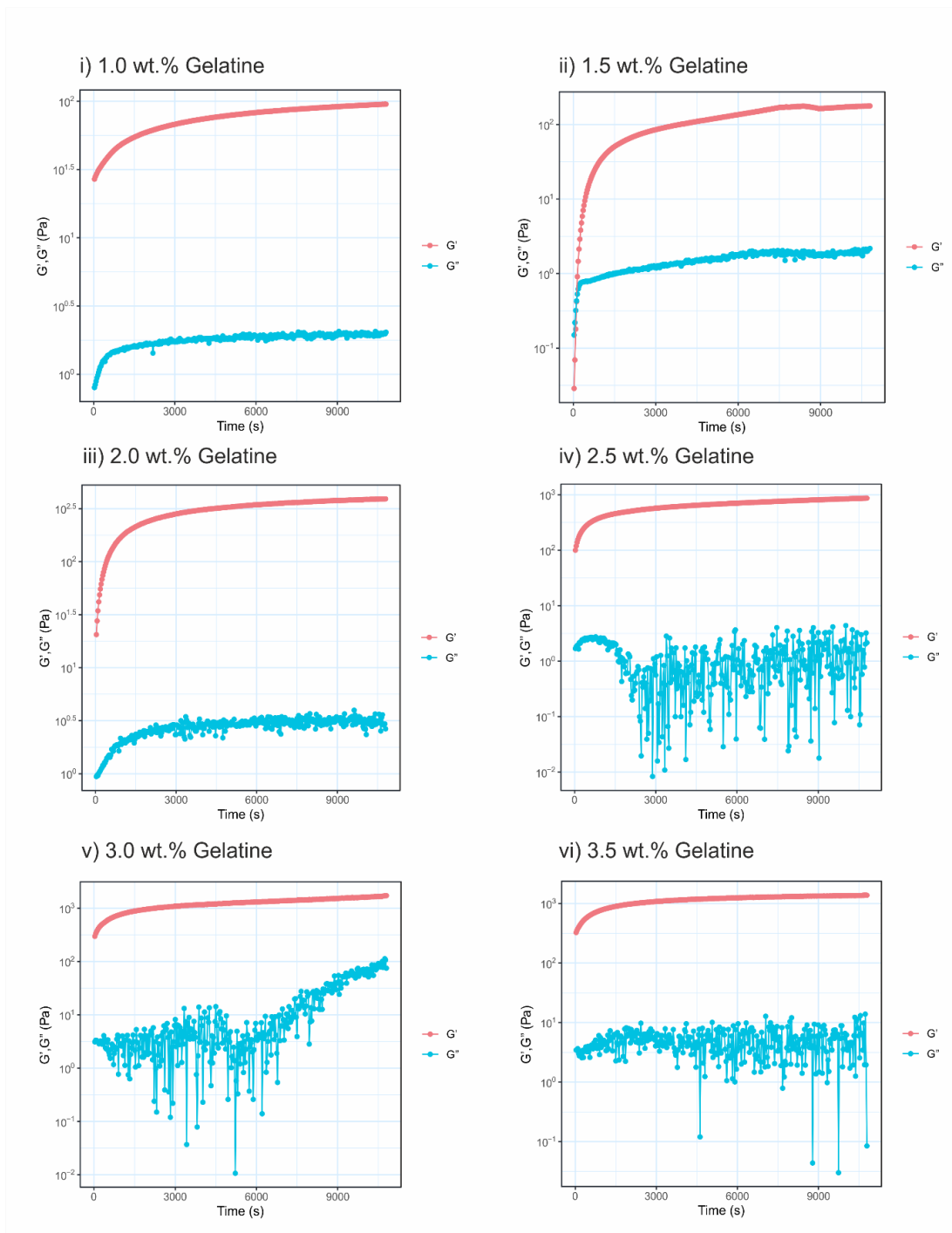


Figure 3.10: G' (shear storage modulus) and G'' (shear loss modulus) plotted against time (seconds) for gelatine at 10°C with concentrations: i) 1.0 wt.%, ii) 1.5 wt.%, iii) 2.0 wt.%, iv) 2.5 wt.%, v) 3.0 wt.% and vi) 3.5 wt.%. (Note the logged y-axis)

3.3.2.2 Gelatine Elastic Regime: Amplitude Sweep Results

The stress-strain evolution of the gelatine samples that was obtained in the amplitude sweep rheometer tests is illustrated in Figure 3.11. For all concentrations (1.0 wt.% - 3.5 wt.% gelatine) and both temperatures (5°C and 10°C) the results show a positive linear trend, indicating that the gelatine samples undergo almost perfect elastic deformation over time. As the material approaches its yield point, after which the material begins to accumulate permanent deformation, the gradient of the stress-strain relationship increases (from Strain $\approx 10^{-0.5}$). The failure of the gelatine occurs at Strain $\approx 10^{0.5}$, independent of the concentration or temperature. However, higher concentrations of gelatine require larger amounts of stress to reach the yield point. This level of stress is referred to as the yield stress. Higher concentrations of gelatine (e.g. 3.5 wt.%) will only reach its yield point when the applied stress is around 10^4 Pa. Lower concentrations of gelatine (e.g. 1.0 wt.%) require less applied stress, around $10^{2.5}$ Pa for the same amount of strain to reach a similar yield point. This shows that the yield stress increases with concentration of gelatine. At low gelatine concentration (1.0 wt.%), a low temperature resulted in a lower yield stress; however, this pattern was not observed at the higher concentrations where the linear elastic trend for both temperatures across all other concentrations (1.5 wt.%, 2.0 wt.%, 2.5 wt.%, 3.0 wt.% and 3.5 wt.%) are almost overlapping.

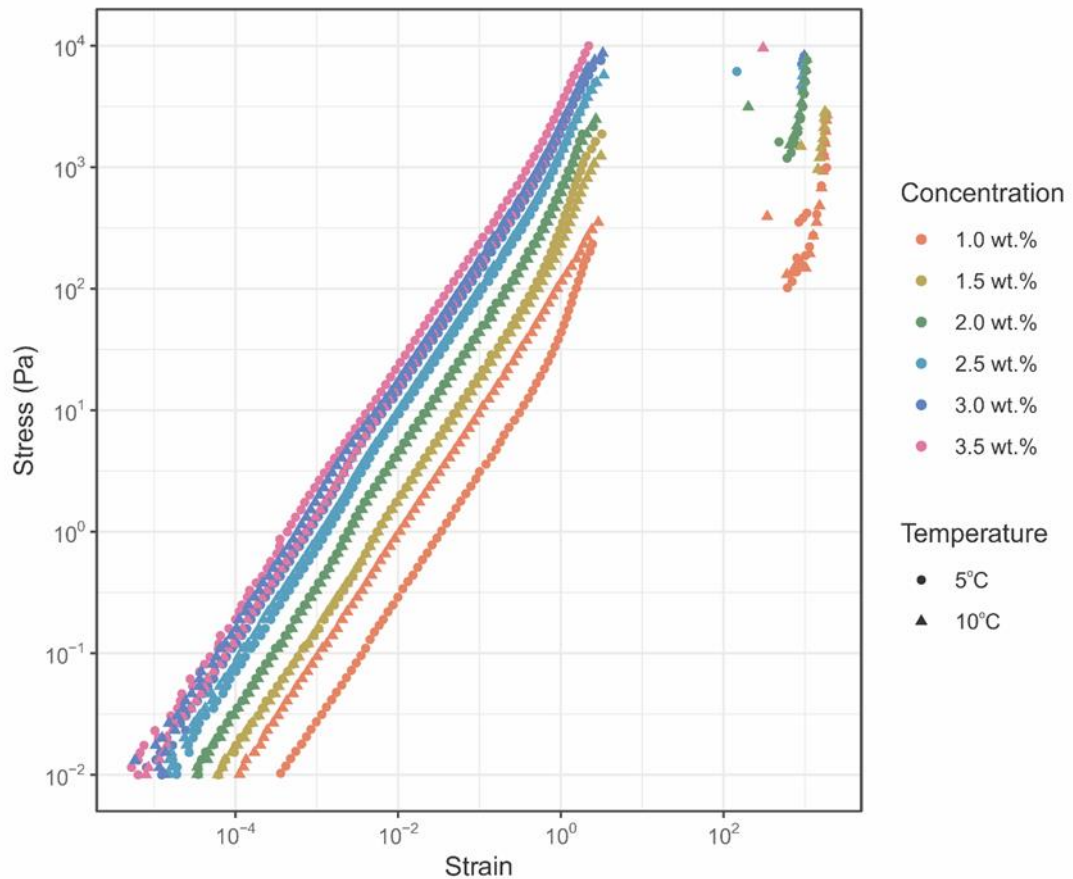


Figure 3.11: Rheometer amplitude sweep test results showing Stress vs. Strain of gelatine samples with different concentration (colours) and temperature (5°C = circles, 10°C = triangles).

3.4 Discussion

The results from these experiments are now compared with results from other experiments carried out by different research groups to check the validity of the results.

First, a direct comparison is made between the results of experiments using the indentation method. Kavanagh et al. (2013) concluded that the Young's modulus plateau value depends linearly on the concentration of gelatine showing an R^2 value of 0.9992. The results presented in this chapter show a similar strong linear relationship between the Young's modulus plateau value and the concentration of gelatine with an R^2 value of 0.9489 (Figure 3.8). Kavanagh et al. (2013) also highlights that at 5°C – 10°C, gelatine behaves as a solid with an

almost linear elastic deformation. This was proven to be true using the results from rotational rheometry for gelatine samples deformed at 5°C and 10°C, presented in Figure 3.11.

Next, a comparison is made between the results of experiments using a rotational rheometer (Di Giuseppe et al., 2009; Kavanagh et al., 2015; van Otterloo and Cruden, 2016). The results from both the oscillation sweep and amplitude sweep for 2.5 wt.% gelatine at 5°C (this chapter: Figure 3.9 (iv)) closely match the findings from Kavanagh et al. (2015) where during the oscillation sweep, the plateau of G' is reached at approximately 10^3 Pa in both laboratory setups. Both amplitude sweeps show a positive linear correlation between stress and strain where the material deforms elastically for strains up to 1 (10^0) at a maximum stress of 1000 Pa. This relationship is confirmed in this chapter, presented in Figure 3.11. Another comparison of results produced by oscillation sweep is done, comparing the data for 2.5 wt.% gelatine at 10°C by Di Giuseppe et al. (2009). The data presented shows that the onset of the plateau (material stability achieved) is at approximately 7500 seconds into the experiment. Results for the same experiment (Figure 3.10 (iv)) show the onset of the plateau to be approximately the same time, between a range of 7000-8000 seconds into the experiment. The results presented by Di Giuseppe et al. (2009) however, shows a higher maximum G' value at 10^4 Pa compared to the values presented in this chapter, 10^3 Pa. The experiments run by van Otterloo and Cruden (2016) had the longest running time for the oscillation sweep at 24 hours. However, the trendlines are very similar to the trendlines in this chapter, as well as the trendlines shown by Kavanagh et al. (2015) and Di Giuseppe et al. (2009) where the value of G' increases rapidly at the start of the experiment before hitting a plateau when the gelatine has achieved a stable arrangement. The comparison of these trends across different time scales ~2 hours (Kavanagh et al., 2015), 3 hours (this chapter), 6 hours (Di Giuseppe et al., 2009) and 24 hours (van Otterloo and Cruden, 2016) show that gelatine achieves material stability and has the ability to retain it over time unless acted upon by external forces. This information is particularly useful for preparation of layered elastic media to infer the Young's

modulus values or G' values based on the evolution of Young's modulus or G' values over time. Identifying the plateau value will provide modellers with a base time to work with when modelling with the assurance that the material has achieved a constant stiffness and is no longer evolving.

3.5 Conclusion

Results from characterising gelatine using the indentation method and rotational rheometry have both provided insights on the mechanical properties of gelatine as a crustal analogue. Similar trends are observed over time using both techniques where the gelatine continuously evolves over time until it reaches a stable arrangement and hits a plateau. Results from both techniques show that the concentration of the gelatine used affects the stiffness of the gelatine as well as the time taken to achieve a stable arrangement. Lower concentrations of gelatine are less stiff and take longer to achieve material stability while gelatine of higher concentrations are stiffer and achieve material stability faster. The results have been compared to other works in the literature and have proven to produce similar values to published works. This is evidence that the methods presented in the chapter are robust and can be reproduced in different laboratory settings provided that the same methodology is observed.

3.6 Chapter References

- Burchardt, S., 2018a. Chapter 1 - Introduction to Volcanic and Igneous Plumbing Systems—
Developing a Discipline and Common Concepts. In: Burchardt, S.B.T.-V. and I.P.S. (Ed.), .
Elsevier, pp. 1–12.
- Burchardt, S., 2018b. Chapter 12 - Synthesis on the State-of-the-Art and Future Directions in
the Research on Volcanic and Igneous Plumbing Systems. In: Burchardt, S.B.T.-V. and
I.P.S. (Ed.), . Elsevier, pp. 323–333.

- Crisp, J.D.C., 1952. The use of gelatin models in structural analysis. *Proc. Inst. Mech. Eng. Part B J. Eng. Manuf.* 1, 580–604.
- Di Giuseppe, E., Funicello, F., Corbi, F., Ranalli, G., Mojoli, G., 2009. Gelatins as rock analogs: A systematic study of their rheological and physical properties. *Tectonophysics* 473, 391–403.
- Djabourov, M., Leblond, J., Papon, P., 1988a. Gelation of aqueous gelatin solutions. I. Structural investigation. *J. Phys.* 49, 319–332.
- Djabourov, M., Leblond, J., Papon, P., 1988b. Gelation of aqueous gelatin solutions. II. Rheology of the sol-gel transition. *J. Phys.* 49, 333–343.
- Djabourov, M., Lechaire, J.P., Gaill, F., 1993. Structure and rheology of gelatin and collagen gels. In: *Biorheology*. pp. 191–205.
- Fairclough, J.P.A., Norman, A.I., 2003. Structure and rheology of aqueous gels. *Annu. Reports Prog. Chem. - Sect. C*.
- Fiske, R.S., Jackson, E.D., 1972. Orientation and Growth of Hawaiian Volcanic Rifts: The Effect of Regional Structure and Gravitational Stresses. *Proc. R. Soc. A Math. Phys. Eng. Sci.* 329, 299–326.
- Galland, O., Burchardt, S., Troll, V., 2013. Volcanic and Igneous Plumbing Systems: State-of-the-Art and Future Developments. *Eos (Washington. DC)*. 94, 2013.
- Galland, O., Holohan, E., van Wyk de Vries, B., Burchardt, S., 2015. Laboratory Modelling of Volcano Plumbing Systems: A Review. In: *Advances in Volcanology*. Springer Berlin Heidelberg, pp. 1–68.
- Hubbert, M.K., 1937. Theory of scale models as applied to the study of geologic structures.

Geol. Soc. Am. Bull. 48, 1459–1520.

Hyndman, D.W., Alt, D., 1987. Radial Dikes, Laccoliths, and Gelatin Models. *J. Geol.*

Jackson, M.D., Pollard, D.D., 1988. The laccolith-stock controversy: New results from the southern Henry Mountains, Utah. *Bull. Geol. Soc. Am.* 100, 117–139.

Kavanagh, J.L., Boutelier, D., Cruden, A.R., 2015. The mechanics of sill inception, propagation and growth: Experimental evidence for rapid reduction in magmatic overpressure. *Earth Planet. Sci. Lett.* 421, 117–128.

Kavanagh, J.L., Burns, A.J., Hilmi Hazim, S., Wood, E.P., Martin, S.A., Hignett, S., Dennis, D.J.C., 2018. Challenging dyke ascent models using novel laboratory experiments: Implications for reinterpreting evidence of magma ascent and volcanism. *J. Volcanol. Geotherm. Res.* 354, 87–101.

Kavanagh, Janine L., Engwell, S., Martin, S., 2017. A review of analogue and numerical modelling in volcanology. *Solid Earth Discuss.* 95194, 1–80.

Kavanagh, J.L., Menand, T., Daniels, K.A., 2013. Gelatine as a crustal analogue: Determining elastic properties for modelling magmatic intrusions. *Tectonophysics* 582, 101–111.

Kavanagh, J.L., Menand, T., J. Sparks, R.S., Sparks, R.S.J., 2006. An Experimental Investigation of Sill Formation and Propagation in Layered Elastic Media. *Earth Planet. Sci. Lett.* 245, 799–813.

Kavanagh, J. L., Rogers, B.D., Boutelier, D., Cruden, A.R., 2017. Controls on sill and dyke-sill hybrid geometry and propagation in the crust: The role of fracture toughness. *Tectonophysics* 698, 109–120.

McLeod, P., Tait, S., 1999. The growth of dykes from magma chambers. *J. Volcanol. Geotherm.*

Res. 92, 231–246.

Menand, T., 2008. The mechanics and dynamics of sills in layered elastic rocks and their implications for the growth of laccoliths and other igneous complexes. *Earth Planet. Sci. Lett.* 267, 93–99.

Merle, O., 2015. The scaling of experiments on volcanic systems . *Front. Earth Sci.* .

Mezger, T.G., 2009. The Rheology Handbook. *Pigment Resin Technol.* 38, 790–797.

Reber, J.E., Cooke, M.L., Dooley, T.P., 2020. What model material to use? A Review on rock analogs for structural geology and tectonics. *Earth-Science Rev.*

Righetti, R., Ophir, J., Srinivasan, S., Krouskop, T.A., 2004. The feasibility of using elastography for imaging the Poisson's ratio in porous media. *Ultrasound Med. Biol.* 30, 215–228.

Ross-Murphy, S.B., 1992. Structure and rheology of gelatin gels: recent progress. *Polymer (Guildf)*. 33, 2622–2627.

Schrieber, R., Gareis, H., 2007. *Gelatine Handbook: Theory and Industrial Practice*, *Gelatine Handbook: Theory and Industrial Practice*.

Taisne, B., Jaupart, C., 2009. Dike propagation through layered rocks. *J. Geophys. Res. Solid Earth* 114, B09203.

Taisne, B., Tait, S., 2011. Effect of solidification on a propagating dike. *J. Geophys. Res. Solid Earth* 116, B01206.

Takada, A., 1999. Variations in magma supply and magma partitioning: The role of tectonic settings. *J. Volcanol. Geotherm. Res.* 93, 93–110.

Timoshenko, S., Goodier, J.N., 1970. *Theory of Elasticity*. *J. Elast.*

van Otterloo, J., Cruden, A.R., 2016. Rheology of pig skin gelatine: Defining the elastic domain and its thermal and mechanical properties for geological analogue experiment applications. *Tectonophysics* 683, 86–97.

3.7 MAGMA Lab Gelatine Preparation: Quick Guide

The following recipe is to make 40 litres of 2.5 wt.% gelatine as done in the MAGMA Lab. The guide below is from the Geo Hub Liverpool Resources page, and was prepared by myself.

- HOW IT'S MADE -

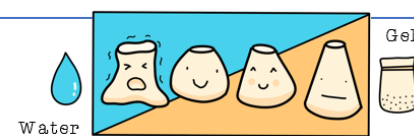
1) Weigh out the **gelatine powder** and **hot water** using the guide provided:

Gelatine to water ratio

Example:
Preparing 2.0 wt.% gelatine for a 40 L experimental tank

40 L = 40 kg = 40000 g

2.0 wt.% = $(2/100) * 40000 \text{ g} = 800 \text{ g}$




	800 g	Gelatine powder
	39200 g	Water
	40000 g	TOTAL

2) [**QUICKLY!**] Using enough **hot water** (~80°C) to wet all the **gelatine** granules, stir together to make a concentrated gelatine mixture

3) Continue to stir the concentrated gelatine mixture until smooth and there are no visible lumps

4) Top up with the remaining **water** to dilute the mixture. Mix well. (Tip: Add cold water at this stage to gradually bring the temperature down and help the gelatine set faster)

5) Carefully pour the mixture into the experimental tank. Remove all bubbles from the surface and cover with cling film for a smooth gelatine surface



3.7.1 Notes:

Gelatine powder:

- MAGMA Lab uses gelatine powder supplied by Gelita UK (260 bloom, 10 mesh)

Water:

- The best water to use is distilled/deionised water. This is to prohibit the growth of bacteria as some experiments could take longer than two days to prepare and could spoil and turn cloudy
- The following calculator is useful to calculate the ratio of hot water to cold water in order to reach the ideal cooling temperature:
http://www.onlineconversion.com/mixing_water.htm
- This is particularly important in experiments using tracer particles where the gelatine mixture needs to be stirred constantly until it reaches approximately 20°C, the onset of gelling, allowing the particles to be suspended throughout the gelatine.

4 Analogue Modelling of Surface Deformation Driven by Magma Movement at Depth

4.1 Introduction to Chapter

The previous chapter presented the results from two series of tests which were used to justify the suitability of gelatine as an analogue material. This chapter will delve into the development of a sophisticated laboratory experiment setup designed to monitor the propagation of sheet intrusions in three dimensions in real time. This setup is coupled with four imaging techniques to observe and quantify the formation of surface and subsurface deformation patterns induced by the propagation of dykes and sills (magma-filled fractures). Gelatine is used as an analogue material for the Earth's upper crust in these laboratory experiments.

4.2 Background

Ground deformation surrounding volcanic regions can be the surface manifestations of magma movement at depth. (Acocella and Mulugeta, 2001; Al Shehri and Gudmundsson, 2018; Galland, 2012). Before the advent of remote sensing, monitoring and research of volcanoes relied heavily on fieldwork to measure ground deformation, gas emissions and deposit characteristics (Pinel et al., 2014). Increased availability of geodetic measurements in volcanic regions today allow geoscientists to better mitigate hazards based on more detailed records of changes in surface topography recorded over time (e.g. Fukushima et al., 2010; Pedersen and Sigmundsson, 2006; Sigmundsson et al., 2014). These studies have evolved over time to try and constrain the relationship between the deformation expressed at the surface with the underlying intrusion geometry, with focus on geometries such as dykes (Letourneur et al., 2008; Sigmundsson et al., 2014), sills (Galland and Scheibert, 2013; Magee et al., 2017), laccoliths (Castro et al., 2016) and magmatic diapirs (Fialko and Pearse,

2012). Understanding the relationship between the surface deformation and the dynamics of the underlying volcanic plumbing system can provide greater insights on the depth of the magma and the intrusion geometry, with the potential to constrain when and where an eruption may happen. Modelling this relationship in a laboratory setting can be done using appropriately selected materials to emulate the physical properties of both the host rock and intrusive body. The comprehensive guide of analogue materials in Table 1.1 (Chapter 1) provides an excellent starting point to help select appropriate analogues for the magma and host rock based on the desired conceptual framework. As the models on this chapter will be developed based on the Linear Elastic Fracture Mechanism (LEFM) conceptual framework, gelatine has been chosen as the host rock analogue.

4.3 Methodology and Experiment Setup

4.3.1 Gelatine Preparation and Scaling

The gelatine was prepared according to the guidelines of Kavanagh et al. (2013). Detailed preparation steps as well as the steps taken to scale the gelatine for these experiments can be found in Chapter 3 of this thesis.

4.3.1.1 Single-Layered Experiments

A single homogeneous layer of gelatine is used to model the growth of dykes in an elastic medium. In these experiments, 40 litres of gelatine of a predetermined concentration is prepared in an experimental Perspex tank measuring 40 x 40 x 30 cm³. The gelatine is allowed to cool in the refrigerator for a minimum of 15 hours before running an experiment to ensure that the stiffness of the gelatine falls within the elastic regime (see Chapter 3). This timeframe works specifically with gelatine mixtures with concentrations ranging between 2.0 wt.% and 3.5 wt.%. For gelatine mixtures of lower concentrations, the gelatine is left to cool in the refrigerator for an additional 24 hours.

4.3.1.2 Two-layered Experiments

To prepare an experimental tank with two layers of gelatine, there are two key parameters to consider (Kavanagh et al., 2017): 1) the rigidity contrast between the two layers and 2) the strength of the interface. To prepare an experiment with two layers of equal thickness with contrasting rigidity, the layers must be prepared sequentially. First, the bottom layer is prepared using 20 litres of gelatine of a specific concentration ranging between 1.5 wt.% and 3.5 wt.% gelatine (Refer Table 4.1). This layer is left to cool and solidify for 24 hours in the refrigerator. In the case of gelatine mixtures with low concentration (<2.0 wt.%) the gelatine required cooling in the refrigerator for an additional 24 hours. After the bottom layer is solidified, the next 20 litres of gelatine are gently poured onto the surface of the bottom layer. Pouring the gelatine mixture gently onto a metal spoon helps to prevent the mixture from damaging the bottom layer, especially when the bottom layer is fragile. Previous studies have highlighted how the strength of the interface between the two layers is controlled during this stage by varying the temperature at which the top layer of gelatine is poured onto the bottom layer of colder solidified gelatine (Kavanagh et al., 2015, 2006). A 'strong' interface is created if the top layer is emplaced at a temperature several degrees higher than the gelling temperature of the bottom layer. The hotter gelatine poured on temporarily melts the surface of the solid bottom layer, allowing the top layer to weld onto the bottom layer. Inversely, when the top layer is poured on cold (20°C or lower), a 'weak' contact is formed as there is minimal melting of the surface of the bottom layer (Kavanagh et al., 2017).

4.3.1.3 Gelatine Seeding

In addition to the basic setup mentioned in the previous subsections, in some experiments the gelatine solid is seeded with 20-50 µm spherical poly (methyl methacrylate), PMMA particles with a Rhodamine-B coating which gives off peak fluorescence at a wavelength of 590 nm. The general method of preparation is the same, except 1 litre of water used to dilute

the gelatine mixture is reserved to be mixed with the fluorescent particles. Having a water-particle mixture ensures that the particles do not clump together and will be well distributed within the gelatine solid. Another step that needs to be taken to ensure that the particles are evenly distributed throughout the gelatine solid is to continuously stir the gelatine until it cools down to gelling point, where the temperature is less than 20°C (Kavanagh et al., 2017, 2015). At this temperature, the gelatine will have just begun to set, holding the fluorescent particles in suspension.

4.3.2 Experimental Setup

In both setups (see Figure 4.1 and Figure 4.2), the experiment is carried out by injecting water into the base of the experimental tank. The injection delivers water into the experimental tank at a constant volumetric flux (Q) of $3.9 \times 10^{-7} \text{ m}^3/\text{s}$ with the aid of a peristaltic pump. Prior to injection, the orientation of the growing intrusion is controlled by introducing a vertical fracture in the base of the gelatine in the y-z orientation using the flat tip of a metal spatula. The quality of this introductory fracture is vital to the experiments as it dictates the orientation in which the experimental intrusion grows. This is especially important in Digital Image Correlation (DIC) experiments which heavily rely on the orientation of the intrusion in a specific plane. Should the intrusion undergo rotation, it could grow off-grid to the observation plane (where the laser sheet cuts through the gelatine). The injector tip is then aligned parallel to the vertical fracture to encourage the intrusion to grow in the desired orientation. The following subsections elaborate further on the various imaging techniques used to monitor these experiments.

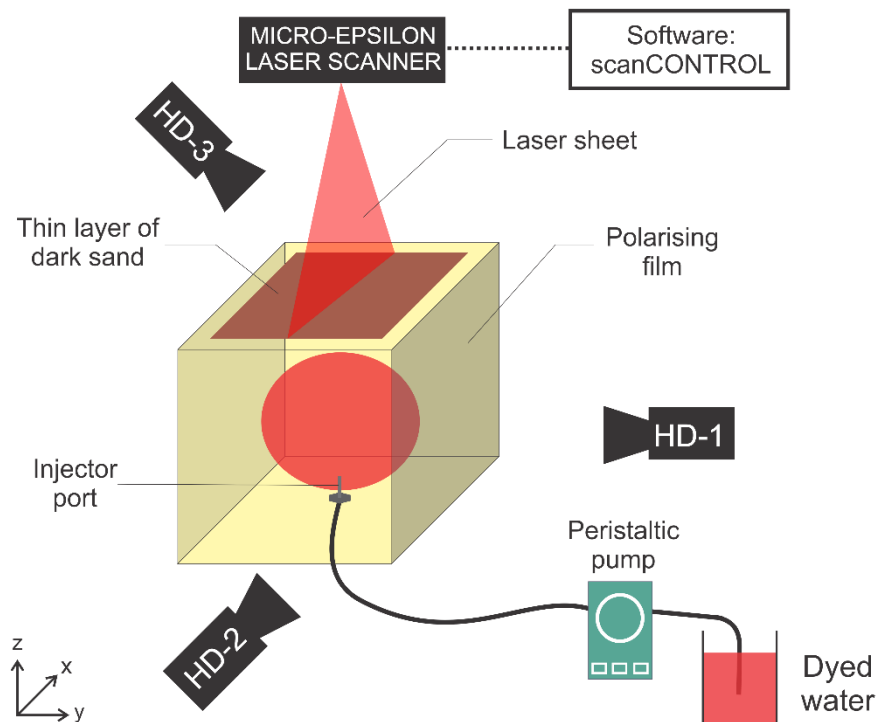


Figure 4.1: Experimental setup to record changes in surface topography using the Micro-Epsilon laser scanner, an overhead laser scanner that records the changes in surface elevation (x-y plane). The laser scanner is paired with software ScanCONTROL which acquires data from the laser transect. The growing intrusion is monitored by cameras HD-1 (x-z plane), HD-2 (y-z plane) and HD-3 (x-y plane). Camera HD-1 films the evolution of internal stresses through a pair of polarising sheets attached to the outside of the tank. Camera HD-2 records the changes in intrusion geometry. Camera HD-3 records changes on the surface of the experiment.

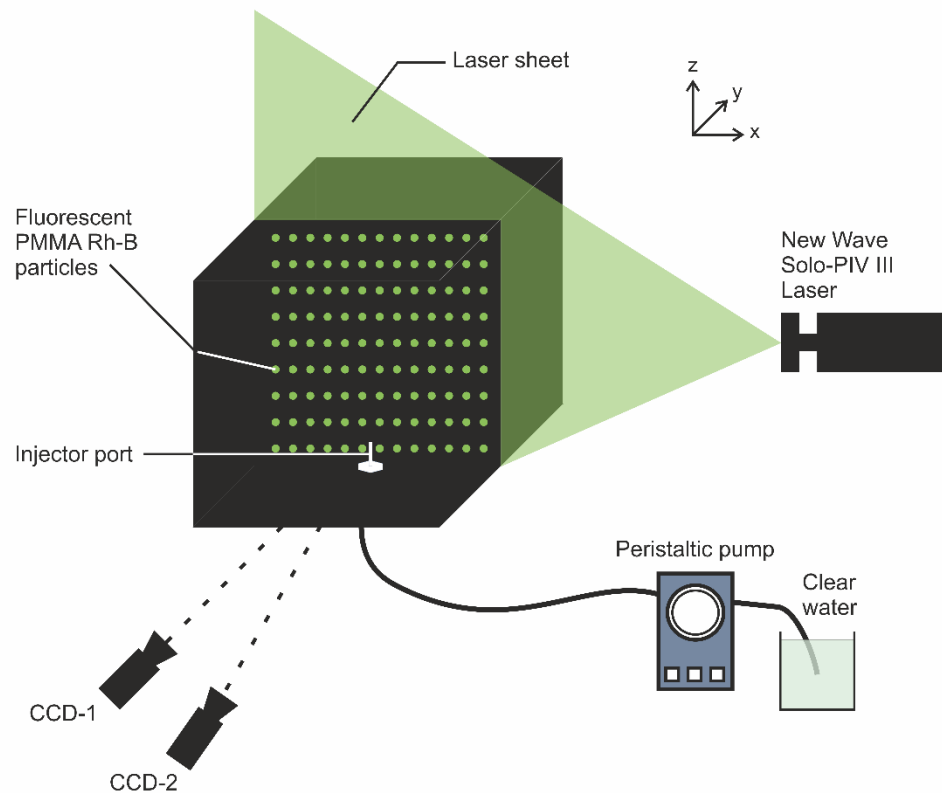


Figure 4.2: Experimental setup for Tracer Particles. The gelatine is seeded with fluorescent particles and is illuminated by a laser sheet fired from a New Wave Solo-PIV III Laser positioned at the side of the tank. The laser sheet is positioned to intercept the central injection port. The displacement of particles during the experiment is recorded on two CCD cameras.

4.3.2.1 Photo-elasticity and Surface Deformation Setups

Solid gelatine is a photo-elastic material which allows the evolution of strain within the gelatine to be observed using polarised light (Crisp, 1952). The analysis of stress distribution in gelatine exploits gelatine's photo-elastic properties where the evolving internal stresses within the gelatine solid are expressed as coloured fringes. As the gelatine solid is in an elastic state, these colour fringes can be used to infer the intensity of stress through the elastic properties. These colour fringes will be referred to as "stress fields" throughout this chapter. Sheets of polarising film are attached on the outside of the experimental tank (Figure 4.1),

specifically on the panels showing dyke growth perpendicular to the dyke strike (as viewed in the x-z plane). Three high definition cameras are used in these experiments to record three key observations: 1) Evolution of stresses within the solid gelatine (x-z plane), 2) Geometries of the intrusion during propagation (y-z plane) and 3) Changes in the surface topography over time (x-y plane). Camera HD-1 is positioned in the x-z plane, parallel to the polarising sheets and is used to record the dyke growth in polarised light. Camera HD-2 is positioned in the y-z plane to record the dyke growth parallel to the dyke strike, illuminated by artificial light.

In addition to the overhead camera recordings, the changes in surface topography over time is measured quantitatively using a high-precision Micro-Epsilon laser scanner positioned over the experimental tank, centred over the injector port. The laser scanner projects a vertical sheet of light onto the surface of the gelatine in the x-z plane, perpendicular to the dyke strike. As the gelatine solid is transparent, a thin layer of dark-coloured medium-sized sand is spread evenly over the surface of the gelatine to aid the deflection of the laser sheet. The laser scanner is paired with the software ScanCONTROL (Version 5.0) to collect data at timed intervals of 4 scans per second along a 140 mm long transect with measurement points positioned every 0.5 mm along the projection. Each point along the linear transect is assigned a height value during each scan, which corresponds to the distance between the source of the laser sheet and the surface of the gelatine.

4.3.2.2 Tracer Particle Setup

The fluorescent particles in the gelatine are illuminated by a vertical laser sheet fired from the side of the tank (x-z plane). The laser is positioned central to the x-z plane to allow the laser sheet to intersect with the central injection point, as shown in Figure 4.2. The New Wave Solo-PIV III Laser uses a cylindrical lens which excites the fluorescent particles at a repetition rate of 1 Hz (illuminating 1 frame per second). Images are captured on CCD cameras over a controlled interval of 1 frame per second, which matches the pulse of the firing laser. The

images used in these experiments are captured using two 2 MP CCD cameras fitted with 35 mm Nikon lenses, one looking head on at the growing intrusion, central to the y-z plane and another looking up at an angle of 15° in the y-z plane which is useful for imaging the growth of sills along the contact zone between two layers of gelatine. Dantec Dynamic Studio, the imaging software paired to the laser setup, has been set to record a maximum of 2000 frames.

4.3.3 Post-Processing Data

4.3.3.1 Tracker

In order to measure the velocity of the vertical (and horizontal) tip as it propagates through the host material and the dimensions of the evolving intrusion geometry, video recordings from Cameras HD-1 and HD-2 and imported into Tracker Version 4.96, an open source video analysis and modelling tool. Using audio and visual cues from the original video recordings, the range of frames for analysis is identified. The physical space shown in the video is calibrated by marking two points of known coordinates and the distance between them. For all experiments, the bottom of the injector port is marked as (0,0) and the surface of the gelatine is marked as (0, 24), with the distance between the two points is measured to be $24 \text{ cm} \pm 0.5 \text{ mm}$. This central axis is used to mark the position of the dyke tip relative to the injector port, which can be mapped out using the footage from Camera HD-1 (x-z plane). The calibrated distance is used as a scale to measure the intrusion's geometric properties such as length and width, using the footage from Camera HD-2 (y-z plane). The time steps are calibrated by marking the first frame (dyke inception) and last frame (eruption of dyke or sill growth) of the video recording and dividing the steps in between into 10 second intervals (i.e. 500 frame intervals for 50 fps recordings). The output is exported in the form of a table containing the time steps, coordinates and velocities corresponding to each mapped out point. This dataset is then manipulated using the statistical analysis software R to produce

scatterplot graphs showing the geometrical evolution of intrusions and the changes in intrusion velocity over time.

4.3.3.2 ScanCONTROL and MATLAB

The progressive elevation change of the surface of the gelatine is measured using the Micro-Epsilon laser scanner. ScanCONTROL works in tandem with the overhead laser scanner as the main command centre to run data collection during experiments. After the experiment is complete, ScanCONTROL exports data in the form of a series of .slk (Symbolic Link format) files, which carry the information of height values corresponding to each point along the 140-mm horizontal transect line. These files are then subsampled using a MATLAB script (See appendix) to produce a new dataset containing the height and position of each point at 10 second intervals. This is done for the final 120 seconds prior to dyke eruption or for 120 seconds of sill propagation approximately 8 cm away from the dyke for experimental sills. Using this new dataset, the script then calculates the cumulative sum of displacement across the horizontal transect for the defined time interval. This step provides the values needed to plot a graph of surface profile changes over time, which is done using statistical analysis software, R. The data points are plotted as a scatterplot of cumulative surface deformation values against the horizontal distance and smoothed using a non-parametric fit LOESS (Locally Weighted Scatterplot Smoothing) curve with a span width of 0.3 for the smoothing window.

4.3.3.3 Digital Image Correlation

Digital Image Correlation (DIC) is the technique used to quantify the subsurface strain evolution in the intruded gelatine solid by tracking the changes between. Before running experiments using the Tracer Particle setup, a series of images of a 2D calibration plate is acquired for calibration purposes. This plate (Figure 4.3) consists of evenly-spaced black dots (3 mm diameter, with 10 mm spacing) on a white background. The dot in the centre of the

plate is 4 mm in size, used to visually highlight the centre of the calibration plate and to inform the imaging software of the central position on the calibration plate. The imaging software uses these images to define the area of interest for quantitative analysis. These images are later used in post-processing to: 1) Correct for any distortion in the image and 2) To provide a consistently accurate conversion between pixels and physical space.

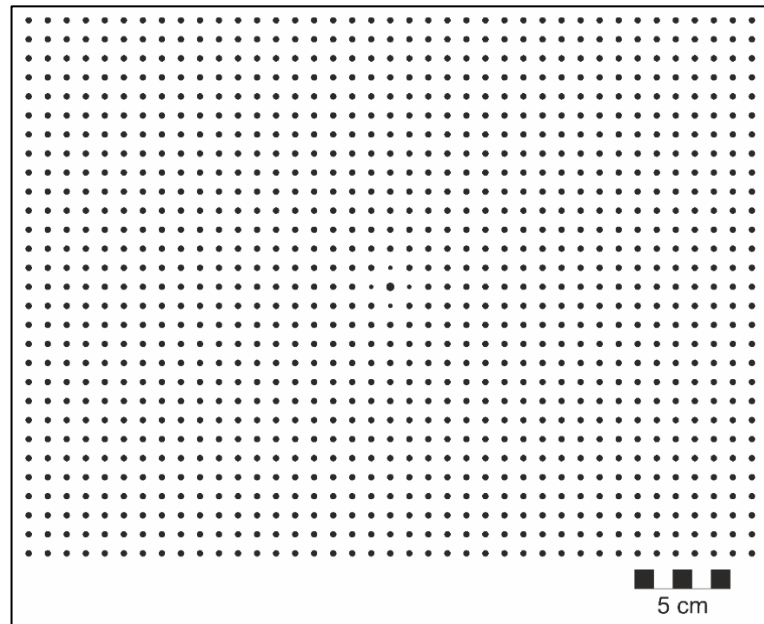


Figure 4.3: Calibration plate used to calibrate the camera for Digital Image Correlation (DIC) on Dantec Dynamic Studio. The calibration plate consists of evenly-spaced black dots (3 mm diameter, 10 mm spacing) on a white background. The dot in the centre is 4 mm in size with the smaller dots (2 mm) acting as axis markers to the top and bottom and left and right of the dot in the centre.

First, the images recorded from the Tracer Particle experiment are de-warped using the Imaging Model Fit function on Dantec Dynamic Studio. This de-warping step is done to straighten out the images captured which may have been warped (distorted) by the positioning of the camera. The Imaging Model Fit compares the images from the experiment to the images captured from the calibration stage using the x-y-z camera model which has been identified to have the smallest pixel error. After de-warping, the images are then processed using the Analysis toolbox in Dantec Dynamic Studio using the "Adaptive

Correlation" technique which is an iterative computation carried out over a predefined interrogation area. The interrogation area is set to an area of 32 pixels by 32 pixels with an overlap of 50%. This step creates a series of vector maps which illustrates the direction and intensity of particle movement between images. Once this step is completed, the numerical values such as coordinates, length, velocities related to the displacement of the tracer particles are exported as .txt files (see Appendix for example). Finally, the de-warped images are exported as images (.tiff) and the recording of the experiment is exported as a video. The vector maps produced by Dantec Dynamic Studio are then post-processed in MATLAB to produce incremental strain evolution colour maps (scripts used are attached in Appendix).

4.4 Results

A total of 25 experiments were performed to study dyke and sill propagation in layered elastic media with contrasting mechanical properties (Young's Modulus) and thickness. In total, 15 dykes, 10 sills and 1 dyke-sill hybrid were created. The results from two single-layer experiments (see Section 4.4.1) are part of the attached publication (see Appendix). The results from nine representative experiments will be described in this section starting with dykes (single and two-layered) and followed by sills (two-layered). Observation of dyke geometry and qualitative sub-surface stress are first described, followed by surface elevation change, and finally quantitative sub-surface strain. The full experimental parameters for each experiment are elaborated in Tables 4.1 and 4.2. Note that this table has been divided as follows: Table 4.1 summarises the experimental parameters for single layer experiments and Table 4.2 summarises the experimental parameters for two-layer experiments.

4.4.1 Experimental Dyke Intrusions: Single Layer Experiments

4.4.1.1 Dyke Geometry and Sub-Surface Stresses

The dyed water injected into the base of the tank propagates vertically into the gelatine solid, forming a penny-shaped fluid-filled fracture. The experimental dyke is described to be penny-shaped as it is a three-dimensional fluid-filled fracture, where it appears to be a two-dimensional circle of approximately equal length and width in the y-z plane, with the component of thickness viewed in the third dimension visible in the x-z plane.

The growth of the experimental dyke can be divided into three key stages, as illustrated in Figure 4.4. Figure 4.4(a) illustrates the changes in length and width as observed in the y-z plane (Camera HD-2). Figure 4.4(b) shows the changes in the rate of dyke growth, denoted by the change in dyke length velocity which shows how quickly or slowly the experimental dyke is propagating vertically. In Stage 1, the dyke grows equally in length and width with a rapid deceleration in the rate of growth in the first 100 seconds. The dyke then undergoes a stage of constant growth in Stage 2 where it continues to grow equally in length and width. Stage 3 leads to eruption, where the rate of length growth rapidly increases and the geometry of the intrusion evolves into a more elliptical shape, where the dyke is growing at a faster rate lengthwise compared to its width. The dyke then breaches the surface creating a fissure 30 mm in length. The data presented in Figure 4.4(a) and Figure 4.4(b) shows the results taken from two identical experiments, SD-07 and SD-09 (see Table 4.1 for properties).

Table 4.1: Experimental parameters of laboratory experiments. The experiment reference tags are in the column “Experiment.” Other notations and units: Concentration of gelatine “ C_{gel} ” (wt.%), height “ H ” (cm), mixture temperature “ T_{mix} ” (°C), temperature of the gelatine solid at the beginning of the experiment “ T_{exp} ” (°C), Young’s modulus values “ E ” (Pa), volumetric flux of the injected fluid “ Q ” (m^3/s). Imaging technique: “PL” = Polarised Light, “SD” = Surface Deformation, “TP” = Tracer Particles.

Experiment	C_{gel}	H	T_{mix}	T_{exp}	t_{set}	E	Q	Imaging technique	Result
SD_01	2.5	0.24	23.0	5	21 hours 45 minutes	2688	3.9×10^{-7}	PL, SD	Dyke
SD_02	2.5	0.24	21.0	5	15 hours 30 minutes	2027	3.9×10^{-7}	PL, SD	Dyke
SD_03	2.5	0.24	22.0	5	47 hours	4662	3.9×10^{-7}	PL, SD	Dyke
SD_04	2.5	0.24	22.0	5	16 hours	1864	3.9×10^{-7}	PL, SD	Dyke
SD_05	2.5	0.24	24.0	5	45 hours 30 minutes	4685	3.9×10^{-7}	PL, SD	Dyke
SD_06	2.2	0.24	22.0	5	20 hours 30 minutes	2450	3.9×10^{-7}	PL, SD	Dyke
SD_07	2.5	0.24	22.0	5	24 hours	2921	3.9×10^{-7}	PL, SD	Dyke
SD_08	2.5	0.24	21.0	5	22 hours	2950	3.9×10^{-7}	PL, SD	Dyke
SD_09	2.5	0.24	22.0	5	23 hours	3042	3.9×10^{-7}	PL, SD	Dyke
SD_10	1.5	0.24	25.0	5	46 hours	1428	3.9×10^{-7}	PL, SD	Dyke
ADD-01	2.5	0.24	21.0	5	48 hours	2818	3.9×10^{-7}	TP	Dyke

Table 4.2: Continuation of Table 4.1 with the same notations and units. For experiments in two-layered media, the Subscript (1) is used to describe the bottom layer in the experimental tank and Subscript (2) is used to describe the top layer in the experimental tank.

Exp.	C_{gel1}	C_{gel2}	H_1	H_2	T_{mix}	T_{top}	T_{exp}	t_{set}	E	Q	Imaging Technique	Result
SD_11	2.5	2.5	0.20	0.04	21.0	25.0	5	221 hours 13 minutes	5303	3.9×10^{-7}	PL, SD	Dyke
SD_13	2.0	3.5	0.20	0.04	24.0	23.0	5	193 hours 30 minutes	4021	3.9×10^{-7}	PL, SD	Dyke
SD_14	2.0	3.5	0.20	0.04	22.0	23.0	5	216 hours 30 minutes	5108	3.9×10^{-7}	PL, SD	Dyke
SD_15	2.0	3.0	0.12	0.12	21.0	21.0	5	101 hours	6880	3.9×10^{-7}	PL, SD	Dyke-Sill Hybrid
SD_16	2.0	3.0	0.12	0.12	23.0	21.5	5	121 hours 50 minutes	8006	3.9×10^{-7}	PL, SD	Sill
SD_17	1.5	3.0	0.12	0.12	21.1	21.5	5	91 hours 15 minutes	6999	3.9×10^{-7}	PL, SD	Sill
PLT-0	2.5	3.0	0.12	0.12	21.6	21.7	5	160 hours 30 minutes	8686	3.9×10^{-7}	TP	Sill
PLT-2	2.5	3.0	0.12	0.12	21.3	20.7	5	329 hours	8040	3.9×10^{-7}	TP	Sill
PLT-3	2.5	3.0	0.12	0.12	22.0	22.0	5	216 hours	5018	3.9×10^{-7}	TP	Sill
PLT-4	2.5	3.0	0.12	0.12	21.4	21.0	5	141 hours 30 minutes	9504	3.9×10^{-7}	TP	Sill
PLT-5	2.0	2.5	0.12	0.12	24.0	17.0	5	94 hours 30 minutes	5232	3.9×10^{-7}	TP	Dyke
PLT-6	2.0	3.0	0.12	0.12	22.0	24.0	5	93 hours	6330	3.9×10^{-7}	TP	Sill
PLT-7	2.0	3.0	0.12	0.12	22.0	21.1	5	93 hours	8223	3.9×10^{-7}	TP	Sill
PLT-8	1.5	3.0	0.12	0.12	20.0	21.0	5	119 hours	6599	3.9×10^{-7}	TP	Sill

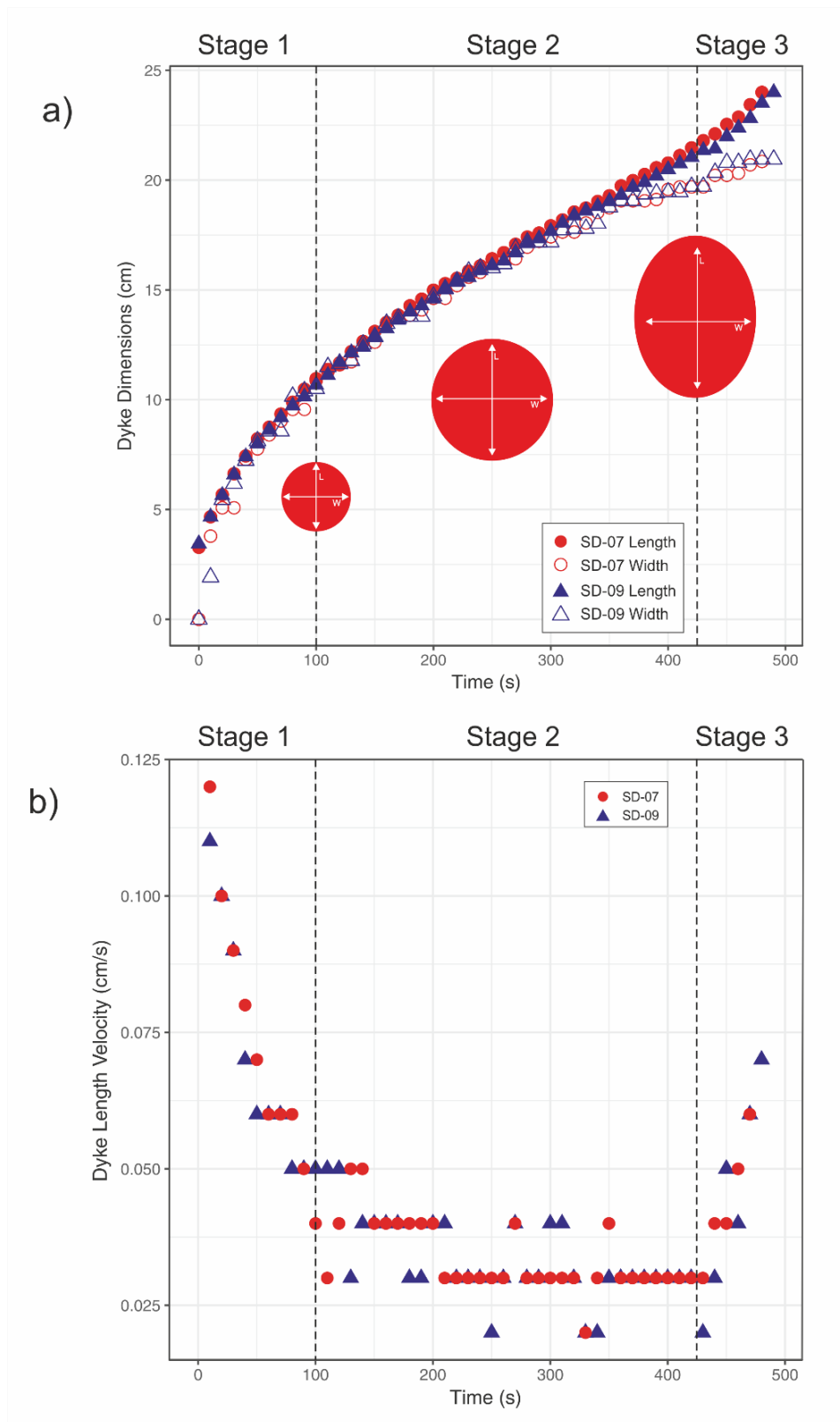


Figure 4.4: The three key stages of experimental dyke growth as illustrated by: (a) Changes in intrusion geometry (height and width) and (b) Changes in vertical growth rate over time.

The striking similarity in trends between the two experiments illustrate the high degree of reproducibility between experiments, given that the conditions at which the experiments are run are kept the same.

Figure 4.5 shows a series of cropped images taken at three different time steps (60 seconds, 240 seconds and 480 seconds) representing the three stages of dyke growth and propagation as observed in two orientations. Figure 4.5(a) shows the dyke growth and propagation as observed in the y - z plane (Camera HD-2). Figure 4.5 (b) shows the dyke growth and propagation as observed in the x - z plane (Camera HD-1). Figure 4.5 (c) shows the images in Figure 4.5 (b) in greyscale to bring emphasis to the shapes of the stress fields at the tip of the dyke. The laser transect can be seen in coloured images (Figure 4.5 (a) and Figure 4.5 (b)) as a red line at the top of the frame. The three stages are denoted as follows: (i) Stage 1: Dyke inception, (ii) Stage 2: Dyke propagation and growth and (iii) Stage 3: Pre-eruption.

Figure 4.5(a)(i) presents the dyke as a penny-shaped intrusion with approximately equal width and length. 120 seconds into the experiment, this penny-shaped dyke expands outwards equally in length and width as shown in Figure 4.5(a)(ii). Prior to eruption, the dyke is observed to have stretched upwards, forming an ellipse-shaped dyke where the length of the dyke is greater than its width (Figure 4.5(a)(iii)).

Figure 4.5(b) and Figure 4.5(c) show the dyke growth as observed through polarising film. The stress fields associated with the dyke propagation appears as two lobes flanking the dyke tip resembling a bow-tie (Figure 4.5(b)(i) and Figure 4.5(c)(i)). These stress fields are small and localised at the beginning of the experiment (Stage 1) before growing bigger and wider in extent in Stage 2 (Figure 4.5(b)(ii) and Figure 4.5(c)(ii)). In Stage 3 the stress fields interact with the surface of the gelatine until the dyke erupts at the surface and the stress fields visually dissipate with the eruption. (Figure 4.5(b)(iii) and Figure 4.5(c)(iii)).

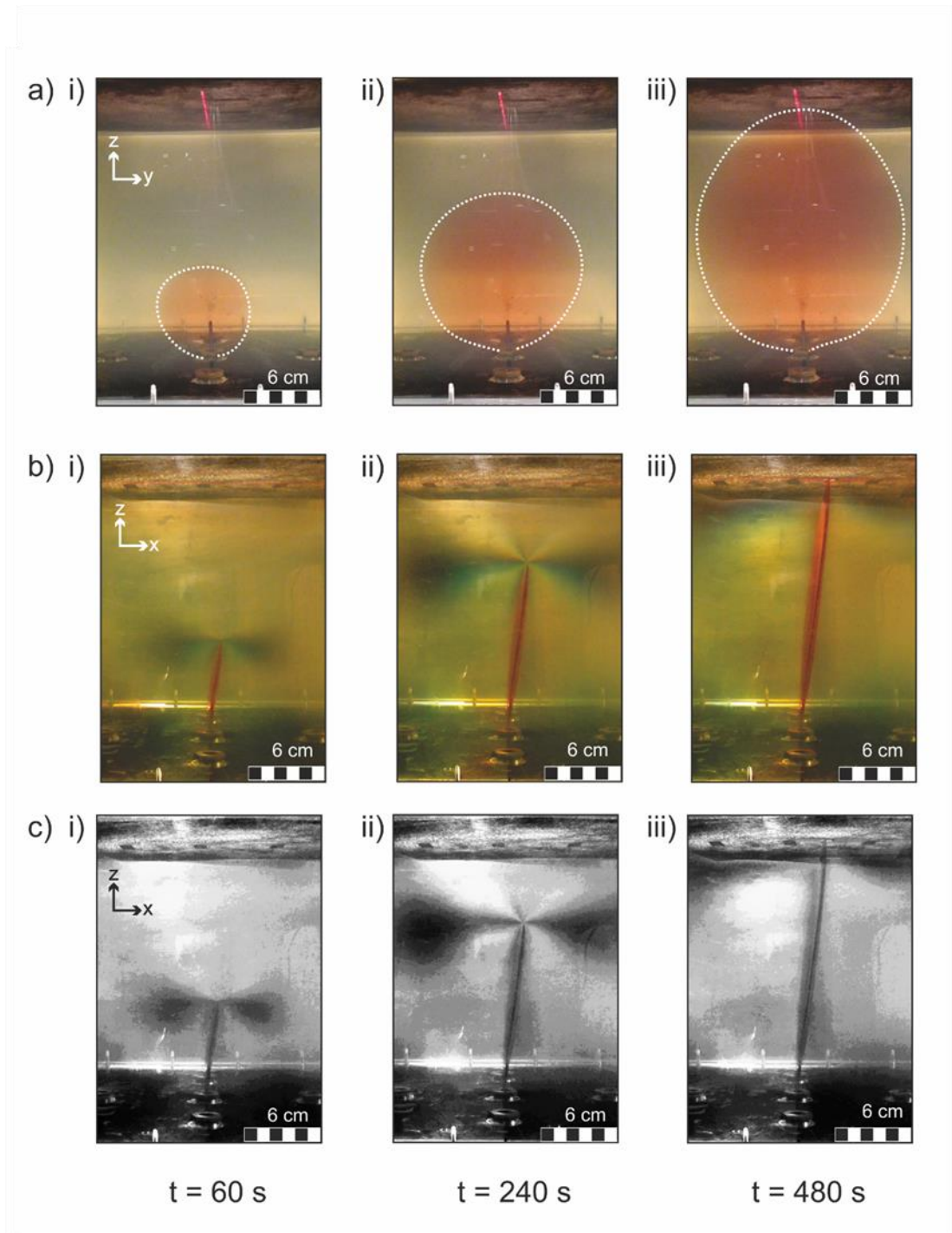


Figure 4.5: Photographs of Experiment SD-07 taken at three different time steps: (i) 60 seconds, (ii) 240 seconds and (iii) 480 seconds. The photographs are captured in the following orientations: (a) y-z plane, (b) x-z plane and (c) x-z plane. The photographs in row (c) are greyscale photographs of the photographs in row (b) where the bow-tie shape is more pronounced. The position and orientation of the laser transect is visible at the top of the frame in all coloured photographs.

4.4.1.2 Surface Elevation Change Profiles

Figure 4.6 shows the progressive change in surface elevation in Experiments SD-07 and SD-09, where the vertical axis shows the magnitude of uplift resulting from the propagation of the experimental dyke (mm) and the horizontal axis shows the position of each data point along the length of the laser transect (-70 mm to 70 mm). Surface profiles for the final 120 seconds leading up to eruption are selected as there was no prominent change in surface topography detected during most of the dyke ascent.

The elevation change at the surface of the gelatine is observed to be most prominent immediately prior to eruption. Figure 4.6(a) shows that the surface has deformed to form two asymmetrical regions of topographic high, measuring 1.5 mm and 0.8 mm high at the highest peaks, flanking a region of topographic low. Figure 4.6(b) on the other hand only shows one region of topographic high, measuring approximately 1.8 mm at its peak, greater than the maximum displacement shown in Experiment SD-07.

While the experiments have been carried out using the same experimental parameters, the experiment-specific pattern of deformation expressed at the surface show slight differences. This difference can be attributed to the different propagation paths taken by the experimental dyke. When the experimental dyke propagates sub-vertically (Experiment SD-07), both peaks are picked up by laser transect. When the dyke propagates at an inclined angle (Experiment SD-09), there is a chance of the second peak being formed outside of the laser transect. It is inferred that another region of topographic high is present outside of the laser transect to match the observations in Experiment SD-07.

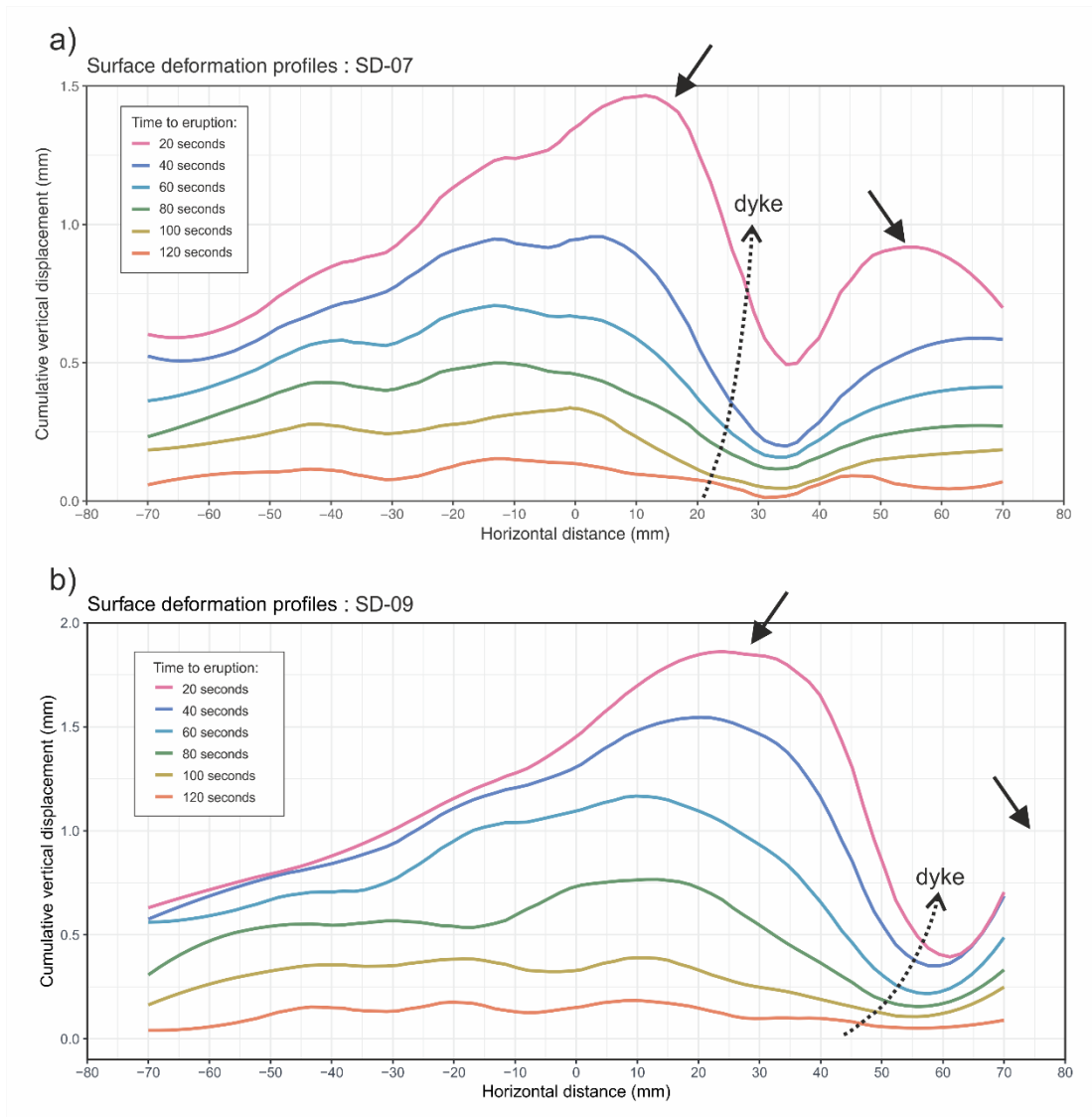


Figure 4.6: Progressive change in surface topography 120 seconds prior to eruption in Experiments SD-07 and SD-09. Figure (a) highlights the patterns produced by the dyke in Experiment SD-07: Two regions of topographic high flanking a region of topographic low. Figure (b) illustrates the surface deformation patterns resulting from the inclined propagation path of the dyke in Experiment SD-09. There is a single prominent region of topographic high expressed next to a region of topographic low.

4.4.1.3 Incremental Strain Evolution

Figure 4.7 show the results from experiment ADD-01, an experiment conducted by introducing a central water injection into a homogeneous gelatine host. Figure 4.7(a)(i)

shows the inception of the experimental dyke as viewed in the e_{xx} plane with the strain focussed on the tip of the experimental dyke in red, flanked by two local negative regions highlighted in blue. This pattern is observed throughout the propagation of the experimental dyke with vectors radiating outwards from the tip region as seen in Figures 4.7(b)(i). The vectors are largest parallel to the horizontal axis and focussed around the dyke tip, emphasizing that the displacement is largest along the horizontal component and smaller along the vertical component of the growing experimental dyke. This observation supports the idea that the fracture is being pushed open along the horizontal axis as the dyke propagates towards the surface (Mode 1 fracturing). Note that there is no incremental strain expressed in the tail region of the experimental dyke as the fracture opening is maintained throughout the experiment. The incremental strain maps in the e_{zz} plane show that in addition to displacing the host material along the horizontal axis during growth, the experimental dyke also pushes the host material upwards as highlighted by the regions in blue in Figures 4.7(b)(ii). The vertical displacement is smaller and more localised at the start of the experiment (Figure 4.7(a)(ii)) before becoming larger and wider in extent as the dyke approaches the surface of the gelatine (Figure 4.7(b)(ii)). Immediately after the experimental dyke has erupted, the tail zips behind it. This "zipping closed" of the experimental dyke post-eruption is illustrated across all three plots (e_{xx} , e_{zz} and e_{xz}) as vectors rotating inwards (Figure 4.7(c)) along the length of the experimental dyke in a progressive zipping motion.

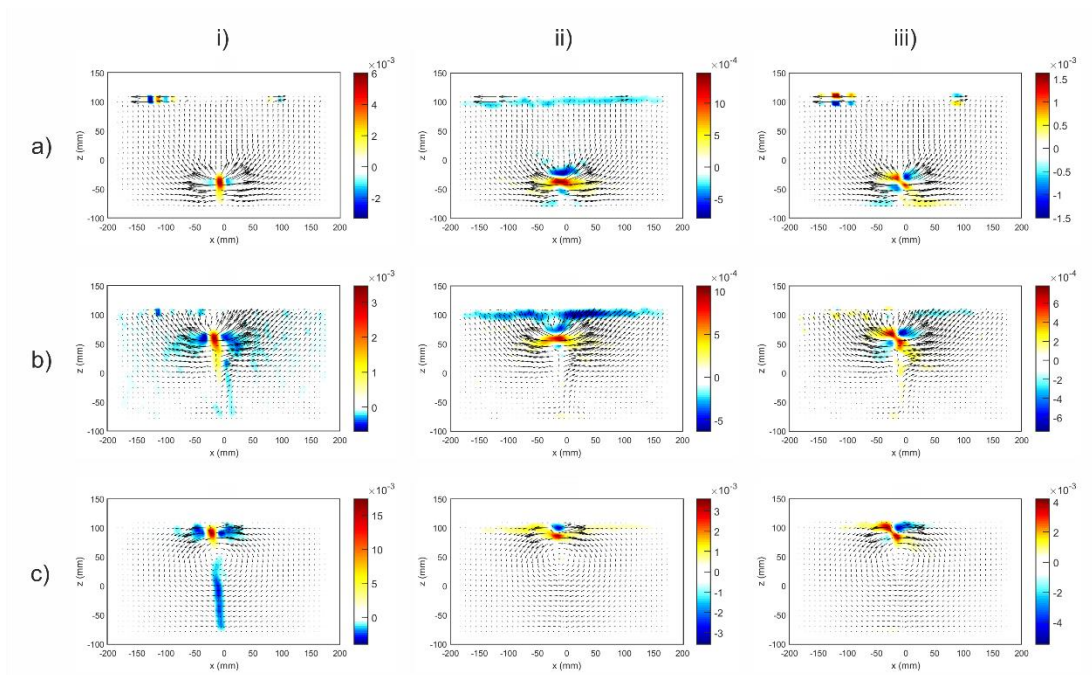


Figure 4.7: The results are presented as a series of vector maps which highlight the following key observations: 1) The vector arrows highlight the direction and magnitude of host material displacement and 2) The coloured contours show the intensity of strain as viewed through cross-sectional planes e_{xx} (horizontal displacement), e_{zz} (vertical displacement) and e_{xz} (shear displacement). Regions in red represent the local positive, where fluorescent particles are moving closer together and regions in blue represent the local negative, where the fluorescent particles are moving further away from one another.

4.4.2 Experimental Dyke Intrusions: Two-Layered Experiments

4.4.2.1 Dyke Geometry and Sub-Surface Stresses

The following section presents the evolution of dyke geometry and its sub-surface stresses over time as it propagates through two layers of superposed gelatine that are bonded along the interface. The preparation of these experiments take into consideration the effective acquisition parameters outlined in the previous section (Section 4.3.1), such as the acquisition time frame (120 seconds prior to eruption) and its corresponding depth (maximum depth from surface to be a minimum of 4 cm). Taking these observations into

account, the top layer of gelatine is prepared to be 4 cm thick ($m_t = 7$ kg) and the bottom layer is 20 cm thick ($m_t = 33$ kg) to best capture the effects of the bonded interface on the propagation of the experimental dyke. Similar to the previous experiments, the dyed water is injected into the centre of the gelatine solid at a constant volumetric flux creating a penny-shaped fluid-filled fracture.

The results from HD video analysis of footage from in the x-z and y-z plane shows that the experimental dyke in experiment SD-13 undergoes similar phases of growth to the experimental dykes propagating in a single layer of gelatine. The velocity profiles (Figure 4.8(a)) show rapid deceleration in growth within the first 100 seconds (Stage 1), followed by a stage of constant growth (Stage 2) before transitioning into rapid acceleration around the 450-second mark (Stage 3). Recordings from Camera HD-2 however reveal that there is a difference in the dimensions of the experimental dyke, where the experimental dyke appears visibly wider in diameter compared to the experimental dykes in the previous section. Video analysis confirms this observation showing that while the experimental dyke has taken a similar amount of time to propagate and erupt at the surface (approximately 500 seconds), the majority of the growth occurs below the interface of the two superposed layers (Figure 4.8(b)) before breaching the interface around 450 seconds into the experiment resulting in a wider experimental dyke. Comparing the time taken for the experimental dyke to transition from being penny-shaped (length = width) to becoming an ellipse (length > width) in single-layer and two-layer experiments show that the vertical growth is significantly dampened by the presence of a bonded interface.

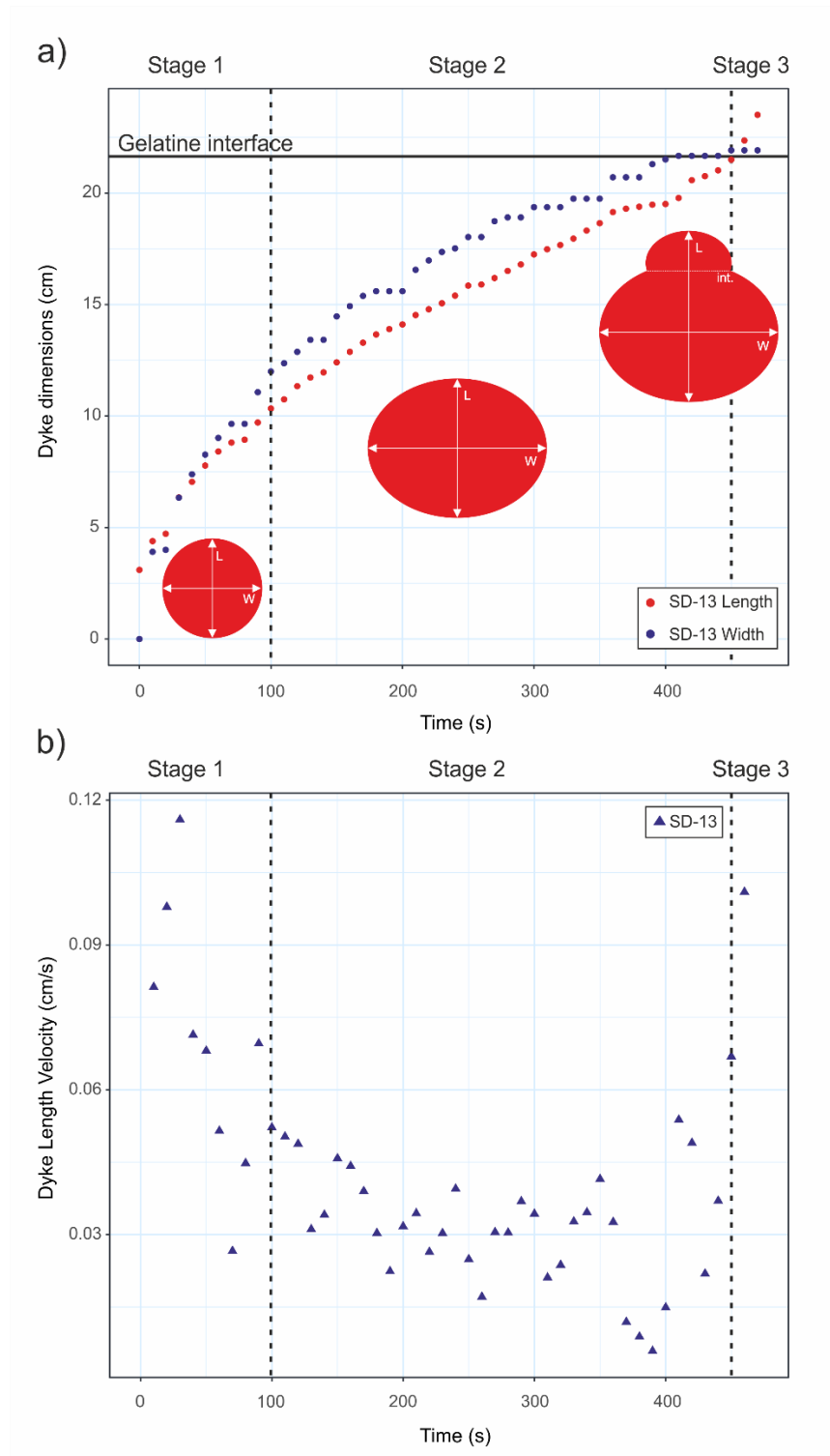


Figure 4.8: Three key stages of dyke growth in a two-layered experiment (Experiment SD-13): (a) Changes in intrusion geometry and (b) Changes in vertical growth rate over time. The position of the interface separating the top and bottom layer is marked on the figure. The experimental dyke comes into contact with the stiffer upper layer approximately 450 seconds into the experiment.

The evolution of sub-surface stresses within the gelatine host is shown in Figure 4.9. Similar to the propagation of experimental dykes in a single layer of gelatine, the stress fields expressed at the tip region of the experimental dyke are bowtie-shaped. The bowtie-shaped stress fields are small and localised at the beginning of the experiment before growing wider in extent as the experimental dyke propagates towards the surface. The size and extent of the stress fields do not appear to be affected by the presence of the bonded interface.

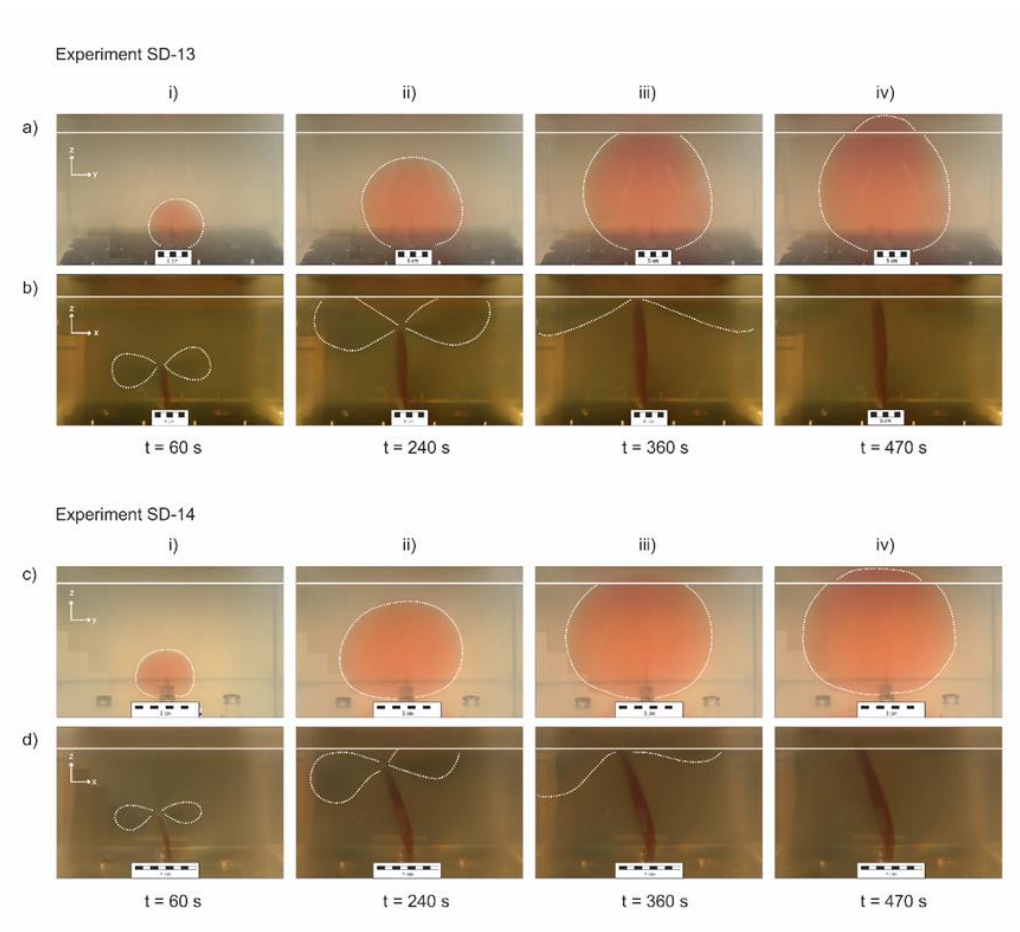


Figure 4.9: Annotated photographs of Experiment SD-13 and Experiment SD-14 taken at four different time steps: (i) 60 seconds, (ii) 240 seconds and (iii) 360 seconds and (iv) 470 seconds. The photographs were captured in the following orientations: (a) and (c) y-z plane, (b) and (d) x-z plane. The position of the gelatine interface is marked at the top of each frame. **Note:** The scale bar for Experiment SD-13 = 5 cm. The scale bar for Experiment SD-14 = 8 cm.

4.4.2.2 Surface Elevation Change Profiles

The progressive change in surface topography of a dyke propagating in a layered material is presented in Figure 4.10(a) where the cumulative vertical displacement in the final 120 seconds leading up to eruption is shown on the y-axis and the position along the laser transect is shown on the x-axis. The deformation profile starts off broad at a depth of around 5 cm and does not show any obvious changes in topography. As the experimental dyke continues to propagate towards the surface (depth < 4 cm), an asymmetrical pattern begins to emerge showing two regions of topographic high flanking a region of topographic low. The asymmetrical deformation pattern is similar to patterns observed in experiments SD-07 and SD-09 (Section 4.3.1.2) which has developed as a result of the inclined propagation of the experimental dyke. The vertical displacement is again most prominent is on the “hanging wall” of the experimental dyke with a maximum cumulative displacement of about 1.2 mm. The vertical displacement on the “footwall” of the experimental dyke has a maximum cumulative displacement of 0.9 mm. The effects of inclined propagation on the pattern and magnitude of deformation expressed at the surface can be further observed in the results of experiment SD-14 (Figure 4.10(b)). The experimental dyke in experiment SD-14 has propagated through the gelatine host at an angle away from the central injection point. The surface deformation profiles correspond well to this change in propagation angle, showing greater deformation in the “hanging wall” block (approximately 1.4 mm) compared to Figure 4.10(a).

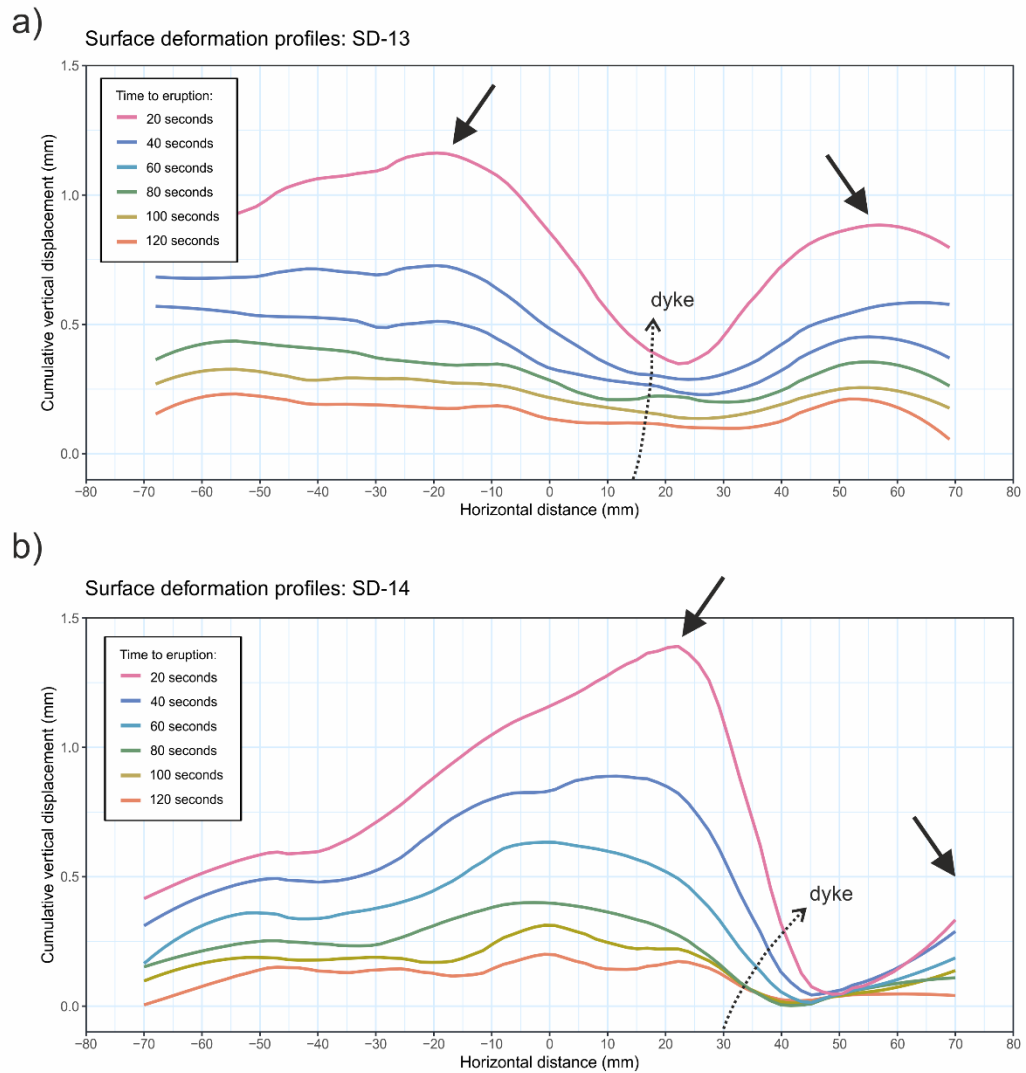


Figure 4.10: The progressive change in surface topography as a dyke propagates through layered elastic media: (a) Experiment SD-13 and (b) Experiment SD-14. The profiles show two elevated regions on each side of the dyke tip. Note the inclination of the propagation path in both experiments: (a) approximately 5° and (b) approximately 15° . Note that the dykes are dipping in the opposite direction to the experiment photographs in Figure 4.9 due to camera being positioned on the opposite side of the experimental tank.

4.4.2.3 Incremental Strain Evolution

The incremental strain and displacement of the growth of an experimental dyke in two superposing layers of gelatine of contrasting stiffness with a bonded interface is shown in

Figure 4.11. The results show a striking similarity to the results shown in Section 4.3.1.3 where the dyke tip region is prominently visible in the e_{xx} plots as a region of local positive (red) at the tip with regions of local negative (blue) expressed adjacent to the dyke tip (Figures 4.11(i)). The tail region expresses no incremental strain as the fracture is kept open throughout the propagation of the experimental dyke. Upon eruption, the tail progressively zips behind the propagating dyke, clearly presented across all plots (e_{xx} , e_{zz} and e_{xz}) as vectors rotating inwards effectively “closing” the experimental dyke along its length (Figures 4.11(d)).

The results from this experiment differs slightly to that of experiment ADD-01, a dyke propagating in a single layer of gelatine (Section 4.3.1.3), as the experimental dyke is slightly inclined. The inclined growth of this experimental dyke however provides useful insights on how inclination affects the intensity of the strain surrounding the tip of the propagating dyke. This effect can be seen best in the frames leading up to eruption (Figures 4.11(c)) where the displacement of the host material is larger on the “hanging wall” side on the intrusion compared to its “footwall”. The vector arrows on the “hanging wall” are the more prominent set of vectors affecting surface displacement in this experiment and can be clearly observed even as the experimental dyke breaches the surface in Figures 4.11(d).

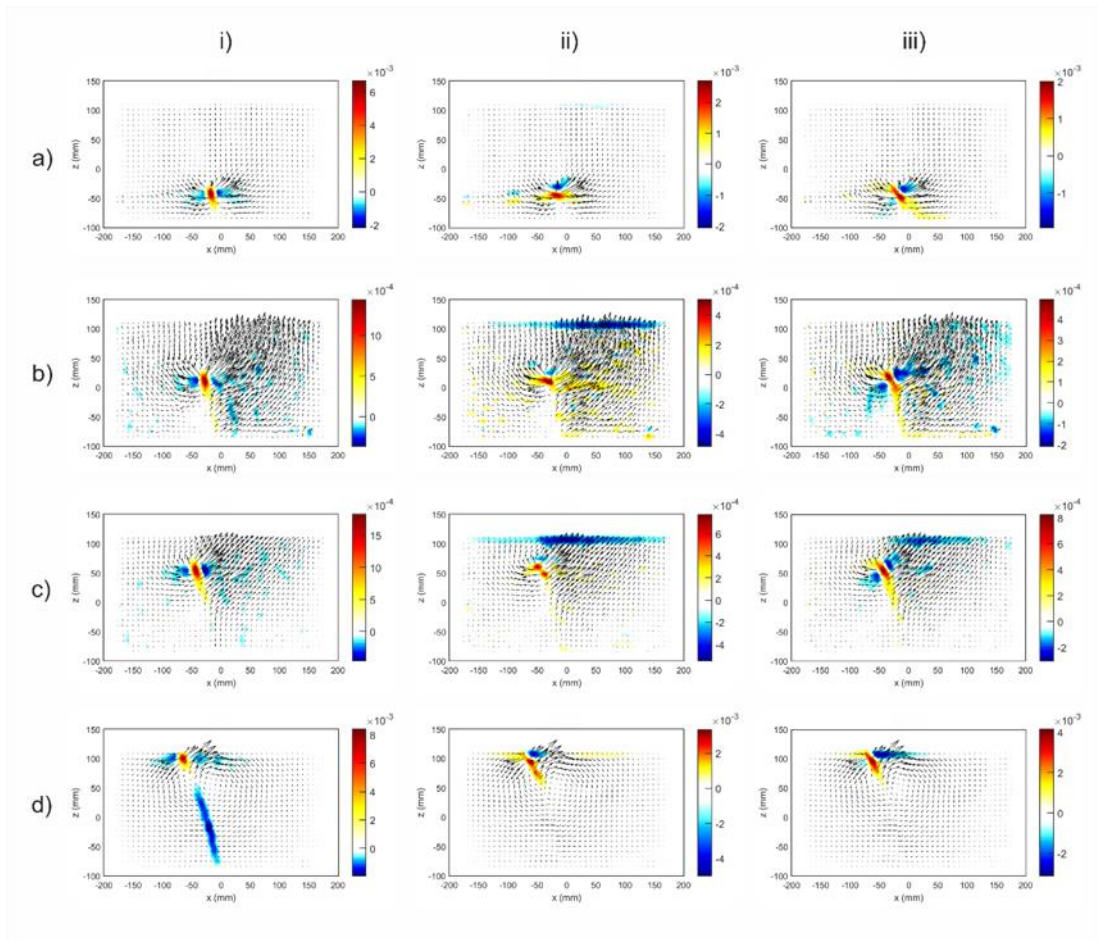


Figure 4.11: The evolution of strain in the host material (gelatine) during dyke propagation in layered elastic media (Experiment PLT-5) as seen through three planes: (i) e_{xx} : Strain along the horizontal axis, (ii) e_{zz} : Strain along the vertical axis and (ii) e_{xz} : Shear strain in the x-z plane. The images are arranged to show four key stages of dyke propagation: (a) Inception of the experimental dyke, (b) Propagation and growth of the experimental dyke where the dyke meets the interface and stalls, (c) Pre-eruption ascent towards the surface and (d) Eruption at the surface.

4.4.3 Experimental Sill Intrusions

4.4.3.1 Evolution of Sub-Surface Stresses

Figure 4.12 shows a compilation of images highlighting the evolution of sub-surface stresses in experiments SD-16 and SD-17 across three different stages of intrusion growth: 1)

Inception and propagation of the experimental dyke, 2) Contact at the interface and 3) Propagation of the experimental sill.

During inception and propagation of the experimental dyke in experiment SD-16, the subsurface stresses at the tip region are observed to be prominently expressed as two symmetrical lobes in the shape of a bow-tie (Figure 4.12 (a)(i)). The colour fringes are smaller and more localised at the beginning of the experiment before growing wider in extent. However, in this experiment, the growing intrusion approaches the stiffer upper layer and weak interface (Figure 4.12 (a)(ii)) and the intrusion changes to propagate laterally along the interface between the two layers forming an experimental sill. The inception and propagation of the experimental sill gives rise to a second set of colour fringes focussed on the tip of the growing sill. As the experimental sill propagates away from the point of sill inception, the colour fringes emerge more prominently as two lobes flanking the top and bottom of the sill tip, resembling the shape of a slightly tilted hourglass (Figure 4.12 (a)(iii)). It is observed that while the tip of the experimental sill propagates outwards, the symmetrical colour fringes at the tip of the dyke also retains its bow-tie shape throughout the experiment indicating that stress remains formed at the dyke to sill transition.

The experimental dyke in experiment SD-17 has propagated not only on an inclined path, but it has also undergone a 45° rotation (Figure (b)(iii)) which gives the illusion of experimental dyke being wider than it is when viewed through Camera HD-2. Despite the rotation of the experimental dyke, the sub-surface stress patterns are still observed as symmetrical colour fringes during the inception and propagation stages (Figures 4.12(b)(i) and (b)(ii)) and as hourglass shaped stress fields at the tip region of the propagating experimental sill (Figure 4.12(b)(iii)).

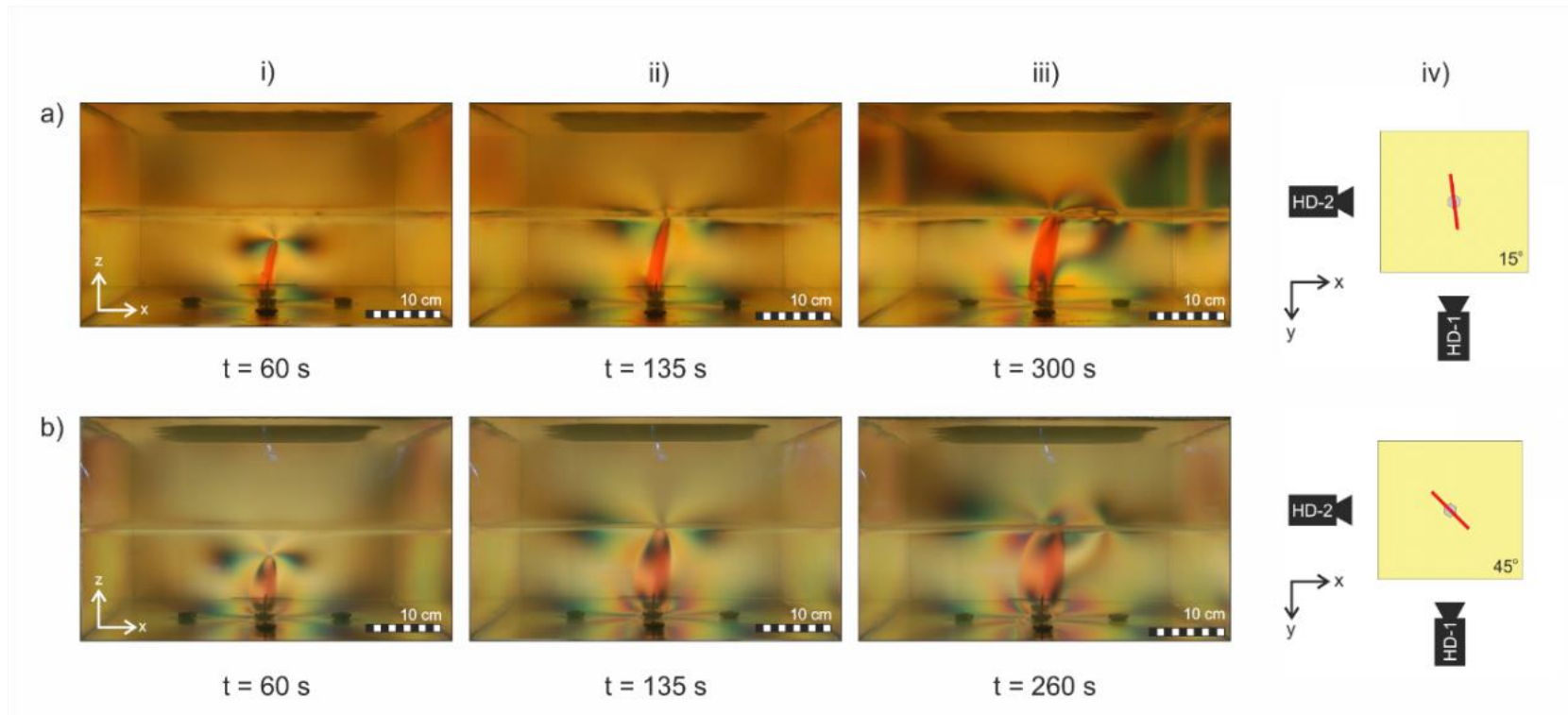


Figure 4.12: Photographs of (a) Experiment SD-16 and (b) Experiment SD-17 taken at three different time steps: (i) 60 seconds, (ii) 135 seconds, (iii)(a) 300 seconds and (iii)(b) 260 seconds respectively. Figure (iv) shows the top-down view (x-y plane) of each experiment to show the angle of rotation of experimental dyke.

4.4.3.2 Surface Elevation Change Profiles

The overall change in surface topography as a sill forms from a dyke is shown in Figure 4.13. These two plots capture the displacement of the surface resulting from the growth of the experimental sill. Note that the vertical scale for these plots have been removed to better illustrate the changes in surface topography over time (time stamps labelled next to each profile line). The plots illustrate the progressive change of surface topography from the inception of the dyke up to when the sill has grown to a length of 80 mm away from the tip of the dyke. This particular length is defined to keep the changes of surface topography within the predefined area of interest (140 mm-long laser transect with position markers between -70 mm and 70 mm. The sill length of 80 mm was found to still be within the area of interest as the dykes grew at an angle). Unlike the prominent changes recorded in dyke experiments, the surface deformation expressed in sill experiments was less defined and was found to show more regional uplift where the surface of the gelatine is progressively uplifted above the growing sill.

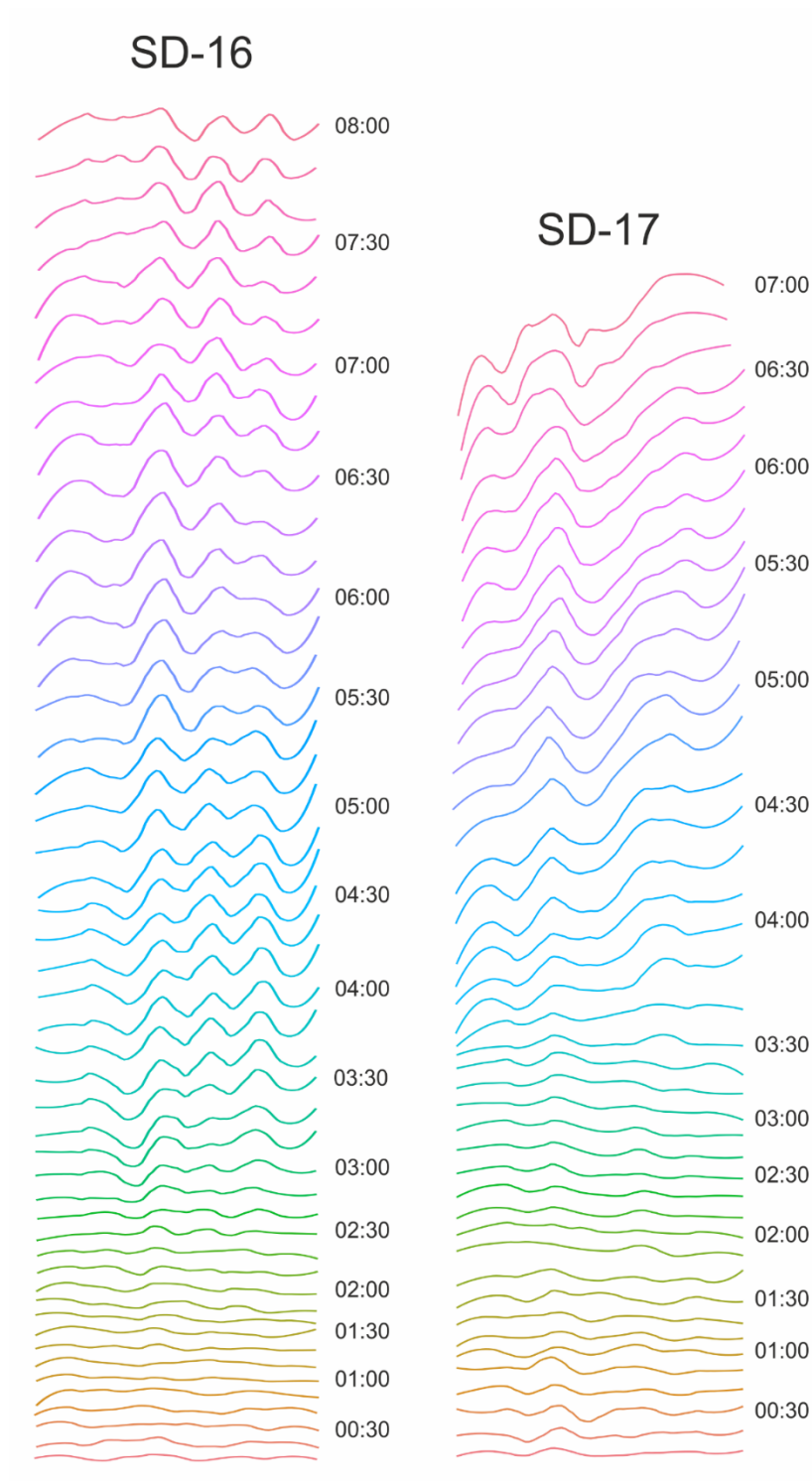


Figure 4.13: The plots above show the progressive change in surface topography for Experiments SD-16 and SD-17. The vertical scale has been removed to exaggerate the changes observed between each time stamp. The cumulative surface displacement for Experiment SD-16 is 2.25 mm. The cumulative surface displacement for Experiment SD-17 is 2.5 mm.

4.4.3.3 Incremental Strain Evolution

Figure 4.14 show the results of incremental strain when a dyke feeds a sill. The growth and propagation of experimental sills can be divided into two stages: 1) The inception and propagation of the dyke and 2) The propagation of the experimental sill. The inception and propagation of the dyke (Figures 4.14(i)) shows the strain is focussed at the tip region (e_{xx}). The vector arrows radiate outwards from the tip region emphasizing displacement along the horizontal axis, which matches the “unzipping” pattern previously observed in experiments ADD-01 and PLT-5. When the dyke reaches the interface between the two superposed layers of gelatine, the strain becomes even more focussed at the tip as the dyke continues to push upwards. During this stage (Figure 4.14(c)(i)) the incremental strain is zero in the horizontal axis (e_{xx}). Note that surface displacement at this stage is not only expressed as a region of local negative directly above the dyke, but also across the surface of the gelatine as regional displacement, as seen in e_{zz} . Once the experimental sill begins to propagate along the interface, vertical displacement becomes more prominent with the regions of high displacement now focussed at tips of the propagating sill as seen in Figure 4.14(d)(ii) (e_{zz}). This supports what has been observed in the progressive surface topography change plots shown in Figure 4.13.

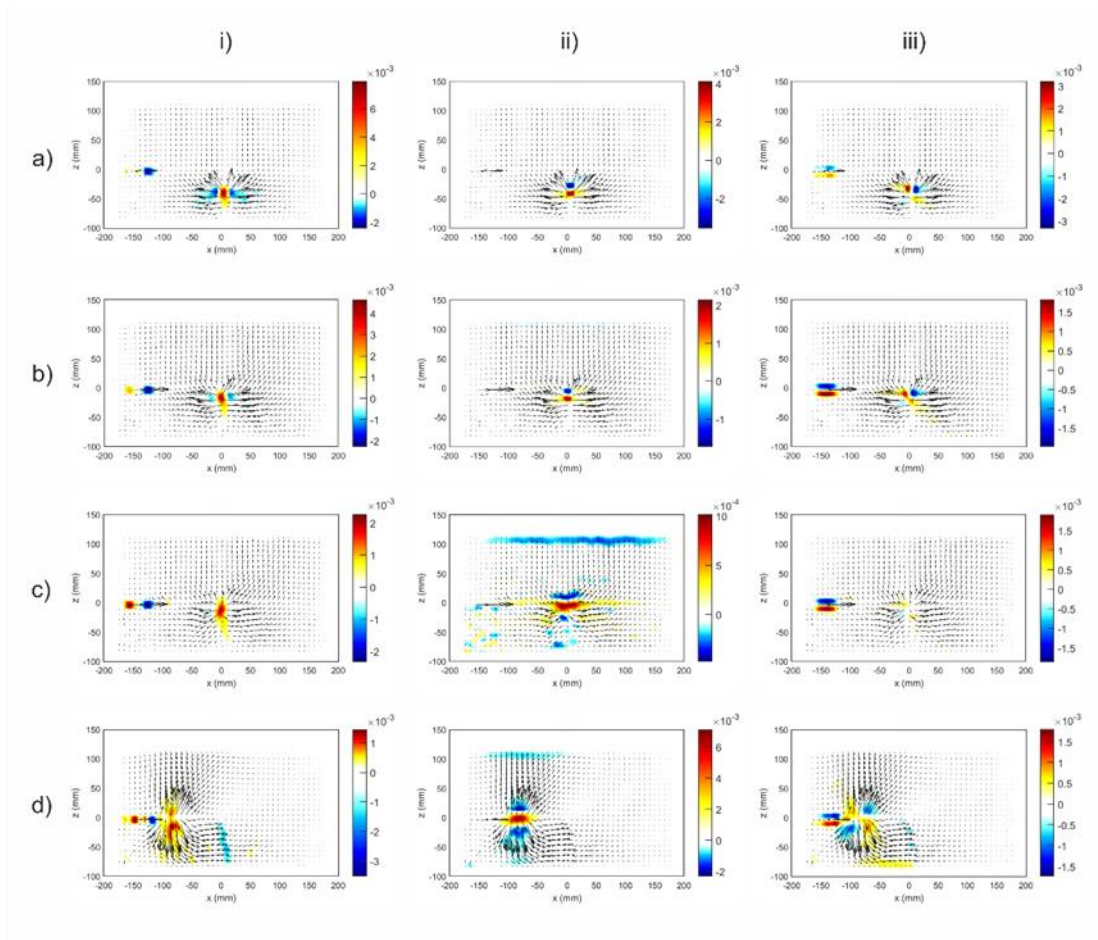


Figure 4.14: The evolution of strain in the host material (gelatine) during dyke and sill formation as observed through three planes: (i) e_{xx} : Strain along the horizontal axis, (ii) e_{zz} : Strain along the vertical axis and (iii) e_{xz} : Shear strain in the x-z plane. The images are arranged to show four key stages of sill inception and propagation: (a) Inception of the experimental dyke, (b) Propagation and growth of the experimental dyke where the dyke meets the interface and stalls, (c) Diversion of the propagating dyke along the interface (sill formation) and (d) Sill propagation.

4.5 Discussion

The following methods have been employed and described in this chapter: 1) Recording the changes in intrusion geometry using a digital camera, aided by artificial light, 2) Recording the deformation of the host material using a digital camera, through polarising sheets attached on the outside of the tank, 3) Seeding the gelatine host with fluorescent particles to record host material deformation using two CCD cameras and a laser sheet illuminating

the experimental tank, and 4) Recording the surface deformation using an overhead laser positioned over the experimental tank. Using a combination of the qualitative and quantitative methods described here, future researchers will be able to: 1) visualise and quantify the geometry of the intrusion over time, 2) visualise and quantify the sub-surface deformation in the host material during intrusion propagation, and 3) visualise and quantify the deformation at the surface of the gelatine resulting from the propagation of the intrusion.

The experiments highlight four key stages in the propagation and growth of dykes and sills. The first stage is the inception of the dyke, forming a penny-shaped fluid-filled fracture of equal length and width. Next in the second stage, the penny-shaped dyke continues to grow outwards forming a larger penny-shape of equal length and width. The third and fourth stages differ depending on the experimental setup. The third stage of growth in single layer experiments capture the ascent of the dyke towards the surface where the penny-shaped dyke evolves into an ellipse-shaped dyke. The change in geometry is due to the dyke growing faster vertically than horizontally, stretching the dyke into an ellipse. As the dyke approaches the surface, the vertical growth accelerates until the dyke breaches the surface as a fissure eruption in the fourth stage. The surface deformation pattern above experimental dykes are expressed as two topographic highs flanking a region of topographic low, reflecting the pattern of the bow-tie shaped colour fringes observed through polarised light. The third stage of growth in two-layer sill-forming experiments highlight the stage at which the dyke propagation gets diverted at the gelatine interface. When the intrusion propagation is recorded using polarised light, the bow-tie shaped colour fringes at the tip of the dyke near the interface remains present while a new set of colour fringes appear at the edge of the growing sill. However, no prominent deformation is detected at the surface during this stage. The fourth stage captures the propagation and growth of the experimental sill as it continues to propagate along the interface. The colour fringes at the edge of the sill as viewed using

polarised light continues to grow as the sill propagates away from the dyke. The surface deformation pattern above sills are expressed as regional uplift above the growing sill.

These results have important implications on our understanding of dyke and sill propagation and how the processes are modelled, in particular modelling the host-rock as an elastic material, modelling magma as a Newtonian fluid, the effect of tectonic stresses on magma intrusion and comparison of experimental surface deformation patterns with intrusions in nature.

4.5.1 Modelling the host-rock as an elastic material

The results from the experiments presented in this chapter emphasise how gelatine is an excellent material for modelling elastic crustal behaviour. Other experimental models in literature such as studies by Le Corvec et al. (2013), Kavanagh et al. (2015) and Pansino et al. (2019) also support the use of gelatine as the host rock analogue for an elastically deforming crust (see Table 1.1, Chapter 1 for other examples). The caveat of using gelatine as the host-material however is that the methods presented can only be applied to models which assume that the intrusions are emplaced in an elastically deforming crust. It is worth noting that models developed by geophysicists and geodesists assume that the crust deforms elastically (Fialko et al., 2001) and common analytical models such as the Mogi model (Mogi, 1958) and Okada model (Okada, 1985) also assume an elastically deforming crust. Taking these points into account, it is not only be relevant, but is also greatly beneficial to explore this modelling framework to test against the methods in this chapter.

4.5.1.1 Mechanical heterogeneities and other host-rock analogues

The experiments described in this chapter use a homogeneous (sometimes layered) solid which behaves elastically to represent the upper crust and host-rock of the intrusions. Having a mechanically layered crust would better represent the natural system, and this was

required for sills to form in the experiments. However, this setup neglects any heterogeneities in the Earth's upper crust occurring within layers; factors such as faulting or lateral changes in composition, which might affect the mechanical properties of the layer.

In addition, the nature of fracturing in elastically deforming models (pure hydraulic fractures) mean that these experimental intrusions do not exhibit any 'damage zones' around their tips as they grow. Rocks in nature break and brecciate to accommodate the propagation of magma which creates a material that is less coherent and behaves in a non-elastic/plastic manner (Daniels et al., 2012; Schofield et al., 2012). Therefore, should the researcher wish to explore the growth and evolution of intrusion in a host material that deforms in a brittle-ductile manner, then a granular host material would be more favourable (Brown et al., 2007).

Creating models in a granular host presents a different set of challenges compared to gelatine models as the model being opaque requires the experimental intrusions to be excavated post-experiment in order to study the intrusion geometry (Galland, 2012; Guldstrand et al., 2017). These hurdles can now be overcome by employing 3D scanning techniques which allow the researcher to image the evolution of the intrusions in real time. One method that has recently been employed is by using an X-Ray Computed Tomography scanner, also commonly referred to as CT scanners (Poppe et al., 2019). However, this specific imaging method has a size limitation to allow the experimental setup to fit inside the aperture of the CT scanner and achieve the best imaging resolution. The experiments by Poppe et al. (2019) are smaller than most analogue models (see Table 1.1, Chapter 1), where granular material is placed in a plexiglass box measuring 20 cm x 20 cm x 16 cm. Analogue models which use granular materials as the host analogue often use a mixture of two materials to achieve the desired rheology of the host material. Examples of commonly-used granular mixtures in literature include sand-flour mixtures (Donnadiou and Merle, 1998), sand-plaster mixtures (Kervyn et al., 2009) and sand-gypsum mixtures (Holohan et al., 2013; Poppe et al., 2019).

One caveat of using a mixture of two (or more) granular materials is ensuring that the mixture has been uniformly mixed to create a homogenous mixture. Other challenges researchers need to address when using granular materials as the host rock analogue are the effect of humidity on the strength of the granular material as well as how to effectively compact the material for experiments. The problem of humidity can be tackled by oven-drying the materials overnight and closely monitoring the ambient humidity of the room in which the experiments are carried out (Poppe et al., 2019). Manual compaction, while straightforward, could result in uneven compaction of the granular materials used. One method to ensure even compaction is by using a high-frequency vibrator which shakes the experimental box containing the granular materials until the desired bulk density is achieved (Guldstrand et al., 2018).

4.5.1.2 Thermal effects on the host-rock

Lastly, it should be noted that the experiments in this chapter do not address the effects of intrusion temperature on the mechanical properties of the host rock, which in turn affects the way magma intrudes and propagates. Shallow crustal rocks near intrusions could be porous or unconsolidated due to brecciation, stoping or weathering (Daniels et al., 2012), and heat from the magmatic intrusion can vaporise water present in the crustal rocks which fluidises the surrounding rocks with propagation. For example, aerial observation of the Golden Valley Sill in South Africa show an example of how intrusions propagate by fluidisation, where a series of tube-like fingers have formed at the edge of the sheet (Schofield et al., 2010). The presence of hydrothermally deposited calcite and in-filled gas bubbles in the lobate part of these fingers further imply that the propagation of these fingers have been driven by the mobilisation of hot fluids and gases in the host rock which has deformed in a non-brittle manner (Schofield et al., 2010, 2012). Providing there is sufficiently high heat flux, magma propagating through the crust can melt the surrounding host rock and assimilate it

into the melt. This process is more prominent at depth and is associated with larger igneous bodies such as plutons (Annen et al., 2015).

There are a few studies which have incorporated heated magma analogues into their experiments using materials such as vegetable oil (Chanceaux and Menand, 2016; Daniels and Menand, 2015; Galland, 2012) and molten wax (Taisne and Tait, 2011). While these models address the effects of crustal melting on the geometry of the intrusions (dyke thickness, formation of lobes, formation of sills, etc.) they do not address how the temperature difference between the intrusion and the host rock as well as the proximity of the intrusion to the magma source may affect the rheology of the intruded host rock (Chanceaux and Menand, 2016). Introducing a thermal parameter to these models creates a magma analogue that is closer in behaviour to its natural counterpart. However, this also introduces a layer of complexity to the models as the progressive melting and evolving mechanical properties of the host analogue would also be difficult to track and quantify.

4.5.2 The effect of magma rheology on intrusion dynamics

The rheology or flow behaviour of magmas can be described by the relationship between shear stress and strain rate as shown in Figure 4.15 (Kavanagh et al., 2018). This graph of shear stress (Pa) against strain rate (s^{-1}) shows how different fluids behave when increasing levels of stress are applied. The slopes of the individual curves represent the viscosity of the fluids, which indicate how easy (low viscosity = gentle slope, e.g. crystal-poor or low silica magma) or difficult (high viscosity = steep slope, e.g. crystal-rich or high silica magma) it is for the fluid to flow. The examples shown can be divided into two groups: 1) Newtonian fluids (high viscosity and low viscosity) and 2) Non-Newtonian fluids (Herschel-Bulkley fluids, Bingham fluids, shear thinning fluids and shear thickening fluids).

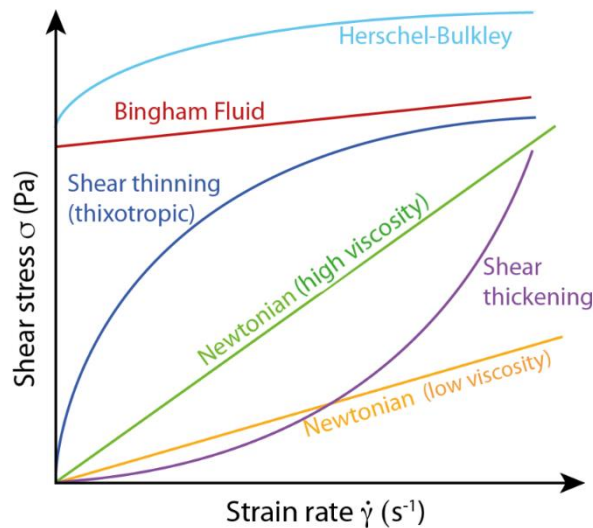


Figure 4.15: The flow curves of different fluid rheologies based on the relationship between shear stress and strain rate (Kavanagh et al., 2018)

Newtonian fluids are fluids that do not change viscosity no matter how much shear stress is applied, and this is reflected in the graph as a linear relationship between shear stress and strain rate. Analogue models often use Newtonian fluids such as water, a low viscosity Newtonian fluid (Fiske and Jackson, 1972; Kavanagh et al., 2013; McLeod and Tait, 1999; Takada, 1990) or vegetable oil, a higher viscosity Newtonian fluid (Chanceaux and Menand, 2016; Daniels and Menand, 2015; Galland, 2012). These single-phase magma analogues are representative of a crystal and bubble-free magma which would hypothetically form at depth near the source of magma with little to no cooling involved. This pure melt type magma possibly never occurs in nature as magma is almost always a multiphase liquid which consists of various proportions of melt, crystal and bubbles (Jones et al., 2020; Kavanagh et al., 2018). The physical and mechanical properties of low-viscosity Newtonian fluids such as water and silicone oils however make them appropriate analogues for modelling the intrusion of low-viscosity magmas such as basalts (Galland et al., 2013). Therefore while the magma analogue used in this chapter (dyed water) does not directly address the effects of heterogeneity of magma in a natural system, the chosen analogue is suitable for modelling the propagation of

low-viscosity magma in the shallow crust. Nevertheless, the effects of crystals and bubbles on magma rheology should be addressed in analogue models in order to better emulate the behaviour of magma in a natural system.

The effect of crystals on the rheology of magma, specifically the effects of solidification of magma, has been explored using experiments with solidifying fluid such as molten wax (Taisne and Tait, 2011) and vegetable oil (Chanceaux and Menand, 2016, 2014) as the magma analogue. Compared to the models presented in this chapter, the models which employ solidifying fluid as the magma analogue result in different intrusion geometries where the intrusions exhibit a more complex lobate geometry instead of a simple penny-shaped or ellipse-shaped intrusion. When the solidification effects were low, the intrusions were found to propagate in a quasi-continuous manner. When the solidification effects were high however, the propagation would occur in a step-like manner (Taisne and Tait, 2011). This step-like propagation is more prominent in sill-forming experiments with high solidification effects where the sill propagation continues after momentary arrest (due to solidification), forming breakout intrusions at the margins of the sill and not necessarily at its leading tip (Chanceaux and Menand, 2016). These experiments show how discontinuous propagation is related to the process of solidification and this can be associated with seismic bursts in nature related to the propagation of magma in volcanically active regions (Chanceaux and Menand, 2014).

The presence of bubbles play an important part in controlling the viscosity and buoyancy of fluids in a shallow magmatic systems and can influence the scale and style of volcanic eruptions (Parmigiani et al., 2016). The presence of bubbles particularly in feeder dykes adds buoyancy to the magma which drives the ascent of magma through the Earth's crust resulting in large-volume effusive eruptions such as the Holohraun eruption in Iceland (Sigmundsson et al., 2020). When bubbles become concentrated at the tip of a feeder dyke close to the

surface this could potentially result in an explosive volcanic eruption depending on the retention of volatiles in the magma due to its increased magmatic overpressure (Geshi et al., 2020).

The effect of bubbles on the rheology of magma, particularly the effects of vesiculation (formation of bubbles) can be complex to model in a laboratory setting. The straightforward method that has been employed in modelling two-phase magmas (bubble-rich, crystal-free magma) has been to introduce bubbles to a Newtonian analogue fluid (Rust and Manga, 2002). However, this presents a set of experimental challenges where: 1) the presence of bubbles in suspension may interrupt the imaging of any fluid dynamics due to its opacity, 2) the size and distribution of bubbles which influences the overall material rheology is difficult to measure and control and 3) the density of bubbles, when less dense than the host fluid, causes the bubbles to rise during experiments which adds complexity to the fluid dynamics being studied (Jones et al., 2020). One approach that has been taken to overcome the challenges listed is by circumventing the need to use both bubbles and fluids as part of the magma analogue and instead using a single-phase analogue which simulates the shear-thinning behaviour of bubble suspension. Experiments by Jones et al. (2020) use hydroxyethyl cellulose (HEC), a shear-thinning polymer which is water-soluble and commonly used in cosmetics, food and pharmaceutical industries as a thickening and gelling agent. The mechanical properties of HEC as a shear-thinning fluid makes it an excellent analogue for bubbly magma but it can be also be used in many existing scaled experimental setups due to its adjustable viscosity and viscoelastic properties (Jones et al., 2020).

Modelling the complex behaviour of a three-phase system while challenging, has been done, using the suspension of crystals and bubbles in a non-Newtonian fluid under steady and unsteady flow conditions (Pistone et al., 2012) and the suspension of crystals and bubbles in a Newtonian fluid undergoing steady flow (Truby et al., 2015). The development of more

models which explore the use of two-phase and three-phase magmas in analogue models however, are still needed in order to better constrain the relationship between magma rheology and how magma propagates through the Earth's crust.

4.5.3 The effect of stresses on magma intrusion

Tectonic stresses have been shown to strongly influence the propagation of magma-filled fractures in the Earth's crust. Intrusions have a tendency to propagate in the direction of maximum compressive stress (σ_1) and this differs between intrusion geometries (Roberts, 1970). The direction of maximum compressive stress in rifting regions is vertical, favouring the formation of dykes (e.g. Daniels and Menand, 2015), and the direction of maximum compressive stress in compressive regions is horizontal, favouring the formation of sills (e.g. Menand et al., 2010). However, it is also possible for intrusions to grow in tectonically quiet areas such as cratons or intra-plate settings. Topographic changes may also affect crustal loading, e.g. a volcanic edifice applies additional stress to the crust (Kervyn et al., 2009; Walter and Troll, 2003), and a graben or caldera creates an unloaded stress (Gaete et al., 2019; Urbani et al., 2018). In addition, it has been shown that pressurised dykes can influence the stress-field surrounding them, which may in turn affect the propagation of neighbouring dykes (e.g. Roman et al., 2004). Therefore, it will be highly likely that any comparison of experimental intrusion growth dynamics or deformation patterns with the natural counterpart will be influenced by tectonic stress, local stress, or both.

The experiments presented in this chapter do not include tectonic stresses but instead are influenced by local stresses from the pressurised intrusions and their interactions with the weakly-bonded interface and presence of a stiff upper layer. Creating a uniform 'tectonic' stress field in the experiments is possible (e.g. Daniels and Menand, 2015; Menand et al., 2010) but ensuring the homogeneous distribution of the stress can be challenging due to boundary effects (e.g. the tank floor and walls). The methodology presented in this chapter

on the other hand can only be directly applied to intrusions in tectonically-quiet area. However, it is important to note that real observations from the rock record and from InSAR (Pinel et al., 2014; Sigmundsson et al., 2014) come from tectonically active regions. Therefore, the consideration of the influence of tectonic stresses on the geometry, velocity and stress distribution around dyke and sill growth need to be addressed in future models.

4.6 Conclusion

The results from the laboratory experiments can be summarised in two parts:

- 1) The stages of propagation and growth of experimental dykes and
- 2) The stages of propagation and growth of experimental sills.

4.6.1 Propagation and Growth of Experimental Dykes

Stage 1: Inception of experimental dyke.

Characterised by the formation of a penny-shaped fluid-filled fracture of equal length and width. The tip of the dyke is flanked by localised small bow-tie shaped stress fields. Deformation is not expressed on the surface of the gelatine.

Stage 2: Growth and propagation of experimental dyke.

The penny-shaped dyke continues to grow outwards forming a larger penny shape with equal length and width. The tip of the dyke is flanked by larger bow-tie shaped stress fields. Deformation is not expressed on the surface of the gelatine.

Stage 3: Ascent approaching surface (Pre-eruption).

The penny-shaped dyke has now stretched out vertically, growing faster vertically than horizontally, creating an ellipse-shaped dyke. The stress fields at the tip of the dyke are now

interacting with the surface of the gelatine. Deformation at the surface is most prominent at this stage, expressed at the surface at two regions of topographic high flanking a region of linear topographic low. The region of topographic low corresponds to the position of the dyke tip.

Stage 4: Fissure eruption.

The experimental dyke erupts at the surface as a fissure eruption. The stress fields dissipate.

4.6.2 Propagation and Growth of Experimental Sills

Stage 1: Inception of dyke.

Characterised by the formation of a penny-shaped fluid-filled fracture of equal length and width. The tip of the dyke is flanked by localised small bow-tie shaped stress fields. Deformation is not expressed on the surface of the gelatine.

Stage 2: Growth and propagation of dyke.

The penny-shaped dyke continues to grow outwards forming a larger penny shape with equal length and width. The tip of the dyke is flanked by larger bow-tie shaped stress fields. Deformation is not expressed on the surface of the gelatine. The dyke then stalls at the interface. Depending on the stiffness of the upper layer and/or the strength of the interface between the two layers, the dyke may continue to grow laterally (creating a dyke with a larger width compared to its length). If the bonded interface is strong, the dyke might pierce the bonded contact to continue propagating vertically as a dyke.

Stage 3: Diversion of intrusion propagation path at interface.

Once the dyke is able to exploit the interface, the dyke is diverted to propagate horizontally along the interface forming a sill. The dyke retains its bow-tie shaped stress fields.

Deformation is not expressed at the surface as two regions of topographic high flanking a region of topographic low as seen in the dyke experiments due to the depth of the formation.

Stage 4: Propagation and growth of experimental sill.

The sill continues to propagate along the interface and a second set of stress fields in the shape of an overturned bow-tie (or an hourglass) flank the tip of the sill, away from the dyke.

The deformation is expressed on the surface as regional uplift above the growing sill.

4.7 Limitations and future work

The deformation at the surface of the gelatine during the sill experiments could not be recorded due to the following limitations:

- The interface was too far away from the laser transect. The deformation in the dyke experiments were only picked up 120 seconds before eruption, approximately 4 centimetres away from the surface. The interface where the sill was formed was 20 centimetres away from the surface.
- The complete surface deformation caused by the growth of the sill could not be recorded as the overhead laser could only record the surface in a sweeping motion which means that it would not be able to record the overall surface change over time. Therefore, using a laser transect only provides a snippet into what the deformation would look like at the surface.

For future work exploring the surface deformation related to sill formation, it is recommended to have the interface closer to the surface of the gelatine (less than 4 centimetres away from the surface of the gelatine) and to have a scanner capable of recording the changes of the entire surface/ to develop a method in which surface changes can be extracted from video recordings of the surface.

4.8 Chapter References

- Acocella, V., Mulugeta, G., 2001. Surface deformation induced by pluton emplacement: The case of Amiata (Italy). *Phys. Chem. Earth, Part A Solid Earth Geod.* 26, 355–362.
- Al Shehri, A., Gudmundsson, A., 2018. Modelling of surface stresses and fracturing during dyke emplacement: Application to the 2009 episode at Harrat Lunayyir, Saudi Arabia. *J. Volcanol. Geotherm. Res.*
- Annen, C., Blundy, J.D., Leuthold, J., Sparks, R.S.J., 2015. Construction and evolution of igneous bodies: Towards an integrated perspective of crustal magmatism. *Lithos* 230, 206–221.
- Brown, R.J., Kavanagh, J., Sparks, R.S.J., Tait, M., Field, M., 2007. Mechanically disrupted and chemically weakened zones in segmented dike systems cause vent localization: Evidence from kimberlite volcanic systems. *Geology* 35, 815–818.
- Castro, J.M., Cordonnier, B., Schipper, C.I., Tuffen, H., Baumann, T.S., Feisel, Y., 2016. Rapid laccolith intrusion driven by explosive volcanic eruption. *Nat. Commun.* 7, 13585.
- Chanceaux, L., Menand, T., 2014. Solidification effects on sill formation: An experimental approach. *Earth Planet. Sci. Lett.* 403, 79–88.
- Chanceaux, L., Menand, T., 2016. The effects of solidification on sill propagation dynamics and morphology. *Earth Planet. Sci. Lett.* 442, 39–50.
- Crisp, J.D.C., 1952. The use of gelatin models in structural analysis. *Proc. Inst. Mech. Eng. Part B J. Eng. Manuf.* 1, 580–604.
- Daniels, K.A., Kavanagh, J.L., Menand, T., Sparks, R.S.J., 2012. The shapes of dikes: Evidence for the influence of cooling and inelastic deformation. *Bull. Geol. Soc. Am.* 124, 1102–

1112.

Daniels, K.A., Menand, T., 2015. An experimental investigation of dyke injection under regional extensional stress. *J. Geophys. Res. Solid Earth* 120, 2014–2035.

Donnadieu, F., Merle, O., 1998. Experiments on the indentation process during cryptodome intrusions: new insights into Mount St. Helens deformation. *Geology* 26, 79–82.

Fialko, Y., Khazan, Y., Simons, M., 2001. Deformation due to a pressurized horizontal circular crack in an elastic half-space, with applications to volcano geodesy. *Geophys. J. Int.* 146, 181–190.

Fialko, Y., Pearse, J., 2012. Sombrero uplift above the Altiplano-Puna magma body: Evidence of a ballooning mid-crustal diapir. *Science* (80-.). 338, 250–252.

Fiske, R.S., Jackson, E.D., 1972. Orientation and Growth of Hawaiian Volcanic Rifts: The Effect of Regional Structure and Gravitational Stresses. *Proc. R. Soc. A Math. Phys. Eng. Sci.* 329, 299–326.

Fukushima, Y., Cayol, V., Durand, P., Massonnet, D., 2010. Evolution of magma conduits during the 1998–2000 eruptions of Piton de la Fournaise volcano, Réunion Island. *J. Geophys. Res. Solid Earth* 115.

Gaete, A., Kavanagh, J.L., Rivalta, E., Hilmi Hazim, S., Walter, T.R., Dennis, D.J.C., 2019. The impact of unloading stresses on post-caldera magma intrusions. *Earth Planet. Sci. Lett.* 508, 109–121.

Galland, O., 2012. Experimental modelling of ground deformation associated with shallow magma intrusions. *Earth Planet. Sci. Lett.* 317–318, 145–156.

Galland, O., Burchardt, S., Troll, V., 2013. Volcanic and Igneous Plumbing Systems: State-of-

the-Art and Future Developments. *Eos* (Washington. DC). 94, 2013.

Galland, O., Scheibert, J., 2013. Analytical model of surface uplift above axisymmetric flat-lying magma intrusions: Implications for sill emplacement and geodesy. *J. Volcanol. Geotherm. Res.* 253, 114–130.

Geshi, N., Browning, J., Kusumoto, S., 2020. Magmatic overpressures, volatile exsolution and potential explosivity of fissure eruptions inferred via dike aspect ratios. *Sci. Rep.* 10, 1–9.

Guldstrand, F., Burchardt, S., Hallot, E., Galland, O., 2017. Dynamics of Surface Deformation Induced by Dikes and Cone Sheets in a Cohesive Coulomb Brittle Crust. *J. Geophys. Res. Solid Earth* 122, 8511–8524.

Guldstrand, F., Galland, O., Hallot, E., Burchardt, S., 2018. Experimental Constraints on Forecasting the Location of Volcanic Eruptions from Pre-eruptive Surface Deformation. *Front. Earth Sci.* 6, 7.

Holohan, E.P., Walter, T.R., Schöpfer, M.P.J., Walsh, J.J., Van Wyk De Vries, B., Troll, V.R., 2013. Origins of oblique-slip faulting during caldera subsidence. *J. Geophys. Res. Solid Earth* 118, 1778–1794.

Jones, T.J., Llewellyn, E.W., Mader, H.M., 2020. The use of a shear-thinning polymer as a bubbly magma analogue for scaled laboratory experiments. *J. Volcanol. Geotherm. Res.* 392, 106768.

Kavanagh, J.L., Boutelier, D., Cruden, A.R., 2015. The mechanics of sill inception, propagation and growth: Experimental evidence for rapid reduction in magmatic overpressure. *Earth Planet. Sci. Lett.* 421, 117–128.

- Kavanagh, J.L., Engwell, S., Martin, S.A., 2018. A review of analogue and numerical modelling in volcanology. *Solid Earth Discuss.* 95194, 1–80.
- Kavanagh, J.L., Menand, T., Daniels, K.A., 2013. Gelatine as a crustal analogue: Determining elastic properties for modelling magmatic intrusions. *Tectonophysics* 582, 101–111.
- Kavanagh, J.L., Menand, T., J. Sparks, R.S., Sparks, R.S.J., 2006. An Experimental Investigation of Sill Formation and Propagation in Layered Elastic Media. *Earth Planet. Sci. Lett.* 245, 799–813.
- Kavanagh, J.L., Rogers, B.D., Boutelier, D., Cruden, A.R., 2017. Controls on sill and dyke-sill hybrid geometry and propagation in the crust: The role of fracture toughness. *Tectonophysics* 698, 109–120.
- Kervyn, M., Ernst, G.G.J., van Wyk de Vries, B., Mathieu, L., Jacobs, P., 2009. Volcano load control on dyke propagation and vent distribution: Insights from analogue modeling. *J. Geophys. Res.* 114.
- Letourneur, L., Peltier, A., Staudacher, T., Gudmundsson, A., 2008. The effects of rock heterogeneities on dyke paths and asymmetric ground deformation: The example of Piton de la Fournaise (Réunion Island). *J. Volcanol. Geotherm. Res.* 173, 289–302.
- Magee, C., Bastow, I.D., de Vries, B. van W., Jackson, C.A.L., Hetherington, R., Hagos, M., Hoggett, M., 2017. Structure and dynamics of surface uplift induced by incremental sill emplacement. *Geology* 45, 431–434.
- McLeod, P., Tait, S.R., 1999. The growth of dykes from magma chambers. *J. Volcanol. Geotherm. Res.* 92, 231–246.
- Menand, T., Daniels, K.A., Benghiat, P., 2010. Dyke propagation and sill formation in a

- compressive tectonic environment. *J. Geophys. Res. Solid Earth* 115, B08201.
- Mogi, K., 1958. Relations of the eruptions of various volcanoes and the deformations of the ground around them. *Bull. Earthq. Res. Inst. Tokyo Univ* 36, 98–134.
- Okada, Y., 1985. Surface deformation due to shear and tensile faults in a half-space. *Bull. Seismol. Soc. Am.* 75, 1135–1154.
- Parmigiani, A., Faroughi, S., Huber, C., Bachmann, O., Su, Y., 2016. Bubble accumulation and its role in the evolution of magma reservoirs in the upper crust. *Nature* 532, 492–495.
- Pedersen, R., Sigmundsson, F., 2006. Temporal development of the 1999 intrusive episode in the Eyjafjallajökull volcano, Iceland, derived from InSAR images. *Bull. Volcanol.* 68, 377–393.
- Pinel, V., Poland, M.P., Hooper, A., 2014. Volcanology: Lessons learned from Synthetic Aperture Radar imagery. *J. Volcanol. Geotherm. Res.*
- Pistone, M., Caricchi, L., Ulmer, P., Burlini, L., Ardia, P., Reusser, E., Marone, F., Arbaret, L., 2012. Deformation experiments of bubble- and crystal-bearing magmas: Rheological and microstructural analysis. *J. Geophys. Res. Solid Earth* 117.
- Poppe, S., Holohan, E.P., Galland, O., Buls, N., Van Gompel, G., Keelson, B., Tournigand, P.Y., Brancart, J., Hollis, D., Nila, A., Kervyn, M., 2019. An inside perspective on magma intrusion: Quantifying 3d displacement and strain in laboratory experiments by dynamic X-ray computed tomography. *Front. Earth Sci.* 7, 62.
- Roberts, J.L., 1970. The intrusion of magma into brittle rocks, *Journal of. ed, Mechanism of Igneous Intrusion*. Liverpool Letterpress Limited, Liverpool.
- Roman, D.C., Moran, S.C., Power, J.A., Cashman, K. V., 2004. Temporal and spatial variation

of local stress fields before and after the 1992 eruptions of Crater Peak vent, Mount Spurr volcano, Alaska. *Bull. Seismol. Soc. Am.* 94, 2366–2379.

Rust, A.C., Manga, M., 2002. Bubble Shapes and Orientations in Low Re Simple Shear Flow. *J. Colloid Interface Sci.* 249, 476–480.

Schofield, N., Stevenson, C., Reston, T., 2010. Magma fingers and host rock fluidization in the emplacement of sills. *Geology* 38, 63–66.

Schofield, N.J., Brown, D.J., Magee, C., Stevenson, C.T., 2012. Sill morphology and comparison of brittle and non-brittle emplacement mechanisms. *J. Struct. Geol.* 169, 127–141.

Sigmundsson, F., Hooper, A., Hreinsdóttir, S., Vogfjörð, K.S., Ófeigsson, B.G., Heimisson, E.R., Dumont, S., Parks, M., Spaans, K., Gudmundsson, G.B., Drouin, V., Árnadóttir, T., Jónsdóttir, K., Gudmundsson, M.T., Högnadóttir, T., Fridriksdóttir, H.M., Hensch, M., Einarsson, P., Magnússon, E., Samsonov, S., Brandsdóttir, B., White, R.S., Ágústsdóttir, T., Greenfield, T., Green, R.G., Hjartardóttir, Á.R., Pedersen, R., Bennett, R.A., Geirsson, H., la Femina, P.C., Björnsson, H., Pálsson, F., Sturkell, E., Bean, C.J., Möllhoff, M., Braidon, A.K., Eibl, E.P.S., 2014. Segmented lateral dyke growth in a rifting event at Bárðarbunga volcanic system, Iceland. *Nature* 517, 191–195.

Sigmundsson, F., Pinel, V., Grapenthin, R., Hooper, A., Halldórsson, S.A., Einarsson, P., Ófeigsson, B.G., Heimisson, E.R., Jónsdóttir, K., Gudmundsson, M.T., Vogfjörð, K., Parks, M., Li, S., Drouin, V., Geirsson, H., Dumont, S., Fridriksdóttir, H.M., Gudmundsson, G.B., Wright, T.J., Yamasaki, T., 2020. Unexpected large eruptions from buoyant magma bodies within viscoelastic crust. *Nat. Commun.* 11, 1–11.

Taisne, B., Tait, S.R., 2011. Effect of solidification on a propagating dike. *J. Geophys. Res. Solid Earth* 116, B01206.

Takada, A., 1990. Experimental study on propagation of liquid-filled crack in gelatin: shape and velocity in hydrostatic stress condition. *J. Geophys. Res.* 95, 8471–8481.

Truby, J.M., Mueller, S.P., Llewelin, E.W., Mader, H.M., 2015. The rheology of three-phase suspensions at low bubble capillary number. *Proc. R. Soc. A Math. Phys. Eng. Sci.* 471, 20140557.

Urbani, S., Acocella, V., Rivalta, E., 2018. What Drives the Lateral Versus Vertical Propagation of Dikes? Insights From Analogue Models. *J. Geophys. Res. Solid Earth* 123, 3680–3697.

Walter, T.R., Troll, V.R., 2003. Experiments on rift zone evolution in unstable volcanic edifices. *J. Volcanol. Geotherm. Res.* 127, 107–120.

4.9 Software Sources

1. Dynamic Studio. Version 3.41.38. Dantec Dynamics. 18 June 2013. [University Purchase]

2. Tracker. Version 4.96. 7 February 2017. A project of: Open Source Physics (www.opensourcephysics.org). Copyright: 2016, Douglas Brown (www.physlets.org/tracker)

3. ScanCONTROL Configuration Tools. Version 5.0. Micro Epsilon.
(https://www.micro-epsilon.co.uk/2D_3D/laser-scanner/Software/downloads/?dl=1)

4. MATLAB 64-bit. Version 9.4.0.813654, R2018a. 23 February 2018. MATLAB.
(<https://www.mathworks.com/downloads/>) [University License]

5. R. Version 3.5.0 "Joy in Playing". 23 April 2018. Copyright (C) 2018 The R Foundation for Statistical Computing. (<https://cran.r-project.org/>)

5 Conclusions

5.1 Objectives Revisited

The following specific objectives were presented at the beginning of this thesis and here are the conclusions drawn from each chapter.

5.1.1 Chapter 2

Objective: To develop a method to quantify field observations using field photographs. The development of this method will cover the process step-by-step from the acquisition of photographs in the field to how photographs are processed for image analysis. The methodology will then be tested on real photographs taken in the field. Successful development of this method would be particularly useful for field campaigns carried out in difficult to access or inaccessible field areas.

This has been achieved by taking a step-by-step approach starting with identifying the features related to intrusion emplacement in the field through field photographs taken in Torres del Paine, Chile. Once the features of interest have been identified, the methodology to extract quantitative information from these field photographs was designed. The field photographs would first need to be converted to a workable format to be analysed using the software ImageJ. Therefore, the first step was to identify potential sources of errors during the image preparation stage using shapes of known dimensions and area. This sensitivity test highlights the errors caused by curved lines and lines drawn at an angle as these two types of lines introduce extra pixels to smooth out the lines (anti-aliasing). While this is a source of error (as calculations are done on a pixel by pixel basis) it would be impossible to avoid these types of lines altogether in tracing out geological features. Therefore, it would be sufficient for users to note that there are errors associated with the data which are relatively small (within the range of 1-3%). Once the errors have been acknowledged, the method used to

deploy the sensitivity test are then applied onto field photographs from Torres del Paine, Chile. Both field areas provide excellent, glacier-carved exposures which make them suitable field areas to collect test photographs for this study. The feature of interest in both test photographs are intrusions in the exposed roof zone found in the field area. ImageJ is used to extract information about the lengths and thicknesses of each intrusion to be used in calculations of magmatic overpressures. This chapter then closes with recommendations both on how to make the most out of existing field data as well as how to plan ahead for collecting the best field data for the purpose of image analysis.

5.1.2 Chapter 3

Objective: To introduce rigorous testing methods to characterise gelatine as an analogue material, with focus on laboratory modelling of shallow intrusions. This methodology will cover two approaches, one using manual indentation and the other using a rotational rheometer. The outcome of this investigation would be of benefit to the intrusion modelling community to establish a benchmark for experiments using gelatine. Having two approaches to characterise gelatine will make the material characterisation process more accessible to more researchers.

The study in Chapter 3 presents the results from two approaches to characterise the physical properties of gelatine: 1) The indentation method and 2) Rotational rheometry. In this chapter, samples with the following concentrations of gelatine were used: 1.0 wt.%, 1.5 wt.%, 2.0 wt.%, 2.5 wt.%, 3.0 wt.% and 3.5 wt.%. Previous work by Kavanagh et al. (2013) has quantified the physical properties of gelatine at concentrations of 2.0-5.0 wt.% using both rotational rheometry and the indentation method. Studies by Di Giuseppe et al. (2009) and van Otterloo and Cruden (2016) have quantified the physical properties of gelatine with concentrations between 1.0 wt.% and 10 wt.% exclusively using a rheometer, employing various rheometry techniques (e.g. oscillation sweep, amplitude sweep and temperature

sweep) This study complements past studies by adding more data to the lower concentration group (in this study: 1.0 wt.% and 1.5 wt.%) by employing the indentation method, which has previously not been carried out by Di Giuseppe et al. (2009) and van Otterloo and Cruden (2016) as well as to add more rheometry data to the higher concentration group (in this study: 2.0 wt.% - 3.5 wt.%). While rheometry data is available for gelatine in this concentration range, the study by Kavanagh et al. (2015) carried out at the University of Liverpool only presents rheometry data for gelatine with a concentration of 2.5 wt.%. The results of this chapter can now be added to the knowledge base of analogue materials to help other laboratories with benchmarking. Having results that are comparable to published values signal the validity of the testing methods used in this chapter.

5.1.3 Chapter 4

Objective: To demonstrate how laboratory modelling using gelatine as an analogue material can be used to study surface and subsurface deformation and how the results from these experiments relate to examples in nature, which can be beneficial for volcano monitoring programmes and hazard mitigation in volcanic regions.

First, three observational techniques used to monitor three different aspects of the growth of the experimental intrusion were introduced: (1) Intrusion geometry: HD-Camera positioned in the y-z plane, (2) Internal stresses formed during intrusion propagation: HD-Camera positioned in the x-z plane looking through a pair of polarising sheets, and (3) Surface deformation: Overhead laser scanner and overhead camera. The Tracer Particle (TP) method maps the displacement of fluorescent particles suspended in the gelatine solid to illustrate the evolution of internal strain. The results from the experiments show that there is a strong correlation between the shape and inclination of the intrusive body, the shape and orientation of the stress fields and the deformation pattern expressed on the surface. While the dyke experiments expressed prominent surface deformation patterns in the form of

“bow-ties” which was observable using all of the observational techniques, the sill experiments only showed regional deformation on the surface with the “bow-tie” patterns constrained to the evolving intrusion and only observable through polarised light and by using the Tracer Particle method. However, the patterns achieved and observed in these experiment nonetheless are excellent examples of how magma movement at depth can be expressed on the surface and how these processes can be modelled in the laboratory. The dyke experiments in particular showed results which were comparable to published works studying the movement of dykes using satellite imagery as well as numerical simulations, where the surface deformation is expressed as two regions of topographic high flanking a region of topographic low.

5.2 Limitations

For Chapter 2 specifically, there were limitations in terms of permissions granted for movement within the national park. This made it difficult to get close-up photographs of contacts (for example, near the feeder zone where it was difficult to make out the contacts from afar). This also made it difficult to collect in-situ samples representative of the field area as most outcrops were off the permitted trail. However, this limitation helped to steer the direction of the study towards creating a methodology which allowed researchers to still get quantitative data from a field campaign to field areas which may be difficult to access. For Chapters 3 and 4, the distilled water machine could not be used over large periods of when the experiments were conducted, which meant that not all planned experiments were able to be carried out. For Chapter 4, the sweeping motion in which the overhead laser records the surface of the experiment meant that it could not continuously record the changes on the surface. Hence, this is why the surface deformation was only recorded along a linear transect at the centre of the experimental tank. Specific experimental or analytical limitations are discussed in depth at the end of each chapter.

5.3 Future Work

The methodology presented in this thesis could serve as a starting point for other researchers interested in studying volcanic and igneous plumbing systems using laboratory modelling or by analysing photographs captured on field campaigns for the first time.

The step-by-step methods presented for both components of this thesis (field and laboratory studies) serves as an excellent base which could be built upon to suit the needs of different research projects. The list below presents some ideas on how the research presented in this thesis can be expanded in the future:

- 1) Incorporating the use of Structure from Motion to better quantify photographs taken in the field to create high resolution Digital Elevation Models
- 2) Using the laboratory modelling setup to investigate different intrusion geometries such as cone sheets and laccoliths, incorporating fluid dynamics and the rheological properties of the intruding magma
- 3) Developing more efficient and accessible methods to record the surface and sub-surface deformation in the laboratory (not all laboratories would have laser scanners, for example. How could this be done using video footage?)

Developing methods that are accessible and reproducible would help more researchers get on board with digital modelling and laboratory modelling, which would help fortify the knowledge bases characterising intrusions and the deformation associated, which in turn would be beneficial to the investigation of volcanic and igneous plumbing systems as a whole.

6 Appendices

This section contains two publications which employ the analogue modelling methodology presented in this thesis (Chapter 4) to study the propagation of dykes and cone sheets. The experiments in these publications focus on the evolution of sub-surface stresses as well as the expression of deformation on the surface caused by the propagation of intrusions. My contribution to each publication is highlighted in the sub-sections below.

6.1 Publication (1): Challenging dyke ascent models using novel laboratory experiments: Implications for reinterpreting evidence of magma ascent and volcanism

Authors: Janine L. Kavanagh, Alec J. Burns, **Suraya Hilmi Hazim**, Elliot P. Wood, Simon A. Martin, Sam Hignett, David J.C. Dennis

Journal: Journal of Volcanology and Geothermal Research, Volume 354, Pages 87-101, 2018

ISSN: ISSN 0377-0273

DOI: <https://doi.org/10.1016/j.jvolgeores.2018.01.002>
(<http://www.sciencedirect.com/science/article/pii/S0377027317304602>)

Keywords: Magma flow; Host-rock deformation; Dyke; Analogue experiment; Particle image velocimetry; Digital image correlation

6.1.1 Contribution to Publication (1):

The Results section (Section 3) of this publication describes the outcome of an experiment repeated four times using the same concentration of gelatine which had the same volume and injection method but with different imaging techniques applied. My contribution to this publication is presented in Section 3.1: “Dyke propagation geometry and sub-surface stress” and Section 3.4: “Surface deformation during dyke ascent” where I present the findings from Experiments SD-07 and SD-09 which have been labelled as Experiment 1 and Experiment 2

respectively in this publication. Three imaging techniques were used in these experiments: (1) Using artificial light to record the changes in dyke geometry, (2) Using polarised light to record the evolution of stress fields during dyke propagation and (3) Using an overhead laser scanner to record the surface deformation during dyke ascent. The results from these experiments are presented in Figures 2, 3 and 6 of the publication. The results from Experiments 1 and 2 coupled with the results from Experiments 3 and 4 (Sections 3.2 and 3.3) tie together the four stages of dyke ascent as observed through these repeated experiments which is presented in Conclusion section (Section 5) of this publication.

6.2 Publication (2): The impact of unloading stresses on post-caldera magma intrusions

Authors: Ayleen Gaete, Janine L. Kavanagh, Eleonora Rivalta, **Suraya Hilmi Hazim**, Thomas R. Walter, David J.C. Dennis

Journal: Earth and Planetary Science Letters, Volume 508, Pages 109-121, 2019

ISSN: 0012-821X

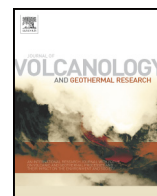
DOI: <https://doi.org/10.1016/j.epsl.2018.12.016>.
(<http://www.sciencedirect.com/science/article/pii/S0012821X18307258>)

Keywords: caldera; cone sheet; gelatin analogue modeling; circumferential dike; digital image correlation

6.2.1 Contribution to Publication (2):

The experiments discussed in this publication were carried out in the MAGMA (Mechanical and Geological Model Analogues) Laboratory at the University of Liverpool by the lead author and myself in 2017. I was directly involved in training the lead author in the laboratory during their time at the University of Liverpool and primarily assisted the lead author during the preparation and running of each experiment. The following imaging techniques were used in these experiments: 1) Using artificial light to record the changing geometry of the intrusion, 2) Using polarised light, to visualise the evolution of stresses around the intrusion and 3)

Using the tracer particle setup, which involves using a high intensity laser sheet to help image the evolving sub-surface stresses. Data processing was carried out by the lead author using Tracker (to quantify evolution of intrusion geometry) and StrainMaster on the software package DaVis Version 8 (to quantify sub-surface displacement vectors and total strain). Two end-member geometries were achieved in these experiments: Circumferential dykes and cone sheets.



Invited research article

Challenging dyke ascent models using novel laboratory experiments: Implications for reinterpreting evidence of magma ascent and volcanism

Janine L. Kavanagh^{a,*}, Alec J. Burns^b, Suraya Hilmi Hazim^a, Elliot P. Wood^a, Simon A. Martin^a, Sam Hignett^a, David J.C. Dennis^b

^a Department of Earth, Ocean and Ecological Sciences, University of Liverpool, Liverpool L69 3GP, United Kingdom

^b School of Engineering, University of Liverpool, Liverpool L69 3GH, United Kingdom

ARTICLE INFO

Article history:

Received 26 July 2017

Received in revised form 21 December 2017

Accepted 2 January 2018

Available online 6 January 2018

Keywords:

Magma flow

Host-rock deformation

Dyke

Analogue experiment

Particle image velocimetry

Digital image correlation

ABSTRACT

Volcanic eruptions are fed by plumbing systems that transport magma from its source to the surface, mostly fed by dykes. Here we present laboratory experiments that model dyke ascent to eruption using a tank filled with a crust analogue (gelatine, which is transparent and elastic) that is injected from below by a magma analogue (dyed water). This novel experimental setup allows, for the first time, the simultaneous measurement of fluid flow, sub-surface and surface deformation during dyke ascent. During injection, a penny-shaped fluid-filled crack is formed, intrudes, and traverses the gelatine slab vertically to then erupt at the surface. Polarised light shows the internal stress evolution as the dyke ascends, and an overhead laser scanner measures the surface elevation change in the lead-up to dyke eruption. Fluorescent passive-tracer particles that are illuminated by a laser sheet are monitored, and the intruding fluid's flow dynamics and gelatine's sub-surface strain evolution is measured using particle image velocimetry and digital image correlation, respectively. We identify 4 previously undescribed stages of dyke ascent. Stage 1, early dyke growth: the initial dyke grows from the source, and two fluid jets circulate as the penny-shaped crack is formed. Stage 2, pseudo-steady dyke growth: characterised by the development of a rapidly uprising, central, single pseudo-steady fluid jet, as the dyke grows equally in length and width, and the fluid down-wells at the dyke margin. Sub-surface host strain is localised at the head region and the tail of the dyke is largely static. Stage 3, pre-eruption unsteady dyke growth: an instability in the fluid flow appears as the central fluid jet meanders, the dyke tip accelerates towards the surface and the tail thins. Surface deformation is only detected in the immediate lead-up to eruption and is characterised by an overall topographic increase, with axis-symmetric topographic highs developed above the dyke tip. Stage 4 is the onset of eruption, when fluid flow is projected outwards and focused towards the erupting fissure as the dyke closes. A simultaneous and abrupt decrease in sub-surface strain occurs as the fluid pressure is released. Our results provide a comprehensive physical framework upon which to interpret evidence of dyke ascent in nature, and suggest dyke ascent models need to be re-evaluated to account for coupled intrusive and extrusive processes and improve the recognition of monitoring signals that lead to volcanic eruptions in nature.

© 2018 The Authors. Published by Elsevier B.V. This is an open access article under the CC BY license (<http://creativecommons.org/licenses/by/4.0/>).

1. Introduction

Nearly all volcanic eruptions are fed by magma-filled fractures that propagate through the crust. The dynamics and propagation of magma intrusions has direct influence on the style, longevity and climatic impact of volcanic eruptions by modulating the supply, ascent rate and rheology of magma that reaches the surface (e.g. Caricchi et al., 2014a, 2014b; Ilyinskaya et al., 2017). Magma intrusion precedes volcanic activity (e.g. Patane et al., 2002), can trigger an eruption (e.g.

Sigmundsson et al., 2010), occurs during volcanism (e.g. Castro et al., 2016) and is active in repose periods between eruptions (e.g. Wright et al., 2012). The majority of dykes do not erupt (e.g. Crisp, 1984; Gudmundsson, 2002) and diverse geophysical, geochemical and geodetic techniques can be readily employed to monitor magma intrusion in the build up to and during volcanic crises, e.g. retrieving seismic profiles, recording volcanic gas emissions, and detecting surface changes in elevation as the magma-filled fractures grow (e.g. Sparks et al., 2012). However, our ability to interpret this data depends on, and is limited by, the validity of model assumptions and field observations.

Volcanic plumbing systems comprise a network of interconnected magma intrusions that vary in orientation relative to stratigraphic layering and span orders of magnitude in volume and aspect ratio (see the collection of papers in the Special Volume by Menand et al., 2011

* Corresponding author.

E-mail address: Janine.Kavanagh@liverpool.ac.uk (J.L. Kavanagh).

for a review). Dykes are vertical to sub-vertical magma-filled fractures that have high aspect ratio (length/thickness), cut across bedding planes of rock strata, and are the primary conduit to transport magma through the crust to potentially erupt (e.g. Geshi et al., 2010; Gudmundsson, 2006). The rock record provides access to ancient volcanic plumbing systems through field studies of the solidified remnants of magma and deformed surrounding host rock in 2D (e.g. Gudmundsson, 2003) and rarely in 3D (e.g. Kavanagh and Sparks, 2011). However, only a partial record will be preserved and it can be difficult to distinguish pre-, syn- and post-magma intrusion processes. Studying dyke propagation in nature is challenging as only remote measurements can be made during an intrusive event. Evidence of recent dyking has been garnered through geophysical and geodetic measurements of intrusions related to on-land rifting, e.g. Afar and Iceland (Wright et al., 2012). The 2014 dyke intrusion associated with the Bardarbunga volcanic system (e.g. Sigmundsson et al., 2014; Gudmundsson et al., 2014) is arguably the most detailed study of an individual dyking event that led to a fissure eruption. Along with studies of eruptive episodes on Etna, Italy (e.g. González and Palano, 2014, Kahl et al., 2011) and Kilauea, Hawaii (e.g. Cervelli et al., 2002) for example, this has done much to shape and inform our understanding of the geophysical signals of magma intrusion that leads to eruption.

Magma ascends through the crust in regional dykes from deep magma reservoirs primarily due to buoyancy; dyke ascent in nature represents the release of gravitational potential energy on a planetary scale (see Putirka, 2017 for a review) and the release of elastic energy on a regional scale. Magma ascent in dykes is facilitated or impeded by the ability of the magma to flow (its rheology) and deformation of mechanically layered and fractured crustal rocks to accommodate the intrusion. Analogue experimentation and numerical modelling are complementary methods to aid the interpretation of field studies and geophysical surveys of magma intrusion (see Rivalta et al. (2015) and Kavanagh et al. (2017b) for reviews). These dyke propagation models have considered a range of physical processes that impact dyke ascent, including magma buoyancy (e.g. Takada, 1990; Rivalta et al., 2005; Taisne and Jaupart, 2009), solidification (e.g. Taisne and Tait, 2011), deformation of the host material (e.g. Abdelmalak et al., 2012; Kavanagh et al., 2015), interaction with a load or stress field (Watanabe et al., 2002; Daniels and Menand, 2015; Menand et al., 2010; Maccaferri et al., 2014; Pinel and Jaupart, 2000), mechanical layering (e.g. Kavanagh et al., 2006) and pre-existing structures or weak boundaries (e.g. Le Corvec et al., 2013a; Kavanagh et al., 2017a). Technical challenges have meant that analogue experiments have studied either the magma or the host solid, and yet the coupled nature of dyke intrusion means that the simultaneous quantification of both aspects is needed.

In this invited paper, here we describe a new series of novel laboratory experiments where, for the first time, coupled magma flow and host rock deformation is studied during dyke initiation, propagation and eruption. By quantifying flow velocity within the analogue magma with contemporaneous surface deformation and sub-surface strain and stress evolution, we identify previously unrecognised processes that relate the interaction of the intruding magma with its host material to dyke propagation dynamics. We discuss our results in the context of monitoring magma intrusion events and the potential of the rock record to preserve both flow dynamics in crystalline fabrics and evidence of sub-surface deformation during magma intrusion. Our results challenge existing dyke models that are used to interpret surface deformation related to magma intrusion that leads to eruption.

2. Experimental setup and data processing methods

2.1. Gelatine preparation, Young's modulus measurement and scaling

To prepare an experiment, forty litres of 2.5 wt% concentration gelatine was made following the guidelines of Kavanagh et al. (2013). To dissolve the mixture, one kilogram of gelatine powder (260 Bloom, 10 mesh, pig-skin gelatine supplied by Gelita UK) was mixed with 19 kg distilled water at approximately 90 °C, and this was then diluted further by 20 kg of cold distilled water to create the final desired concentration. Distilled water was used to inhibit bacterial growth and to ensure no impact of local water composition on the gelatine's properties, which has been shown to be susceptible to pH (e.g. Djabourov et al., 1988; Brizzi et al., 2016). In its sol-state (liquid), the hot gelatine mixture was poured into a clear-Perspex square-based tank measuring 40 × 40 × 30 cm³ (see Fig. 1), any bubbles were then removed from the surface, and the surface was covered in a thin layer of oil to stop dehydration and the development of a tough 'skin'. The experiment tank was then covered in a layer of plastic-wrap and placed into a refrigerator at 5 °C to cool and solidify for approximately 20 h (see Table 1).

The Young's modulus of the gelatine solid was measured immediately prior to running an experiment. To do this the experiment tank was taken out of the refrigerator and the plastic wrap and oil layer was removed. A brass cylindrical load (see Table 2) was then placed in centre of the gelatine's surface, and the deflection it caused was measured using a digital micrometer. Following the guidelines from Kavanagh et al. (2013), the diameter of the load was small compared to that of the experiment tank, and the mass was sufficient to cause a measureable deflection (± 0.005 mm). The Young's modulus E was then calculated using the following equation (Kavanagh et al., 2013):

$$E = \frac{mg(1-\nu^2)}{D\omega} \quad (1)$$

where m is the mass of the experiment load, g is gravity, ν is Poisson's ratio of the gelatine (0.5, according to Righetti et al., 2004), D is the load diameter and ω is the deflection it causes to the gelatine's surface. For each experiment, an average of measurements is reported (Table 1) based on two different loads (Table 2) and three measurements per load.

Kavanagh et al. (2013) showed that gelatine mixtures in the gel-state (2–5 wt% and 5–10 °C) that are injected by water can be appropriately scaled to model dyke propagation in nature. They defined a series of scale factors based on the assumption that the characteristic length scale of the experiment is the buoyancy length L_b , which is the length of the fracture when the buoyancy forces balance the resistive forces of the fracture (Taisne and Tait, 2009):

$$L_b = \left(\frac{K_c}{\Delta\rho} \right)^{\frac{2}{3}}, \quad (2)$$

where K_c is the fracture toughness and $\Delta\rho$ is the density difference between the intruded fluid and the host material. From this follows four scale factors (Kavanagh et al., 2013):

Length scale L^* :

$$L^* = \frac{L_l}{L_n} = \left(\frac{K_c^*}{\Delta\rho^*} \right)^{\frac{2}{3}}, \quad (3)$$

Fig. 1. Schematic sketch of three apparatus setups for imaging dyke experiments where water is injected into the base of a gelatine slab using a peristaltic pump. a) Two polarising sheets (pale grey) are attached to the outside of the tank in the x - z plane. An overhead laser (L_1) monitors surface elevation change along a line projected onto the sand-covered gelatine surface (x - y plane), centred on the injection point and perpendicular to the dyke strike-direction. Three HD cameras monitor the growth of the dyke (HD-1 x - z plane, HD-2 y - z plane, and HD-3 x - y plane). b) Particle image velocimetry: a CCD camera (y - z plane) records fluorescing passive-tracer particles within the injected fluid, in a vertical laser sheet projected through the gelatine (centred on the injector, and parallel to the dyke strike-direction). c) Digital image correlation: a CCD camera (x - z plane) records a vertical laser-illuminated sheet through the gelatine (centred on the injector, perpendicular to the dyke strike-direction), which contains suspended passive-tracer particles. Side (i) and plan (ii) views are shown for each method.

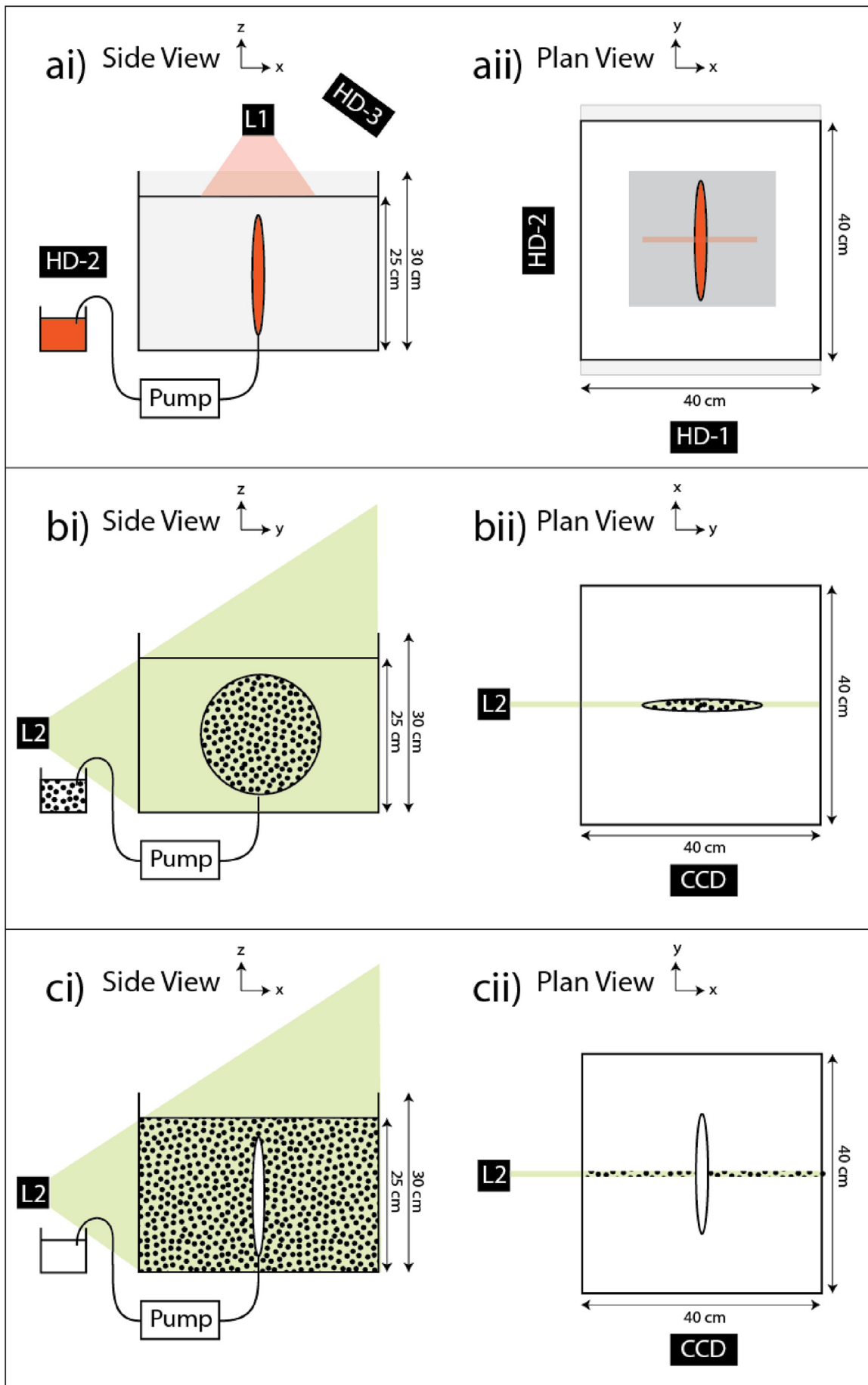


Table 1
Experiment parameters and variables. X = gelatine concentration, H = gelatine layer depth, ρ = gelatine density, T_{mix} = temperature of gelatine mixture when left to solidify, T = gelatine temperature when experiment commenced, t_{set} = time cooling, Q = injection flux, E = Young's modulus, t = time to eruption, and Technique = experimental imaging and analysis technique applied (Pol = polarised light, Surf Def = surface elevation change monitoring, PIV = particle image velocimetry, DIC = digital image correlation).

Experiment # (Ref)	X (wt%)	H (m)	ρ (kg/m ³)	T_{mix} (°C)	T (°C)	t_{set} (hr)	Q (m ³ /s)	E (Pa)	t (s)	Technique
1 (SD07)	2.5	0.24	1002.5	24	5	24	3.9×10^{-7}	2921	480	Pol, Surf Def
2 (SD09)	2.5	0.24	1002.5	23	5	23	3.9×10^{-7}	3042	500	Pol, Surf Def
3 (AJB01)	2.5	0.25	1002.5	22	5	16	3.9×10^{-7}	2030	416	PIV
4 (AJB02)	2.5	0.25	1002.5	21	5	15.5	3.9×10^{-7}	2030	405	DIC

Table 2
Properties of experimental loads used to calculate Young's modulus of the solidified gelatine prior to running an experiment, where 'm' is the mass of the load and 'a' is its radius.

	Geometry	Material	m (kg)	a (m)
Load A	Cylinder	Brass	0.0501	0.0125
Load B	Cylinder	Brass	0.0418	0.0125

Timescale T^* :

$$T^* = \frac{T_l}{T_n} = \rho_{\text{solid}}^{\frac{1}{2}} K_c^{\frac{1}{3}} (\Delta\rho)^{-\frac{5}{6}}, \quad (4)$$

Velocity scale U^* :

$$U^* = \frac{U_l}{U_n} = (\Delta\rho)^{\frac{1}{6}} K_c^{\frac{1}{3}} \rho_{\text{solid}}^{-\frac{1}{2}}, \quad (5)$$

and Stress scale E^* :

$$E^* = \frac{E_l}{E_n} = \Delta\rho^* L_b^* \left(\frac{L_b}{\psi} \right)^*, \quad (6)$$

where subscript l is in the laboratory, subscript n is in nature, ρ_{solid} is the density of the host material and ψ is the thickness of the intrusion. In our experiments where water is injected into gelatine: $L^* = 2 \times 10^{-3}$, and so 1 m in experimental dyke length corresponds with 500 m of dyke length in nature; $T^* = 9 \times 10^{-2}$, meaning 1 s of the experiment corresponds to 11 s in nature; and $U^* = 2 \times 10^{-2}$, such that 0.001 m/s in the experiment represents 0.05 m/s in nature. Kavanagh et al. (2013) found that $E^* = 2 \times 10^{-6}$ to 2×10^{-5} , and as our laboratory measurements of Young's modulus fall within this range and span 2000–3000 Pa (Table 1), this corresponds to rocks in nature that have a Young's modulus of 0.1–1.5 GPa. These values are geologically reasonable and so support the preface that scaled gelatine experiments can be used to describe magma intrusion in nature.

2.2. Experimental setup

An experiment is run by injecting water through the base of the solid gelatine slab, using a tapered syringe connected to a peristaltic pump that delivers fluid at a constant volumetric flux (see Table 1). A valve connected to the injection system and a small petroleum jelly seal at the injector tip ensures only water and no air is injected. The orientation of the dyke that is formed is controlled by making a small, vertical cut in the base of the gelatine and inserting the injector into this. It is ensured that the tapered edge of the injector is orientated parallel to the crack. To this basic setup, additional imaging apparatus are used and these are described in more detail in the following sub-sections. These include: gelatine stress field analysis, surface elevation change, dynamics

of the intruding fluid flow using particle image velocimetry (PIV), and sub-surface strain analysis via digital image correlation (DIC).

2.2.1. Photoelasticity and surface deformation

Polarising sheets are attached to the outside of the experiment tank, on opposite sides and perpendicular to the dyke strike direction (x-z plane, see Fig. 1a). Gelatine solids are photoelastic, meaning that qualitative stresses and their evolution can be visualised using polarised light. Two light sources illuminate the tank from behind, and two HD video cameras are used to record the sub-surface growth of the experimental intrusions; one is positioned to record the polarised-light view (HD-1, x-z plane), and one images the plane of the dyke in artificial light (HD-2, y-z plane). An additional HD video camera positioned above the experiment tank monitors the free-surface of the gelatine (HD-3, x-y plane). Footage from cameras HD-1 and HD-2 was analysed using the open source software Tracker (Version 4.96) to measure the dyke length, width, and tip position relative to the surface of the gelatine over time.

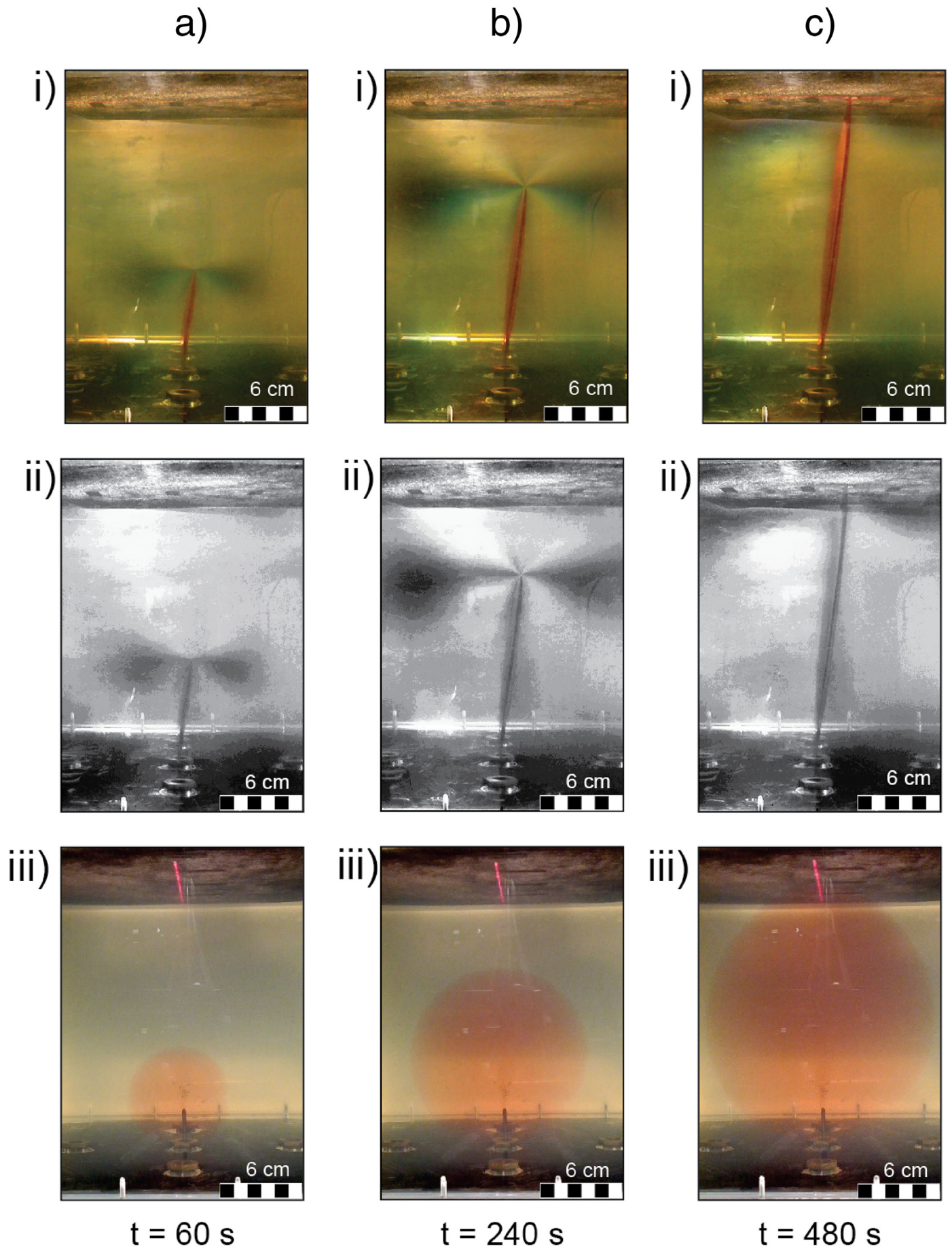
To monitor the changes in surface topography over time, a Micro-Epsilon laser scanner (L1) is positioned above the analogue setup (Fig. 1a). The laser projects a thin, vertical sheet of light onto the surface of the gelatine; this produces a red line on the gelatine surface that is positioned perpendicular to the dyke strike direction and centred on the injector port. As the gelatine solid is transparent, a thin layer of dark-coloured fine sand (approximate particle size 0.25 mm) is spread evenly over the surface of the gelatine to aid deflection of the laser light. The software ScanCONTROL 5.0 is used to collect data along a 140 mm long transect, with measurement points positioned every 0.5 mm along the projection. Each point along the projection is assigned a height value that corresponds to the distance between the surface of the gelatine and the source of the laser sheet. Changes in the surface topography are recorded at timed intervals of 4 scans per second.

After the experiment, data from the Micro Epsilon laser scanner are exported and manipulated in MATLAB (by Mathworks). Sub-sampling of the dataset produces an elevation profile in 10 s intervals. The cumulative sum of displacement is then calculated across the horizontal transect to illustrate the change in topography over time. Using the statistical analysis software R, a non-parametric fit LOESS curve (Locally Weighted Scatterplot Smoothing) is applied with a span width of 0.3 for the smoothing window.

2.2.2. Particle image velocimetry (PIV) and digital image correlation (DIC)

PIV or DIC are used to quantify fluid flow velocities within the injected fluid or sub-surface strain evolution in the intruded gelatine, respectively. A New Wave Solo-PIV III Laser (L2) provides 50 mJ of energy per pulse at 15 Hz, with a pulse width of 3–5 ns and a wavelength of 532 nm. The laser fires at a repetition rate of 8.875 Hz for the PIV fluid flow experiments (Fig. 1b) and 1 Hz for the DIC gelatine sub-surface deformation experiments (Fig. 1c). The laser light is formed into a thin sheet (approximately 1 mm thick) using a cylindrical lens which excites 20–50 μm fluorescent, spherical poly(methyl methacrylate) (PMMA)

Fig. 2. Series of cropped photographs showing the evolution of stress in the gelatine during dyke ascent at 3 time steps: a) 60 s, b) 240 s, and c) 480 s. The position of the overhead laser is clear in all colour images as a red line at the top of the frame. (i) Polarised light, where the photoelasticity of gelatine produces colour fringes that relate to stress intensity, and (ii) these images converted to greyscale to show the stress pattern more clearly. (iii) A perpendicular view of the dyke growth showing the typical penny-shape. (Experiment 1; see Table 1, Fig. 1a and Supplementary Video Fig. S1).



passive tracer particles with a Rhodamine-B coating that gives peak fluorescence at a wavelength of 590 nm. The laser sheet is fired from the side of the tank and positioned vertically so it intersects with the injection point (Fig. 1b, c).

The passive tracer particles are mixed into the injection fluid (Fig. 1b) or the host gelatine during preparation of the experiment (Fig. 1c). Particles within the injecting fluid are added immediately prior to injection, and the fluid is kept in a container placed on a magnetic stirrer to ensure they remain in suspension during extraction. The particles are slightly denser than water and so over time they settle out of suspension, although this occurs over 10's of minutes and so is beyond the time of an individual experiment. The fluorescent particles are added to the hot gelatine mixture prior to it being left to cool, stirring it continuously before being placed in the refrigerator when it reaches 21 °C. This ensures an even distribution of the tracer particles within the solidified gelatine.

Images are captured using a 2 MP CCD camera fitted with a 35 mm Nikon lens (Fig. 1b,c). The light reflected from the experiment is filtered using an optical longpass filter, which passes light with a long wavelength and blocks short wavelengths with a cut-in wavelength of 550 nm. This prevented the laser light that was reflected by the gelatine from entering the camera, thus allowing the light from the fluorescent particles to be clearly observed.

2.2.2.1. Calibration and pre-processing. Before each PIV or DIC experiment, an image is acquired of a 2D calibration target (an array of evenly-spaced black dots on a white background) aligned with the laser sheet and situated in the tank filled with water. Dantec Dynamic Studio imaging software detects the position and size of the filled-circles, and defines the area across which quantitative analysis can be accurately performed. This calibration image is later used in pre-processing to dewarp images of the experiment that are acquired. This process corrects for any distortion (which is minimal in our experiments and only occurs around the edges of the camera image; areas which are of little interest) as well as providing an accurate conversion between pixels and physical space. Great care is taken to ensure that the camera location, camera focus, tank location and laser sheet are not altered between this calibration step and the experiment itself.

2.2.2.2. Data processing and post-processing. After dewarping (described above) PIV cross-correlations produce vector fields (e.g. Adrian, 1991) using Dantec Dynamic Studio software. We utilise an adaptive correlation technique in which the interrogation windows have a 50% overlap. This results in a distance between vectors of 1.8 mm. Spurious vectors are removed using standard range and moving average validation techniques, and replaced with local mean values.

Post-processing of the vector fields is conducted in Matlab. As the region of interest increases in size throughout the experiment as the intrusion grows, we developed a masking technique that creates and applies a different mask for every PIV vector field. This is based on the region of interest being identified in the experimental images using an intensity threshold. This processing step eliminates vectors outside the region of interest that are purely the result of measurement noise.

For visualisation purposes only (figures and movies) a 3-by-3 spatial box is applied to the vector fields before plotting. In addition, it is evident that long time-averaging is not possible due to the constantly varying size of the intrusion. However, given that the timescale of the growth of the intrusion is significantly longer than the PIV capture rate we can average over a limited number of frames (10) such that each plot (or movie frame) is a short time-average (i.e. spanning 1.13 s in the PIV dyke flow experiments). Finally, to improve the clarity of the vectors in the visualisations, they are down-sampled by a factor of

two (i.e. only every second vector is plotted) or three, depending on the type of experiment and visualisation. The colour-maps in all cases are not down-sampled and reflect the resolution of the experiments.

In the DIC experiments, strain is calculated from the post-processed vector field data. For the small strains in the sub-surface gelatine (significantly less than unity) the strain tensor can be linearised to give Cauchy's infinitesimal strain tensor:

$$\epsilon_{ij} = \frac{1}{2} \left(\frac{\partial v_i}{\partial x_j} + \frac{\partial v_j}{\partial x_i} \right), \quad (7)$$

where \mathbf{v} is the displacement vector, and \mathbf{x} is the spatial coordinate. Thus, in the two-dimensions of interest in the DIC experiments, u and w are vector displacements in the x - and z -directions, respectively:

$$\epsilon_{xx} = \frac{\partial u}{\partial x} \quad (8)$$

and

$$\epsilon_{zz} = \frac{\partial w}{\partial z} \quad (9)$$

for the normal components of strain ϵ .

The shear components are equal due to symmetry, so:

$$\epsilon_{xz} = \epsilon_{zx} = \frac{1}{2} \left(\frac{\partial u}{\partial z} + \frac{\partial w}{\partial x} \right). \quad (10)$$

As the DIC provides discrete data on an even grid we simply estimate the gradients using a central differencing scheme, such that:

$$\epsilon_{xx} \approx \frac{u_{n+1,m} - u_{n-1,m}}{2\Delta x}, \quad (11)$$

$$\epsilon_{zz} \approx \frac{w_{n,m+1} - w_{n,m-1}}{2\Delta z} \quad (12)$$

and

$$\epsilon_{xz} \approx \frac{1}{2} \left(\frac{u_{n,m+1} - u_{n,m-1}}{2\Delta z} + \frac{w_{n+1,m} - w_{n-1,m}}{2\Delta x} \right), \quad (13)$$

where ϵ_{xx} is the strain at the location (n, m) . Note that $\Delta x = \Delta z$ as the PIV interrogation windows are square (where Δx and Δz are the spacing between the vectors in the x and z directions, respectively). The error introduced by the discretisation of the equations is second order, $O(\Delta x^2)$.

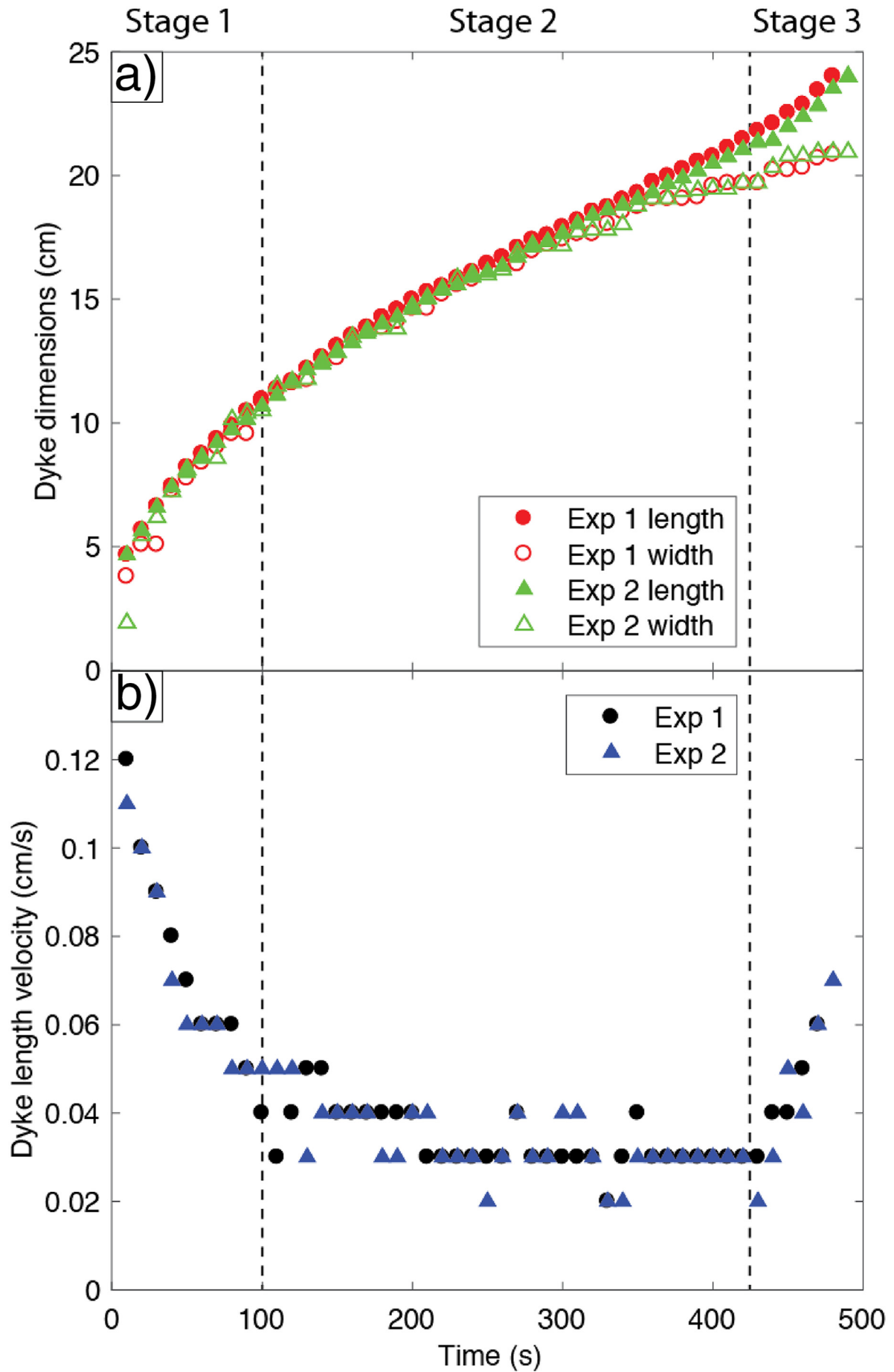
3. Results

The same experiment was carried out four times; each had the same gelatine concentration, volume and injection method, but a different imaging techniques was applied (see Table 1). Across the different techniques, we have identified four stages of dyke growth to eruption: 1) dyke inception, 2) dyke propagation, 3) pre-eruption ascent and 4) fissure eruption. The appearance of these different stages is now described in detail for each technique.

3.1. Dyke propagation geometry and sub-surface stress

A penny-shaped water-filled fracture was produced during injection. This experimental dyke propagated vertically ($\pm 10^\circ$) towards the surface. Although qualitative, polarised light is very useful to

Fig. 3. Dyke growth in length and width over time, showing three stages of dyke intrusion: a) Dyke length and width, and b) dyke length velocity. Data from two equivalent experiments are shown (see Table 1) up to the point of eruption, measured from the base of the injector. Stage 4 is not shown, but occurs at the end of the experiment as the dyke erupts.



demonstrate the evolving stress field during dyke propagation using the photoelastic properties of gelatine. Coloured fringes depict stress contours, with high concentration of these indicating increasing stress intensity. The developing stress field and its distribution around the growing dyke is shown in Fig. 2 and Supplementary Video Fig. S1, showing stress is concentrated at the dyke tip and producing a 'bow-tie' of stress contours in the x-z plane (Fig. 2i and ii). The visually-stressed region of gelatine is initially localised (Fig. 2ai,ii), but increases in extent as the dyke ascends (Figure 2bi,ii). Towards the surface, the stress field begins to intersect the surface and this continues to eruption (Fig. 2ci,ii).

Three stages of pre-eruption dyke growth can be identified based on the growing dyke geometry. Dyke length and width measurements based on HD video images are shown in Fig. 3a. In Stage 1 a circular geometry is developed (Fig. 2aiii), and this corresponds with approximately equal dyke length and width (Fig. 3a) although the rate of their growth decelerates over approximately the first 100 s of the experiment (Fig. 3b). In Stage 2, the dyke length and width continue to steadily grow at approximately constant velocity (Fig. 3b). Stage 3 marks the lead up to eruption, where the dyke begins to accelerate towards the surface, its length increases at a faster rate than its width, and it develops an elliptical geometry towards eruption (Fig. 2iii,c). At stage 4 the dyke tip reached the surface and it erupted to form a short fissure, and fluid was extruded onto the gelatine surface. The fissure measured approximately 5 cm in length, and the fissure margins were practically closed with an opening <0.1 mm through which fluid flowed. The data presented in Fig. 3 are from two identical experiments (Table 1), and they demonstrate the high degree of reproducibility between experiments.

3.2. Mapping fluid flow within a propagating and erupting dyke

In PIV experiments, passive tracer particles suspended in the injected fluid fluoresced in the y-z plane of the experimental dyke (see Supplementary Video Fig. S2a). Based on the fluid dynamics, the dyke propagation can be described in four stages (see Fig. 4 and Supplementary Video Fig. S2b):

Stage 1: Fluid flow vectors within the first minute of experimental dyke growth were complex, but organised into two jets; one making a curved trajectory that is clockwise near the base of the injector, and the other moving in an anti-clockwise direction in the upper part of the dyke at the dyke margin (Fig. 4a). At this time the dyke was small (approximately 70 mm wide and 70 mm high), far from the gelatine surface (160 mm depth) and close to the injector, with a maximum flow velocity of 14.6×10^{-3} m/s.

Stage 2: After the initial dyke growth, the dyke fluid flow stabilises into one pseudo-steady, upward rising jet along the centre of the dyke (Fig. 4b). Flow velocities are maximum close to the injector, but the maximum flow speed has reduced to 6.6×10^{-3} m/s compared to stage 1. Flow vectors at the growing tip fan out and rotate to flow downwards at the dyke margin. The slowest flow velocities occur in two elliptical regions between the upward-flowing channel and the down-flowing margin, where the fluid is almost static.

Stage 3: As the dyke approaches the surfaces to erupt, an instability develops in the flow. The central, upward jet meanders from side to side and at the base the fluid flow comprises two upward jets (Fig. 4c). The fastest moving fluid has migrated away from the injector and occupies a central band within the growing dyke, with slower velocities at the vertical tip and continued down-flow at the dyke margins. The maximum flow velocities in Stage 3 have slightly increased compared to stage 2 and are up to 6.9×10^{-3} m/s. The two elliptical, almost-static, fluid regions between the upward jet and dyke margin remain and have grown in size.

Stage 4: The final stage of dyke ascent is the fissure eruption (Fig. 4d) when the flow dynamics within the dyke dramatically change. At the onset of eruption, all flow vectors are rapidly re-oriented upwards and towards the small fissure that formed in the gelatine surface. The upward jet from the injector and two jets at its base remain, though the region of static fluid rapidly increase in size from depth upwards. The fastest flow velocities of all dyke ascent stages are recorded, reaching 32.2×10^{-3} m/s as fluid is rapidly expelled and the dyke is drained.

3.3. Sub-surface incremental strain evolution during dyke ascent

In DIC experiments, passive-tracer particles within the gelatine solid were illuminated in the x-z plane presenting a cross-section around the growing experimental dyke (see Supplementary Video Fig. S3). The laser-illuminated plane reveals sharp margins of the dyke as it grows, and offers the opportunity to record in detail the evolving cross-sectional thickness variation as the dyke grows; in addition to quantifying the evolving incremental strain (ϵ_{xx} , ϵ_{zz} and ϵ_{xz}) using DIC. Based on the dyke thickness change and evolution in incremental strain, we identify four stages of dyke growth (Fig. 5):

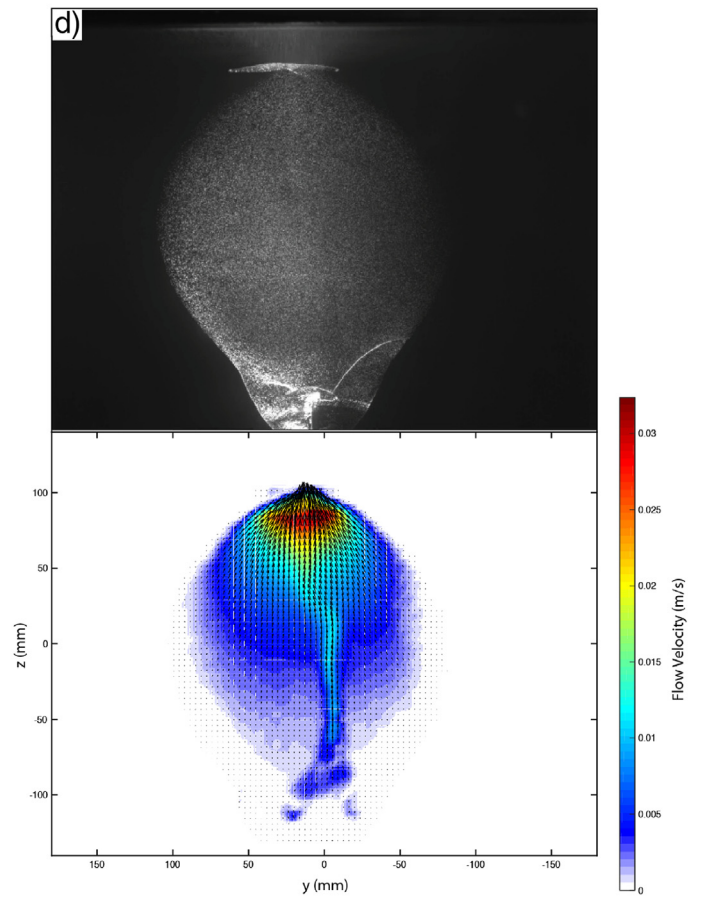
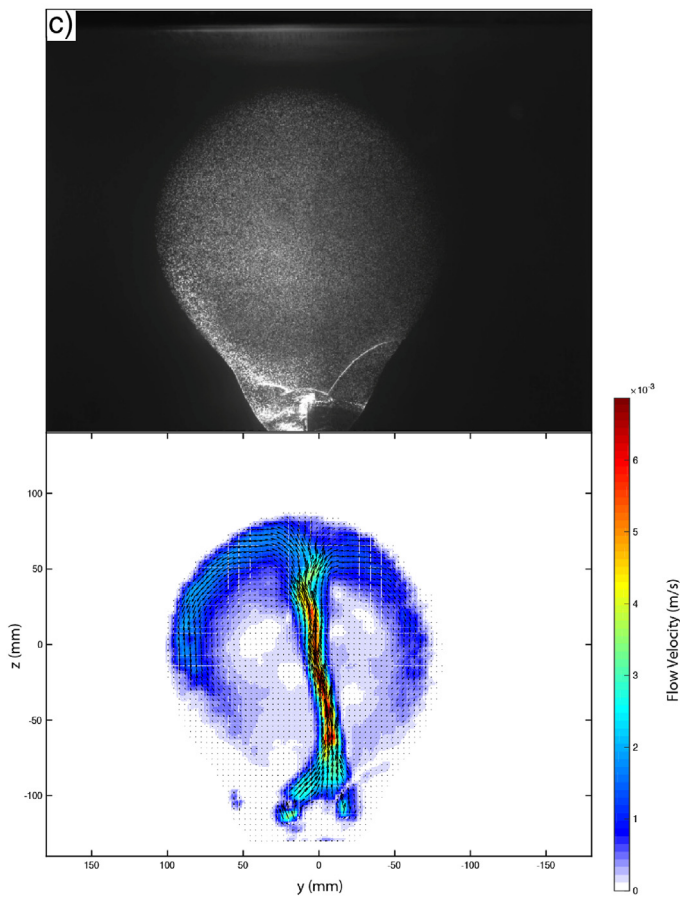
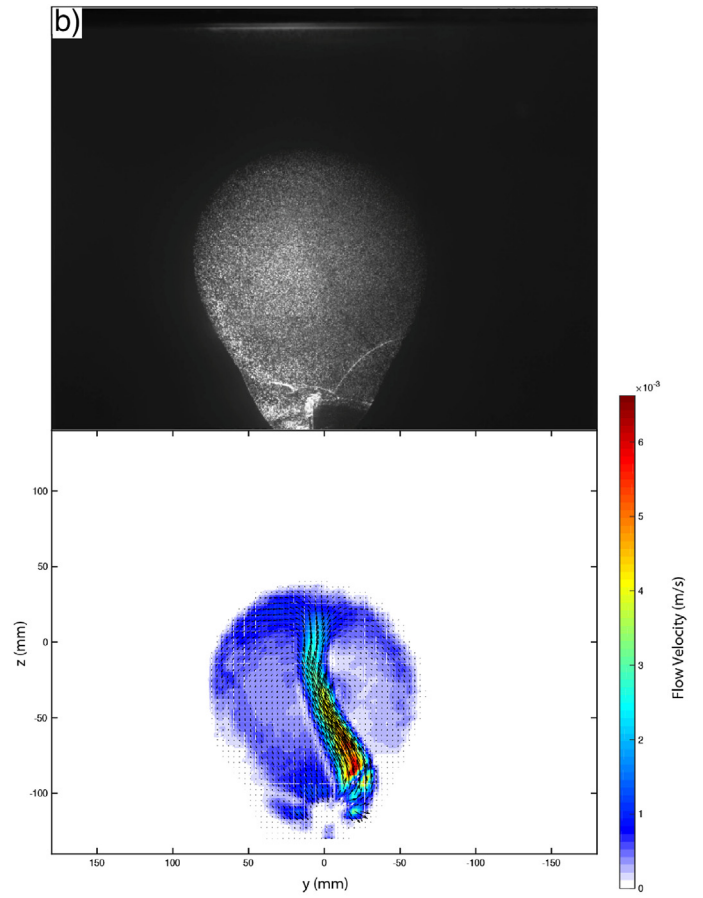
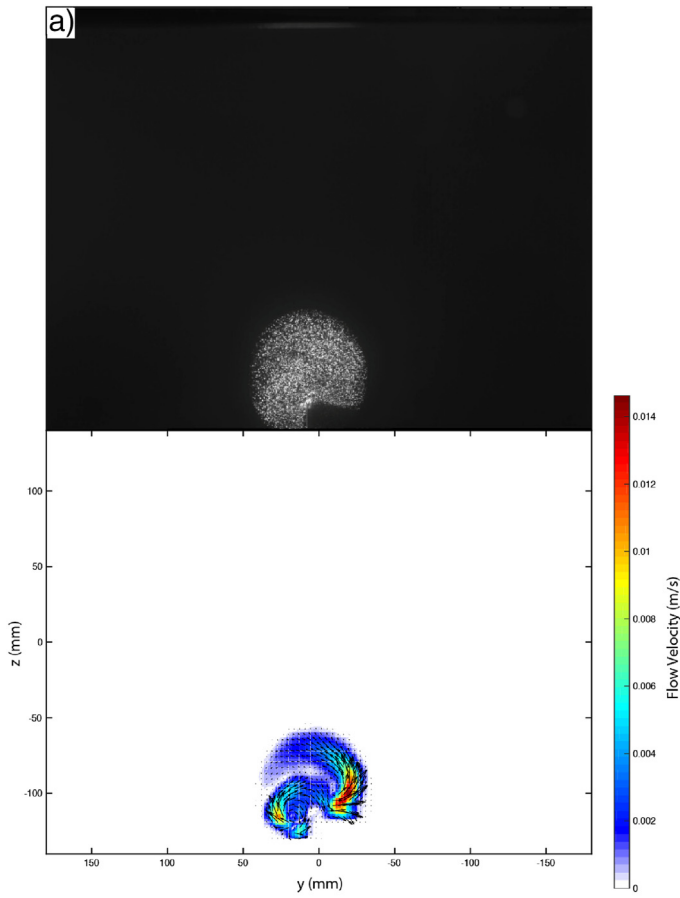
Stage 1: Sub-surface deformation of the gelatine during the early stages of dyke growth show the incremental strain is concentrated at the growing tip (Fig. 5a, 55 s). No incremental strain is recorded at the dyke tail region, indicating its opening is maintained. Vector arrows show the gelatine is displaced predominantly at the dyke margins, radiating from the growing tip, with larger lateral than vertical displacement. The largest component of incremental strain occurs in the horizontal direction (ϵ_{xx}); both vertical (ϵ_{zz}) and shear (ϵ_{xz}) components of strain are small. Overall incremental strain intensity in the early stages of dyke growth spans $-2 - 12 \times 10^{-3} \epsilon_{xx}$, $-2 - 3 \times 10^{-3} \epsilon_{zz}$, and $-2 - 3 \times 10^{-3} \epsilon_{xz}$. Local positive ϵ_{xx} occurs at the dyke tip and local negative ϵ_{xx} occurs adjacent to the dyke tip, whereas local positive ϵ_{zz} occurs just below the dyke tip and local negative ϵ_{zz} just above this. Shear strain is also measured around the dyke tip.

Stage 2: As the dyke ascends, incremental strain continues to be concentrated at the growing tip and displacement arrows show continued outward radial movement at the dyke head with greater lateral than vertical displacement (Fig. 5b, 205 s). Similar patterns of ϵ_{xx} , ϵ_{zz} and ϵ_{xz} occur compared to Stage 1, however their values have all slightly decreased. Uplift of the gelatine free surface is detected by a region of negative ϵ_{zz} developing at the surface. Deflection of the dyke tip from vertical occurs as the dyke begins to propagate in an inclined plane, and this is when an asymmetrical pattern of incremental shear strain (ϵ_{xz}) is detected (lower negative ϵ_{xz} occurs in the upper-right of the dyke tip relative to the lower-left). A small area of negative incremental strain ϵ_{xx} occurs at the dyke tail region. The raw experimental image shows the tail of the dyke has pinched closed. In this stage of dyke propagation: ϵ_{xx} ranges from $-1 - 7 \times 10^{-3}$, ϵ_{zz} ranges from $-1 - 2 \times 10^{-3}$, and ϵ_{xz} ranges from $-1.5 - 1.5 \times 10^{-3}$.

Stage 3: Shortly prior to the dyke erupting, the dyke tip remains the focus of incremental strain; but, the magnitude and extent of the strain components significantly changes. The largest strain values are now in ϵ_{zz} rather than ϵ_{xx} . The intensity of negative vertical incremental strain (ϵ_{zz}) has increased in magnitude and extent. Asymmetry in negative ϵ_{xx} is detected at the dyke tip, and asymmetry in ϵ_{xz} remains. Small amount of incremental shear strain are detected at the gelatine's free surface. Overall in stage 3: ϵ_{xx} ranges from $-1 - 5 \times 10^{-3}$, ϵ_{zz} ranges from $-6 - 12 \times 10^{-3}$, and ϵ_{xz} ranges from $-1 - 1.5 \times 10^{-3}$.

Stage 4: The moment immediately prior to dyke eruption is recorded as opening at the surface and the largest values of ϵ_{xx} are then produced during the experiment. Displacement vectors are oriented towards the

Fig. 4. Four stages of fluid flow within a propagating experimental dyke (Experiment 3), quantified using PIV. Flow velocities (m/s) are shown as vectors (black arrows) and magnitude (colour map). See Supplementary Video S2. a) Stage 1: initial growth (frame 500, 56 s), b) Stage 2: established dyke (frame 2000, 225 s), c) Stage 3, instability development in jet (frame 3500, 396 s), and d) Stage 4: fissure eruption (frame 3691, 416 s).



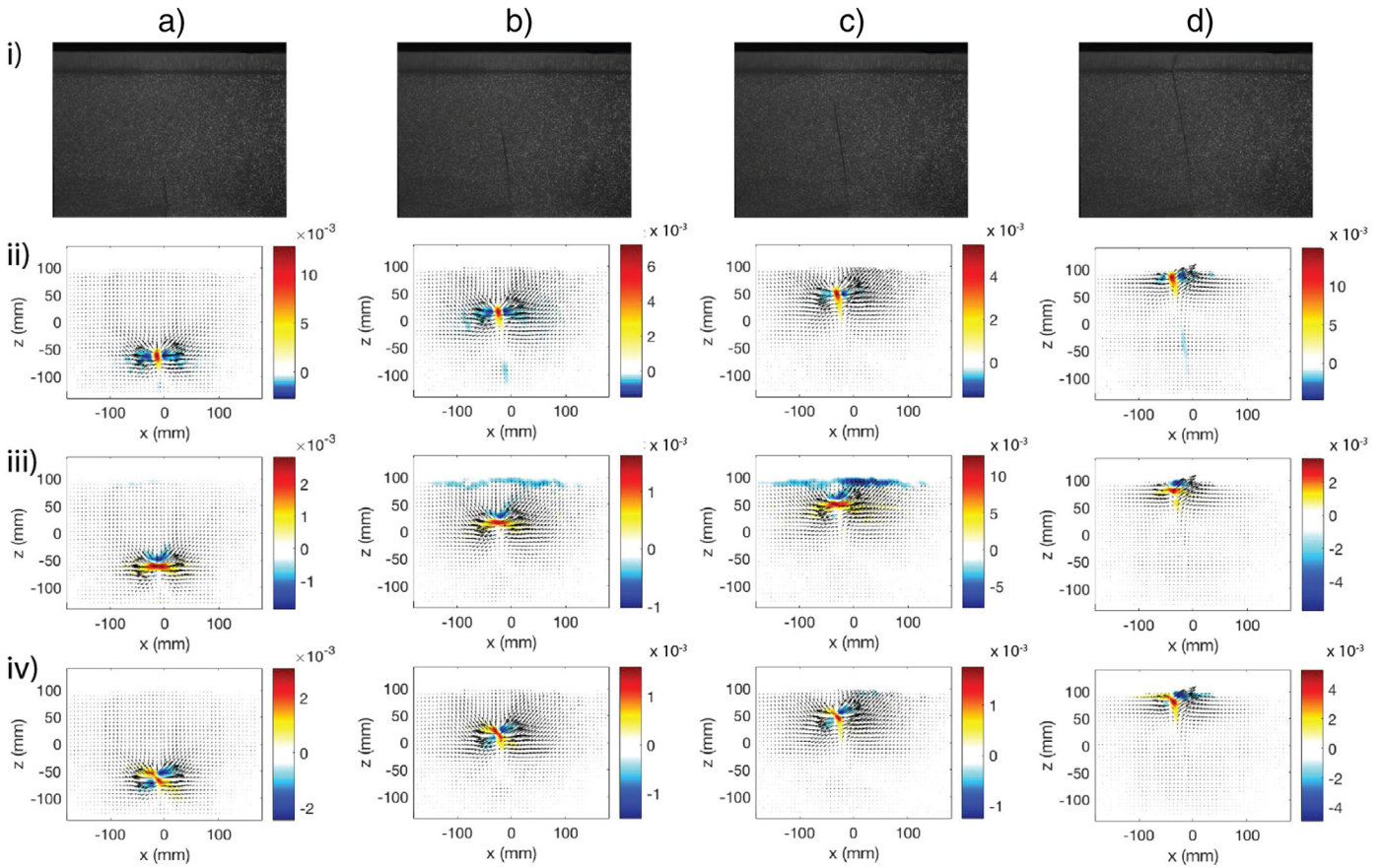


Fig. 5. Four stages of sub-surface incremental strain evolution (colour maps) of experimental dyke ascent to eruption (Experiment 4): i) the de-warped experimental images, ii) ϵ_{xx} , (iii) ϵ_{zz} and (iv) ϵ_{xz} . Displacement is indicated (black arrows), and the DIC analysis is averaged over 10 frames. See Supplementary Video S3. a) Stage 1, dyke inception (frames 55–64, 55 s), b) Stage 2, dyke growth and ascent (frames 205–214, 205 s), c) Stage 3, immediately prior to eruption (frames 400–409, 400 s), and d) Stage 4, fissure eruption (frames 405–414, 405 s).

surface. Progressive ‘zipping’ closed of the tail occurs as displacement vectors rotate inwards at depth where small, localised regions of negative ϵ_{xx} are produced. The largest incremental strain occurs in the horizontal component (ϵ_{xx}), followed by the shear strain ϵ_{xz} (which is at its largest at stage 4) and then ϵ_{zz} as the dyke completes its path to the surface. During this stage of dyke ascent ϵ_{xx} ranges from $-4 - 14 \times 10^{-3}$, ϵ_{zz} ranges from $-5 - 3 \times 10^{-3}$, and ϵ_{xz} ranges from $-5 - 5 \times 10^{-3}$.

3.4. Surface deformation during dyke ascent

Fig. 6 shows the progressive deformation of the gelatine surface during an experiment as the dyke approached the surface. There was no change in surface topography detected during the majority of dyke ascent (see Supplementary Video Fig. S1c), and it was only when the dyke tip reached approximately <4 cm depth (during the final 120 s of ascent, see Fig. 6a) that an elevation change of the free-surface occurred. By the onset of fissure eruption, there was a gradual overall increase in elevation of 0.5 mm across the whole plane that was monitored. Local topographic highs (up to 1.5 mm) developed either side of the dyke tip (Fig. 6a). The elevation change was relatively broad early on, but became increased and focused as the dyke tip approached the surface. The dyke became slightly deflected from its vertical path (as is common in the experiments, e.g. Experiment 2, Fig. 5), as shown by an increase in the tip position relative to the injector (Fig. 6b). This slightly inclined propagation path resulted in the cumulative surface elevation change not being symmetrical, as the ‘hanging wall’ of the dyke developed a larger topography (up to 1.5 mm cumulative displacement) than the ‘footwall’ (approximately 0.9 mm of cumulative displacement).

4. Discussion: Coupled processes during dyke ascent and eruption

Most dykes in nature do not erupt (Gudmundsson, 2002) and the majority of magmas stall within the crust (Crisp, 1984). Determining if magma will breach the surface is of primary concern for volcanic hazard assessments. Dyke ascent in nature can be studied during ascent or post-emplacment; however, in both cases visualising the three-dimensional evolving geometry of the dyke is challenging and requires extrapolation from often two-dimensional datasets (Kavanagh, 2018). Evidence of magma flow, crust deformation and dyke eruption is only partially recorded. Our laboratory experiments can help inform the interpretation of natural data and challenge existing numerical models of dyke ascent.

4.1. Synthesising laboratory experimental results

The range of laboratory experiment monitoring techniques we have employed arguably represent the most detailed and comprehensive description and analysis of coupled fluid flow and host deformation during experimental dyke ascent to eruption. Dyke propagation involves the intrusion of a fluid into a solid, and our results emphasise the strong coupling between the intruding fluid and the deformation of its host-material that influences magma ascent dynamics.

Four common stages of dyke ascent leading to eruption are evident in the experiments. 1) During dyke inception and its early growth, the fluid flow patterns are complex and comprise two circulating fluid jets. Strain is focused at the upper dyke tip as the penny-shape crack is progressively established. 2) As the dyke grows, the fluid flow within it stabilises into a single, rapid and upward flowing jet as the dyke grows in length and width at a constant and steady rate. 3) As the dyke

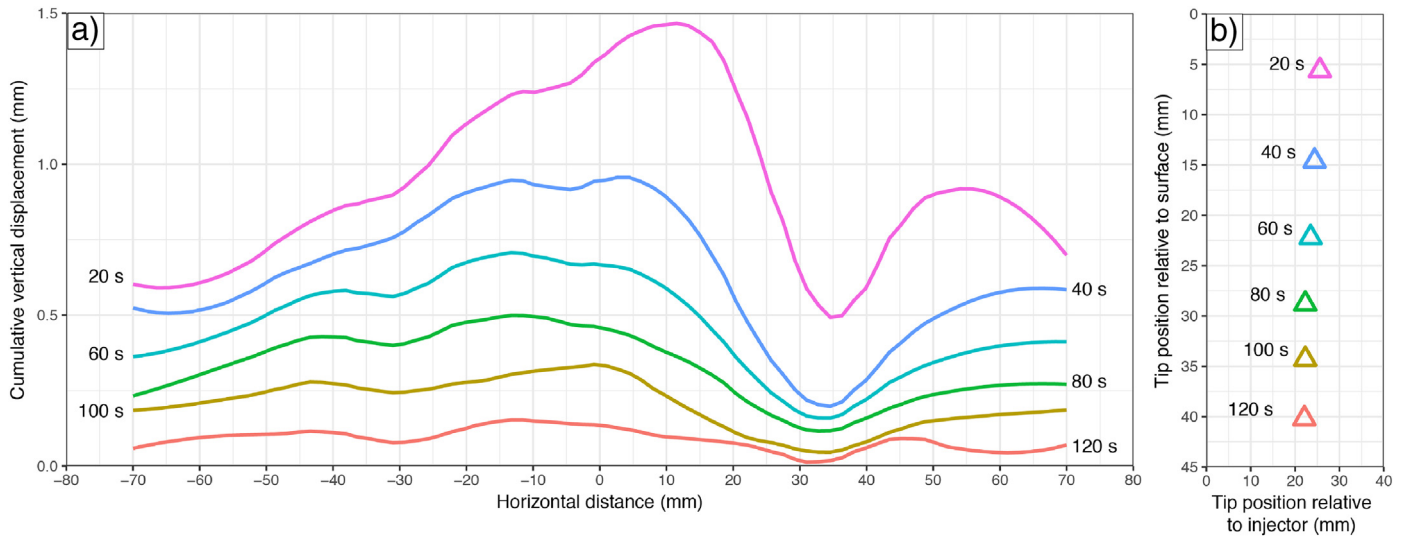


Fig. 6. A series of surface deformation profiles according to dyke tip position of Experiment 1: a) Cumulative surface deformation from 120 to 20 s prior to eruption, where asymmetric topographic highs are produced either side of the dyke tip as it approaches eruption. b) Depth and lateral position of the dyke tip at 20 s intervals before eruption, noting that the tip has gradually deviated from vertical (0 mm) by up to 25.6 mm at 20 s prior to eruption.

approaches the surface our experiments show a fluid instability develops, causing the upward jet to meander and two jets to form at the dyke base. The origin of this instability is not clear, although its appearance corresponds with the time when the dyke tail pinches almost-closed, and when the dyke tip accelerates towards the surface. It is also at this stage that surface deformation is first recorded, resulting in the progressive increase in topography and elevation highs developing above the ascending dyke tip. 4) During dyke eruption, a small fissure is formed at the gelatine surface, a dramatic pressure release induces the rapid evacuation of fluid from the dyke, and the dyke walls ‘zip’ closed from the tail to the surface.

4.2. Challenging dyke ascent models

The patterns of surface elevation change we measured during dyke ascent agree well with that expected by analytical elastic models; the deformation comprised elevated regions either side of the dyke tip, with a relative low directly above it. Measurements of surface deformation at volcanic centres are often inverted for the source depth and source geometry using simple analytical models that assume intrusion into an isotropic, elastic host-rock. Our experimental observations therefore have the potential to be used to bench-mark these inverse models and inform their development.

The numerical models of dyke ascent that have been published can be divided into two end-member approaches (see Rivalta et al., 2015 for a review). Firstly, there are buoyancy-driven dyke ascent models that emphasise elasticity of the intruded media and its fracture toughness. In these models, the dyke becomes disconnected from its source (e.g. Weertman, 1971). Secondly, there are flux-driven dyke ascent models where the dyke is connected to its source and the fluid dynamics of the intrusion are described by applying lubrication theory (e.g. Lister, 1990a, 1990b; and Spence et al., 1987). The circulation of fluid we observe in the experiments agrees well with the flow pattern expected by Dahm’s (2000) dyke model, which emphasises the role of elasticity and fracture toughness but also reconciles the fluid dynamics of the intruding magma. However, this flow pattern contrasts with Roper and Lister (2007) who couple fluid flow and host deformation using lubrication theory and a dyke-scale process zone. Their model anticipates that, when connected to the source, dyke fluid flow should be predominantly vertical inside the dyke. However, our results suggest that, despite not having attained their ‘buoyant length’ and only having a small density contrast between intruding fluid and intruded host, our

experimental dykes have the ascent dynamics expected of buoyant fluid-filled fractures in an elastic material, where the mechanical properties of the intruded host dominate the growth dynamics and the viscous resistance of the fluid to flow is minimal.

In our experiments, fluid is driven into the dyke at a constant volumetric flux and the dyke remains connected to its source. According to Linear Elastic Fracture Mechanics, the fluid-filled crack will propagate when the fluid overpressure exceeds the fracture pressure P_f of the gelatine solid (Lister and Kerr, 1991):

$$P_f = \frac{K_c}{\sqrt{\pi l}}, \quad (14)$$

where K_c is the fracture toughness of the gelatine and l is the crack length. Gelatine’s K_c can be estimated by the relationship (Kavanagh et al., 2013):

$$K_c = 1.4\sqrt{E}. \quad (15)$$

In our experiments, $E = 2000\text{--}3000$ Pa and so we estimate $K_c = 63\text{--}77$ Pa $\text{m}^{1/2}$. However, the density difference between the injected fluid and the intruded gelatine also results in a buoyancy pressure P_b (Rubin, 1995):

$$P_b = (\rho_s - \rho_{liq})gL_b, \quad (16)$$

where ρ_s is the density of the solid (gelatine), ρ_{liq} is the density of the liquid (water), g is gravity and L_b is the buoyant length of the dyke (Eq. 2) (Taisne and Tait, 2009). Following these relationships, the calculated buoyant length of our experimental dykes is 1.3–1.4 m, where $\rho_s = 1002.5$ kg/m³, $\rho_{liq} = 998$ kg/m³ and $g = 9.81$ m/s, which is much greater than the height of the experimental tank (0.3 m). It is therefore expected that the growth of our experimental dykes is flux-driven, and any buoyancy effects should be minimal.

The experimental dyke geometry in profile is circular in the early stages of dyke growth. This penny-shaped geometry is a consequence of intrusion into a homogeneous, isotropic elastic solid; in nature, however, anisotropy and mechanical heterogeneities of the crust are expected to influence the shape of the dyke (e.g. Kavanagh and Sparks, 2011). Fluid may also be fed into the dyke by a slit-like geometry rather than the nozzle-like injector we used. The dyke geometry evolved to become elongate as it approached the surface, in response to an

accelerating dyke tip. In nature, mechanical heterogeneity of the crust will likely affect the dyke ascent rate and whether or not such an acceleration would occur. In cross-section, our experimental dyke developed a pinched tail and ‘teardrop’ morphology as the dyke propagated through the tank towards eruption. This geometry is similar to that expected of a ‘Weertman crack’, where a fixed volume injection ascends buoyantly through an elastic material (Weertman, 1971). This geometry occurred despite the crack receiving a constant flux of fluid, and remaining connected to the source (even if the connection is very small). Our experimental results therefore suggest the Weertman-crack geometry is not restricted to fixed volume injections, but can be developed by dykes that have sustained magma flux too. The analytical models that describe the buoyant length of fluid-filled fractures propagating in an elastic material therefore may not fully capture the dynamical processes of dyke ascent, and so will need to be revisited in the context of these new experimental observations.

4.3. Magma flow in nature

Our understanding of the dynamics of magma flow in dykes is limited to observations of volcanic fissure eruptions (e.g. Lundgren et al., 2013); in the early stages of eruption the magma exits along the fissure length, but rapidly the extrusion becomes focused at a few vents due to

flow channelisation. The crystalline magma within ancient, solidified dykes offers the best access to the dyke; however, exposure is often limited to partial 2-dimensional sections and unravelling *syn*- and *post*-emplacement textures from the time-sequence of magma solidification is difficult. However, there are several macroscopic flow indicators that can be used, including elongated vesicles that are aligned (e.g. Fig. 7), scour marks (e.g. Smith, 1987), phenocryst alignment (e.g. Bhattacharji and Smith, 1964), drag folds (e.g. Walker et al., 2017) and cataclastic elongation of phenocrysts (Smith, 1987). Magnetic fabrics, such as AMS have also been used to infer magma flow (e.g. Herrero-Bervera et al., 2001). Temporal variations in flow are postulated based on, for example, bubble-rich and bubble-poor coupled bands that suggest pressure fluctuations (see Fig. 7c and d). Any flow indicator needs to be used with caution, especially as the final stages of magma flow may be drainage or back-flow towards the source (e.g. Lundgren et al., 2013).

Our experimental results of the vectors of fluid flow during dyke intrusion and eruption provides important dynamical constraints that will likely aid the interpretation of flow fabrics within intrusions, in particular due to the identification of distinct stages of dyke ascent leading to eruption. In our experiments, the fluid initially circulated in two jets as the pre-cut was first filled and then the crack began to propagate. This early flow pattern was potentially an artefact of the initial injection

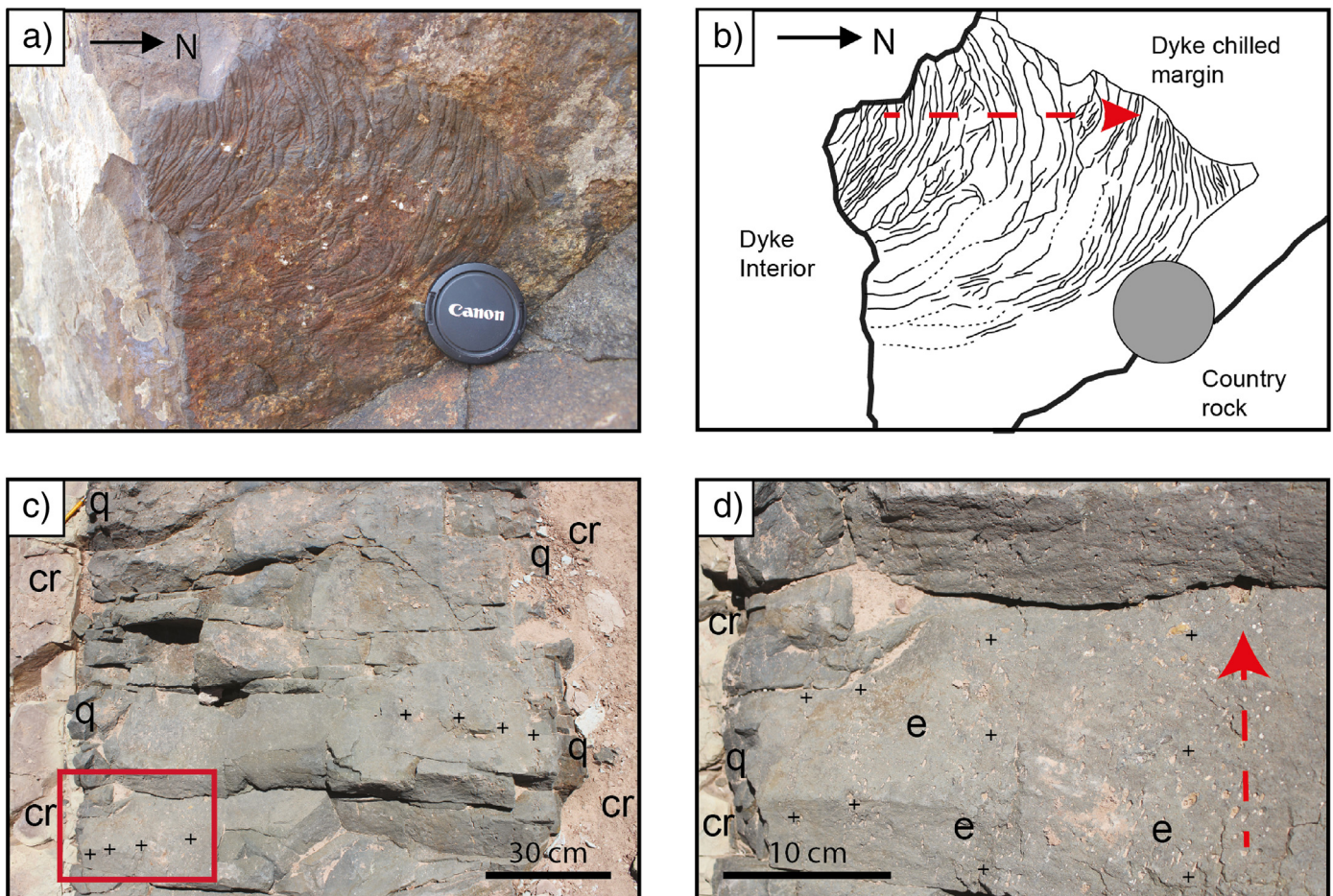


Fig. 7. Field-scale features where orientations of magma flow are preserved within solidified dykes in different planes. a) Dyke's y-z plane: Photograph of a quarry face showing a basaltic dyke margin (Isle of Skye, Scotland); the country rock has eroded away to reveal ropey structures preserved at the contact. b) Complementary sketch diagram of a): ropey structures (thin-solid and thin-dashed lines) on the dyke chilled margin, and the inferred local palaeo-flow direction (red dashed arrow). c) Dyke's x-y plane: Photograph of a complete cross-section of a basaltic dyke viewed from above (San Rafael subvolcanic field, Utah); quenched (q) chilled margins against the country rock (cr), and cm-thick vesicle-rich bands (+) that are bound by vesicle-poor bands and parallel to the dyke margins. The position of the zoomed image (d) is indicated (red box). d) Zoomed photograph of c) additionally showing the location of elongated vesicles (e) within the dyke interior.

conditions, and could have formed by the injector being partially blocked by incomplete breaking of the petroleum jelly seal. This first stage in the experimental dyke growth could vary between experiments, and so directly comparing this early stage of the experiment with natural observations is not recommended. However, after this initial stage the dyke width and length increased at constant velocity and this was when we observed a single jet to form and circulation of fluid within the propagating dyke. This jet persisted from these early stages of dyke growth up to immediately prior to eruption, with rapid evacuation of the dyke when it breached the surface. Our experimental observations therefore suggest that fluid flow trajectories within a non-feeder dyke (that does not erupt) may be highly variable with upward, lateral and downward flow occurring. These would therefore be distinct from a feeder dyke where the flow velocity would be predominantly vertical, proffering the opportunity to assess whether or not a dyke erupted (even with limited exposure of the plumbing system) based on the flow vectors preserved but also depending on the timescale of solidification (e.g. Daniels et al., 2012). Jet formation and channelisation within natural dykes may occur in nature, resulting in progressive and preferred erosion of the country rock due to the sustained and rapid fluid flow, leading to the development of asymmetrical dyke geometries in the rock record (e.g. Kavanagh and Sparks, 2011). Variations in flow, either during intrusion or eruption, may lead to erosion of the mushy and progressively crystallising dyke margins. Our experimental dykes comprised a low viscosity Newtonian fluid, however during magma ascent it is likely that non-Newtonian fluid rheology such as shear-thinning will develop as the crystal and bubble-content of the magma increases. Future experiments will be required to assess the impact of non-Newtonian rheologies on the flow dynamics within a propagating dyke.

4.4. Host-rock deformation in nature

The conceptual framework used in our laboratory study is that dykes can be modelled as hydraulic fractures that intrude an elastic material, which is in-keeping with assumptions used during real-time monitoring and inversion modelling of intrusion-induced deformation at active volcanoes. However, an important consideration in dyke ascent mechanics is understanding under what circumstances they create their own fractures or instead intrude pre-existing weak planes. This is important for hazard assessment and predicting the sites of future vents from dyke ascent e.g. in a monogenetic volcanic field (e.g. Le Corvec et al., 2013b). The sub-surface deformation patterns we observe in our

experiments, such as incremental strain and stress field evolution, could be helpful to interpret seismicity during active intrusion. The surface deformation patterns could be helpful to inform the interpretation of tilt meter data, GPS monitoring networks and InSAR analysis.

Field evidence of host deformation associated with dyke ascent ranges from macro- to micro-scale. Dyke-parallel fractures at the dyke margins within sedimentary (Delaney et al., 1986) or igneous host-rocks (Brown et al., 2007; Kavanagh and Sparks, 2011) may suggest these were pre-existing structures that were exploited by the ascending magma, although the exploitation of existing fractures is likely to be a relatively near-surface process (Rubin, 1995). A potentially valuable, yet unexplored, tool to study the micro-scale damage zone surrounding hydraulic fractures (e.g. dykes) are Fluid Inclusion Planes (FIPs). FIPs appear under optical microscopy as small linear “bubble” trails in individual crystals and are thought to be fossilised microfractures which are the result of healing, or “necking down” of previously open fractures which functioned as fluid pathways (Roedder, 1984). FIPs can provide valuable information when studying rock deformation as they can provide insight into deformation geometries, chronology of deformation (Lespinasse, 1999; Pecher et al., 1985) and are potential indicators to the paleostress field (Lespinasse and Pecher, 1986). The healing process is relatively quick in relation to geological time (Smith and Evans, 1984) and they form as Mode I fractures, occur predominately perpendicular to the least principal compressive stress axis, σ_3 , with no evidence of shear displacement which would be expected from Mode II/III fractures (Lespinasse, 1999). Quartz is a common mineral for FIPs to be observed as, due to its crystallographic properties, fractures in quartz are usually formed in response to the regional stress field (Lespinasse and Cathelineau, 1990). Minerals such as feldspars, however, which have more complex cryptographic features, such as twinning and the presence of cleavages, can alter the preservation or have preferred orientations of FIPs (Lespinasse, 1999). Observations of FIPs can be made optically at magnifications as low as $\times 10$, as shown in Fig. 8a; however optical observations are somewhat hindered due to the healing process, making many FIPs invisible in plane polarised and cross polarised light. The use of a Scanning Electron Microscope fitted with a Cathodoluminescent detector (SEM-CL) can dramatically increase the number of observable FIPs by up to 100% in some cases. This is demonstrated in the optical micrograph Fig. 8a, which shows roughly 8 visible FIPs, compared to the SEM-CL micrograph Fig. 8b, which has 16 potential FIPs. The SEM-CL provides a more complete image of FIPs, making it a more effective structural tool to assess host-rock damage around dykes.

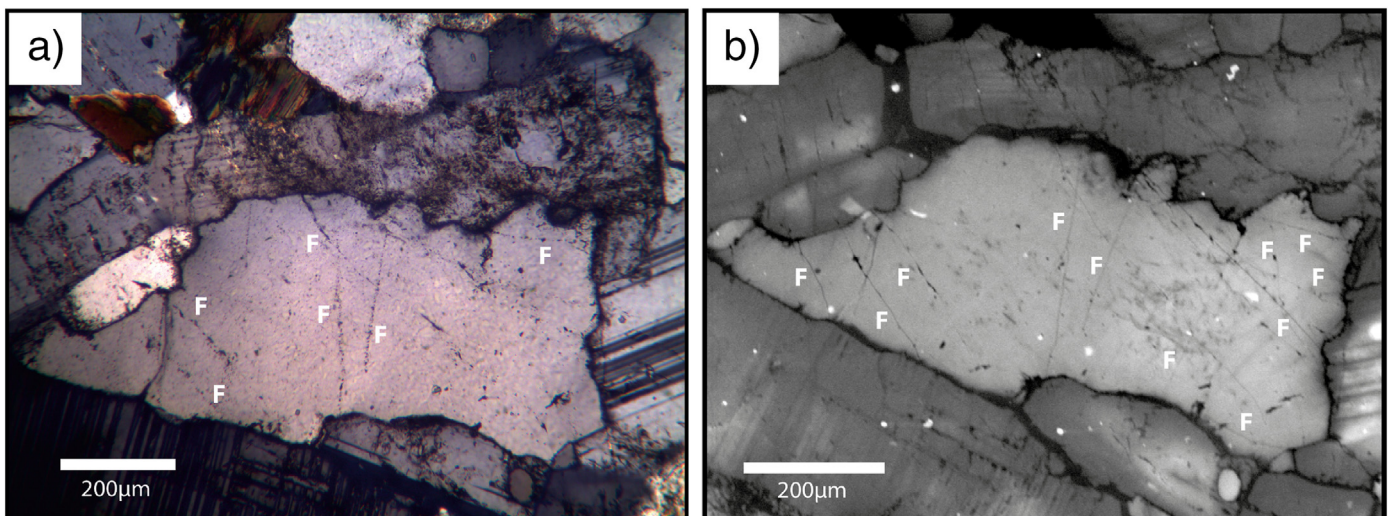


Fig. 8. a) Optical photomicrograph in cross polarised light showing fluid inclusion planes (F) within quartz. b) SEM-Cathodoluminescent image showing comparative view of microfractures visible, note the increased detail and abundance of FIPs (F).

5. Conclusions

The laboratory methods we have employed have allowed the detailed description and quantification of coupled fluid flow and host deformation during the inception, growth and eruption of an experimental dyke. We have identified four phases of dyke ascent:

Stage 1: Dyke inception and early growth. Fluid flow is complex, circulating as the dyke grows equally in breadth and length creating a penny-shaped geometry. Sub-surface deformation is focused at the growing tip, with material at the dyke tip margin progressively displaced outwards, and stress concentration showing a 'bow-tie' geometry. No surface elevation change is recorded as the dyke is formed and begins to grow.

Stage 2: Dyke propagation. Fluid flow comprises a rapid, centralised, upward-rising, pseudo-steady jet with slow down-welling at the dyke margin. Regions of static fluid develop within the circulating flow. Sub-surface deformation remains concentrated at the growing tip, shown by a concentration in incremental strain and stress. The dyke tail pinches almost-closed at depth at the end of this stage.

Stage 3: Near-surface ascent. A flow instability develops as the upward and centralised rapid fluid flow begins to meander and move from side to side. Two jets at the base of the dyke feed into the upper single jet, and slower fluid continues to down-well at the growing dyke margin. The dyke begins to lengthen, developing an elliptical geometry as the dyke tip begins to accelerate towards the surface. The pinched tail of the ascending dyke migrates towards the surface. The dyke trajectory is deflected as shear stresses intensify, and the dyke stress field begins to interact with the surface. The inclined dyke produces an asymmetrical cumulative elevation change centred above the dyke.

Stage 4: Fissure eruption. Rapid opening of the dyke occurs as it intersects the surface and produces a short fissure. This depressurisation causes rapid evacuation of fluid from the dyke. Flow is focused towards the vent and the active-region of flow is increasingly focused towards the surface as the pinched dyke tail zips closed from depth and accelerates towards the surface.

The experimental results emphasise the importance of considering coupled fluid flow and host deformation when developing the next generation of dyke ascent models, to inform the interpretation of the field and geophysical evidence of ancient, ongoing, and future dyke intrusion events.

Supplementary data to this article can be found online at <https://doi.org/10.1016/j.jvolgeores.2018.01.002>.

Acknowledgements

JLK and DJCD acknowledge 'Living With Environmental Change' pump priming grants from the University of Liverpool, and a Natural Environment Research Council Research Experience Placement from the Liverpool-Manchester EAO DTP that funded AJB (NE/L002469/1). JLK acknowledges a Royal Society grant (RG130771). SHH acknowledges support from the Malaysian Government and the National University of Malaysia. EW thanks a Natural Environment Research Council Liverpool-Manchester EAO DTP PhD studentship (NE/L002469/1). SM acknowledges support from a Mineralogical Society Postgraduate Student Bursary which funded fieldwork to Skye. All authors thank the University of Liverpool, and Silvio De Angelis and Rob Duller are thanked for their assistance with the Micro Epsilon laser scanner. Sarah Henton De Angelis is thanked for assistance with the SEM and CL. Joan Martí, Lionel Wilson and Tim Horscroft are thanked for the invitation to write this research paper. Carmen López and Agust Gudmundsson are thanked for thoughtful reviews that improved the manuscript, and Joan Martí is thanked for editorial support.

References

- Abdelmalak, M.M., et al., 2012. Fracture mode analysis and related surface deformation during dyke intrusion results from 2D experimental modelling. *Earth Planet. Sci. Lett.* 359–360 (C), 93–105.
- Adrian, R.J., 1991. Particle-imaging techniques for experimental fluid mechanics. *Annu. Rev. Fluid Mech.* 23, 261–304.
- Bhattacharji, S., Smith, C.H., 1964. Flowage differentiation. *Science* 145, 150–153.
- Brizzi, S., et al., 2016. Salt matters: how salt affects the rheological and physical properties of gelatine for analogue modelling. 679, 88–101.
- Brown, R.J., et al., 2007. Mechanically disrupted and chemically weakened zones in segmented dike systems cause vent localization: evidence from kimberlite volcanic systems. *Geology* 35 (9), 815–818.
- Caricchi, L., et al., 2014a. Frequency and magnitude of volcanic eruptions controlled by magma injection and buoyancy. *Nat. Geosci.* 7 (2), 1–5.
- Caricchi, L., et al., 2014b. The influence of cooling, crystallisation and re-melting on the interpretation of geodetic signals in volcanic systems. *Earth Planet. Sci. Lett.* 388 (C), 166–174.
- Castro, J.M., et al., 2016. Rapid laccolith intrusion driven by explosive volcanic eruption. *Nat. Commun.* 7, 1–7.
- Cervelli, P., et al., 2002. The 12 September 1999 upper east rift zone dike intrusion at Kilauea volcano, Hawaii. *J. Geophys. Res.* 107 (B7), 2150.
- Crisp, J.A., 1984. Rates of magma emplacement and volcanic output. *J. Volcanol. Geotherm. Res.* 20, 177–211.
- Dahm, T., 2000. On the shape and velocity of fluid-filled fractures in the earth. *Geophys. J. Int.* 142 (1), 181–192.
- Daniels, K.A., Menand, T., 2015. An experimental investigation of dyke injection under regional extensional stress. *J. Geophys. Res. Solid Earth* 120, 2014–2035.
- Daniels, K.A., et al., 2012. The shapes of dikes: evidence for the influence of cooling and inelastic deformation. *GSA Bull.* 124 (7–8), 1102–1112.
- Delaney, P.T., et al., 1986. Field relations between dikes and joints: emplacement processes and palaeostress analysis. *J. Geophys. Res.* 91 (B5), 4920–4938.
- Djabourov, M., Leblond, J., Papon, P., 1988. Gelation of aqueous gelatin solutions. II. Rheology of the sol-gel transition. *J. Phys.* 49 (2), 333–343.
- Geshi, N., Kusumoto, S., Gudmundsson, A., 2010. Geometric difference between non-feeder and feeder dikes. *Geology* 38 (3), 195–198.
- González, P.J., Palano, M., 2014. Mt. Etna 2001 eruption: new insights into the magmatic feeding system and the mechanical response of the western flank from a detailed geodetic dataset. *J. Volcanol. Geotherm. Res.* 274, 108–121.
- Gudmundsson, A., 2002. Emplacement and arrest of sheets and dykes in central volcanoes. *J. Volcanol. Geotherm. Res.* 116, 279–298.
- Gudmundsson, A., 2003. Surface stresses associated with arrested dykes in rift zones. *Bull. Volcanol.* 65 (8), 606–619.
- Gudmundsson, A., 2006. How local stresses control magma-chamber ruptures, dyke injections, and eruptions in composite volcanoes. *Earth Sci. Rev.* 79 (1–2), 1–31.
- Gudmundsson, A., et al., 2014. Dike emplacement at Bardarbunga, Iceland, induces unusual stress changes, caldera deformation, and earthquakes. *Bull. Volcanol.* 76 (10), 869.
- Herrero-Bervera, E., et al., 2001. Magnetic fabric and inferred flow direction of dikes, conesheets and sill swarms, Isle of Skye, Scotland. *J. Volcanol. Geotherm. Res.* 106 (3), 195–210.
- Ilyinskaya, E., et al., 2017. Earth and planetary science letters. *Earth Planet. Sci. Lett.* 1–14.
- Kahl, M., et al., 2011. Dynamic plumbing system beneath volcanoes revealed by kinetic modeling, and the connection to monitoring data: an example from Mt. Etna. *Earth Planet. Sci. Lett.* 308, 11–12.
- Kavanagh, J.L., 2018. Mechanisms of magma transport in the upper crust – Dyking. In: Burchard, S. (Ed.), *Volcanic and Igneous Plumbing Systems: Understanding Magma Transport, Storage, and Evolution in the Earth's Crust*. Elsevier (In press).
- Kavanagh, J.L., Sparks, R.S.J., 2011. Insights of dyke emplacement mechanics from detailed 3D dyke thickness datasets. *J. Geol. Soc.* 168 (4), 965–978.
- Kavanagh, J.L., Menand, T., Sparks, R.S.J., 2006. An experimental investigation of sill formation and propagation in layered elastic media. *Earth Planet. Sci. Lett.* 245 (3–4), 799–813.
- Kavanagh, J., Menand, T., Daniels, K.A., 2013. Gelatine as a crustal analogue: determining elastic properties for modelling magmatic intrusions. *Tectonophysics* 582, 101–111.
- Kavanagh, J.L., Boutelier, D., Cruden, A.R., 2015. The mechanics of sill inception, propagation and growth: experimental evidence for rapid reduction in magmatic overpressure. *Earth Planet. Sci. Lett.* 421, 117–128.
- Kavanagh, J.L., et al., 2017a. Controls on sill and dyke-sill hybrid geometry and propagation in the crust: the role of fracture toughness. *Tectonophysics* 698 (C), 109–120.
- Kavanagh, J.L., Engwell, S., Martin, S., 2017b. A review of analogue and numerical modeling in volcanology. *Solid Earth Discussions*. <https://doi.org/10.5194/se-2017-40>.
- Le Corvec, N., Menand, T., Lindsay, J., 2013a. Interaction of ascending magma with pre-existing crustal fractures in monogenetic basaltic volcanism: an experimental approach. *J. Geophys. Res. Solid Earth* 118 (3), 968–984.
- Le Corvec, N., Spörrli, K.B., et al., 2013b. Spatial distribution and alignments of volcanic centers: clues to the formation of monogenetic volcanic fields. *Earth Sci. Rev.* 124 (C), 1–19.
- Lespinasse, M., 1999. Are fluid inclusion planes useful in structural geology? *J. Struct. Geol.* 21, 1237–1243.
- Lespinasse, M., Cathelineau, M., 1990. Fluid percolations in a fault zone: a study of fluid inclusion planes in the St Sylvestre granite, northwest massif central, France. *Tectonophysics* 184, 173–187.
- Lespinasse, M., Pecher, A., 1986. Microfracturing and regional stress field: a study of the preferred orientations of fluid-inclusion planes in a granite from the massif central, France. *J. Struct. Geol.* 8 (2), 169–180.

- Lister, J.R., 1990a. Buoyancy-driven fluid fracture: similarity solutions for the horizontal and vertical propagation of fluid-filled cracks. *J. Fluid Mech.* 217, 213–239.
- Lister, J.R., 1990b. Buoyancy-driven fluid fracture: the effects of material toughness and of low-viscosity precursors. *J. Fluid Mech.* 210, 263–280.
- Lister, J.R., Kerr, R.C., 1991. Fluid-mechanical models of crack propagation and their application to magma transport in dykes. *J. Geophys. Res. Solid Earth* 96 (B6), 10049–10077.
- Lundgren, P., et al., 2013. Evolution of dike opening during the march 2011 Kamoamao fissure eruption, Kilauea volcano, Hawai'i. *J. Geophys. Res. Solid Earth* 118 (3), 897–914.
- Maccaferri, F., et al., 2014. Off-rift volcanism in rift zones determined by crustal unloading. *Nat. Geosci.* 7 (4), 297–300.
- Menand, T., Daniels, K.A., Benghiat, P., 2010. Dyke propagation and sill formation in a compressive tectonic environment. *J. Geophys. Res.* 115 (B08201). <https://doi.org/10.1029/2009JB006791>.
- Menand, T., de Saint-Blanquat, M., Annen, C., 2011. Emplacement of magma pulses and growth of magma bodies. *Tectonophysics* 500 (1–4), 11–19.
- Patane, D., et al., 2002. Tomographic images and 3D earthquake locations of the seismic swarm preceding the 2001 Mt. Etna eruption: evidence for a dyke intrusion. *Geophys. Res. Lett.* 29 (10), 1497.
- Pecher, A., Lespinasse, M., Leroy, J., 1985. Relations between fluid inclusion trails and regional stress field: a tool for fluid chronology—an example of an intragranitic uranium ore deposit (northwest massif central, France). *Lithos* 18, 229–237.
- Pinel, V., Jaupart, C., 2000. The effect of edifice load on magma ascent beneath a volcano. *Philos. Trans. R. Soc. A Math. Phys. Eng. Sci.* 358 (1770), 1515–1532.
- Putirka, K.D., 2017. Down the crater: where magmas are stored and why they erupt. *Elements* 13, 11–16.
- Righetti, R., et al., 2004. The feasibility of using elastography for imaging the Poisson's ratio in porous media. *Ultrasound Med. Biol.* 30 (2), 215–228.
- Rivalta, E., Böttinger, M., Dahm, T., 2005. Buoyancy-driven fracture ascent: experiments in layered gelatine. *J. Volcanol. Geotherm. Res.* 144 (1–4), 273–285.
- Rivalta, E., et al., 2015. A review of mechanical models of dike propagation: schools of thought, results and future directions. *Tectonophysics* 638, 1–42.
- Roedder, E., 1984. Fluid inclusions. *Rev. Mineral.* 12, 646.
- Roper, S.M., Lister, J.R., 2007. Buoyancy-driven crack propagation: the limit of large fracture toughness. *J. Fluid Mech.* 580, 359–380.
- Rubin, A.M., 1995. Propagation of magma-filled cracks. *Annu. Rev. Earth Planet. Sci.* 23 (1), 287–336.
- Sigmundsson, F., et al., 2010. Intrusion triggering of the 2010 Eyjafjallajökull explosive eruption. *Nature* 468 (7322), 426–430.
- Sigmundsson, F., et al., 2014. Segmented lateral dyke growth in a rifting event at Bárðarbunga volcanic system, Iceland. *Nature* 517 (7533), 191–195.
- Smith, R.P., 1987. Dyke emplacement at Spanish Peaks, Colorado. In: Halls, H.C. (Ed.), *Mafic Dyke Swarms*, Geological Association of Canada Special Paper. 34, pp. 47–54.
- Smith, D.L., Evans, B., 1984. Diffusional crack healing in quartz. *J. Geophys. Res.* 89, 4125–4135.
- Sparks, R., Biggs, J., Neuberg, J.W., 2012. Monitoring volcanoes. *Science* 335, 1310–1311.
- Spence, D.A., Sharp, P.W., Turcotte, D.L., 1987. Buoyancy-driven crack propagation: a mechanism for magma migration. *J. Fluid Mech.* 174, 135–153.
- Taisne, B., Jaupart, C., 2009. Dike propagation through layered rocks. *J. Geophys. Res. Solid Earth* 114 (B9). <https://doi.org/10.1029/2008JB006228>.
- Taisne, B., Tait, S., 2009. Eruption versus intrusion? Arrest of propagation of constant volume, buoyant, liquid-filled cracks in an elastic, brittle host. *J. Geophys. Res.* 114 (B6), B06202.
- Taisne, B., Tait, S., 2011. Effect of solidification on a propagating dike. *J. Geophys. Res.* 116 (B1), B01206.
- Takada, A., 1990. Experimental study on propagation of liquid-filled crack in gelatin: shape and velocity in hydrostatic stress condition. *J. Geophys. Res.* 95, 8471–8481.
- Walker, R.J., Branney, M.J., Norry, M.J., 2017. Dike propagation and magma flow in a glassy rhyolite dike: a structural and kinematic analysis. *Geol. Soc. Am. Bull.* B31378, 1.
- Watanabe, T., et al., 2002. Analogue experiments on magma-filled cracks: competition between external stresses and internal pressure. *Earth Planets Space* 54, 1247–1261.
- Weertman, J., 1971. Theory of water-filled crevasses in glaciers applied to vertical magma transport beneath oceanic ridges. *J. Geophys. Res.* 76 (5), 1171–1183.
- Wright, T.J., et al., 2012. Geophysical constraints on the dynamics of spreading centres from rifting episodes on land. *Nat. Geosci.* 5, 242–250.



The impact of unloading stresses on post-caldera magma intrusions

Ayleen Gaete^{a,*}, Janine L. Kavanagh^b, Eleonora Rivalta^a, Suraya Hilmi Hazim^b, Thomas R. Walter^a, David J.C. Dennis^c

^a GFZ German Research Centre for Geosciences, Telegrafenberg, 14473 Potsdam, Germany

^b Department of Earth, Ocean and Ecological Sciences, University of Liverpool, Jane Herdman Laboratories, Liverpool L69 3GP, UK

^c School of Engineering, University of Liverpool, Liverpool L69 3GH, UK

ARTICLE INFO

Article history:

Received 15 August 2018

Received in revised form 8 December 2018

Accepted 17 December 2018

Available online 11 January 2019

Editor: T.A. Mather

Keywords:

caldera
cone sheet
gelatin analogue modeling
circumferential dike
digital image correlation

ABSTRACT

Calderas represent morphological depressions several kilometers in diameter, and the unloaded crustal stresses they produce can form rapidly (e.g. Pinatubo, 1990) or slowly (e.g. Hawaii, 2018). Active calderas are known as sites of persistent magma intrusions, and yet the dynamics of their shallow plumbing system is not well constrained. We use scaled laboratory experiments to study how experimental intrusions are created beneath a caldera by injecting dyed water (magma analogue) into the base of an elastic gelatin solid (crust analogue) with a cylindrical cavity in its surface to mimic a caldera-like topography. The evolving dike geometry and stress field were qualitatively determined using polarized light, and digital image correlation allowed the incremental and total strain to be quantified by tracking passive-tracer particles in the gelatin that fluoresced in a thin 2D vertical laser sheet. Our results show that the unloaded stress field from a caldera can cause a divergence of vertical dikes, and leads to circumferential dikes and cone sheets. When the caldera was large the initially vertical dike became arrested, then grew laterally via circumferentially-propagating en echelon segments; these eventually joined to complete a cone sheet that was parallel to, but extended outside and beneath, the large caldera. When the caldera was small, a circumferential dike erupted, producing a short fissure which was outside, but parallel to, the caldera. We suggest that the distinct curved geometry, velocity, strain and stress characteristics of circumferential dikes and cone sheets can be used to interpret the origin and growth of post-caldera magmatism and the likelihood of eruption in caldera systems.

© 2019 Elsevier B.V. All rights reserved.

1. Introduction

Calderas are associated with some of the largest volcanic systems (e.g. Yellowstone, USA) where topographic lows form due to subsidence along caldera ring faults (Cole et al., 2005). Caldera-forming events can be rapid (Mt Pinatubo in Philippines, 1990, e.g. Pallister et al., 1996) or slow (Kilauea volcano in Hawaii, 2018, e.g. USGS, 2018) and may form due to explosive volcanic eruptions (Cole et al., 2005) or gradual drainage of a deep reservoir by lateral intrusion. Despite the largest cataclysmic eruptions being produced during the formation of the caldera itself (Jellinek and DePaolo, 2003), unrest at calderas and relatively small post-caldera eruptions are frequent and pose a significant hazard to the population. Caldera systems are active sites of mineralization, and understanding their development and impact on the volcanic plumbing system is important for georesources, e.g. copper-porphyry deposits

(e.g. Blundy et al., 2015), and carbonatite-hosted Rare Earth Elements (e.g. Le Bas, 1987). Irregular topographies and crustal loads are common in volcanic terrains, from tectonic rift zones (e.g. Afar and Iceland) to laterally collapsed sectors of a volcanic edifice (e.g. Mt St Helens, USA), unstable volcanic islands (e.g. La Palma, Canary Islands), ice unloading, and excavation of quasi-cylindrical craters associated with volcanic vents, calderas, tuff cones and diatremes.

Field observations suggest that post-caldera magmatism typically occurs via inclined sheet intrusions (Burchardt et al., 2011). These may take a variety of forms (e.g. Burchardt et al., 2018). In this paper we use the terms ‘circumferential dike’, which have an arcuate horizontal section, and ‘cone sheet’, which taper downwards towards a central point and have a circular horizontal section, to distinguish and reflect the end member intrusion geometries, without reference to their process of formation. These intrusion types are common igneous magma bodies, are a major constituent of sub-volcanic plumbing systems, and may feed eruptions in caldera settings (e.g. Bagnardi et al., 2013; Chadwick et al., 2011).

* Corresponding author.

E-mail address: agaete@gfz-potsdam.de (A. Gaete).

There are several contrasting conceptual models to explain cone sheet formation, but these often do not invoke the presence of a caldera. For example, Galland et al. (2014) carried out an experimental study of cone sheet development by injecting oil into compacted silica flour with a flat topography. They found that cone sheets formed due to a dynamic dimensionless ratio which included the effects of magma viscosity and host-rock deformation mode. In comparison, Magee et al. (2012) proposed that cone sheets form by lateral propagation of regional dikes from an adjacent source, whereas other authors invoke stress changes from a central magma chamber at depth (Anderson, 1936; Johnson et al., 1999; Schirnack et al., 1999; Geshi, 2005). These fundamentally different models demonstrate there remains uncertainty in the growth dynamics of the magmatic system, and cone sheets in particular. Accurately interpreting the surface signals of magma movement for hazard assessment at active volcanoes ultimately depends on the quality of the models upon which these inferences are made (Di Vito et al., 2016; Guldstrand et al., 2017).

The emplacement, propagation and geometry of magma intrusions are influenced by several related factors including density contrasts between magma and host-rock, the ambient stress field (tectonic, regional or local), stress barriers, the physical properties of the intruding magma (e.g. viscosity), and mechanical heterogeneities in the crust such as rock layering and faults (see reviews by Burchardt et al., 2018 and Rivalta et al., 2015). A commonly explored scenario is that of dike propagation beneath a volcanic edifice where crustal loading influences the tendency for magma to stall at depth or erupt, and whether an eruption occurs in the summit or flank of the volcano (Kervyn et al., 2009; Maccaferri et al., 2011), depending on the magma buoyancy, edifice size and crustal layering (density, rigidity and interface weakness). The load from a volcanic edifice can cause the attraction of dikes located away from the volcano, and in some cases promote their lateral (blade-like) propagation rather than vertical growth (Watanabe et al., 2002). This supports the hypothesis that dikes change their trajectory during propagation in response to perturbations of the maximum compressive stress (σ_1), whose orientation may vary due to local or regional compression or extension of the medium (Anderson, 1936; Maccaferri et al., 2011; Mathieu et al., 2015; Rivalta et al., 2015).

Magma propagation under a topographic low, such as a caldera, has been relatively unexplored, despite such unloaded stress fields being common features in volcanic terrains (Corbi et al., 2015; Mathieu et al., 2008). Numerical and analogue modeling suggest that a caldera geometry in a volcanic edifice induces unloading stresses that in a cohesive, crystalline rock may favor the emplacement of laminar intrusions with circumferential and/or radial shapes and sills (Corbi et al., 2016, 2015).

Despite the significance of post-caldera magmatism, questions remain regarding the nature of magma intrusion in an unloaded crust. We present results from gelatin laboratory experiments that model the emplacement of a dike in the vicinity of a caldera-like topography. The experiments integrate measurements of sub-surface strain evolution and stress evolution using digital image correlation and polarized light, respectively. Our results test existing models of circumferential dike and cone sheet development and assist in their interpretation by constraining their geometry, propagation pathway, sub-surface deformation and likelihood of eruption.

2. Modeling framework

Following the approach described by Merle (2015), we define a laboratory prototype scaled geometrically (ratio of distances is constant in nature and the prototype), kinematically (the geomet-

ric scaling is maintained over time), and dynamically (the ratio of the mechanical forces between nature and the model is constant). Our selected analogue material for the crust is gelatin, and for magma we have selected water (see Supplementary Table S1 for detailed scaling). Gelatin has been very well studied in scaled laboratory experiments to simulate elastic process in the crust associated with magmatic intrusions (Di Giuseppe et al., 2009; Kavanagh et al., 2013). Gelatin is a visco-elastic material and its transparency allows the evolving dynamic process of dike propagation to be visually tracked in an experiment (Takada, 1990; Watanabe et al., 2002). When used at low concentration (2–5 wt.%) and at low temperature (5–10 °C) it behaves elastically over the timescale of an experiment (Kavanagh et al., 2013), which lasts approximately 10 min. Gelatin has been intruded by a range of fluids to simulate dike emplacement (see Kavanagh et al., 2018b for a review). We have chosen water as the magma analogue as it is a low-viscosity fluid (10^{-3} Pa s) and is slightly less dense than the gelatin ($\Delta\rho = 6 \text{ kg m}^{-3}$). It is a suitable analogue to simulate intrusions of low to intermediate viscosity magma that is mostly driven by the overpressure of liquid from a distant source (Kervyn et al., 2009), and it has been used in several previous experiments that study dike propagation (Kavanagh et al., 2018a; McLeod and Tait, 1999).

We define the geometric scale between nature n and prototype p in our experiments as the length scale factor:

$$L^* = \frac{L_p}{L_n} \quad (1)$$

Giving $L^* = 1.0 \times 10^{-5}$ such that 1 cm in the laboratory represents 1 km in nature, considering that in nature the size of calderas range from 1 km to tens of kilometers in diameter (see Table S1). An alternative length scale factor is the buoyancy length L_b when magma buoyancy drives the rock fracture (Corbi et al., 2016; Kavanagh et al., 2013; Merle, 2015):

$$L_b^* = \left(\frac{K_c}{\pi^{\frac{1}{2}} \Delta\rho g} \right)^{\frac{2}{3}} \quad (2)$$

where K_c is the fracture toughness of the host medium, $\Delta\rho$ is the elastic contrast between host rock and magma, and g is gravity (Taisne and Tait, 2009). Therefore we calculate $L_b^* = 4.1 \times 10^{-5}$ (see Table S1). Overall, the two length scales (Equations (1) and (2)) agree as they are within the same order of magnitude.

We have used two contrasting approaches to scale the stresses in our experiments: firstly we scale the elastic deformation of the host material, and secondly we scale the unloading pressure associated with the caldera. Firstly, we calculate the strain scale factor e^* :

$$e^* = \frac{a}{b} \quad (3)$$

where a is the dike thickness and b is the dike width. This means $e^* = 10$ when $e_n = 0.002$ and $e_p = 0.02$ in gelatin (Kavanagh et al., 2013). We define a Young's modulus scale factor $E^* = 3 \times 10^{-7}$, as $E_n = 10^9\text{--}10^{10}$ (Kavanagh et al., 2013) and $E_p = 300\text{--}3000$ (see Table S1). As the elastic deformation of the gelatin can be defined by the relationship between stress (σ), strain (e) and Young's modulus (E) (Gudmundsson, 2006; Merle, 2015):

$$\sigma^* = E^* e^* \quad (4)$$

This gives $\sigma^* = 3.0 \times 10^{-6}$ (see Table S1). We also use the unloading pressure scale factor:

$$\sigma^* = P_U^* = \rho_r^* g^* D^* \quad (5)$$

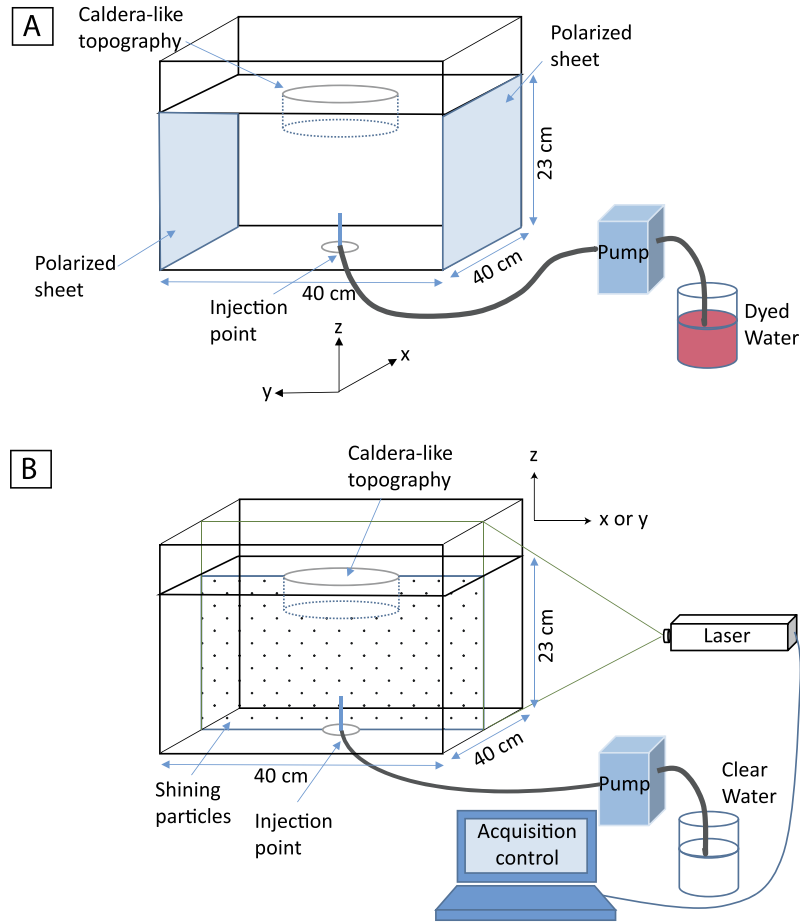


Fig. 1. Schematic diagram of the experimental setups. A) Polarized light experiment: dyed water is injected into the base of a gelatin slab using a peristaltic pump. The gelatin surface is modeled to have a caldera-like topography, and stress in the gelatin is visualized using two parallel polarized sheets attached to the tank walls on the x - z plane and perpendicular to the initial dike profile. Two HD video cameras (not shown) record images the x - z and y - z directions. B) Tracer particle experiment: a high intensity vertical laser sheet illuminates a 2D profile (either x - z plane or y - z plane) through the center of the tank and exciting passive-tracer fluorescent particles in the gelatin. A CCD camera records the illuminated plane at 1 frame per second, synchronized with the laser.

where D is the caldera depth and ρ_r is the host rock density. As $\rho_r^* = 0.37$ and $D^* = 1 \times 10^{-5}$, this gives $\sigma^* = 3.7 \times 10^{-6}$. The agreement between the stress values calculated from both of these approaches (Equations (4) and (5)) confirms that we have properly scaled our experiments.

3. Experimental methodology

3.1. Gelatin preparation and Young's modulus measurement

We use pigskin gelatin solids (20 Mesh, 260 Bloom; supplied by Gelita UK) prepared at 2.5 wt.% by dissolving the appropriate amount of gelatin powder into water at 80 °C. The mixture preparation requires three stages: an initial stage where a concentrated mixture is created and left to cool until it reaches ~ 30 °C, then the remaining water is added at 5 °C to achieve a mixture temperature of ~ 23 °C. Some experiments required the addition of passive-tracer particles, coated in Rhodamine-B which fluoresces in laser light, to the liquid gelatin in order to apply Digital Image Correlation (DIC) analysis (Sutton et al., 1983). For this purpose, 20–50 μm diameter fluorescent particles (peak fluorescence wavelength: 590 nm) are added to the gelatin mixture following the method described by Kavanagh et al. (2015). A clear-Perspex tank (40 cm square-base, 30 cm high; Fig. 1) is then filled up to 23 cm height and the mixture stirred until it reaches the gel point (21 °C) to obtain a homogeneous distribution of particles in the solid gel.

A caldera-like geometry is established using a round, plastic container (9 or 12 cm diameter) placed onto the gelatin surface and fixed into position relative to the central injection port in the base of the experimental tank using plastic tape. The depth of the caldera is controlled by adding water to the plastic container so that it is submerged by 4 cm depth. Subsequently, the gelatin mixture is covered with vegetable oil which is carefully poured onto its surface to inhibit dehydration, the tank is then covered with plastic wrapping and then left to cool and solidify in a refrigerator set at 5 °C for 20 h. The tank is then taken from the refrigerator, and the plastic container is removed from the center of the gelatin solid by filling it with hot water to allow an easy release and avoid any damage at the floor and/or wall of the caldera that is formed. The oil is then carefully removed using a spoon and paper towel, and the actual depth of the caldera is measured (typically 3–4 cm, see Table 1).

Immediately prior to the experiment starting, the Young's Modulus of the gelatin is calculated by measuring the deflection to the gelatin surface caused by two cylindrical brass loads placed sequentially on the gelatin slab (see Supplementary Table S2 for load properties). The load is placed away from the corner of the tank to minimize any wall effects. The Young's Modulus is calculated using the following equation (Kavanagh et al., 2013):

$$E = \frac{mg(1 - \nu^2)}{\psi w} \quad (6)$$

Table 1
Model parameters, observed results, and methods applied in the experiment analysis. The experiments are listed in order of caldera diameter C and offset injection position X . The measured caldera depth D , gelatin concentration wt.%, thickness of gelatin slab H , time left to cure t , refrigerator temperature T , average Young's modulus E , and injection flux of fluid Q is reported. 'Result' corresponds to the final geometry of the intrusion classified as 'C. dike' (circumferential dike), 'Cone sheet', or 'Cone-Trans' for transitional geometries, and the final depth of bending h , and extent of intrusion d are also reported. The analysis methods used are: Polarized light (PL), vertical tip tracking (TT) and tracer particles (TP).

Experiment code	C (cm)	X (cm)	D (cm)	Wt. (%)	H (cm)	t (h)	T (°C)	E (Pa)	Q (m ³ /s)	Result	h (cm)	d (cm)	Analysis method
AG-07	9.0	0.0	3.31	2.5	22.6	20.5	5	2675	3.9×10^{-7}	C. dike	8.2	13.0	PL, TT
AG-13	9.0	0.0	3.78	2.5	23.1	20.5	5	2843	3.9×10^{-7}	C. dike	10.7	13.3	TP
AG-09	9.0	1.0	3.04	2.5	23.2	21.0	5	2490	3.9×10^{-7}	C. dike	8.8	13.8	PL, TT
AG-08	12.0	0.0	3.94	2.5	23.5	20.0	5	3113	3.9×10^{-7}	Cone sheet	12.1	22.4	PL, TT
AG-06	12.0	0.0	3.52	2.5	22.4	19.8	5	2779	3.9×10^{-7}	Cone-Trans	10.7	17.5	–
AG-14	12.0	0.0	4.20	2.5	23.5	21.0	5	2739	3.9×10^{-7}	Cone-Trans	11.1	16.9	–
AG-15	12.0	0.0	3.65	2.5	23.5	21.1	5	2586	3.9×10^{-7}	Cone-Trans	9.8	17.7	–
AG-16	12.0	0.0	3.77	2.5	23.2	20.5	5	2902	3.9×10^{-7}	Cone-Trans	16.8	17.5	–
AG-10	12.0	1.0	3.55	2.5	22.5	21.0	5	2401	3.9×10^{-7}	Cone sheet	12.0	23.4	PL, TT
AG-05	12.0	1.0	3.58	2.5	23.1	19.7	5	2721	3.9×10^{-7}	Cone sheet	14.3	23.7	TT
AG-17	12.0	1.0	3.95	2.5	23.2	19.7	5	2580	3.9×10^{-7}	Cone sheet	15.2	24.5	TP
AG-19	12.0	1.0	3.80	2.5	23.1	19.0	5	2964	3.9×10^{-7}	Cone sheet	15.3	24.0	TP
AG-18	12.0	2.0	3.90	2.5	23.2	22.0	5	3031	3.9×10^{-7}	Cone sheet	14.5	23.9	TP

where m is the load mass, g is the acceleration due to gravity, ν is the Poisson's ratio (0.5 for gelatin (e.g. Kavanagh et al., 2013; Watanabe et al., 2002)), Ψ is the load diameter, and w is the deflection of the surface produced by the load. The average Young's modulus from each load placement is then reported (see Table 1).

3.2. Experiment setup

Two imaging techniques were used on the experiments to study the subsurface processes associated with dike growth and evolution using two different sets of apparatus: photoelasticity for visualizing stress (Fig. 1A), and tracer particle for measuring subsurface strain and displacement (Fig. 1B). To create an experimental dike, a small cut is made in the bottom of the gelatin slab, which controls the orientation of the initial dike. A metal pipe with a tapered end is inserted into this slit and dyed water is injected using a peristaltic pump at a constant volumetric flow rate (Q) of 3.9×10^{-7} m³/s. The fluid velocity (V) is approximated by dividing Q by the cross-sectional area of the 1 mm-diameter injection outlet. Injections were made at two different offset positions (0.0 cm and 1.0 cm, relative to the center of the caldera) beneath two different caldera sizes (see Table 1).

3.2.1. Photoelasticity setup

Polarized light is known to be a useful tool to visualize the stress distribution in two dimensional elastic problems (Crisp, 1952; Watanabe et al., 2002). We use the photoelastic property of gelatin with the purpose of understanding the interaction of the local stresses with those of the pressurized experimental dike, making a qualitative description of the changes in the stress field during the intrusion development. The sequence of colored fringes represents the gradient of the differential stress ($\sigma_1 - \sigma_3$) perpendicular to the light propagation direction, and the increasing fringe order represents linearly increasing stress (Crisp, 1952); which in the experiments depend on the caldera diameter and caldera depth. The photoelasticity experimental setup (Fig. 1A) consists of two polarized sheets attached to the front and back walls of the tank (x - z plane), and two HD video cameras positioned to record images with polarized light (x - z plane, perpendicular to the dike plane) and artificial light (y - z plane, parallel to the dike plane).

3.2.2. Tracer particle setup

The tracer particle experiment setup requires the use of a high intensity laser that was configured to fire at 1 Hz and produce a vertical, thin sheet (approximately 1 mm thick) in the gelatin slab centered on the injection point (Fig. 1B, see also Kavanagh et

al., 2015). A New Wave Solo-PIV III Nd-YAG Laser provides 50 mJ pulses of energy between 3 and 5 ns and 532 nm wavelength. The laser firing and acquisition is controlled by Dantec Dynamic Studio software and synchronized to a MP CCD camera fitted with a 35 mm Nikon lens (Fig. 1B). Longpass (550 nm wavelength) filters fitted to the CCD camera allow only the fluorescent light reflected by the particles to be captured.

A 2D calibration image is required for post-experiment image processing. Prior to the experiment tank being filled with gelatin, the tank is filled with water and a white calibration plate with equally-spaced black dots of known size and spacing was aligned with the laser beam in the center of the experimental tank. An image is then captured for later data pre-processing using DIC.

3.3. Data processing

In order to study the evolution of the growing intrusion geometry, we first track the vertical dike tip trajectory in the x - z plane using video images from the polarized light setup (Fig. 1A). This is conducted at intervals of one frame every 5 s using the free Java software Tracker vs 4.10.0 (Brown, 2012). The coordinate origin is set as the top of the needle in the calibrated model, and the position of the vertical dike tip is manually tracked over time. The velocity of the dike tip and the local dip angle relative to horizontal is simultaneously computed.

DIC is then used to quantify the sub-surface displacement vectors and total strain due to the dike intrusion, at an interval of one image every 5 s (0.2 Hz), by using the commercial image analysis tool StrainMaster, implemented in the DaVis software package vs. 8 (LaVision). The calibration image captured prior the experiment is imported into DaVis in a pre-processing stage to scale the results in dimensional units. This process converts the scale from pixels to distance units, and corrects any distortions through the de-warping function. The incremental strain is then calculated by implementing a 'Least Square Matching' algorithm (LSM-algorithm), which operates using an optical flow approach (Fleet and Weiss, 2006). Three seeding points are defined within the reference image, and these are static windows of initial size 121×121 pixels that experience no deformation in the experiment. The interrogated area then increases in size with each iteration implementing the 'region grow' algorithm. Outlier and Smoothing filters are then applied, and a mask function is added to exclude the tank walls and caldera cavity from the analysis. The incremental strain is summed to give the total strain. For very small displacement gradients,

the strain tensor values are defined by Cauchy's infinitesimal tensor:

$$\epsilon_{ij} = \frac{1}{2} \left(\frac{\partial v_i}{\partial x_j} + \frac{\partial v_j}{\partial x_i} \right) \quad (7)$$

where v is the vector component and x the spatial axis. As the experiment observations are carried out in two dimensions (x - z or y - z plane), the lineal deformation in the x - or y -direction and in the z -direction are determined by the normal strain components:

$$\epsilon_{xx} = \frac{\partial u}{\partial x} \quad \text{or} \quad \epsilon_{yy} = \frac{\partial v}{\partial y} \quad (8)$$

and,

$$\epsilon_{zz} = \frac{\partial w}{\partial z} \quad (9)$$

Thus, the shear strain is given by:

$$\epsilon_{xz} = \epsilon_{zx} = \frac{1}{2} \left(\frac{\partial u}{\partial z} + \frac{\partial w}{\partial x} \right) \quad \text{or} \quad \epsilon_{yz} = \epsilon_{zy} = \frac{1}{2} \left(\frac{\partial v}{\partial z} + \frac{\partial w}{\partial y} \right) \quad (10)$$

4. Results

In total 19 experiments were conducted to explore the influence of caldera unloading and injection offset on dike propagation, geometry and growth. The experimental results are grouped into two end-member geometries: circumferential dikes and cone sheets, however transition geometries are also observed (see Table 1). We detail our experimental observations and results below using representative experiments as examples grouped by their end-member geometries.

4.1. Circumferential dikes

Circumferential dikes are formed in our experimental series only in the presence of a small caldera (Table 1) and in three stages: 1) sub-vertical dike, 2) inclined sheet, and 3) ascent to eruption (see Supplementary Video Fig. S1). When the injection position is offset, these three stages occur earlier and their transitions happen at greater depth than when the injection is central. The details of each stage of circumferential dike formation and eruption are now described.

4.1.1. Stage I: sub-vertical dike

Polarized light shows the unloading stress field induced by the caldera in the pre-injection state (Fig. 2Ai). When the injection starts, a vertical dike is produced (Fig. 2Aii and 2Bii) creating its own stress field that is focused in a small region around the dike tip and intensifying in magnitude and extent as the dike grows upwards until it reaches a vertical length of 9.2 cm by the end of this stage (Fig. 2Aii). At this time, the dike grows near vertical with a dip angle of approximately 80° (Fig. 3A). During this stage there is an initial rapid acceleration followed by velocity deceleration (Fig. 3B). The DIC analysis (Fig. 4) shows the displacement vectors are small and radiate out from the entire dike length, and the total normal strain component e_{xx} (Fig. 4Bi) is large (14×10^{-2}) compared with the vertical ($e_{zz} 4 \times 10^{-2}$, Fig. 4Ci) and shear components ($e_{xz} 4.5 \times 10^{-2}$, Fig. 4Di).

4.1.2. Stage II: inclined sheet

In Stage II, the dike moves away from the caldera center with a maximum height of 12.8 cm in the end of this stage (Fig. 2Aiii

and 2Biii). In terms of stress, this stage is distinguished by the colored fringes from the dike visually interacting with those of the caldera (Fig. 2Aiii). It coincides with a rapid decrease in the dip angle (from 80° to 40°, Fig. 3A) and a slight acceleration of the vertical tip (Fig. 3B). Overall the direction of displacement is upwards and towards the caldera, and its maximum amplitude is less than 5 mm (Fig. 4Aii, Bii, Cii). The total strain during Stage II (Fig. 4Aii) has slightly decreased in the normal horizontal strain (e_{xx} down to 11×10^{-2}), but has increased in the vertical and shear components (e_{zz} and e_{xz} up to 10×10^{-2} and 9×10^{-2} , respectively); e_{xx} is distributed along the length of the vertical dike and inclined limb (Fig. 4Bii), whereas there are local concentrations in e_{zz} (Fig. 4Cii) and e_{xz} (Fig. 4Dii) at the tip.

4.1.3. Stage III: ascent to eruption

The final stage of circumferential dike development is acceleration to eruption to form a circumferential fissure (Fig. 2Aiv and 2Biv). In our experiments all circumferential dikes erupted. During this final stage, there is no visual interaction between the dike stress field and that from the caldera. The dike dip angle gradually increases to 60° and then broadly maintains this (Fig. 3A). The vertical tip decelerates gradually, but then accelerates towards eruption (Fig. 3B). The maximum opening of the inclined limb of the dike is 7.8 mm thick (Fig. 4Aiii), generating the largest magnitude of the total displacement vectors which are oriented towards the caldera (Fig. 4Biii, Ciii, Diii). The total strain just before eruption produces the maximum deformation during injection, producing visible uplift of the caldera floor. The largest component of total strain is vertical at $e_{zz} 22.5 \times 10^{-2}$ (Fig. 4Ciii), with similar values in total horizontal and shear strain (e_{xx} and e_{xz} up to 17.5×10^{-2} ; Fig. 4Biii and 4Diii).

4.2. Cone sheets

Cone sheets were formed in the presence of the large caldera six times (see Table 1), and transitional geometries (partial cone, but with dike eruption) were formed four times. The cone sheets are formed in four stages (see Supplementary Video Fig. S2), with the first two stages being identical to the circumferential dike formation. Stage I is a sub-vertical dike, Stage II is an inclined sheet, Stage III is lateral growth, and Stage IV is cone sheet completion. Similarly to the circumferential dike, when the injection position is offset this results in earlier and deeper transitions between the stages.

4.2.1. Stage I: sub-vertical dike, and Stage II: inclined sheet

The pre-injection stress pattern induced by the large caldera shows more fringes that extend to greater depths in the gelatin slab (Fig. 5Ai) compared to the small caldera (Fig. 2Ai). Similarly to the small caldera experiments, the first two stages of cone sheet growth are: 1) sub-vertical dike (Fig. 5Aii, Bii), which then changes dip and develops into 2) an inclined sheet (Fig. 5Aiii, Biii). During Stage I we observe a moderate decrease in the dip angle from 85° to 75° (Fig. 3C) and velocity deceleration (Fig. 3D), as the dike reaches 9.3 cm height. During Stage II the dike changes dip angle from 75° to 35°, accelerates from 0.6 to 1.4 cm/s, and reaches 12.6 cm height by the end of Stage II.

The total displacement and total strain (normal and shear components) of cone sheet growth are measured in the x - z plane (Fig. 6) and y - z plane (Fig. 7). During Stages I and II, the majority of the propagation is out of the y - z plane and so only minor displacements and total strain are recorded in this view (Fig. 7Ai, Bi, Ci, Di, Aii, Bii, Cii, Dii). Stage I of cone sheet formation (Fig. 6Ai) has maximum total strain in the horizontal normal component ($e_{xx} = 11 \times 10^{-2}$, Fig. 6Bi), with this distributed across

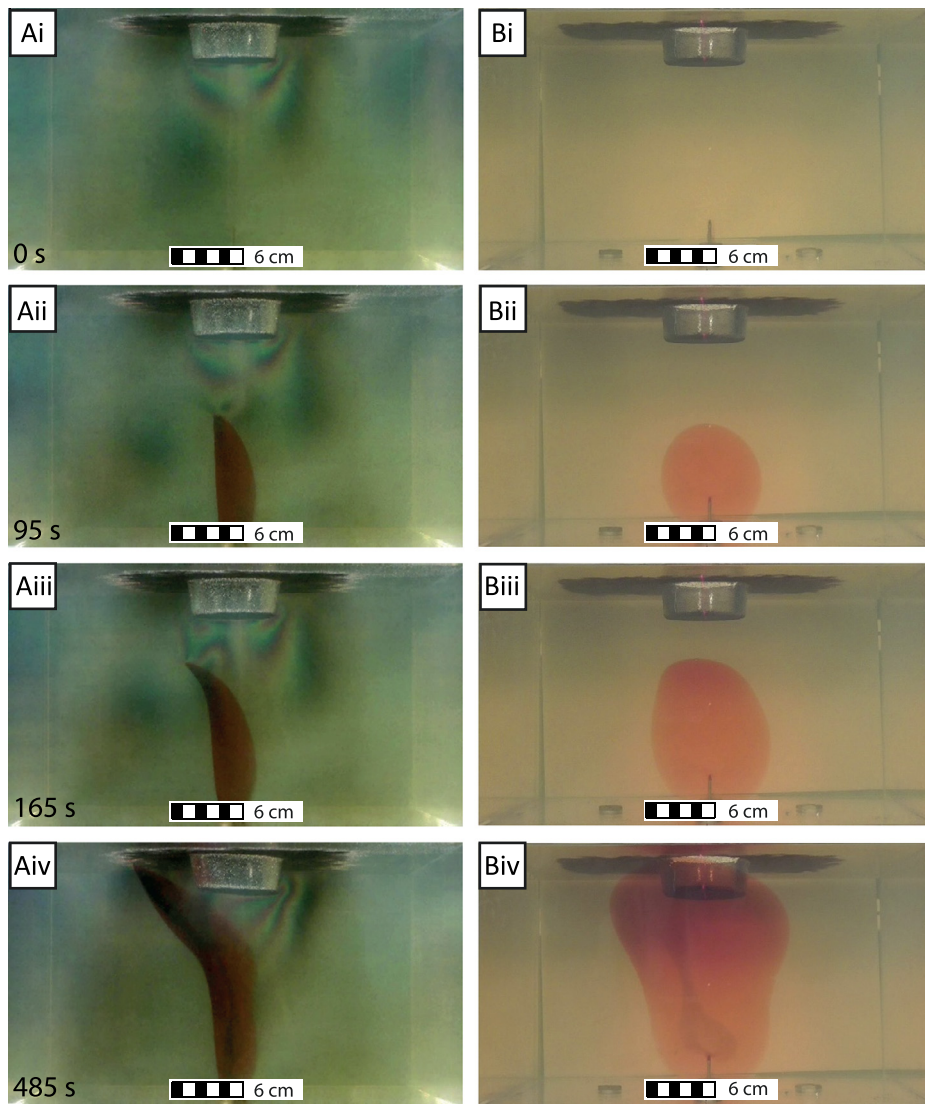


Fig. 2. Photographs of circumferential dike development in the presence of a small caldera (Experiment AG-07, see Table 1): A) Polarized light (x - z plane), and B) artificial light (y - z plane). i) Pre-injection state, ii) Stage I: sub-vertical dike (95 s), iii) Stage II: inclined sheet (165 s), iv) Stage III: ascent to eruption (485 s). See also Supplementary Video Fig. S1.

the whole dike, with lower vertical and shear total strain components (e_{zz} and $e_{xz} = 4 \times 10^{-2}$; Fig. 6Ci and 6Di). In contrast, Stage II has maximum total strain in the vertical normal component ($e_{zz} = 12 \times 10^{-2}$; Fig. 6Cii), with lower horizontal and shear total strain components (e_{xx} and $e_{xz} = 8 \times 10^{-2}$; Fig. 6Bii and 6Dii). There are also similar displacement vectors to those observed in Stages I and II of the circumferential dike formation, with low magnitude displacements (<5 mm in Stage I, and 5–10 mm in Stage II) radiating out from the dike.

4.2.2. Stage III: lateral dike growth by arcuate segments

Following initial vertical dike growth (Stage I) and then divergence to a dipping dike (Stage II), a new direction of intrusions establishes at the turning point h (see Table 1). Stage III of cone sheet growth is marked by the Stage II dike dip angle stabilizing at approximately 60° (Fig. 3C), and the vertical growth rapidly decelerating indicating an arrested dike (Fig. 3D). Two circumferential and laterally-propagating en echelon arcuate segments then form close to the turning point (Fig. 3C), specifically from the lower part of the inclined sheet (Fig. 5Aiv and 5Biv). In the x - z plane, the total displacement vectors increase in magnitude relative to Stage II to be >10 mm, and the maximum displacement

continues being oriented radially towards the caldera (Fig. 6Bii, Cii, Dii). The largest total strain is the vertical normal component ($e_{zz} = 37.5 \times 10^{-2}$; Fig. 6Ciii) followed by the shear component ($e_{xz} = 23 \times 10^{-2}$; Fig. 6Dii) and horizontal normal component ($e_{xx} = 20 \times 10^{-2}$; Fig. 6Bii). In Stage III, the cone sheet emerges in the y - z plane as the inclined, laterally-propagating arcuate segments penetrate the laser sheet (Fig. 7Aiii). This produces maximum total displacement of 10 mm (which is slightly less than measured in the x - z plane), and a maximum vertical deformation ($e_{zz} = 12 \times 10^{-2}$; Fig. 7Cii) compared to horizontal ($e_{yy} = 7 \times 10^{-2}$; Fig. 7Bii) and shear components ($e_{yz} = 9 \times 10^{-2}$; Fig. 7Dii); which are all lower than strains measured in the x - z plane.

4.2.3. Stage IV: cone sheet completion

The fourth and final stage of cone sheet formation is the completion of the cone geometry (Fig. 5Av and 5Bv). This occurs when the laterally-propagating arcuate segments of Stage III join to create a circular profile in the horizontal plane without erupting. The final cone sheet geometry has a range of forms spanning 'cocktail-glass', 'bowl' and 'trumpet' forms (Figs. 5, 6 and 7), in agreement with cone sheet geometries described by Burchardt et al. (2018).

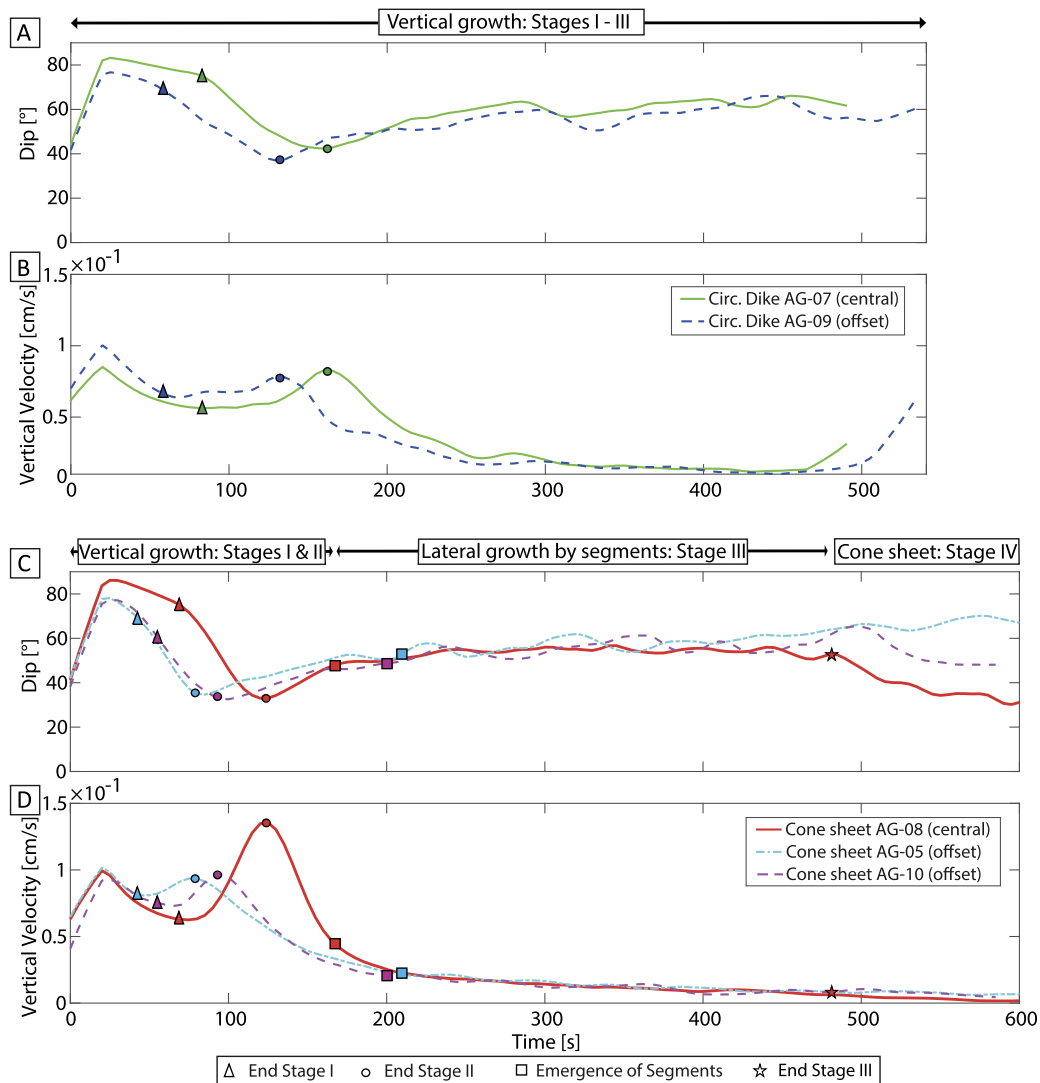


Fig. 3. Three stages of circumferential dike (A–B) and four stages of cone sheet (C–D) growth shown by changes in Dip angle ($^{\circ}$) and velocity (cm/s) of the vertical dike tip in the presence of the caldera. The approximate timings of stage transitions is indicated at the top of the graphs [A] for circumferential dikes, and C] for cone sheets]. In the graphs the triangle indicates the end of Stage I (sub-vertical dike), the circle indicates the end of Stage II (inclined sheet), and the star indicates the end of Stage III (lateral growth by arcuate segments in cone sheet emplacement). Stage III shows the ascent to eruption in circumferential dike emplacement. The Stage III of cone sheet growth produces laterally propagating arcuate segments (the time of their emergence is indicated by a square) and these join at the start of Stage IV to complete the geometry.

In transitional geometries, Stage III still produces the lateral sub-surface arcuate segments but they do not join. Instead, at some moment the vertical ascent of the dike is reinitiated, at the location where it first became arrested, and this results in an eruption. Therefore, transitional geometries do not reach Stage IV and have growth behavior and a final geometry that is intermediate to the circumferential dike and cone sheet.

Stage IV has a slight decrease in the dip angle starting immediately after the arcuate segments join (Fig. 3C), and the velocity decrease is maintained (Fig. 3D). The thickest opening of the inclined sheet was 13.63 mm (Fig. 6Aiv), which produced displacements greater than 10 mm focused directly beneath and towards the caldera (Fig. 6Biv, Civ, Div). The maximum strain occurs in the vertical normal component, reaching $e_{zz} = 55 \times 10^{-2}$ in the x - z plane (Fig. 6Civ) and $e_{zz} = 50 \times 10^{-2}$ the y - z plane (Fig. 7Civ). The total strain is up to $e_{xx} = 20 \times 10^{-2}$ and $e_{yy} = 12 \times 10^{-2}$ in the horizontal components (Figs. 6Biv and 7Biv, respectively), and $e_{xz} = 35 \times 10^{-2}$ and $e_{yz} = 22.5 \times 10^{-2}$ in the shear component (Figs. 6Div and 7Div, respectively).

5. Discussion

5.1. Circumferential dike or cone sheet? Comparison with previous experiments

Our experimental series has produced a spectrum of thin sheet-like intrusions, all of which were parallel to the circular caldera, and with end-member geometries of an erupted circumferential dike (Fig. 2) and an intrusive cone sheet (Fig. 5). The development of these different end-member geometries was similar. Both circumferential dikes and cone sheets propagated at dip angles which reached almost vertical (Fig. 3A, C, and Fig. 8), but the circumferential dikes dip angle ranged from $\sim 40^{\circ}$ compared to 30° for the cone sheets (Fig. 8). These dip values are similar to those in nature, for example the trachytic to phonolitic cone sheets of the Tejada Complex, Gran Canaria which intruded intra-caldera deposits (Schirnick et al., 1999), and the mafic cone sheets of the Ardnamurchan central igneous complex, NW Scotland which intruded into the base of an ancient basaltic volcano (Richey and Thomas, 1930).

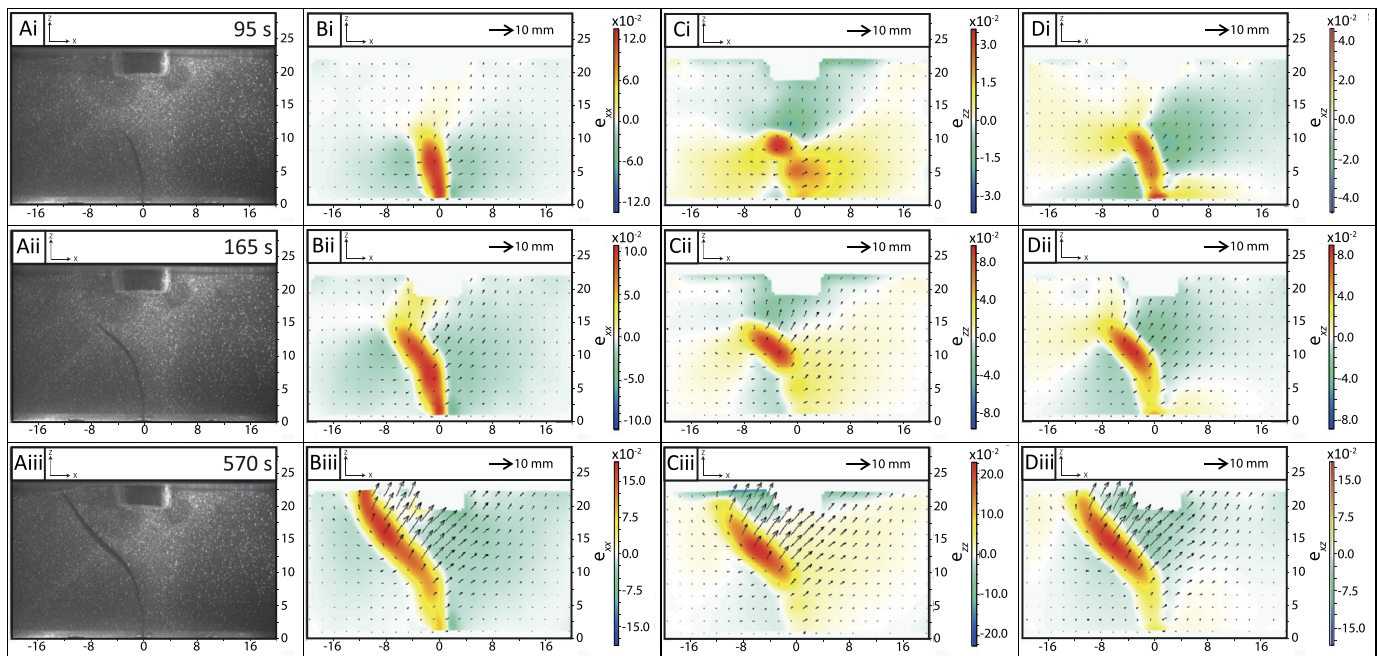


Fig. 4. Three stages of circumferential dike development in the presence of a small caldera, imaged in the x - z plane, with sub-surface total strain (color maps) and displacement (vector arrows) calculated using DIC (Experiment AG-13, see Table 1): i) Stage I: initial sub-vertical dike (95 s), ii) Stage II: inclined sheet (165 s), and iii) Stage III: ascent to eruption (570 s). A) Dewarped experimental images, B) horizontal total normal strain e_{xx} , C) vertical total normal strain e_{zz} , and D) total shear strain component e_{xz} are shown. The red color represents extensional deformation in the normal components and anticlockwise rotational deformation in the shear component. See also Supplementary Video Fig. S1. (For interpretation of the colors in the figure(s), the reader is referred to the web version of this article.)

Circumferential dikes and cone sheet geometries have been studied in previous laboratory experiments. Using a granular material to represent the properties of the brittle crust and a flat topography, Galland et al. (2014) found that cone sheets form when the magma source is shallow with respect to the intrusion's width, or when the injection velocity or viscosity is high. Corbi et al. (2016) created buoyant air-filled dikes in gelatin edifices which had a topographic depression simulating a caldera. Similarly to our experiments, they observed that the unloading stress field leads to the formation of circumferential dikes. They found that magma buoyancy plays a key role in the dike geometry and the eruption location, and our experiments support this work even though we did not include a volcanic edifice. When the unloading stresses were particularly large we found this was able to stop eruption and cause a full-cone sheet to develop, whereas Corbi et al. (2016) did not form cone sheets.

The caldera diameter was the key parameter in determining the outcome of our experiments: circumferential dikes always developed in the presence of the 9 cm caldera diameter, and a spectrum of transitional to cone sheet geometries were associated with the 12 cm caldera diameter topography (see Table 1). Following the approach of Galland et al. (2014), we have analyzed our experiments further by considering the outcomes related to dimensionless Pi-numbers (Fig. 9). The first Pi-number is geometric:

$$\Pi_1 = \frac{h}{d} \quad (11)$$

where h is the depth at which bending of the dike first occurs, and d is the horizontal extent of the intrusion (see Table 1). The second Pi-number considers the fluid-flow properties and extent of unloading stress relative to lithostatic loading:

$$\Pi_2 = \frac{\mu v}{d(P_L - P_U)} \quad (12)$$

where μ is the fluid viscosity, v is the velocity of the fluid, P_L is the lithostatic pressure, and P_U is the unloading pressure due to

the presence of the caldera (see Supplementary Table S1). Fig. 9 shows our experiments occupy three distinct regions in this non-dimensional space, with cone sheets forming at low Π_1 and Π_2 values, circumferential dikes forming at high Π_1 and Π_2 values, and transitional geometries forming at intermediate Π_1 and Π_2 values. Geophysical constraints on parameter values that would populate the Π_1 and Π_2 equations in nature (see Supplementary Table S1 for example) suggest that magnitudes of Π_1 and Π_2 in nature are high compared to our experiments. For example, at Rabaul Volcano in Papua New Guinea (Kennedy et al., 2018) the corresponding Π_1 value is 1.5 and the Π_2 value is 3×10^{-5} . This means, according to our models, the most likely intrusion form geometry at Rabaul Volcano would be circumferential dikes.

5.2. Circumferential dikes and cone sheets in nature

The Ardnamurchan cone sheets are perhaps the most-famous of all cone sheets, but there are contrasting models to explain their origin. Burchardt et al. (2013) used 3D projections to propose that the Ardnamurchan cone sheets originate from a single, elongated and temporally evolving magma chamber. This model is in contrast to Richey and Thomas (1930) who originally proposed three centers, and Magee et al. (2012) who proposed lateral magma flow from an adjacent magmatic source in a compressional stress field. We show experimentally that local unloading stresses can cause an initially vertical dike originating from directly beneath a caldera to stall in the crust and grow laterally to form a cone sheet. This is relevant to the Ardnamurchan central igneous complex, as our model does not require input from neighboring systems to build a cone sheet (in contrast to Magee et al., 2012) and does not make assumptions about the nature of the magma chamber at depth (as is the case in Burchardt et al., 2013). Instead we demonstrate that such geometries could be formed purely due to local unloading stresses. It is unclear whether or not there was a caldera present

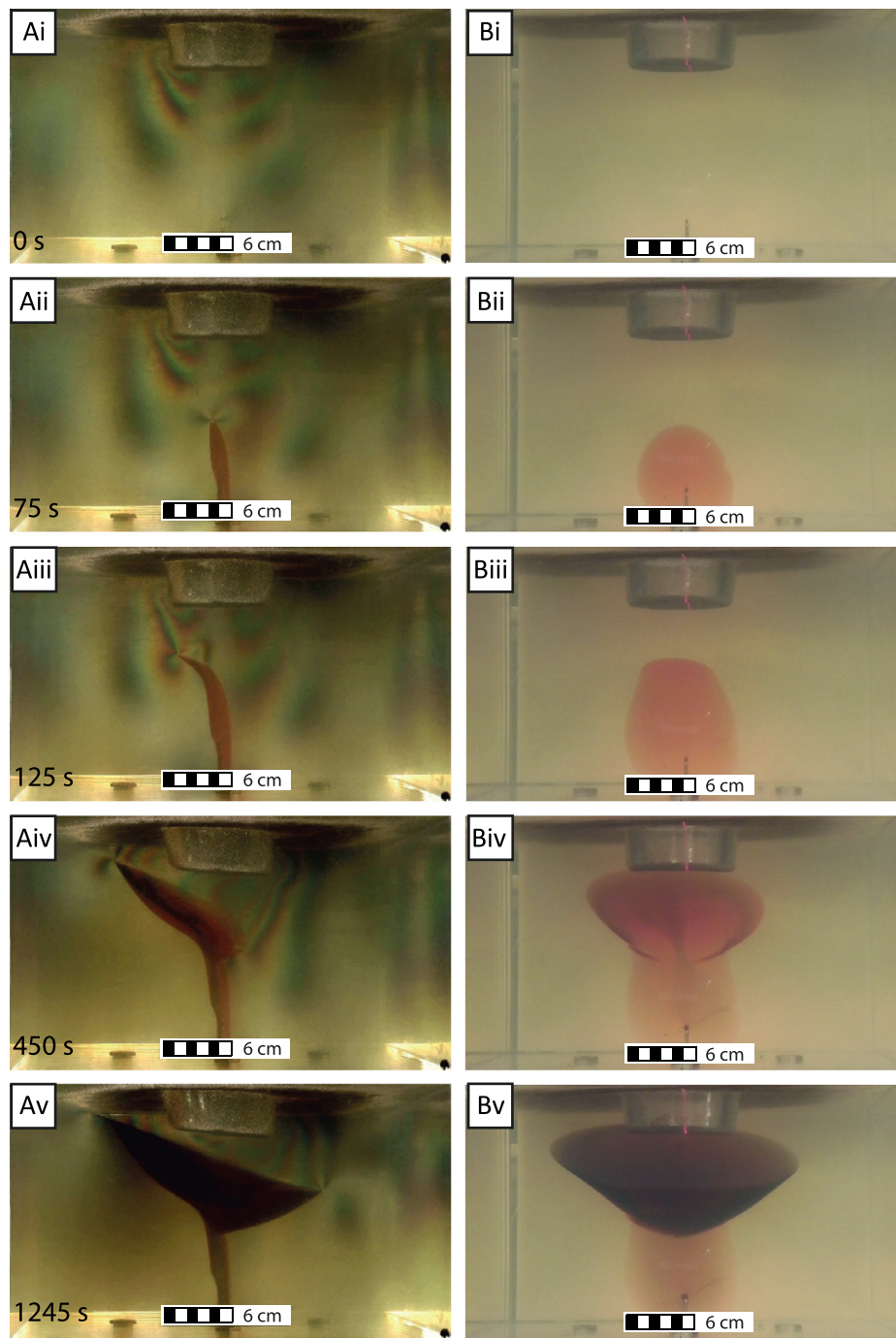


Fig. 5. Photographs of cone sheet development in the presence of a large caldera (Experiment AG-08, see Table 1): A) Polarized light (x - z plane), B) artificial light (y - z plane). i) Pre-injection stress state, ii) Stage I: sub-vertical dike (75 s), iii) Stage II: inclined sheet (125 s), iv) Stage III: lateral growth by en echelon arcuate segments (450 s), and v) Stage IV: cone sheet completion with no eruption (1245 s). See also Supplementary Video Fig. S2.

at the time when the Ardnamurchan cone sheets formed (Brown and Bell, 2006), but calderas are thought to have been present in the region at the time of intrusion (Troll et al., 2000).

Articulated magma intrusion geometries, made up of circumferential sub-vertical dikes close to the caldera rim which dip towards sub-horizontal sills below the caldera floor, have often been needed to fit crustal deformation data at calderas. Geodetic studies of magma intrusion associated with the 2005 circumferential fissure eruption of Fernandina volcano in the Galapagos (summit caldera: 5 km \times 6.5 km) presented pre-eruptive (Bagnardi et al., 2013) and co-eruptive (Chadwick et al., 2011) surface deformation that was recorded using Interferometric synthetic aperture radar

(InSAR). Inverse models of the data suggested the intrusion which fed the eruption had a curved and circumferential laminar geometry and originated from a sill, thus showing similar geometry to our experimental circumferential dikes. The continuous vertical growth and final eruption of our experimental circumferential dike agrees well with the Chadwick et al. (2011) model of intrusion leading to the 2005 eruption of Fernandina (Corbi et al., 2015).

Overall, we suggest that the common modeling assumption of flat geometries, such as planar sheets opening dislocations or cracks, the availability of suitable analytical solutions, and the need to keep the number of model parameters low, may have limited our ability to recognize curved geometries such as those we pro-

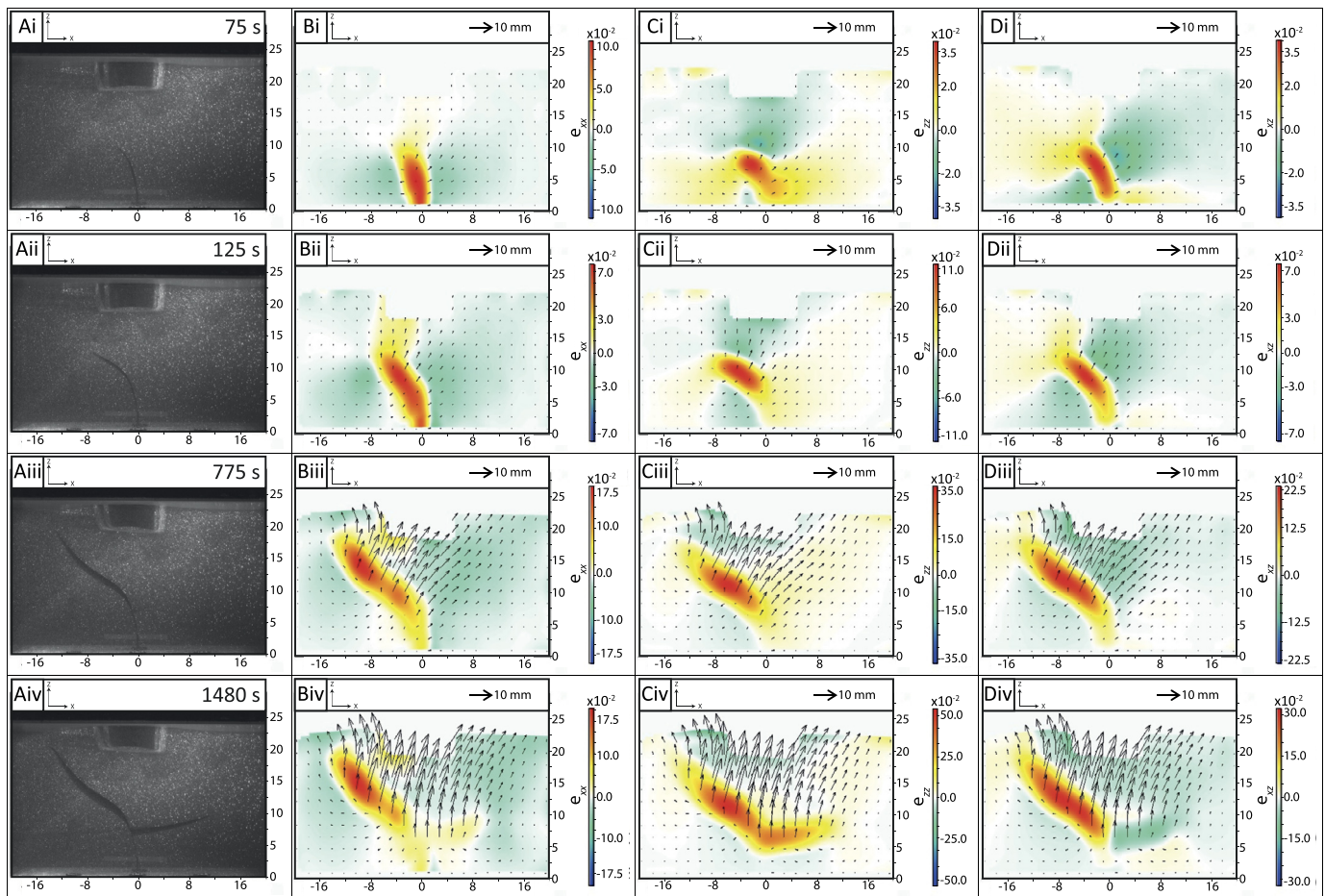


Fig. 6. Cone sheet development in the presence of a large caldera, viewed in the x - z plane, with sub-surface total strain (color maps) and displacement (vector arrows) calculated using DIC (Experiment AG-17, see Table 1). Four stages of cone sheet development are shown: i) Stage I: initial sub-vertical dike (75 s), ii) Stage II: inclined sheet (125 s), iii) Stage III: arrest and increased opening of the inclined sheet (775 s), and iv) Stage IV: cone sheet geometry completion with no eruption (1480 s). A) Dewarped experimental images, B) horizontal total normal strain e_{xx} , C) vertical normal strain e_{zz} , and D) shear strain component e_{xz} . The red color represents extensional deformation in the normal components and anticlockwise rotational deformation in the shear component. See also Supplementary Video Fig. S3. (For interpretation of the colors in the figure(s), the reader is referred to the web version of this article.)

pose here. Deep cone sheet intrusions may produce low-amplitude uplift that may be a satisfyingly fit for pressurized sub-horizontal cracks below the caldera floor, which is a feature ubiquitously found by geophysical and geodetic surveys at calderas worldwide.

5.3. Arcuate segment development and lateral dike growth

Lateral propagation of a circumferential dike has been evidenced by geological records, but rarely from geophysical monitoring. Geological evidence of lateral flow during cone sheet development was found by Magee et al. (2012) using magnetic fabrics preserved within crystalline cone sheets. However, they interpreted this as evidence of magma being sourced from an adjacent magma chamber, but our results show that such crystalline fabrics could result from a cone sheet intrusion whose magma source was directly beneath an unloaded topography. Geophysical evidence of lateral propagation of a circumferential dike firstly came from the 1989 seismic swarm at Mammoth Mountain, Long Valley caldera, California (Prejean et al., 2003) where earthquake hypocenter migration into a ring structure was interpreted as fluid which triggered seismicity on a ring fault, but it would be also consistent with lateral propagation (0.4 km/month) of a conical opening crack filled with magma or other magmatic fluid evidenced by the migration of seismicity over time. Therefore, our model observations are support the interpretation of lateral magma migration recorded by the seismic data. Secondly, reconstructing ground displace-

ment at the pre-eruptive phase in Monte Nuovo, Campi Flegrei caldera (1935 AD), Di Vito et al. (2016) recognized a circumferential source extending from the center, eccentrically towards the caldera rim, that transfers felsic magma laterally to feed eruptions at the caldera margin, which has been the eruptive magma path for the last 5 ka. In the laboratory, both circumferential dikes and cone sheets had their lowest ascent velocities when the dikes were growing at intermediate dip angle (40–80°), and their highest velocities coincided with the lowest and highest dip angles (Fig. 8).

Circumferential lateral propagation was present in the growth of our experimental cone sheet intrusions by the establishment of laterally propagating arcuate segments, and the cone sheet geometry initiated at the bending location of the dike (h). We interpret the development of en echelon arcuate segments in our experiments to be associated with stress rotation, due to the influence of the caldera stress field which causes lateral propagation and crack opening under mixed-mode loading (Mode I and Mode III) thus creating shear at the growing tip (Pollard et al., 1982).

5.4. Limitations of our models

Our experimental approach was not to reproduce the natural complexity of magma intrusion in the presence of calderas, but to focus on the effect of the magnitude and extent of the unloading stress on the type of intrusion formed and how it grew. Inelastic host-rock deformation was not considered in our mod-

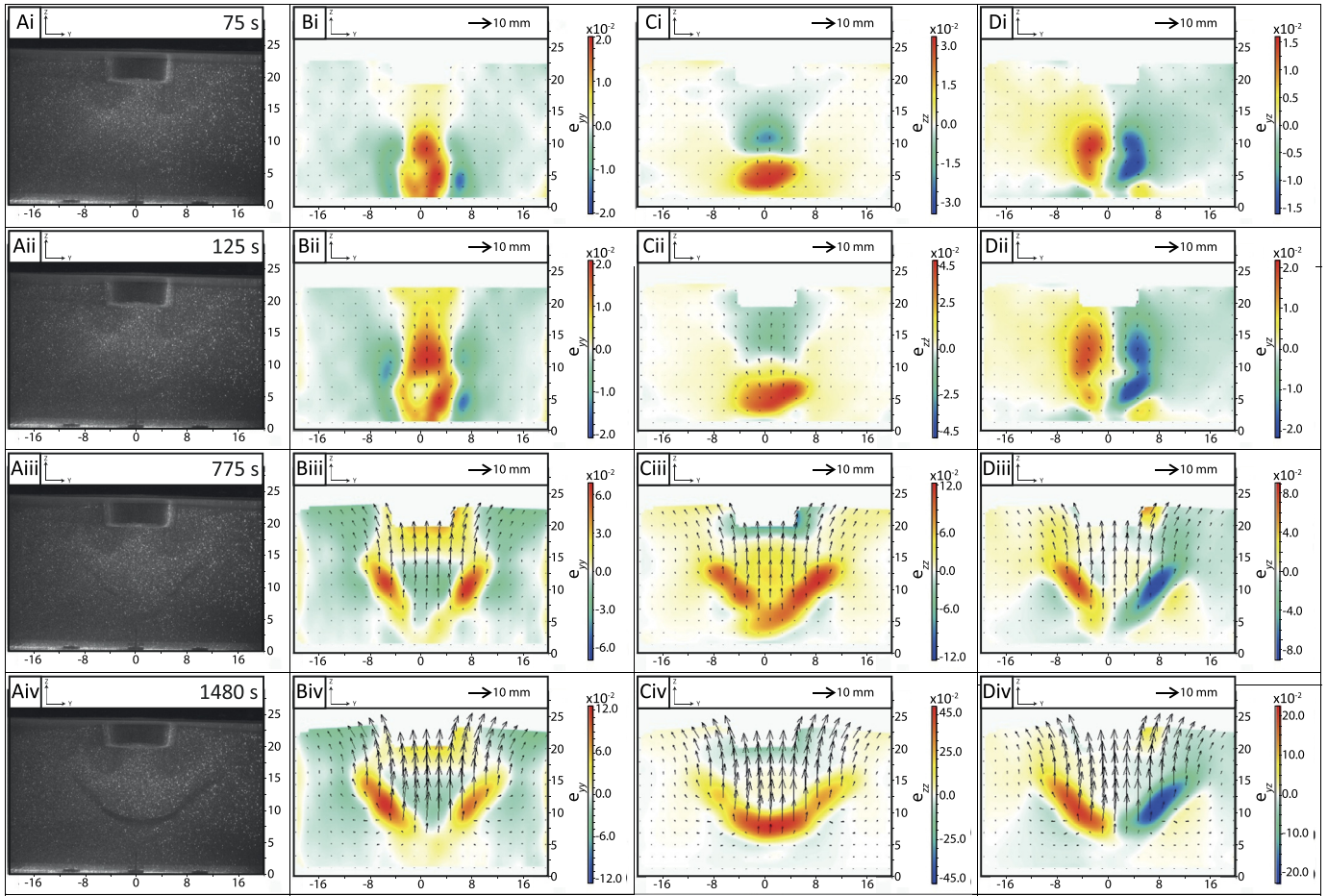


Fig. 7. Cone sheet development in the presence of a large caldera, viewed in the y - z plane, with sub-surface total strain (color maps) and displacement (vector arrows) calculated using DIC (Experiment AG-19, see Table 1). Four stages of cone sheet development are shown: i) Stage I: initial sub-vertical dike (75 s), ii) Stage II: inclined sheet (125 s), iii) Stage III: arrest and increased opening of the inclined sheet (775 s), and iv) Stage IV: cone sheet geometry completion with no eruption (1480 s). A) Dewarped experimental images, B) horizontal normal strain e_{yy} , C) vertical normal strain e_{zz} , and D) shear strain component e_{yz} . The red color represents extensional deformation in the normal components and anticlockwise rotational deformation in the shear component. See also Supplementary Video Fig. S4. (For interpretation of the colors in the figure(s), the reader is referred to the web version of this article.)

els, and yet this may be important in the shallow crust and in a caldera setting in particular, where rocks may have been damaged due to the caldera-forming process (see Galland et al., 2018 for a review). On a local scale, an inelastic host-rock rheology may dampen the transference of rock deformation signals, due to local compaction and grain rotation, and may increase the possibility of dike segmentation occurring. We did not consider rock layering, yet volcanic settings are likely to be mechanically variable, and previous work has demonstrated how rigidity layering can promote the formation of sills beneath a rigid layer (Kavanagh et al., 2006). Calderas also have fault systems that are likely to influence magma propagation (Browning and Gudmundsson, 2015). Recent experimental work using particle image velocimetry (Kavanagh, 2018; Kavanagh et al., 2018b) to model magma flow in dikes is challenging existing dike propagation models, and demonstrates how consideration of the host rock deformation and the magma flow dynamics are needed to develop the next generation of dike emplacement models. The additional impacts of faults, mechanical layering and magma flow dynamics on magma propagation in caldera settings should be the focus of future multidisciplinary and experimental work.

6. Conclusions

We produced experimental circumferential dikes which erupted, and intrusive cone sheets that grew by lateral propagation of en

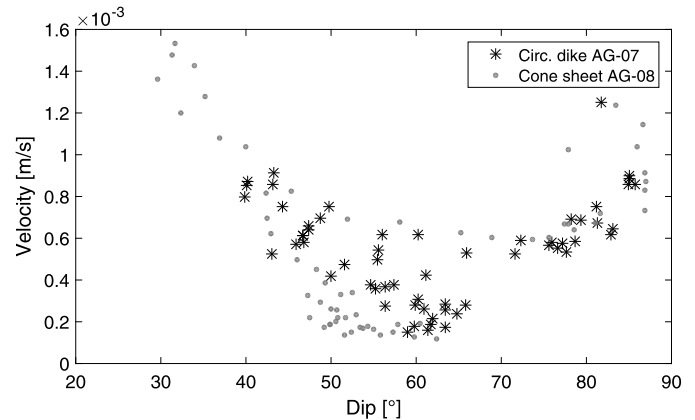


Fig. 8. The local dip angle relative to vertical ascent velocity for circumferential dike (AG-07) and cone sheet development (AG-08). See Table 1 for experimental conditions.

echelon arcuate dike segments. Both originated from a single dike beneath a caldera-like topography in an elastic material. We also formed transitional geometries that were intermediate to these end-member forms. Circumferential dike and cone sheet intrusion dynamics occurred in stages of development which are reflected by their geometric (dip angle), kinematic (velocity) and dynamic (stress and strain) evolution. We identified 3 stages of circumfer-

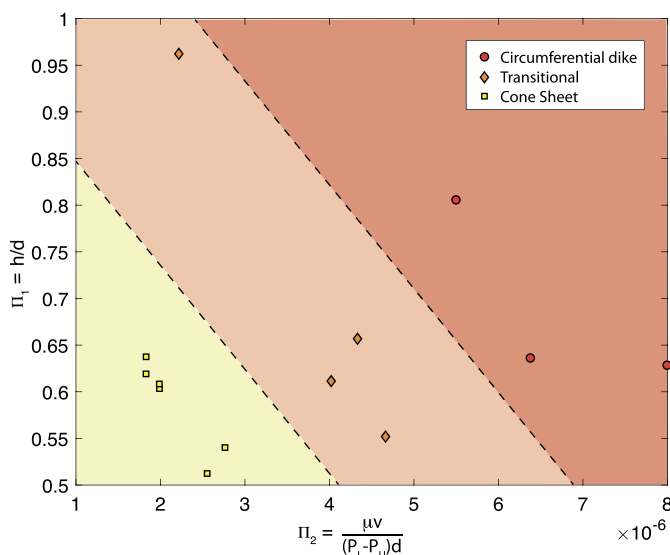


Fig. 9. Dimensionless phase diagram presenting the range of intrusion geometries formed in the experiments: circumferential dikes (red circles), Transitional geometries (orange diamonds) and cone sheets (yellow squares). The dimensionless parameters represent the model conditions $\Pi_1 = h/d$ and $\Pi_2 = \mu\nu/(P_L - P_U)d$. The cone sheets and circumferential dikes plot in distinct fields with transitional geometries formed in the intermediate zone.

ential dike development (I. Sub-vertical dike; II. Inclined sheet; III. Ascent to erupt) and 4 stages of cone sheets (I. Sub-vertical dike; II. Inclined sheet; III. Lateral growth by arcuate en echelon dike segments, and IV. Completion of the cone sheet). Our results show there are many similarities between the dynamics of cone sheets and circumferential dikes. Our summative dimensionless phase diagram suggests that their occurrence can be related to geometric, fluid flow, and lithospheric unloading conditions.

We have proposed a new origin and emplacement for cone sheets that originate from purely vertical dike growth. However, our analysis suggests that conditions in nature seem to be unfavorable for cone sheets to form due to crustal unloading in a caldera setting, and that circumferential dikes and transitional-cone sheet geometries are more likely to form. Our models can help the interpretation of InSAR, GPS and seismic data from active systems, and contribute to the production of more accurate models of magma sources beneath calderas. An important new implication of our models for volcano monitoring is that the conditions for circumferential dike formation appear to be more prevalent in nature. Significantly, it may not be possible to distinguish whether an intrusion will be likely to erupt or not until it has propagated into the shallow crust, which is when it is also likely to be propagating at its fastest rate. This new understanding of magma intrusion dynamics will help to reconstruct the history of ancient calderas, and to forecast unrest and eruptions in active ones.

Acknowledgements

This research was supported by the GFZ German Research Centre for Geosciences and the ERC Volcapse project, and by the program Forschungsstipendium für Doktorat from Deutscher Akademischer Austausch Dienst DAAD awarded to AG. AG and SHH wish particular thanks to members of the Liverpool MAGMA Laboratory Elliot Wood and Simon Martin for their assistance in the development of this work. SHH acknowledges support from the Malaysian Government and the National University of Malaysia. AG especially thanks to Mehdi Nikkhoo for long discussions and advice related to this work and other topics and for help with conducting earlier models. We thank Steffi Burchardt and Craig Magee for

thoughtful reviews which improved the manuscript, and we thank Tamsin Mather for editorial support.

Appendix A. Supplementary material

Supplementary material related to this article can be found online at <https://doi.org/10.1016/j.epsl.2018.12.016>.

References

- Anderson, E.M., 1936. The dynamics of the formation of cone-sheets, ring dykes, and caldron-subsidence. *Proc. R. Soc. Edinb.* 56, 128–163. <https://doi.org/10.1017/S0370164600014954>.
- Bagnardi, M., Amelung, F., Poland, M.P., 2013. A new model for the growth of basaltic shields based on deformation of Fernandina volcano, Galápagos Islands. *Earth Planet. Sci. Lett.* 377–378, 358–366. <https://doi.org/10.1016/j.epsl.2013.07.016>.
- Blundy, J., Mavrogenes, J., Tattitch, B., Sparks, S., Gilmer, A., 2015. Generation of porphyry copper deposits by gas-brine reaction in volcanic arcs. *Nat. Geosci.* 8, 235–240. <https://doi.org/10.1038/ngeo2351>.
- Brown, D., 2012. Tracker video analysis and modeling tool for physics education [www document]. <http://physlets.org/tracker/>. (Accessed 21 September 2017).
- Brown, D.J., Bell, B.R., 2006. Intrusion-induced uplift and mass wasting of the Paleogene volcanic landscape of Ardnamurchan, NW Scotland. *J. Geol. Soc. Lond.* 163, 29–36. <https://doi.org/10.1144/0016-764905-016>.
- Browning, J., Gudmundsson, A., 2015. Caldera faults capture and deflect inclined sheets: an alternative mechanism of ring dike formation. *Bull. Volcanol.* 77 (4). <https://doi.org/10.1007/s00445-014-0889-4>.
- Burchardt, S., Tanner, D.C., Troll, V.R., Krumbholz, M., Gustafsson, L.E., 2011. Three-dimensional geometry of concentric intrusive sheet swarms in the Geitafell and the Dyrfjöll volcanoes eastern Iceland. *Geochem. Geophys. Geosyst.* 12, 1–21. <https://doi.org/10.1029/2011GC003527>.
- Burchardt, S., Troll, V.R., Mathieu, L., Emeleus, H.C., Donaldson, C.H., 2013. Ardnamurchan 3D cone-sheet architecture explained by a single elongate magma chamber. *Sci. Rep.* 3, 1–7. <https://doi.org/10.1038/srep02891>.
- Burchardt, S., Walter, T.R., Tuffen, H., 2018. Growth of a volcanic edifice through plumbing system processes—volcanic rift zones, magmatic sheet-intrusion swarms and long-lived conduits. In: *Volcanic and Igneous Plumbing Systems*, pp. 89–112.
- Carmichael, R.S., Klein, C., 2018. Rock [www document]. *Encycl. Br. Inc.* <https://www.britannica.com/science/rock-geology>. (Accessed 26 July 2018).
- Chadwick, W.W., Jónsson, S., Geist, D.J., Poland, M., Johnson, D.J., Batt, S., Harpp, K.S., Ruiz, A., 2011. The May 2005 eruption of Fernandina volcano, Galápagos: the first circumferential dike intrusion observed by GPS and InSAR. *Bull. Volcanol.* 73, 679–697. <https://doi.org/10.1007/s00445-010-0433-0>.
- Cole, J.W., Milner, D.M., Spinks, K.D., 2005. Calderas and caldera structures: a review. *Earth-Sci. Rev.* 69, 1–26. <https://doi.org/10.1016/j.earscirev.2004.06.004>.
- Corbi, F., Rivalta, E., Pinel, V., Maccaferri, F., Acocella, V., 2016. Understanding the link between circumferential dikes and eruptive fissures around calderas based on numerical and analog models. *Geophys. Res. Lett.* 43, 6212–6219. <https://doi.org/10.1002/2016GL068721>.
- Corbi, F., Rivalta, E., Pinel, V., Maccaferri, F., Bagnardi, M., Acocella, V., 2015. How caldera collapse shapes the shallow emplacement and transfer of magma in active volcanoes. *Earth Planet. Sci. Lett.* 431, 287–293. <https://doi.org/10.1016/j.epsl.2015.09.028>.
- Crisp, J., 1952. The use of gelatin models in structural analysis. *Proc. IB Inst. Mech. Eng.* 12, 580–604.
- Di Giuseppe, E., Funicello, F., Corbi, F., Ranalli, G., Mojoli, G., 2009. Gelatins as rock analogs: a systematic study of their rheological and physical properties. *Tectonophysics* 473, 391–403. <https://doi.org/10.1016/j.tecto.2009.03.012>.
- Di Vito, M.A., Acocella, V., Aiello, G., Barra, D., Battaglia, M., Carandente, A., Del Gaudio, C., De Vita, S., Ricciardi, G.P., Ricco, C., Scandone, R., Terrasi, F., 2016. Magma transfer at Campi Flegrei caldera (Italy) before the 1538 AD eruption. *Sci. Rep.* 6, 32245. <https://doi.org/10.1038/srep32245>.
- Fleet, D., Weiss, Y., 2006. Optical flow estimation. In: Paragios, N., Chen, Y., Faugeras, O. (Eds.), *Handbook of Mathematical Models in Computer Vision*. Springer US, Boston, MA, pp. 239–257.
- Galland, O., Bertelsen, H.S., Eide, C.H., Guldstrand, F., Haug, Ø.T., Leanza, H.A., Mair, K., Palma, O., Planke, S., Rabbel, O., Rogers, B., Schmiedel, T., Souche, A., Spacapan, J.B., 2018. Storage and transport of magma in the layered crust—formation of sills and related flat-lying intrusions. In: *Volcanic and Igneous Plumbing Systems*, pp. 113–138.
- Galland, O., Burchardt, S., Hallot, E., Mourgues, R., Bulois, C., 2014. Dynamics of dikes versus cone sheets in volcanic systems. *J. Geophys. Res., Solid Earth*, 6178–6192. <https://doi.org/10.1002/2014JB011059>.Received.
- Gercek, H., 2007. Poisson's ratio values for rocks. *Int. J. Rock Mech. Min. Sci.* <https://doi.org/10.1016/j.ijrmm.2006.04.011>.

- Geshi, N., 2005. Structural development of dike swarms controlled by the change of magma supply rate: the cone sheets and parallel dike swarms of the Miocene Otago igneous complex, Central Japan. *J. Volcanol. Geotherm. Res.* 141 (3), 267–281.
- Gudmundsson, A., 2006. How local stresses control magma-chamber ruptures, dyke injections, and eruptions in composite volcanoes. *Earth-Sci. Rev.* 79, 1–31. <https://doi.org/10.1016/j.earscirev.2006.06.006>.
- Guldstrand, F., Burchardt, S., Hallot, E., Galland, O., 2017. Dynamics of surface deformation induced by dikes and cone sheets in a cohesive Coulomb Brittle crust. *J. Geophys. Res., Solid Earth* 122, 8511–8524. <https://doi.org/10.1002/2017JB014346>.
- Jellinek, A.M., DePaolo, D.J., 2003. A model for the origin of large silicic magma chambers: precursors of caldera-forming eruptions. *Bull. Volcanol.* 65, 363–381. <https://doi.org/10.1007/s00445-003-0277-y>.
- Johnson, S.E., Paterson, S.R., Tate, M.C., 1999. Structure and emplacement history of a multiple-center, cone-sheet bearing ring complex: the Zarza Intrusive Complex, Baja California, Mexico. *Geol. Soc. Am. Bull.* 111, 607–619.
- Kavanagh, J.L., 2018. Mechanisms of magma transport in the upper crust—dyking. In: *Volcanic and Igneous Plumbing Systems*, pp. 55–88.
- Kavanagh, J.L., Boutelier, D., Cruden, A.R., 2015. The mechanics of sill inception, propagation and growth: experimental evidence for rapid reduction in magmatic overpressure. *Earth Planet. Sci. Lett.* 421, 117–128. <https://doi.org/10.1016/j.epsl.2015.03.038>.
- Kavanagh, J.L., Burns, A.J., Hazim, S.H., Wood, E.P., Martin, S.A., Hignett, S., Dennis, D.J., 2018a. Challenging dyke ascent models using novel laboratory experiments: implications for reinterpreting evidence of magma ascent and volcanism. *J. Volcanol. Geotherm. Res.* 354, 87–101.
- Kavanagh, J.L., Engwell, S.L., Martin, S.A., 2018b. A review of laboratory and numerical modelling in volcanology. *Solid Earth* 9, 531–571. <https://doi.org/10.5194/se-9-531-2018>.
- Kavanagh, J.L., Menand, T., Daniels, K.A., 2013. Gelatine as a crustal analogue: determining elastic properties for modelling magmatic intrusions. *Tectonophysics* 582, 101–111. <https://doi.org/10.1016/j.tecto.2012.09.032>.
- Kavanagh, J.L., Menand, T., Sparks, R.S.J., 2006. An experimental investigation of sill formation and propagation in layered elastic media. *Earth Planet. Sci. Lett.* 245, 799–813. <https://doi.org/10.1016/j.epsl.2006.03.025>.
- Kennedy, B.M., Holohan, E.P., Stix, J., Gravley, D.M., Davidson, J.R.J., Cole, J.W., 2018. Magma plumbing beneath collapse caldera volcanic systems. *Earth-Sci. Rev.* 177, 404–424. <https://doi.org/10.1016/j.earscirev.2017.12.002>.
- Kervyn, M., Ernst, G.G.J., Van Wyk De Vries, B., Mathieu, L., Jacobs, P., 2009. Volcano load control on dyke propagation and vent distribution: insights from analogue modeling. *J. Geophys. Res.* 114, 26. <https://doi.org/10.1029/2008JB005653>.
- Le Bas, M.J., 1987. Nephelinites and carbonatites. *Geol. Soc. (Lond.), Spec. Publ.* 30, 53–83. <https://doi.org/10.1144/GSL.SP.1987.030.01.05>.
- Maccaferri, F., Bonafede, M., Rivalta, E., 2011. A quantitative study of the mechanisms governing dike propagation, dike arrest and sill formation. *J. Volcanol. Geotherm. Res.* 208, 39–50. <https://doi.org/10.1016/j.jvolgeores.2011.09.001>.
- Magee, C., Stevenson, C., O'Driscoll, B., Schofield, N., McDermott, K., 2012. An alternative emplacement model for the classic Ardnamurchan cone sheet swarm, NW Scotland, involving lateral magma supply via regional dykes. *J. Struct. Geol.* 43, 73–91. <https://doi.org/10.1016/j.jsg.2012.08.004>.
- Mathieu, L., Burchardt, S., Troll, V.R., Krumbholz, M., Delcamp, A., 2015. Geological constraints on the dynamic emplacement of cone-sheets—the Ardnamurchan cone-sheet swarm, NW Scotland. *J. Struct. Geol.* 80, 133–141. <https://doi.org/10.1016/j.jsg.2015.08.012>.
- Mathieu, L., van Wyk de Vries, B., Holohan, E.P., Troll, V.R., 2008. Dykes, cups, saucers and sills: analogue experiments on magma intrusion into brittle rocks. *Earth Planet. Sci. Lett.* 271, 1–13. <https://doi.org/10.1016/j.epsl.2008.02.020>.
- McLeod, P., Tait, S., 1999. The growth of dykes from magma chambers. *J. Volcanol. Geotherm. Res.* 92, 231–245. [https://doi.org/10.1016/S0377-0273\(99\)00053-0](https://doi.org/10.1016/S0377-0273(99)00053-0).
- Merle, O., 2015. The scaling of experiments on volcanic systems. *Front. Earth Sci.* 3, 1–15. <https://doi.org/10.3389/feart.2015.00026>.
- Murase, T., McBirney, A.R., 1973. Properties of some common igneous rocks and their melt at high temperatures. *Geol. Soc. Am. Bull.* 84, 3563–3592. [https://doi.org/10.1130/0016-7606\(1973\)84%3C3563:POSCIR%3E2.0.CO;2](https://doi.org/10.1130/0016-7606(1973)84%3C3563:POSCIR%3E2.0.CO;2).
- Pallister, J., Hoblitt, R., Meeker, G., 1996. Magma mixing at Mount Pinatubo: petrographic and chemical evidence from the 1991 deposits. In: *Fire Mud: Eruptions and Lahars of Mount Pinatubo, Philippines*, pp. 1–27.
- Pollard, D.D., Segall, P., Delaney, P.T., 1982. Formation and interpretation of dilatation echelon cracks. *Geol. Soc. Am. Bull.* 93, 1291–1303. [https://doi.org/10.1130/0016-7606\(1982\)93<1291:FAIODE>2.0.CO](https://doi.org/10.1130/0016-7606(1982)93<1291:FAIODE>2.0.CO).
- Prejean, S., Stork, A., Ellsworth, W., Hill, D., Julian, B., 2003. High precision earthquake locations reveal seismogenic structure beneath Mammoth Mountain, California. *Geophys. Res. Lett.* 30. <https://doi.org/10.1029/2003GL018334>.
- Richey, J., Thomas, H., 1930. The geology of Aardnamurchan, North-West Mull and Coll: memoir for geological sheet 51, part 52 (Scotland). HM Stationery Office.
- Rivalta, E., Taisne, B., Bungler, A.P., Katz, R.F., 2015. A review of mechanical models of dike propagation: schools of thought, results and future directions. *Tectonophysics* 638, 1–42. <https://doi.org/10.1016/j.tecto.2014.10.003>.
- Schirnick, C., Van Den Bogaard, P., Schmincke, H.U., 1999. Cone sheet formation and intrusive growth of an oceanic island—the Miocene Tejada complex on Gran Canaria (Canary Islands). *Geology* 27, 207–210. [https://doi.org/10.1130/0091-7613\(1999\)027<0207:CSFAIG>2.3.CO;2](https://doi.org/10.1130/0091-7613(1999)027<0207:CSFAIG>2.3.CO;2).
- Sutton, M., Wolters, W., Peters, W., Ranson, W., McNeill, S., 1983. Determination of displacements using an improved digital correlation method. *Image Vis. Comput.* 1, 133–139. [https://doi.org/10.1016/0262-8856\(83\)90064-1](https://doi.org/10.1016/0262-8856(83)90064-1).
- Taisne, B., Tait, S., 2009. Eruption versus intrusion? Arrest of propagation of constant volume, buoyant, liquid-filled cracks in an elastic, brittle host. *J. Geophys. Res., Solid Earth* 114, B06202. <https://doi.org/10.1029/2009JB006297>.
- Takada, A., 1990. Experimental study on propagation of liquid-filled crack in gelatin: shape and velocity in hydrostatic stress condition. *J. Geophys. Res.* 95, 8471. <https://doi.org/10.1029/JB095iB06p08471>.
- Troll, V.R., Emeleus, C.H., Donaldson, C.H., 2000. Caldera formation in the Rum Central Igneous Complex, Scotland. *Bull. Volcanol.* 62, 301–317. <https://doi.org/10.1007/s004450000099>.
- USGS, H.V.O., 2018. Preliminary Analysis of the Ongoing Lower East Rift Zone (LERZ) Eruption of Kilauea Volcano: Fissure 8 Prognosis and Ongoing Hazards.
- Watanabe, T., Masuyama, T., Nagaoka, K., Tahara, T., 2002. Analog experiments on magma-filled cracks: competition between external stresses and internal pressure. *Earth Planets Space* 54, 1247–1261. <https://doi.org/10.1186/BF03352453>.